Rates and Mechanism of Changing in Rock Properties Due to Weathering of Sandstone Gravel

Ken-ichi NISHIYAMA

A dissertation submitted to the Doctoral Program
in Geoscience, the University of Tsukuba
in partial fulfillment of the requirements
for the degree of Doctor of Philosophy (Science)

Contents

Abstract

Temporal changes in colour as well as mineralogical, chemical, physical and mechanical properties due to weathering during 350,000 years were examined using sandstone gravel in fluvial terrace deposits with a known emergence time that were distributed in Miyazaki Plain, South Kyushu. The time between the age of each terrace formation (20, 70, 90, 110, 120, 250 and 350 ka) and the present was assumed to be the weathering period. Naked-eye observation shows that (1) no weathering rind is found in whole cut sections and (2) younger gravels (70-, 110-, 120-ka gravels) and older ones (250- and 350-ka gravels) have a yellowish and reddish colour, respectively.

The main results of the measurements are as follows: (1) According to the observation of mineral texture in thin sections, pore volume increases as the weathering period increases, and connected pores form in the matrix of sandstone; (2) matrix minerals such as illite, kaolinite and chlorite gradually decrease as the weathering period increases; (3) the a^*-value of the colour index increased from the period of 120 to 350 ka, and the b^*-value increased during the period of 0 to 120 ka; (4) visible diffuse reflectance increases in the zone of longer wavelengths in older gravels; (5) chemical composition of SiO_2, K_2O, MgO, Na_2O and CaO gradually decrease as the weathering period increases, while $FeO+Fe_2O_3$ and Al_2O_3 are constant during 350 ka; (6) X-ray computed tomography (CT) images are homogeneous in the whole cross section, and weathering rinds cannot be recognised; (7) the *CT*-value decreases as the weathering period increases; (8) specific gravity decreases but effective porosity increases as the weathering period increases; (9) pore radius and pore volume increase as the weathering period increases, and in particular, pore radius increased rapidly from the period of 110 to 120 ka; (10) specific surface area changes occurred at a constant rate during 350 ka; (11) the results of energy dispersive X-ray spectrometry (EDS) analysis show

that Fe concentrates in the matrix of sandstone and Si and alkali elements leach as the weathering period increases; and (12) the rock strength index decreases drastically from the period of 0 to 120 ka.

Taken together, these results suggest that (1) the increase in pores in gravel that occurs as the weathering period increases is caused by the leaching of matrix material, that is, decreasing SiO_2 and alkali elements; (2) iron concentration and the formation of goethite and hematite occur in older gravels, which is compatible with the evidence that the colour of the older gravel changes from yellowish to reddish; (3) connected pores formed owing to the leaching of matrix minerals; (4) the distribution of pores is homogeneous in the whole of gravel, so a weathering rind cannot be recognised; and (5) while pore size and pore volume increase as the weathering period increases, owing to the fact that winding pores are rare, the rate of change of a specific surface area and the chemical weathering indices are constant during 350 ka. In summary, leaching of matrix materials and increasing pore volume play major roles in the weathering of sandstone.

Key words: weathering, weathering rate, sandstone, rock properties, pore structure, terrace deposits, Miyazaki Plain

List of Tables

Table **Page**

List of Figures

Figure **Page**

1. Introduction

1.1. Previous researches on weathering and weathering rates

Weathering influences the processes and rates of landform development. The study of these processes and rates of rock weathering is important for understanding geomorphology. Moreover, problems concerning rock weathering are widespread and affect many other research fields in earth sciences and engineering such as mineralogy, geochemistry, soil science, engineering geology, petroleum geology and civil engineering.

The weathering process has been classified into three types: (1) physical weathering, (2) chemical weathering and (3) biological weathering (e.g., Ollier, 1984; Yatsu, 1988). Physical weathering consists of processes such as wet-dry slaking, salt weathering and frost action. This type of weathering has been studied by many researchers (e.g., Goudie, 1970; Fookes et al., 1971; Baynes, 1978; Koroneous, et al., 1980; McGreevy, 1981; Lautridou and Ozouf, 1982; Hall and Hall, 1996). Chemical weathering consists of processes such as mineral alteration, solution, oxidation, and hydration, and this type of weathering has also has been studied by many researchers (e.g., Ruxton, 1968; Huang, 1973; Drever, 1985; Harnois, 1988; Cooke and Doornkamp, 1990; Jayawardena and Izawa, 1994). Biological weathering consists of processes such as burrowing plants and animals and bacterial activity. Biological weathering has also been studied extensively (e.g., Webley et al., 1963; Krumbein, 1978; Dorn and Oberlander, 1981; Grote et al., 1981).

The study of weathering was classified into the following three types by Matsukura (1994): (1) the process of weathering (the mechanism of weathering), (2) weathering products and changes in rock properties, and (3) rates of weathering. Many studies on weathering processes have been accumulated through laboratory experiments on chemical weathering (e.g.,

Berner et al., 1980; Lagasa, 1984) and experiments on physical weathering (e.g., Cooke and Smalley, 1968; Matsukura and Yatsu, 1982). Most of the experimental approaches are carried out to monitor short-term weathering processes. The approach to long-term weathering processes and their relation to geomorphic processes needs to be discussed using weathering products observed in the field. For example, Suzuki et al. (1977) and Matsukura et al. (1981) have studied vertical changes in rock properties of granites due to weathering. However, these works on weathering profiles have not been written with the intention to estimate long-term weathering rates because of the difficulty in time estimation.

The meaning of the term 'weathering rates' varies among researchers (Yatsu, 1981; Matsukura, 1994). In some studies, the term has been used as a synonym for chemical denudation rates (Colman and Dethier, 1986; Matsukura and Hirose, 1999), while other studies use the term to indicate the changing rates of rock properties due to weathering (Kimiya, 1975a,b; Crook and Gliespie, 1986; Oguchi et al., 1994, 1996, 1999a,b; Suzuki and Hachinohe, 1995; Sunamura, 1996; White et al., 1998; Hachinohe et al., 1999a,b). These researchers estimated the weathering period using fluvial and marine terrace deposits and lava domes. This type of research became possible through the recent development of the Quaternary stratigraphy and dating methods. However, studies on the changes in rock properties due to mineralogical, chemical, physical and mechanical weathering have been limited in number (e.g., Chigira and Sone, 1991; Oguchi et al., 1999a,b; Hachinohe et al., 1999a,b).

Analyses of the mechanical, physical and chemical properties of weathering products are also important because these rock properties are closely related to each other. For example, chemical changes often result in the reduction of rock strength (Matsukura et al., 1983; Oguchi and Matsukura, 1996). So far a limited number of studies (Saito et al., 1974a,b; Oguchi et al., 1994) have investigated chemical and/or mineralogical properties along with

mechanical and/or physical properties. Further investigation is necessary to estimate the changing rock properties due to weathering.

1.2. Previous researches on weathering of sandstone

Sandstone is composed of four principal ingredients: (1) quartz grains, (2) feldspar grains, (3) rock fragments and (4) matrix and/or cement. The matrix consists of clay minerals that fill pores during diagenesis. Sandstone is divided into arenite-type and wacke-type. Arenite-type is sandstone containing less than 15% fine-grained matrix, while wacke-type contains more than 15% fine-grained matrix.

The physical properties of sandstone have been studied from the viewpoint of petroleum geology by many researchers (e.g., Scholle, 1979; Doyen, 1988; Krohn, 1988a,b; Uchida and Tada, 1992). These studies discussed the pore geometry and permeability of sandstone as a simulation model of an oil reservoir.

Previous studies on the weathering processes of sandstone have been limited in number (e.g., Bell, 1978; Chigira and Sone, 1988a,b, 1991; Pentecost, 1991; Robinson and Williams, 1994; Urusay et al., 1994; Halsey, 1996; Tugrul and Zarif, 1998; Butenuth et al., 1998; Bell and Rinsay, 1999), and research involving measuring rock properties as a way of researching the weathering process has been even more limited (Chigira and Sone, 1988a,b, 1991). Table 1 shows some studies dealing with the changes in rock properties due to weathering. Chigira and Sone (1991) discussed the chemical weathering of sandstone cemented by zeolite in detail. In that same study, they showed that changes in rock properties due to weathering are caused by zeolite dissolution and iron precipitation in matrix. Thus leaching of zeolite plays an important role in the changes in rock properties due to weathering. Since Chigira and Sone (1991) discussed only tuffaceous

sandstone cemented by zeolite, it is not clear that their conclusion can be applied to different kinds of sandstone.

Studies on the weathering rates of sandstone have been limited in number (e.g., Matsukura and Matsuoka, 1996; Hachinohe et al., 1999). Further investigation is necessary to evaluate the rates and mechanisms of sandstone weathering.

1.3. The purpose of this study

Clarifying the rates and mechanism of sandstone weathering is necessary for researchers working in the earth sciences because sandstone is widely distributed in earth's land surface. The review of previous studies on this subject shows that the rates and mechanism of sandstone weathering are not well understood. In order to solve the rates and mechanism of sandstone weathering, this study investigates the rock properties of sandstone gravel taken from terrace deposits in a series of dated fluvial terraces in the Miyazaki Plain. The rates of long-term weathering are estimated based on the assumption that the weathering period is equal to the period between the age of emergence of these terraces and the present. This study can discuss the changes in rock properties due to weathering during 350 ka.

The measured sandstone properties include the following: (1) rock texture and mineralogical properties (observation of thin sections, mineral compositions using X-ray diffraction and visible diffuse spectra), (2) colours, (3) physical properties (effective porosity, pore-size distribution, specific surface area, permeability and distribution of density), (4) chemical properties (chemical compositions using X-ray fluorescence analysis and distributions of chemical elements using energy dispersive X-ray spectrometry) and (5) mechanical properties (point load strength). Using these data, the relationships between rock properties and weathering period

in an attempt to clarify the rates and mechanism of weathering of sandstone gravel.

2. Geomorphological and geological setting of Miyazaki Plain.

2.1. Geomorphological and climatological setting of the Miyazaki Plain

The Miyazaki Plain is located along the Pacific coast of Southeast Kyushu (Fig. 1). On the northwest side of the Miyazaki Plain lie the Kyushu Mountains, which are chiefly composed of Mesozoic to Cenozoic sedimentary complex. The plain has an area of ca. 900 km^2 and altitudes from 0 to 200 m above sea level. Three large rivers (Omaru, Hitotsuse and Ohyodo) flow across the plain from northwest to southeast.

Many terrace surfaces are developed in the Miyazaki Plain, as described later. Paleo red soils are widespread in South Kyushu (Fig. 2), and some of the terrace deposits are topped with paleo red soils. Tephrochronological investigations have indicated that all of the paleo red soils were formed in the middle Pleistocene. Paleo red soils are considered to have been formed under the warmer climate during the interglacial stages in the middle Pleistocene (e.g., Matsui and Kato, 1962).

Figure 3 summarises the meteorological data at the Miyazaki Meteorological Station (31° 55' N, 131° 25' E. 6.3 m a.s.l.), located 10 km south of the studied area. The mean air temperature is 6.8 ℃ in the coldest month (January), 27.2℃ in the warmest month (August) and 17.0℃ through the year. The average annual precipitation is 2434.6 mm (Natural Astronomical Observatory, 1995).

2.2. Quaternary stratigraphy and tephrochronology of the Miyazaki Plain

The Miyazaki Plain (Fig. 1) has the best-developed middle to late Quaternary deposits in Kyushu. The stratigraphy of this plain has been

investigated in previous studies (e.g., Otsuka, 1930a,b; Endo, 1968; Hoshino, 1971; Kino et al., 1984; Nagaoka, 1984; 1986; Endo and Suzuki, 1986; Kimura et al., 1991). A comparison of the Quaternary sediments in each study is summarised in Table 2. Recently, the stratigraphy of marine sediments and terrace deposits were discussed by Nagaoka et al. (1998; 1999), and this study used their classification of marine sediments and terrace deposits.

The terrace surfaces in the Miyazaki Plain are classified into two groups, the middle to lower terrace group and the higher terrace group. The middle to lower terrace group contains the following terraces in order from the youngest to the oldest: Fukadoshi surface, Ikatsuno surface, Saitobaru surface, Nyutabaru surface, Baba surface and Sanzaibaru surface. The higher terrace group contains the following terraces in order from youngest to oldest: Chausubaru surface, Urushinobaru surface, Kukino surface, Higashibaru surface and Shiibaru surface (Figs. 5 and 6). Projected longitudinal profiles of each terrace surface along the Hitotsuse River are shown in Fig. 7. In these terraces, Sanzaibaru surface has a marine origin, while the other surfaces have a fluvial origin. Geological sections of these terraces are shown in Fig. 8. All of the terrace deposits unconformably cover the Neogene Miyazaki Group and/or the Paleogene Shimanto Supergroup.

The thick tephra layers overlying the terrace surfaces are subdivided into the younger and the older groups based on geologic age (Table 3). The younger and the older tephra groups were deposited in the late Pleistocene and the middle Pleistocene, respectively. The older tephra groups contain many marker tephra layers, such as, from youngest to oldest, Ata-Torihama (Ata-Th), Kakuto (Kkt), Kobayashi-Kasamori (Kb-Ks) and Hiwaki (Hwk). The younger tephra also contains many marker tephra layers, such as, beginning with the youngest, Kikai-Akahoya (K-Ah), Kirishima-Kobayashi (Kr-Kb), Aira-Tanzawa (AT), Kirishima-Awaokoshi (Kr-Aw), Kirishima-Iwaokoshi (Kr-Iw), Aira-Iwato (A-Iw), Aso-4, Aira-Fukuyama

(A-Fk), Kikai-Tozurahara (K-Tz), Ata and Aso-3. Each type of tephra was identified by naked-eye observation, microscope observation and measurements of the refractive index of pyroxene, hornblende and volcanic glass. The younger tephra group covers the middle to lower terraces in the late Pleistocene, and the older tephra group covers the higher terrace group in the middle Pleistocene.

Quaternary marine sediments distributed in the Miyazaki Plain were named the Tohriyamahama formation by Otsuka (1930a). Since Otsuka, opinions are diverse concerning the stratigraphic position of the middle Pleistocene marine sediments (Otsuka, 1930a; Endo, 1968, Hoshino, 1971; Nagaoka, 1986; Endo and Suzuki, 1986). Quaternary marine sediments are divided into three formations by marker tephra, the Nanukigawa formation, the Omarugawa (Hedagawa) formation and the Sanzaibaru formation (Nagaoka et al., 1998). The Nanukigawa and the Omarugawa formations contain as marker tephras the Kb-Ks and the Kkt, respectively. The Sanzaibaru formation formed the Sanzaibaru surface, while the other formations are overlain unconformably by the Chausubaru terrace deposits, the Sanzaibaru formation and Ikatsuno terrace deposits.

The middle to late Pleistocene marine and fluvial sediments distributed in the Miyazaki Plain can be divided into the 12 stratigraphic units described below. Columnar sections of each stratigraphic unit are shown in Figs. 9 through 15, and the stratigraphy of the Miyazaki Plain is summarised in Table 4.

(1) *Recent river floodplain (recent river gravel)*: The fluvial surface has been formed in the present. The gravel is mainly composed of sandstone and shale with smaller amounts of greenstone, acidic tuff, granodiorite and welded tuff, with a diameter of 5 to 30 cm.

(2) *Fukadoshi terrace deposits*: The Fukadoshi surface is widely distributed at 30 to 70 m elevation in the middle to south part of the Miyazaki Plain. Typical columnar sections of the Fukadoshi terrace deposits are shown in Fig.

9. The Fukadoshi terrace deposits are almost directly overlain by the Kr-Kb pumice fall layer (16 ka: Machida and Arai, 1992). The terrace is, therefore, considered to have been formed around 20 ka before the present (BP). The gravel is mainly composed of sandstone and shale with smaller amounts of greenstone and acidic tuff, with a diameter of 5 to 20 cm. These deposits are about 2 m thick and unconformably cover the Neogene Miyazaki Group.

(3) *Ikatsuno terrace deposits*: The Ikatsuno surface is distributed at 40 to 70 m elevation. Typical columnar sections of the Ikatsuno terrace deposits are shown in Fig. 10. The Ikatsuno terrace deposits are almost directly overlain by the Kr-Iw scoria fall layer. The age of the Kr-Iw scoria fall layer was calculated by proportional allotment (40 ka?). This method assumes that the sedimentation rate of loam beds is constant. Thus the terrace is considered to have been formed around 40 ka BP. The gravel is mainly composed of sandstone and shale with smaller amounts of greenstone and acidic tuff, with a diameter of 5 to 20 cm. These deposits are about 3 m thick and unconformably cover the Nanukigawa formation, the Omarugawa (Hedagawa) formation and the Neogene Miyazaki Group.

(4) *Saitobaru terrace deposits*: The Saitobaru surface is widely distributed at 50 to 80 m elevation. Typical columnar sections of the Saitobaru terrace deposits are shown in Fig. 11. The Saitobaru terrace deposits are almost directly overlain by the A-Iw ash fall layer. The age of the A-Iw ash fall layer was also calculated by proportional allotment (70 ka?). Thus the terrace is considered to have been formed around 70 ka BP. The gravel is mainly composed of sandstone and shale with smaller amounts of greenstone and acidic tuff, with a diameter of 5 to 20 cm. These deposits are about 5 m thick and cover the Neogene Miyazaki Group.

(5) *Nyutabaru terrace deposits*: The Nyutabaru surface is widely distributed at 60 to 90 m elevation. Typical columnar sections of the Nyutabaru terrace deposits are shown in Fig. 12. The Nyutabaru terrace deposits are almost directly overlain by the Aso-4 pyroclastic flow deposits (89 ka: Matsumoto

et al., 1991). Thus the terrace is considered to have been formed around 90 ka BP. The gravel is mainly composed of sandstone and shale with smaller amounts of greenstone and acidic tuff, with a diameter of 5 to 20 cm. These deposits are about 5 m thick and unconformably cover the Sanzaibaru formation and the Neogene Miyazaki Group.

(6) *Baba terrace deposits*: The Baba surface is distributed at 90 to 110 m elevation in the south part of the Miyazaki Plain. Typical columnar sections of the Baba terrace deposits are shown in Fig. 13. The Baba terrace deposits are almost directly overlain by the Ata ash fall layer (110 ka: Matsumoto and Ui, 1997). Thus the terrace is considered to have been formed around 110 ka BP. The gravel is mainly composed of sandstone and shale with smaller amounts of greenstone and acidic tuff, with a diameter of 5 to 20 cm. These deposits are about 10 m thick and unconformably cover the Neogene Miyazaki Group.

(7) *Sanzaibaru terrace deposits*: The Sanzaibaru surface is widely distributed at 90 to 110 m elevation. The Sanzaibaru terrace deposits (the Sanzaibaru formation) are thick transgressive deposits made in the middle Pleistocene (Nagaoka et al., 1998). Typical columnar sections of the Sanzaibaru terrace deposits are shown in Fig. 14. The Sanzaibaru terrace deposits are almost directly overlain by the Ata ash fall layer (110 ka; Matsumoto and Ui, 1997) and the K-Tz ash fall layer (100 ka: Machida and Arai, 1992) and contain the Aso-3 ash fall layer (120 ka: Matsumoto et al., 1991) in the lower member (Nagaoka et al., 1998). Thus the terrace is considered to have been formed around 120 ka BP. The gravel is mainly composed of sandstone and shale with smaller amounts of greenstone and acidic tuff, with a diameter of 5 to 20 cm.

The Sanzaibaru terrace deposits are lithologically subdivided into three members (Nagaoka, 1986; Nagaoka et al., 1998). The lower member is composed of fluvial gravely deposits in the regressive stage. The middle member consists of alternating layers of sand and silt with fossils of

mollusca; it was formed in the transgressive stage of Marine Isotope Stage 5e (120 ka). The upper member is composed of sand with smaller amounts of gravely deposits under deltaic or beach condition at the maximum stage of the transgression.

Paleo red soils are recognised on the top of the deposits. Since paleo red soils are buried under the Ata ash fall deposits (110 ka), they are considered to have been formed during the period from 120 ka to 110 ka BP.

(8) *Chausubaru terrace deposits*: The Chausubaru surface is widely distributed at 120 to 130 m elevation in the middle part of the Miyazaki Plain. Typical columnar sections of the Chausubaru terrace deposits are shown in Fig. 15. The Chausubaru terrace deposits contain the Ata-Th pyroclastic flow deposits (230-250 ka: Machida and Arai, 1992) in the middle part. Thus the terrace is considered to have been formed around 250 ka BP. The gravel is mainly composed of sandstone and shale with smaller amounts of greenstone and acidic tuff, with a diameter of 5 to 20 cm. These deposits, having a thickness of about 20 m, unconformably cover the Omarugawa (Hedagawa) formation and the Neogene Miyazaki Group.

Paleo red soils are recognised on the top of the deposits. Paleo red soils are buried under A-Iw air fall deposits (70 ka?), which are considered to have been formed during the period from 250 to 70 ka BP.

(9) *Urushinobaru terrace deposits*: The Urushinobaru surface is distributed at 190 to 210 m elevation in the southwestern part of the Miyazaki Plain. Typical columnar sections of the Urushinobaru terrace deposits are shown in Fig. 13. The Urushinobaru terrace deposits are almost directly overlain by the Ata-Th pyroclastic flow deposits (230-250 ka: Machida and Arai, 1992). Thus the terrace is considered to have been formed around 300 to 250 ka BP. The gravel is mainly composed of sandstone and shale with smaller amounts of greenstone and acidic tuff, with a diameter of 5 to 30 cm. These deposits are about 10 m thick and unconformably cover the Kukino formation.

Paleo red soils are recognised on the top of the deposits. Paleo red

soils are buried under the Ata-Th pyroclastic flow deposits, they are considered to have been formed during the period 300 to 250 ka BP.

(10) *Higashibaru terrace deposits*: The Higashibaru surface is distributed at 150 to 230 m elevation in the middle to south part of the Miyazaki Plain. Typical columnar sections of the Higashibaru terrace deposits are shown in Fig. 9. The Higashibaru terrace deposits are almost overlain by the paleo red soils and the Kkt ash fall layer (300 ka: Machida and Arai, 1992). Thus the terrace is considered to have been formed around 350 ka BP. These deposits are about 20 m thick and unconformably cover the Neogene Miyazaki Group and the Paleogene Shimanto Supergroup. Some outcrops lack the marker tephra Kkt and are directly overlain by the Ata-Th ash fall layer.

Paleo red soils are recognised on the top of the deposits (Akagi et al., 1997). Paleo red soils are buried under A-Iw air fall deposits (70 ka?) and are considered to have been formed during the period 300 to 70 ka BP.

(11) *Kukino terrace deposits*: The Kukino surface is distributed at 200 to 240 m elevation in the southwestern part of the Miyazaki Plain. Typical columnar sections of the Kukino terrace deposits are shown in Fig. 13. The Kukino terrace deposits are almost directly overlain by the Kkt pyroclastic flow deposits (300 ka: Machida and Arai, 1992) and contain the Hwk pyroclastic flow deposits (600 ka: Machida and Arai, 1992) and the Kb-Ks pyroclastic flow deposits (500 ka: Machida and Arai, 1992) in the lower part. Thus this formation is considered to have been formed during the period 600 to 300 ka BP. The gravel is mainly composed of sandstone and shale with smaller amounts of greenstone and acidic tuff, with a diameter of 5 to 50 cm. These deposits are about 60 m thick and unconformably cover the Neogene Miyazaki Group and Paleogene Shimanto Supergroup.

(12) *Shiibaru terrace deposits*: The Siibaru surface is distributed at 200 to 300 m elevation in the north part of the Miyazaki Plain. The Siibaru terrace deposits are directly overlain by an unidentified weathered tephra layer (Hwk?, 600 ka: Machida and Arai, 1992). In addition, the Siibaru

surface is strongly eroded, and distribution of the terrace surface is scattered. Therefore, the terrace is considered to have been formed before 500 ka BP. The gravel is mainly composed of welded tuff and granodiorite, with a diameter of 5 to 50 cm. These deposits are distributed around Mt. Osuzuyama and consist of welded tuff and granodiorite. These deposits are about 10 m thick and unconformably cover the Osuzuyama acidic rocks.

2.3. Geological features of sampling points and rock samples for analysis.

The locations of the eight rock sampling sites are shown in Figs. 6 and 8. All sampling points are directly covered with tephra layers (Fig. 16), except for the recent river floodplain. All sampling points at each site are above the groundwater level to avoid the possible influence of groundwater levels on weathering (Nishiyama et al., 1999).

Figure 25 lists the characteristics of the rock based on naked-eye observations of cutting surfaces. All examined sandstones belong to the Paleogene Shimanto Supergroup. All sandstone gravel samples are fine- to medium-grain wacke-type. About 20 samples of rounded sandstone cobbles and pebbles were taken from each sampling point. The characteristics of the eight sampling sites and sandstone sample gravel taken from the sampling sites are as follows:

(1) *Recent river floodplain (0-ka rocks)*: The sampling point is located on a gravel bar of river floodplain in the Omaru River (Fig. 17). The gravel taken from this site is not visibly weathered. The cutting surface of this gravel shows that it is dark gray coloured and has no weathering rind. This gravel is hard, and sounds made by hammer blows to it are clear.

(2) *Fukadoshi terrace deposits (20-ka rocks)*: Gravely deposits of this sampling point are almost directly covered by the tephra Kr-Kb and black

humic soils (the so-called 'Kuroboku'). The covering tephra layer is about 1 m thick (Fig. 18). The gravel taken from this point is slightly weathered, and its colour is light gray. This gravel has no weathering rind. It is hard, and sounds made by hammer blows to it are clear.

(3) *Saitobaru terrace deposits (70-ka rocks)*: Gravely deposits of the sampling point are almost directly covered by the tephra A-Iw. The covered tephra layer is about 3 m thick (Fig. 19). The gravel taken from this site is slightly weathered, and its colour is light gray. This gravel is hard, and sounds made by hammer blows to it are a little dim.

(4) *Nyutabaru terrace deposits (90-ka rocks)*: Gravely deposits of this sampling point are almost directly covered by the tephra A-Fk. The covered tephra layer is about 7 m thick (Fig. 20). The gravel taken from this site is slightly weathered, and its colour is light gray to brown. This gravel is brittle, and sounds made by hammer blows to it are somewhat dim.

(5) *Baba terrace deposits (110-ka rocks)*: Gravely deposits of this sampling point are almost directly covered by the tephra Ata. The covered tephra layer is about 7 m thick (Fig. 21). This gravel is slightly weathered, and its colour is brown. This gravel is brittle, and sounds made by hammer blows to it are dim.

(6) *Sanzaibaru terrace deposits (120-ka rocks)*: Gravely deposits of this sampling point are almost directly covered by the tephra K-Tz. The covered tephra layer is about 6 m thick (Fig. 22). The gravely deposits are correlated with the non-marine upper member of the Sanzaibaru formation. The gravel taken from this site is strongly weathered, and its colour is brown to reddish brown. This gravel is brittle, and sounds made by hammer blows to it are dim.

(7) *Chausubaru terrace deposits (250-ka rocks)*: Gravely deposits of this sampling point are almost directly covered by the tephra Kr-Iw. The covered tephra layer is about 4 m thick (Fig. 23). Deposits contain the Ata-Th in the middle part. The gravel taken from this site is strongly weathered, and its

colour is reddish brown. This gravel is brittle, and sounds made by hammer blows to it are dim.

(8) *Higashibaru terrace deposits (350-ka rocks)*: Gravely deposits of this sampling point are almost directly covered by the tephra Ata-Th. The covered tephra layer is about 4 m thick (Fig. 24). The gravel taken from this site is strongly weathered, and it is reddish in colour. This gravel is brittle, and sounds made by hammer blows to it are dim.

3. Analyses and results

3.1. Rock texture and mineralogical properties

3.1.1. Rock texture based on microscope observation

The petrographical, mineralogical and chemical properties of sandstone in Kyushu Shimanto terrene have been described by Okada (1977), Teraoka (1977; 1979), Teraoka et al. (1995; 1999) and Kimura et al. (1991). These papers show that the sandstone is mostly fine- to medium-grained wacke-type, which consists of phenocrysts of quartz and feldspar (plagioclase and alkali feldspar) with smaller amounts of chert, rock fragments, heavy minerals and mica. The matrix in sandstone mostly consists of clay minerals. Okada (1977) recognised a small amount of calcite cements in the matrix.

Microscope observation was carried out using three rock samples taken from each sampling site. Figs 26 and 27 show representative photomicrographs of sandstone in the thin sections. Most of the rock samples are fine-grained wacke-type, consisting of phenocrysts of quartz and plagioclase, and clay and iron minerals in the matrix. Although the appearance of quartz phenocrysts has not changed as the weathering period has grown longer, plagioclase has been decomposed during the past 350 ka. Matrix minerals have also decomposed, as shown by the fact that the thin sections of matrix become increasingly unclear as the weathering period increases, while iron minerals with a diameter of about 10 to 100 μm have gradually concentrated in matrix during 350 ka. Small particles of iron minerals surround sand grains, and big particles of iron minerals in 350-ka rocks fill the pore space produced by leaching of feldspar grains.

Observations of pores in thin sections have been included in previous studies (e.g., Takahashi et al., 1992; Suzuki and Takahashi, 1994; Nishiyama et al., 1992; Hirono and Nakashima, 2000). Since pores are filled with

petropoxy resin, the area of pores can be recognised as a yellowish zone in matrix, as shown in Figs. 26 and 27. Pores are stretched and connected from the outer parts to the inner parts.

3.1.2. Mineral compositions

Minerals were identified by X-ray diffraction analysis (XRD; Rigaku Co., Ltd., RAD-C System). The operating conditions included an X-ray target of CuK α , tube voltage of 50 kV and tube current of 20 mA. Matrix samples were analysed using three rock samples taken at each sampling site. The analysis followed the methods of Suzuki (1992) using silt size specimens in addition to treatments with ethylene-glycol.

The results of XRD are shown in Table 5 and Fig. 28. Samples include quartz, plagioclase and clay minerals such as kaolinite, chlorite and illite. Chlorite can be identified because the 2 θ of diffracted pattern has not shifted after treatments with ethylene-glycol. The intensity of diffracted peaks of plagioclase, illite and kaolinite gradually decreased during 350 ka, while a diffracted peak of chlorite cannot be recognized after 250-ka rocks. These results are compiled in Fig. 29, showing that plagioclase and clay minerals decompose as the weathering period increases.

3.1.3. Identification of iron minerals

The visible diffuse reflectance spectra of rocks and minerals have been used recently to characterise the origins of the colours of rocks (e.g., Nakashima et al., 1989, Matsunaka and Uwasawa, 1992; Nakashima, 1994; Kuchitsu et al.,1999; Sasaki and Otani,1999; Hiroi,1999). For example, iron minerals such as goethite and hematite can be identified by this technique.

Using about 20 pieces of gravel from each sampling site, visible diffuse reflectance spectra on the cutting surface of rock samples were

measured using a Minolta CM-500 spectrophotometer in a visible wavelength region (400 to 700 nm). The measuring area was 3 mm in diameter. There are two kinds of reflection processes of light on solid materials: (1) that occurring when light is reflected from a polished surface of the mineral (specular reflection), and (2) that occurring when the light is reflected by the finely powdered mineral (diffuse reflection). The latter arises from radiation that has penetrated the crystals and reappeared at the surface after multiple scatterings. When light is reflected from the rock surface, diffuse reflection occurs. If the intensity of the diffuse spectra reflectance light from the surface of a white plate ($BaSO_4$) is I_0 and that from the rock sample is I, the diffuse reflectance R is given by

$$R = I / I_0 \qquad \cdots \ (3\text{-}1)$$

The results of the measurements are shown in Fig. 30. Reflectance spectra ranged from 8 to 42 %, increasing as the weathering period increases, while reflectance slightly decreases at 480 nm. As a significant trend from 90- to 250-ka rocks, increase at 500 to 600 nm. Reflectance for 350-ka rocks increases from 540 to 700 nm.

Nakashima (1994) and Kuchitsu et al. (1999) have investigated in detail the visible reflectance spectra of iron minerals goethite: α -FeOOH, and hematite: α -Fe_2O_3). They have pointed out that the spectra of the two iron minerals show different patterns in the visible region: the reflectance of spectra of goethite increases in the 500- to 600-nm range and slightly decreases at 480 nm, and that of hematite increases at 540 to 700 nm. According to these previous studies, the reflectance spectrum of 90- to 250-ka rocks seems to be correspond to the spectra of goethite, and that of 350-ka rocks to the spectra of hematite. These findings suggest that iron minerals in the sandstone of the present study changes from goethite to hematite as the weathering period increases.

3.2. Colour

Soil colour is closely related to the soil's goethite and hematite contents (e.g., Torrent et al., 1983). Recent researchers in earth sciences have used a spectrophotometer to measure the colour of rocks, minerals and soils (e.g., Nakashima et al., 1989, 1992; Nagano et al., 1992; Oguchi et al., 1995; Nakashima, 1994; Ota and Kiya, 1996; Mitsushita et al., 1998; Shinohara et al., 1998; Wakizaka et al., 1998).

The colour of rock samples were determined using a Minolta CM-500 Spectrophotometer as having components L^*, a^* and b^*, i.e., L^* a^* b^* colour space. The L^*-value is the degree of lightness: $L^* = 0$ corresponds to black, and $L^* = 100$ corresponds to white. A positive value of a^* expresses red, and a negative value green. A positive value of b^* indicates yellow, and a negative value blue. Positive a^*- and b^*-values express an increase in iron minerals such as goethite and hematite (Nakashima 1994). Colour measurements were carried out on a measuring line on a cutting surface of each rock sample at intervals of 5 mm using about 20 intact rock samples taken from each sampling site.

All data of the L^*-, a^*- and b^*-values are shown in Table 6. An example of colour measurements of the b^*-value is shown in Fig. 31. This figure shows that distributions of the b^*-value are almost uniform from the surface to the inner zone. Thus the mean value of all the measured values in each measuring line of individual rock samples is the representative colour value of each rock sample.

The results of colour measurements arranged by weathering time are shown in Fig. 32. The a^*-value ranges from –1.45 to 18.78, and the b^*-value ranges from –4.51 to 27.05. The a^*-value increases during the 250- to 350-ka period, and the b^*-value increases during the 0- to 250-ka period. These

results support that the colour of rock samples becomes more yellowish during the 0 to 250 ka period and then more reddish during the 250- to 350-ka period.

The a^*-b^* diagram shows that the gradient of the trend line from plotted data is higher during the 0- to 250-ka period, while the gradient is gentle during the 250- to 350-ka period (Fig. 33). Nakashima (1994) suggested that an increase in the b^*-value expressed an increase in goethite and than an increase in the a^*-value expressed an increase in hematite. Therefore, the present data of the a^*-b^* diagram indicate that goethite increases during the 0- to 250-ka period, and hematite increases during the 250- to 350-ka period.

3.3. Physical properties

3.3.1. Effective porosity and apparent specific gravity

The effective porosity, n_e (%), and the apparent specific gravity, G_n, are widespread indices for physical properties of rocks. The methods of analysis were used employed by the Japanese Geotechnical Engineering Society (1989). The effective porosity, n_e (%), and the apparent specific gravity, G_n, were calculated by the following equations:

$$G_n = W_1 / (W_3 - W_4) \quad \cdots (3\text{-}2)$$

$$n_e = 100 \times (W_3 - W_2) / (W_3 - W_4) \quad \cdots (3\text{-}3)$$

where W_1 is the sample weight in natural conditions, W_2 is the sample weight in dry conditions, W_3 is the sample weight in a saturated condition, and W_4 is the sample weight in water. The measurements were carried out using about 20 samples taken from each sampling site.

Table 7 shows the effective porosity and the apparent specific gravity

of all the samples. The effective porosity ranges from 0.75 to 30.19 %, and the apparent specific gravity ranges from 1.72 to 2.77. Temporal changes in the effective porosity and the apparent specific gravity are shown in Fig. 34. The effective porosity increases as the weathering period increases, while the specific gravity decreases during 350 ka. The effective porosity rapidly increases during 0 to 20 ka, and 90 to 120 ka, and after that a little increase in the n_e-value occurs during 120 to 350 ka. On the other hand, the apparent specific gravity rapidly decreases during 0 to 20 ka, and 90 to 120 ka, and its decreasing rate is slow during 120 to 350 ka.

3.3.2. Pore size distribution

Using three rock samples taken from each sampling site, pore-size distribution (PSD) was measured with a mercury intrusion porosimeter, the Porosimeter 2000 manufactured by the Karulo-Elva Co., Italy. The PSD of various rock types has been investigated in previous studies (e.g., Tamura and Suzuki, 1984; Uchida, 1984; Uchino et al., 1984; Yamashita and Suzuki, 1986; Yamaguchi et al., 1988; Nishiyama et al., 1990; Uchida et al., 1991,1992; Suzuki and Matsukura, 1992; Oguchi et al., 1996; Matsukura and Matsuoka, 1996; Tanaka et al., 1996; Rin et al., 1998; 1999a,b; Takahashi et al., 1999). The method was devised by Washburn (1921), who assumed open pores with cylindrical shape. The pore diameter, d, is calculated by the following equation:

$$d = 4\gamma \cos\theta / P \qquad \cdots \text{(3-4)}$$

where γ is the surface tension of mercury (484 dyne/cm), θ is the contact angle between mercury and solid (about 131°) and P is the pressure of mercury intrusion.

The significant range of PSD readings is from 3×10^{1} μm to 3.3×

10^{-3} μ m. Pores are tentatively divided into the following four ranges (Suzuki and Matsukura, 1992), d_a through d_d: large ($3.3 \times 10^1 \geqq d_a > 3.3 \times 10^0$), medium ($3.3 \times 10^0 \geqq d_b > 3.3 \times 10^{-1}$), small ($3.3 \times 10^{-1} \geqq d_c > 3.3 \times 10^{-2}$) and very small ($3.3 \times 10^{-2} \geqq d_d > 3.3 \times 10^{-3}$). Pore volumes per unit weight of rock samples are denoted as V_a, V_b, V_c and V_d (mm^3/g) for the four grades, respectively. The sum of V_a, V_b, V_c and V_d is called the total pore volume, V_{sum} (mm^3/g).

All PSD data are shown in Table 8. A representative example of the histogram of pore size distribution is shown in Fig. 35. The pattern of pore size distribution of 70- to 110-ka rocks mostly shows the normal distribution. In histograms for 120- to 350-ka rocks, the mode-value of pore volume is exceptionally rich. Both the mean pore radius and the total pore volume increase with as the weathering period increases.

Temporal changes in the pore volume fractions V_a, V_b, V_c and V_d are shown in Table 9 and Fig. 36. The values of V_a and V_b increase rapidly during the 120- to 350-ka period and during the 90- to 120-ka period, respectively. On the other hand, V_c and V_d increase only slightly as the weathering period increases. These facts show that the pore radius of sandstone increases as the weathering period increases, and increasing pore size is mostly more than 1 μ m (V_a and V_b).

The mean pore radius, r (μ m), and the specific surface area, S (m^2/g), were calculated from the pore size distribution data from each sample. These results are shown in Table 9 and Fig. 37. The mean pore radius, r, ranges from 0.005 to 4.994 μ m, and the specific surface area, S, ranges from 0.46 to 6.01 m^2/g. The mean pore radius increases as the weathering period increases, most rapidly during 90 to 120 ka. The specific surface area increases at a nearly constant rate during 350 ka. Thus the pore radius increases varying amounts, but the specific surface area increases at a constant rate as the weathering period increases.

3.3.3. Permeability

The permeability of sandstone is usually measured by the transient pulse technique (e.g., Ishijima et al., 1991, 1993). This method uses a cylindrical test specimen. The gravel used for the present analysis is too hard to form into a cylindrical specimen because the pebbles are irregularly shaped and small. Therefore, the permeability was calculated using PSD data based on the hydraulic radius model (Peterson, 1983). Calculation was carried out by employing the method of Rin et al. (1999a), which uses the following equation:

$$k = C_s \gamma \phi \{1 / 2[\Sigma f(r_i) / r_i]\}^2 / \mu \qquad \cdots (3\text{-}5)$$

where k is the permeability (cm/s), C_s is a constant value of 0.5, γ is the weight per unit volume, ϕ is the effective porosity, $f(r_i)$ is the frequency of pore size distribution, r_i is the capillary diameter (μm) and μ is the coefficient of viscosity (dyne · s · cm^{-2}, μ is 1 for water).

The results are shown in Table 9 and Fig. 38. The permeability of sandstone ranges from 10^{-11} to 10^{-7} cm/s and increases as the weathering period increases. There was an especially rapid increase during 0 to 20 ka and 90 to 120 ka. After that, a small increase in permeability occurred during 120 to 350 ka.

3.3.4. Distribution of density

X-ray computed tomography analysis (X-ray CT), originally used for medical analysis, has been applied as a new non-destructive method of measuring internal density and pore structure of rock and soil samples (e.g., Raynaud et al., 1989; Nishizawa et al., 1995; Ikehara, 1997; Nakano et al., 1997; Sugawara et al., 1998, 1999; Duliu, 1999; Geet et al, 1999; Otani et al., 2000a,b). An X-ray CT scanner generates a cross-sectional image through the

rock samples by digitizing shadow pictures taken from various directions. The method is based on the measurements of the attenuation of the X-ray beam. For monochromatic radiation of known intensity, I_0, across a homogeneous substance, the intensity, I, received after attenuation in the material is given by Lambert's Law (Raynaud et al., 1989), as follows:

$$I = I_0 e^{-\mu \rho x} \quad \cdots (3\text{-}6)$$

where μ is the absorption value per unit mass (cm^2/g), ρ is the density (g/cm^3) and x is the length of the material along the X-ray pass. Intensity I is converted to the CT-value using the following equations:

$$I = I_0 \exp(-U_t \rho x) \quad \cdots (3\text{-}7)$$

$$CT = K(U_t - U_w) / U_w \quad \cdots (3\text{-}8)$$

where U_t is the absorption value of the sample, U_w is the absorption value of water (0.171) and K is a constant of 1,000. The CT-value of water is zero. Since the absorption value of air is very small, 0.29×10^{-4}, the CT-value of air becomes –1,000. The CT-value depends mainly on material density reflecting pore structure.

Using 8 to 12 samples taken at each sampling site, X-ray CT images were measured with an X-ray CT scanner, a Toscanar 23200 mini manufactured by Toshiba Co., Japan, with 300-kV tube voltage and a 0.5-mm X-ray beam. The equipment can analyse a resolution area of less than 0.2×0.2 mm^2.

Representative CT images are shown in Fig. 39. The CT-value distribution of each sandstone is mostly uniform in the whole section of each type of gravel. Weathering rind cannot be recognised on CT images.

Decreasing CT-value seems to indicate decreasing density (i.e., an increased porous zone). This shows that the distribution of pores in

sandstone is uniform in the whole section of each specimen. Distribution of pores in the CT images is in good agreement with the result of microscope observation showing uniform pore distribution in the thin sections (Figs. 26 and 27).

Inner cracks are expressed as a low *CT*-value zone on CT images, as recognised in 120-ka rock (Fig. 39). CT images for samples having inner cracks are collected in Fig. 40. This figure shows that the apparent width of each crack is a few millimeters.

Although X-ray CT analysis shows that no weathering rinds exist in most of the samples shown in Fig. 39, a few samples have indistinct weathering rinds (Fig. 41). These results are in good agreement with the results of naked-eye observations of the cutting surfaces of rock samples.

A rapid decrease in the mean *CT*-value as the weathering period increases can be noted on CT images of the period between 90 and 120 ka BP (Fig. 39). Fig. 42 shows the detail of the changes in CT images of the sandstone between 90 and 120 ka. This figure shows that the *CT*-value rapidly decreases during the period 110 to 120 ka. In the CT images of 110-ka rock samples, the *CT*-value at the corner areas in the outer zone is higher than that of the inner zone. This phenomenon is considered to be a false image caused by the X-ray CT method itself (Nakano et al., 2000).

The average value of *CT*-value, denoted as CT_m, of each rock sample was calculated from the data of CT images. The results are shown in Table 10 and Fig. 43. The value of CT_m ranges from 807 to 1594 and follows a trend of decreasing as the weathering period increases, particularly during the 90- to 120-ka period. This finding indicates that sandstone pored increased during that period.

3.4. Chemical properties

3.4.1. Chemical composition using X-ray florescence analysis

Chemical composition of three rock samples taken from each sampling site was determined using X-ray florescence analysis (XRF: Rigaku model 3270) with a tube voltage of 50 kV and a tube current of 50 mA. The powdered samples were mixed with a wax binder at a proportion of 30:1. The mixed powder was put into aluminum rings and pressed for one minute with a 25-ton load to make tablet-like pellets 3 cm in diameter and 2 mm in height.

The following ten major elements were analysed: SiO_2, TiO_2, Al_2O_3, $FeO+Fe_2O_3$, MnO, MgO, CaO, Na_2O, K_2O and P_2O_5. All chemical data are shown in Table 11. Temporal changes in chemical compositions are shown in Fig. 44. Plotted data in this figure are limited to SiO_2, Al_2O_3, $FeO+Fe_2O_3$, MgO, CaO, Na_2O and K_2O.

Figure 44 shows that the chemical compositions of SiO_2, MgO, CaO, Na_2O and K_2O gradually decrease as the weathering period increases, while those of Al_2O_3 and $FeO+Fe_2O_3$ are mostly constant during 350 ka. Although SiO_2 is a compound with low solubility in natural water, it leaches out easily due to weathering. Alkali elements such as MgO, CaO, Na_2O and K_2O with high solubility also leach out easily due to weathering, while Al_2O_3 and $FeO+Fe_2O_3$ tend to remain in the internal part of gravel because both compounds have a low solubility. Quartz, plagioclase and clay minerals such as illite and kaolinite consist of silica. Decreasing silica is considered to be caused by leaching of clay minerals because they are more soluble than is quartz. Plagioclase consists of alkali elements such as Na_2O, K_2O and CaO. The decrease of these elements is considered to be caused by the decomposition of plagioclase.

Since the solubility of Al and Fe in natural water is lower than that of alkali elements, it remains in the matrix of sandstone. Aluminum is considered to be supplied by the decomposition of plagioclase, chlorite and kaolinite, and iron is considered to be supplied by the leaching of chlorite.

The *CIA*- and *PI*-values are excellent indices of leaching of chemical elements due to weathering (Reiche, 1943; Nesbitt and Young, 1982). *CIA*- and *PI*-values are calculated as follows:

$$CIA = 100 \times Al_2O_3 / (Al_2O_3 + Na_2O + K_2O + CaO) \quad \cdots \quad (3\text{-}9)$$

$$PI = 100 \times SiO_2 / (SiO_2 + (FeO + Fe_2O_3) + Al_2O_3) \quad \cdots \quad (3\text{-}10)$$

where Al_2O_3, Na_2O, K_2O, CaO, SiO_2 and $FeO+Fe_2O_3$ are given by weight %. The *CIA*-value expresses the degree of leaching of SiO_2, and the *PI*-value expresses the degree of leaching of alkali elements (CaO, Na_2O and K_2O).

Temporal changes in the calculated *CIA*- and *PI*-values are shown in Table 11 and Fig. 45. The *CIA*-value ranges from 70.14 to 89.17, while *PI*-value ranges from 77.58 to 84.09. *CIA*- and *PI*-values change at a constant rate during 350 ka. Using the least squared fit method, the relationship between *CIA*-value and weathering period, t (ka), and *PI*-value and t are calculated as follows (R^2 is the contribution ratio):

$$CIA = 0.05\, t + 70.22, \quad R^2 = 0.89 \quad \cdots \quad (3\text{-}11)$$

$$PI = -0.01\, t + 82.81, \quad R^2 = 0.58 \quad \cdots \quad (3\text{-}12)$$

3.4.2. Distribution of chemical elements using energy dispersive X-ray spectrometry

Energy dispersive X-ray spectrometry (EDS) was conducted to examine the concentration map of major elements in polished thin sections. Using three samples taken at each sampling site, the chemical mapping of Si, Fe, Al, K, Na, Ca and Mg was carried out.

The results of a concentration map of Si, Fe, Al, K and Na for 0-, 70-, 120-, 250- and 350-ka rocks are shown in Figs. 46 to 50, respectively. The EDS mapping images show that (1) the amount of Si in matrix decreases as

the weathering period increases (Fig. 46), and (2) the amount of K and Na in plagioclase decreases as the weathering period increases (Figs. 49 and 50). A decrease of Si in matrix is considered to be caused by the leaching of clay minerals such as kaolinite, illite and chlorite. Decreases in the amount of K and Na are caused by leaching of plagioclase. The amount of Fe in matrix gradually concentrated during 350 ka (Fig. 47). The amount of Al in matrix gradually concentrated during 0 to 250 ka, and after that the amount decreased during 250 to 350 ka (Fig. 48).

3.5. Mechanical properties

The point loading tensile test (Hiramatsu et al., 1965) is a simple method for examining the mechanical properties of rocks. The strength of about 20 samples from each terrace deposit was measured with a point load strength apparatus (Model TS-40; Maruto Co., Japan). Tensile strength, σ_t (kgf/cm^2), is calculated by the following equation:

$$\sigma_t = 0.9F_0 / d^2 \quad \cdots \quad (3\text{-}13)$$

where F_o is load at failure (kgf), and d is the diameter of the rock sample at failure (cm). Point loading tensile strength was calculated to be the index of point load strength, τ, which is defined by Kimiya (1975a) as follows:

$$\tau = \log \sigma_t \quad \cdots \quad (3\text{-}14)$$

All data of the point load strength test are shown in Table 12. The σ_t ranges from 0.41 to 5400 (kgf), and the τ ranges from –0.10 to 3.48. Temporal changes in the τ are shown in Fig. 51. This figure shows that the value of τ decreases during 0 to 120 ka, but after that the value of τ is

constant during 120 to 250 ka. The rock strength decreases most rapidly during 90 to 120 ka.

3.6. Summary of the results

Figure 52 summarises temporal changes in the quantitative parameters, including colour, physical properties, chemical properties and mechanical properties. The average of the measured values in each rock property is plotted in this figure.

(1) Changes in colour

Figure 52 shows that the a*-value increases during the 250 to 350 ka period and the b*-value increases during the 0- to 120-ka period, indicating that the colour of rock samples changes from grey to yellowish during 0 to 250 ka and subsequently changes to reddish during 250 to 350 ka. These results suggest that iron minerals in rock samples change from ferrihydrite to goethite during 0 to 250 ka and from ferrihydrite to hematite during 250 to 350 ka.

(2) Changes in physical properties

Effective porosity: Figure 52 shows that the effective porosity, n_e, increases as the weathering period increases. The effective porosity mostly increases during the 0- to 120-ka period, and after that a small increase in n_e occurs during the 120- to 350-ka period. This result shows that the volume of open pores rapidly increases during 0 to 120 ka.

Pore size distribution: Figure 36 shows that the pore volumes, V_c, and V_d, increase slightly as the weathering period increases, while V_b rapidly increases during 90 to 120 ka and V_a rapidly increases during 120 to 350 ka. This result shows that the pore radius of sandstone increases as the

weathering period increases, but that enlargement occurs mainly in large pores more than 1 μm (V_a and V_b). As shown in Fig. 52, the mean pore radius, r, increases as the weathering period increases, particularly rapidly during 90 to 120 ka. On the other hand, the specific surface area, S, increases at a constant rate during 350 ka.

Distribution of density: Figure 52 shows that the CT_m-value decreases as the weathering period increases, and in particular it decreases rapidly during 90 to 120 ka. The latter supports the result that the pore radius of sandstone increases during 90 to 120 ka.

(3) Changes in chemical properties

Figure 44 shows that the chemical compositions of SiO_2, MgO, CaO, Na_2O and K_2O gradually decrease as the weathering period increases, while those of Al_2O_3 and $FeO+Fe_2O_3$ are mostly constant during 350 ka. This result shows that SiO_2 leaches easily due to weathering despite its low solubility. High-solubility compounds such as MgO, CaO, Na_2O and K_2O (consisting of alkali elements) also leach easily due to weathering, but Al_2O_3 and $FeO+Fe_2O_3$ tend to remain in the internal part of gravel because both compounds have low solubility. As in Fig. 52, the *CIA*-value increases and the *PI*-value decreases constantly as the weathering period increases. Thus, changing rates of chemical weathering are constant during 350 ka.

(4) Changes in mechanical properties

Figure 52 shows that the index of point load strength, τ, decreases during the 0- to 120-ka period, but after that it is constant during the 120- to 250-ka period. Rock strength decreases most rapidly during 90 to 120 ka.

4.Discussion

4.1. Temporal changes in rock properties

The temporal changes in rock properties due to weathering during 350 ka are examined using the above results. Patterns of temporal changes in rock properties shown in Fig. 52 can be subdivided into the following three types:

(Type-1): b^*-value, effective porosity, n_e, mean pore radius, r, mean CT value, CT_m and index of point load strength, τ. These rock properties have high rates of changing during 90 to 120 ka, while they change only slightly during 0 to 90 ka and 120 to 350 ka.
(Type-2): a^*-value. These rock properties change rapidly during 250 to 350 ka but only slightly during 0 to 250 ka.
(Type-3): Specific surface area, S, and two chemical weathering indices (*CIA*- and *PI*-values). These rock properties change constantly during 0 to 350 ka.

Quantities showing the Type-1 pattern include physical properties except for the specific surface area, mechanical properties and the colour index of the b^*-value: the patterns of temporal changes in physical and mechanical properties and the colour index of the b^*-value are similar. The changing patterns of physical properties are similar to those of mechanical properties.

The physical properties and the colour indices change during the 0- to 120-ka period. The index of point load strength has decreased to the minimum value before 120 ka, i.e., rock strength first decreases in comparison to the other rock properties of Type-1. This result corresponds well to the results of previous studies (i.e., Oguchi et al., 1994). This relation

suggests that rock strength is reduced by even slightly increasing pore volume and/or inner cracks.

The Type-2 pattern occurs only in the a^*-value. The a^*-value increases with the amount of hematite and degree of mineralization of hematite (e.g., Nakashima, 1994). The changes of iron minerals due to weathering are discussed in detail in section 4.3.2.

The Type-3 pattern includes the specific surface area and the chemical weathering indices (*CIA*- and *PI*-values). The changing rates of both indices are almost constant during 350 ka. This changing pattern suggests that chemical reactions occurred actively at the surface of the materials with a large specific surface area, as indicated by Oguchi et al. (1994) and Matsukura et al. (2000). Since the specific surface area of sandstone increases at a constant rate during 350 ka, the chemical weathering indices change at a constant rate during 350 ka.

Temporal changes in rock properties of Type-1 accelerate during 90 to 120 ka. The period corresponds to the Last Interglacial Stage (Marine Isotope Stage 5: MIS 5) during 70 to 120 ka BP. The age of the maximum interglacial stage (MIS 5e) is estimated to be about 120 ka BP. Thus the rapid changes in these rock properties occurred during the Last Interglacial Stage (MIS 5). This agreement may suggest that a warm climate during the MIS 5 accelerated changes in rock properties. However, not all the rock properties changed rapidly during the MIS 5, and it is not clear that the relationships between changing rock properties were due to weathering and effects of changes of climate during the Quaternary.

4. 2. Relationships between rock properti es

Rock properties belonging to the same type may be considered to be closely related to each other. The relationships of these rock properties and

changing mechanisms are discussed below.

At first, relations with clear causality are discussed. Although no discussion was carried out about pore volume, V_b, and permeability, k, both parameters belong to Type-1. Rock strength is affected by properties such as the effective porosity, n_e, the mean CT-value, CT_m, the index of point load strength, τ, and pore volume, V_b. The relationships between τ, CT_m and n_e are shown in Fig. 53, and that between τ and V_b is shown in Fig. 54. These figures show that τ has a high correlation with CT_m, n_e and V_b. Using the least-squares fit method, the relationships between τ and the other three values are expressed as the following equations (R^2 is the contribution ratio):

$$\tau = 0.003\ CT_m - 0.872, \quad R^2 = 0.690 \qquad \cdots (4\text{-}1)$$

$$\tau = -0.064\ n_e + 2.862, \quad R^2 = 0.682 \qquad \cdots (4\text{-}2)$$

$$\tau = -0.022\ V_b + 2.571, \quad R^2 = 0.792 \qquad \cdots (4\text{-}3)$$

The maximum amount of the contribution ratio was obtained using linear equations. Since R^2 reaches more than 0.6 in these equations, the relationships among τ, CT_m, n_e and V_b can be significant. Equations (4-1), (4-2) and (4-3) show that decreasing τ is affected by physical properties such as CT_m, n_e and V_b. The scattering in the relationship of τ to CT_m, n_e and V_b is recognised. The reason for this scattering is that strength is a sensitive parameter that depends on the existence of inner pores and/or cracks.

The relationship between CT_m and n_e is shown in Fig. 54b. This figure shows that CT_m has a high correlation with n_e. Using the least-squares fit method, the relationship between CT_m and n_e is expressed as follows:

$$CT_m = -23.39\ n_e + 1459.92, \quad R^2 = 0.869 \qquad \cdots (4\text{-}4)$$

The maximum amount of the contribution ratio was obtained using a linear

equation. Since CT_m reflects the density of materials, it seems to be in good relation to the volume of pores, i.e., the effective porosity. Although X-ray CT analysis is not a common method for estimation of rock properties because it involves the use of very expensive equipment, CT_m is easily estimated from n_e using Equation (4-4).

The permeability, k, has a high correlation with r and n_e (Fig. 55). Using the least-squares fit method, the relationships between k and r or n_e are expressed as follows:

$$k = 7 \times 10^{-10} r^{0.968}, \quad R^2 = 0.877 \qquad \cdots (4\text{-}5)$$

$$k = 3 \times 10^{-12} n_e^{1.964}, \quad R^2 = 0.855 \qquad \cdots (4\text{-}6)$$

The maximum amount of the contribution ratios was obtained using power function. Since R^2 reached more than 0.8 in both equations, permeability of rocks seems to be strongly affected by the mean pore radius and the effective porosity.

The relationships between the chemical weathering indices of *CIA*- and *PI*-values and the specific surface area, S, are shown in Fig. 56. This figure shows that S has a high correlation to *CIA*- and *PI*-values. Using the least-squares fit method, the relationships between *CIA*- or *PI*-values and S are expressed as follows:

$$CIA = 5.182\,S + 67.664, \quad R^2 = 0.940 \qquad \cdots (4\text{-}7)$$

$$PI = -1.410\,S + 83.718, \quad R^2 = 0.917 \qquad \cdots (4\text{-}8)$$

The maximum amount of the contribution ratio was obtained using a linear equation. R^2 reaches more than 0.9 in both equations. Equations (4-7) and (4-8) show that increasing *CIA*-value and decreasing *PI*-value are affected by increasing S. If S increases due to weathering, the *CIA*-value increases and the *PI*-value decreases. Since increasing rates of the specific surface area are

constant due to weathering, rates of chemical weathering seem to be constant during 350 ka.

Although causality is not clear, correlation is observed between the mean pore radius, r, and the pore volume, V_b, or the effective porosity, n_e (Fig. 57). This figure shows that r has a high correlation to V_b and n_e. Using the least-squares fit method, the relationships between r and V_b, r and n_e, are expressed as follows:

$$r = 0.051\ V_b^{\ 0.878},\quad R^2 = 0.772 \qquad \cdots (4\text{-}9)$$

$$r = 0.004\ n_e^{\ 1.935},\quad R^2 = 0.767 \qquad \cdots (4\text{-}10)$$

The maximum amount of the contribution ratio was obtained using power function. R^2 reaches more than 0.7 in both equations. These equations show that r increases with V_b value and n_e. The r-value can, therefore, be estimated from V_b and n_e.

The relationships between chemical weathering indices (*CIA*- and *PI*-values) and n_e are shown in Fig. 58. Using the least-squares fit method, the relationships between chemical weathering indices and n_e are expressed as follows:

$$CIA = 0.635\ n_e + 69.249,\quad R^2 = 0.775 \qquad \cdots (4\text{-}10)$$

$$PI = -0.194\ n_e + 83.567,\quad R^2 = 0.956 \qquad \cdots (4\text{-}11)$$

Although the two chemical weathering indices and effective porosity belong to another type of temporal change, the contribution ratio in these equations is high. Therefore, if the *CIA*-value increases and/or the *PI*-value decreases due to weathering, n_e will increase. These relationships indicate that the increased porosity was caused by leaching of chemical elements such as SiO_2 and alkali elements (K_2O, Na_2O, MgO and CaO). As shown in Fig. 52, a similar pattern is recognised between the colour index (b*-value) and the

effective porosity.

Relationships between the b^*-value, the effective porosity, n_e and the permeability, k, are shown in Fig. 59. Changes of the b^*-value have a high correlation to the effective porosity and the permeability. Using the least-squares fit method, the relationships between the b^*-value and n_e or k are expressed by the following equations:

$$n_e = 2.526\ e^{0.094b^*},\quad R^2 = 0.814 \qquad \cdots (4\text{-}12)$$

$$k = 10^{-11}\ e^{0.208\ b^*},\quad R^2 = 0.680 \qquad \cdots (4\text{-}13)$$

The maximum amount of the contribution ratio was obtained using power function. In trying to determine the weathering mechanism of sandstone, the high correlation among n_e, k and the b^*-value cannot be explained because these parameters are irrespective of each other directly. However, high correlations among n_e, k and the b^*-value are recognised because (1) changes in the effective porosity, the permeability and colour occurred in the whole rock samples, and (2) these changes progress with a similar pattern as the weathering period increases. Since changes in colour (b^*-value) conform with changes in porosity and permeability, some changes in colour seem to be good indicators of certain rock properties.

The relationships between rock properties are described quantitatively by Equations (4-1) to (4-13). Equations (4-12) and (4-13) can be applied to the problems in engineering geology described in section 4.4.

4.3. Mechanism of weathering in sandstone gravel

4.3.1. Change in pore structure in sandstone due to leaching of matrix minerals

The weathering mechanism of sandstone has been explained by

increasing pore volume and radius caused by leaching of matrix minerals (e.g., Chigira and Sone, 1991). The primary pore geometry of sandstone has been examined in previous studies from the viewpoint of oil reservoir assessment in petroleum geology (e.g., Krohn, 1988; Uchida and Tada, 1991). The pore geometry of sandstone is approximated to the skeleton network in previous studies (e.g., Peterson, 1983; Doyen, 1988). Doyen (1988) has constructed a model of pore structure, shown in Fig. 60, that assumes that the distribution of pores and the pore radius are uniform throughout the whole rock.

The changing pore structure in sandstone due to weathering can be explained as shown in Fig. 61 based on the skeleton network model like that shown in Fig. 60. Observations of photomicrographs (Figs. 26 and 27) and PSD data (Figs. 35 and 36) show that (1) connected and elongated pores with a diameter of 1 to 10 μ m are mainly formed in matrix, and (2) micro-pores with a diameter of less than 1 μ m are rare. Observations of photomicrographs and CT images suggest that the distribution of pores is uniform throughout the whole gravel. The process of pore formation seems, therefore, to occur simultaneously throughout the gravel. This supports the field evidence that sandstone has no weathering rind.

The measurements of the effective porosity and pore-size distribution show that the pore volume and the mean pore radius of sandstone increase as the weathering period increases, as follows: (1) pore volume, V_b, and effective porosity, n_e, rapidly increased during 90 to 120 ka, as shown in Figs. 34 and 36, respectively, and (2) although V_a rapidly increased during 120 to 250 ka, n_e increased only slightly during 120 to 250 ka (Figs. 34 and 36). These changes are explained by the connection of pores that caused changes to the pore structure. For example, if neighboring pores running parallel are connected by leaching of matrix with each other, the V_{sum}-value would increase but effective porosity would remain constant. CT_m rapidly decreased during 110 to 120 ka (Fig. 43), which seems to have been caused by the

increasing pore radius, not by the increasing pore volume.

The changing pattern of the *CT*-value corresponds to the changing pattern of V_b. On the other hand, the rate of change of the chemical weathering indices of sandstone is constant during 350 ka. The apparent inconsistency of the changing pattern between the chemical weathering indices and the *CT*-value can be explained by the increase of connected pores. XRF data shows that there is no evidence of rapid leaching of chemical during the 90- to 120-ka period. The increased *r*-value and decreased *CT*-value seems to be caused by the degree of increased pore connection during the 90- to 120-ka period.

Some studies of the weathering of sandstone have been carried out (e.g., Chigira and Sone, 1991; Buntenuth et al., 1998). Chigira and Sone noted that weathered tuffaceous sandstone is cemented by zeolite, and Buntenuth et al. wrote that the weathered sandstone they studied is cemented by silica gels. These studies both indicated that leaching of matrix minerals plays an important role in weathering of sandstone. It is well known that calcite, zeolite, silica gels and pyrite are easily dissolved. As described above, XRD results show that these minerals are not included in sandstone of the present study. In general, plagioclase changes into some kinds of clay minerals such as kaolinite due to weathering (e.g., Ollier, 1969; Chida, 1996). However, clay minerals and plagioclase monotonously decrease as the weathering period increases during 350 ka, and increasing clay minerals due to weathering cannot be recognised from the XRD results.

Chigira and Sone (1991) discussed that (1) concentrated iron minerals filled the pore space in matrix with weathering, and (2) decreased effective porosity and increased density occurred as a result of iron concentration. Photomicrographic observation and PSD data show that the effective porosity, n_e, increases as the weathering period increases (Figs. 26, 27, 34 and 46), although iron minerals concentrate in the matrix of sandstone. Cementation of sand particles by iron minerals is not clear in sandstone

gravel of the present study because rock strength decreases as the weathering period increases.

Although the pore volume and the pore radius increase as the weathering period increases, the specific surface area and the chemical weathering indices change at a constant rate during 350 ka. Microscope observation shows that the pores caused by leaching of matrix minerals are mostly straight and cylindrical in shape. The specific surface area of straight-like cylindrical pores seems to be small, even though the pores' radius is big. Characteristic properties of sandstone weathering are that (1) the pore radius increases as the weathering period increases, and (2) the changing rate of the specific surface area is constant. In general, chemical reaction occurred at the surface of the materials. Chemical weathering rates are constant because the increasing rate of the specific surface area is constant. Changing patterns of chemical weathering of rocks corresponds to that of the specific surface area of rocks. The results of XRF data confirm that the rates of chemical weathering are constant.

The weathering mechanism of sandstone can be understood as the sequential leaching of matrix, as shown in Fig. 61. At the early stage of weathering, the porosity of sandstone is low because the matrix consists of clay minerals such as illite, kaolinite and chlorite. At the later stage of weathering, elongated and connected pores form in the matrix as a result of the leaching of clay minerals.

PSD data and the results of microscope observation show that geometrically, the pores are elongated and connected to each other. The pores are in accordance with an elongate pore model described by Scholle (1977). Thus the leaching of matrix in sandstone is mostly uniform in each of the whole rock samples. A weathering rind cannot be seen in the sandstone because of the leaching that has occurred. The pore shape is also in accordance with the model of Doyen (1988) (Fig. 60). Doyen (1988) suggests that the pore space morphology of sandstone is similar to the skeleton

structure, having a network of cylindrical channels. In sandstone, cylindrical channels seem to be formed in matrix like those in the model shown in Fig. 60. In addition, the pore volume and the mean pore radius increase as the weathering period increases, and, thus, the radius of cylindrical channels seems to increase as the weathering period increases. To summarise, the leaching of matrix and the resulting increased pore volume play a major role in the weathering of sandstone.

4.3.2. Concentration of iron minerals in matrix of sandstone

The changing process of iron minerals due to weathering affects rock structure and changes in colour of sandstone. The results of observation of microphotographs show that iron minerals accumulated in matrix as the weathering period increased. Small amounts of iron minerals are found in 0- to 20-ka rocks, and the amounts increase in 70- to 350-ka rocks. Particles of iron minerals with a maximum diameter of 100 μm are recognised in 350-ka rock. In addition, the results of EDS show that Fe concentrates in matrix as the weathering period increases. In 0- to 70-ka rocks, the concentration of Fe is low over the whole thin section, while concentrated Fe forms particles in 120- to 350-ka rocks in matrix, with a maximum diameter of as much as 100 μm. Fe^{2+} is formed by leaching of chlorite due to weathering. Fe^{2+} is easily oxidized to Fe^{3+} in an oxidative environment such as in terrace deposits. Fe^{3+} is precipitated within the rock because Fe^{3+} has a low solubility in natural water (e.g., Ichikuni, 1972). Hydroxides such as ferrihydrite are formed by precipitation of Fe^{3+}. The reaction of iron precipitation is expressed by the following equations:

$$Fe^{3+} + 3OH^- \rightarrow Fe(OH)_3 \quad \cdots (4\text{-}14)$$

$$5Fe(OH)_3 \rightarrow Fe_5HO_8 \cdot 4H_2O + 3H_2O \quad \cdots (4\text{-}15)$$

where ferrihydrite ($Fe_5HO_8 \cdot 4H_2O$) is an amorphous mineral commonly recognised in red soils (e.g., Torrent et al., 1982; Schwertman and Murad, 1983, 1988; Campbell and Schwertman, 1984; Araki and Kyuma, 1987).

The colour of sandstone gravel changes to yellowish or reddish as the weathering period increases. The colour of rocks is affected by the iron minerals contained therein. For example, if hematite is added to powdered white almina by 0.77 and 0.05 weight percent, the powder changes to red and pink, respectively. This suggests that when sandstone becomes reddish due to weathering, it is caused by an increase in iron minerals such as hematite. The type of iron minerals could not be detected by XRD analysis of the sandstone because it has a relatively low iron mineral content. The results of colour measurement and spectroscopy analysis suggest that iron minerals in rock samples change from ferrihydrite to goethite (α -FeOOH) during the 0- to 250-ka period and from ferrihydrite to hematite (α -Fe_2O_3) during the 250- to 350-ka period.

Several studies have been carried out that examined the changing mechanism of iron minerals in red soils (e.g., Torrent et al., 1982; Schwertman and Murad, 1983, 1988; Campbell and Schwertman, 1984; Araki and Kyuma, 1987). Ferrihydrite could not identified by XRD because it is amorphous. Mizukami et al. (1999) have shown hydrogen-containing minerals in weathered sandstone using near infrared spectroscopy analysis. In addition, many amorphous iron minerals were included in red soils on the Higashibaru terrace in the Miyazaki Plain (Akagi et al, 1997). These hydrogen-containing minerals and amorphous iron minerals in the present study seem to be considered ferrihydrite.

Experimental studies of the dehydration of ferrihydrite have been carried out by Torrent et al. (1982) and Schwertmann and Murad (1983). These studies show that hematite increases at high temperature, low humidity and neutrality conditions, and goethite increases at low temperature, high humidity, and acidic and/or alkaric conditions. The formation process of

goethite and hematite from ferrihydrite ($Fe_5HO_8 \cdot 4H_2O$) is discussed by Torrent et al. (1982). The results of this paper show that ferrihydrite can transform to hematite and goethite at high relative humidity, about 93 % (Torrent et al, 1982: Fig. 62). When there is a lower relative humidity and a high temperature, the transformation to hematite is highly favored over transformation to goethite. These reactions are described by the following chemical equations:

$$2Fe_5HO_8 \cdot 4H_2O \rightarrow 5\,\alpha\text{-}FeOOH + 2H_2O \quad \cdots (4\text{-}16)$$

$$2Fe_5HO_8 \cdot 4H_2O \rightarrow 5\,\alpha\text{-}Fe_2O_3 + 5H_2O \quad \cdots (4\text{-}17)$$

The results of colour measurement and spectroscopic analysis show that goethite increased during 70 to 250 ka BP, and hematite increased during 250 to 350 ka BP (Figs. 30 and 33). Although changes of iron minerals seem to be caused by changes in environmental conditions such as temperature and humidity at 250 ka, this contradicts the many studies concerning the Quaternary environmental changes. For example, as glacial-interglacial cycles are recognised in the Quaternary, drastic environmental changes around 250 ka contradict the above results. Because of this, changes in iron minerals cannot be explained by environmental changes that occurred around 250 ka. These considerations suggest that the formation of hematite required more time than did the formation of goethite. The reaction in Equation (4-16) seems to have occurred during the early stage of weathering, between 70 and 250 ka, and the reaction in Equation (4-17) seems to have occurred during the later stage of weathering, between 250 and 350 ka.

The paleo red soils are recognised at the top of terrace deposits during 110 to 350 ka. The soils are yellowish during 110 to 120 ka and reddish during 250 to 350 ka. The changing pattern of soil colour is correlated to the changing pattern of sandstone gravel due to weathering. Matsui (1963), for example, discussed that paleo red soils are formed by oxidation of soil

forming minerals under high temperatures during the interglacial period. Formation processes of both reddish weathered gravel and red and yellow soils are thought to have occurred because the weathering of gravel and soil occurred at high temperatures in the interglacial period. Field evidence shows that weathered gravel beds gradually transform into red and yellow soils on the surface. Oxidation of iron minerals may accelerate under high temperature conditions, as in the interglacial stage. The *CIA*- and *PI*-values change at a constant rate during 350 ka. There is no evidence of rapid changes in the chemical weathering indices during the 90- to 120-ka period. The effect of global climate changes on chemical weathering was not observed in the present study. Further investigation will be needed to clarify the effect of global climate changes on rock weathering.

4.3.3. Summary

The behavior and crystallization of iron in sandstone gravel due to weathering are summarised in Fig. 63. Iron originates from chlorite. Changing iron by oxidation, hydration and mineralization during weathering ultimately produces goethite and hematite. The rock structure and colour of sandstone gravel seem to be affected by changes of iron minerals in matrix. In summary, the weathering mechanism of sandstone, as illustrated in Fig. 64, is that an increase in pore volume and pore radius is caused by leaching of clay minerals in matrix. In addition, the pore volume and the mean pore radius increase as the weathering period increases. Increasing pore volume and concentration of iron minerals in matrix lead to the conclusion that changes in rock properties of sandstone are due to weathering.

4.4. Application to engineering geology

Study of the effects of weathering on rock mass is of great importance in the field of engineering geology. For example, the rock mass quality is significantly affected by deterioration caused by rock weathering. Considered as an engineering material, rock displays extreme variation in three important engineering properties, namely (1) strength, (2) permeability and (3) deformability (Japan Society of Engineering Geology, 1992). In general, weathered rock usually becomes weak, highly deformable and highly permeable (e.g., Nishida, 1986).

The physical and mechanical properties of small rock pieces such as drilling cores or hand specimen samples can be easily obtained, but these properties of large rock masses cannot be easily obtained, since they are assemblies of rock pieces and various kinds of geological discontinuity such as bedding planes, schistosity, joints and faults (e.g., Goodman, 1976; 1989). Therefore, some simple methods must be developed for technically evaluating the foundation rock masses. A rock mass classification system has been used to evaluate the foundation rock masses (Tanaka, 1964; Japan Society of Engineering Geology, 1992), but it provides only limited information. This system focuses on factors related to the degree of weathering. In the rock mass classification, weathered rocks are roughly classified into several degrees of weathering with the aid of the following properties: (1) colour and change of structure observed with the naked eye, and (2) strength when hit with a rock hammer. However, precise determination of the degree of weathering based on rock colour is hardly carried out, even though the change in colour is the first observed feature of weathered rocks.

Rock mass classification has been widely used to design dams, tunnels, deep underground caverns and foundations of electric power plants (e.g., Tanaka, 1964; Makita et al., 1991; Japan Society of Engineering Geology, 1992). However, this classification is mostly based on the experience of engineering geologists. It is important to develop clear standards for rock mass classification. If it were possible to quantitatively record rock colour,

one might achieve a somewhat objective view of classification based on weathering. As mentioned in section 4.3.1, colour measurement and visible spectroscopy analysis are significant tools for the classification of weathered rock.

As mentioned in section 4.2., the relationships among rock properties can be described quantitatively by equations (4-1) to (4-13). These equations can be applied to engineering geological problems. In particular, effective porosity and b^*-value are closely related to many other rock properties. In addition, since both parameters can be measured easily, they can be widely applicable for many engineering problems. Colour measurement is an especially useful technique for engineering geology. For example, since rock colour can be obtained by rapid measurement in a few seconds in the field, effective porosity and permeability can be calculated by Equations (4-12) and (4-13). Colour measurement can be applied to the evaluation of aggregate materials, too. The judgement of aggregates requires that the researcher know the absorption ratio of water, a_b, and the apparent dry specific gravity, G_d. The relationships between b^*-value and a_b and G_d can be discussed, because these parameters were obtained as shown in Tables 6 and 7. These relationships are shown in Fig. 65. Changes of b^*-value have a high correlation to the absorption ratio of water and apparent dry specific gravity. Using the least-squares fit method, the relationships between b^*-value and a_b and G_d are expressed by the following equations (R^2 is the contribution ratio):

$$a_b = 0.927\, e^{0.107\, b^*}, \quad R^2 = 0.830 \qquad \cdots (4\text{-}18)$$

$$G_d = -0.028\, b^* + 2.699, \quad R^2 = 0.781 \qquad \cdots (4\text{-}19)$$

Aggregate materials for dam concrete require that the upper limit of the absorption ratio of water be 3 % and that the lower limit of apparent dry specific gravity be 2.5 (Japan Society of Civil Engineers, 1996). The results of calculation using Equations (4-18) and (4-19) show that the upper limit of the

b^*-value correlated to the absorption ratio of water is 1.17, and correlation to the apparent dry specific gravity is 7.10. Using colour measurement of sandstone in the field, the judgment of aggregates can be done in a few seconds. In order to use aggregate materials, the relationships between each rock type and colour value must be clarified.

Good relationships between the rock mass classification rank, such as D, CL, CM and CH, and the colour value (b^*-value) are expected. When those relationships have been established, a more objective classification of rock masses will be possible using colour measurement. However, relationships between rock types and colour value differ depending on the rock type, so each type of rock and colour value will have to be classified before an objective rock mass classification system can be completed.

In summary, colour measurement can be a very useful method in engineering geology for the estimation of a variety of other rock properties such as the effective porosity and the permeability.

5. Conclusions

Changes in several rock properties due to weathering have been investigated, and the weathering mechanism of sandstone has been clarified using sandstone gravel in dated terrace deposits whose formative ages are 0, 20, 70, 90, 110, 120, 250 and 350 ka. The following conclusions can be drawn from this study:

(1) Although the appearance of quartz phenocrysts does not change as the weathering period increases, plagioclase has decomposed during 350 ka. Clay minerals in matrix also decomposed as the weathering period increased, while iron minerals have gradually concentrated in matrix during 350 ka.

(2) The a^*-value increased during 250 to 350 ka, and the b^*-value increased during 0 to 120 ka. This result suggests that iron minerals in rock samples change[d] from ferrihydrite to goethite between 0 and 250 ka and from ferrihydrite to hematite between 250 and 350 ka.

(3) Effective porosity increases as the weathering period increases. Pore volume indicators such as V_c, and V_d increased slightly as the weathering period increased, while V_b increased rapidly during 90 to 120 ka and V_a increased rapidly during 120 to 350 ka. These results show that the pore diameter of sandstone increases as the weathering period increases, and the increased pore size is mostly more than 1 μm (V_a and V_b). The mean pore diameter increases as the weathering period increases, particularly rapidly during the 90- to 120-ka period. On the other hand, the specific surface area increases at a constant rate during 350 ka. Observation of X-ray CT images shows that the distribution of pores in sandstone is uniform throughout each sandstone gravel.

(4) The chemical composition of SiO_2, MgO, CaO, Na_2O and K_2O gradually decreases as the weathering period increases, while that of Al_2O_3 and $FeO+Fe_2O_3$ is mostly constant during 350 ka. These results show that SiO_2 is leached easily due to weathering, even though it has low solubility. Highly

soluble compounds such as MgO, CaO, Na_2O and K_2O also leach easily due to weathering, but Al_2O_3 and $FeO+Fe_2O_3$ tend to remain in the internal part of gravel because both compounds have low solubility. The *CIA*-value increases and the *PI*-value decreases at constant rates as the weathering period increases. Thus rates of chemical weathering are constant during 350 ka.

(5) The index of point load strength decreases during 0 to 120 ka, but after that remains constant during 120 to 250 ka. In particular, rock strength decreases during 90 to 120 ka.

(6) The rock structure and colour of sandstone gravel seems to be affected by changes in the iron minerals in matrix. The behavior and crystallization of Fe due to weathering caused by oxidation, hydration and mineralization during weathering, which ultimately produces goethite and hematite.

(7) Weathering causes the leaching of matrix materials in sandstone, which increases pore volume and pore radius. In addition, pore volume and mean pore radius increase throughout gravel as the weathering period increases. These findings lead us to conclude that changes in the rock properties of sandstone due to weathering are the result of increased pore volume and the concentration of iron minerals in the sandstone matrix.

Acknowledgments

This research was conducted with supports from many people. I thank my Ph D supervisor, Professor Yukinori Matsukura, University of Tsukuba, for valuable discussion, guidance, and encouragement. Suggestions from Professor Eiji Matsumoto, Professor Masamu Aniya, Professor Hiroshi Ikeda, Dr. Norikazu Matsuoka, Dr. Yuichi Onda, and Dr. Chiaki T. Oguchi, University of Tsukuba, are very helpful.

The experimental work would not have been possible without help from people in various institutes and universities. I am grateful to Dr. Katsuaki Koike, Kumamoto University, and Mr. Yosei Mizukami, Tokyo Institute of Technology, for measuring X-ray CT analysis. I am also grateful to Professor Seiji Takaya, Minami Kyushu University, and Dr. Shinji Nagaoka, Nagasaki University, Professor Yoshitaka Nagatomo, Miyazaki University, Mr. Yudzuru Inoue and Mr. Isao Akagi, Kagoshima University, Mr. Akira Shishido, Engineering geologist, and Mr. Kunihiro Yamamura, Komaki Co. Ltd and Masunaga Co. Ltd Joint venture, for their help with geological survey in Miyazaki Plain. I thanks Professor Shozo Yokoyama and Professor Kazunori Watanabe, Kumamoto University, for their help of microscope observation of tephra. Chemical and mineralogical analyses were performed under assistance of Dr. Kosei Komuro, University of Tsukuba, and Dr. Tamao Hatta, Japan International Research Center for Agricultural Sciences. Measurements of pore-size distribution were performed under assistance of Dr. Manabu Takahashi, The Geological Survey of Japan, Dr. Weirin Lin, Dia Consultants Co. Ltd., and Xiaochun Li, Ibaraki University.

Special thanks go to Dr. Takashi Hirose, in University of Ryukyus, and Dr. Yosuke Komatsu, Mr. Yasuhiko Takaya, Mr. Hisashi Aoki, University of Tsukuba, for their support and encouragement. This research has been financially supported by Fukada Geological Institute in 1998-1999.

References

Akojima, I. (1974) Red weathering crust in terrace gravel as a key to terrace chronology. *The Sci. Rep. Tohoku Univ. 7th Series (Geogr),* **23**, 91-119.

Akagi, I, Takaki, H. and Nagatomo, Y. (1997) Chemical composition of ferromagnetic minerals of the tephra deposits in the paleoredsoils on Miyazaki Coastal Plain. *Programme and abstract, Japan Assoc. Quat. Res.*, **27**, 212-213 (in Japanese).

Araki, S. (1988) Genesis and dating of red soils. *Pedologist*, **32**, 203-209 (in Japanese).

Araki, S. and Kyuma, K. (1987) Weathering of Fe-Mg rich smectite in red soils developed on tuffaceous sandstone and andesite. *Soil Sci. Plant Nutr.*, **33**, 1-11.

Baynes, F. J., Dearman, W. R. and Irfan, T. Y. (1978) Practical assessment of grade in a weathered granite. *Bull. Int. Assoc. Engng. Geol.*, **18**, 101-109.

Bell, F. and Linsay, P. (1999) The petrographic and geomechanical properties of some sandstones from the newspaper member of the Natal Group near Durban, South Africa. *Engng. Geol.*, **53**, 57-81.

Bell, F. (1978) The physical and mechanical properties of the fell sandstones, Northumberland, England. *Engng. Geol.*, **12**, 1-29.

Berner, R. A., Sjoverg, M. A.Velvel, and Krom, M. D. (1980) Dissolution of pyroxenes and amphiboles during weathering, *Science*, **207**, 1205-1206.

Butenuth, C., Fey, M., Freitas, M., Passas, N. and Forero-Duenas, C. (1998) Silica gels: a possible explanation for slope failures in certain rocks : *In* Maund, J. G. and Eddleston, M. eds., *Geohazards in Engineering Geology*, Geological Society, London, Engineering Geology Special Publications, **15**, 185-191.

Campbell, A. and Schwertman, U. (1984) Iron oxide mineralogy of placic horizons, *Jour. Soil Sci.*, **35**, 569-582.

Chigira, M. and Sone, K. (1988) Weathering mechanism of sandstone (part 1)

–weathering of coarse-grained sandstone cemented by zeolite. *Abiko Research Laboratory Rep.* **U.88039**, 32p (in Japanese with English abstract).

Chigira, M. (1988) Weathering mechanism of sandstone (part 2) –weathering of fine-grained sandstone. *Abiko Research Laboratory Rep.* **U.88040**, 36p (in Japanese with English abstract).

Chigira, M. (1991) Chemical weathering mechanisms and their effects on engineering properties of soft sandstone and conglomerate cemented by zeolite in a mountainous area. *Engng. Geol.*, **30**, 195-219.

Colman, D. P. (1986) An overview of rates of chemical weathering. In *Rates of Chemical Weathering of Rocks and Minerals* (eds., Colman, S. and Dethier, D.), Academic Press, Inc, pp.1-17.

Cooke, R. U. and Smalley, I. J. (1968): Salt weathering in deserts, *Nature*, **220**, 1227-1227.

Crook, R. and Gillespie, A. (1986) : Weathering rates in granitic boulders measured by P-wave speeds. In *Rates of Chemical Weathering of Rocks and Minerals* (eds., Colman, S. and Dethier, D.), Academic Press, Inc, pp.395-417.

Dorn, R. I. And Oberlander, T. M. (1981) Microbial origin of desert vanish, *Science*, **213**, 1245-1247.

Doyen, P. (1988) Permeability, conductivity, and pore geometry of sandstone. *Jour. Geophy. Res.*, **93**, 7729-7740.

Drever, J. I., ed., (1985) *The Chemistry of Weathering*: D. Reidal Publ., Dordrecht, 324p.

Duliu, O. G. (1999) Computer axial tomography in geosciences: an overview. *Earth-Science Rev.*, **48**, 265-281.

Endo, H., and Suzuki, Y. (1986) *Geology of the Tsuma and Takanabe district, with geological sheet map at 1:50,000*, Geol. Surv. Japan. 105p (in Japanese with English abstract).

Endo, T. (1968) Geological study of the Miyazaki Coastal Plain, southeastern Kyushu, Japan. *Bull. Fac. Educ. Miyazaki Univ.*, **24**, 17-64.

Fookes, P. G., Dearman, W. R. and Franklin, J. A. (1971) Some engineering aspects of rock weathering with field examples from Dartmoor and elsewhere. *Quarterly Jour. Engng. Geol*, **4**, 139-185.

Geet, M. V., Swennen, R. and Wevers, M. (2000) Quantitative analysis of reservoir rocks by microfocus X-ray computerised tomography. *Sedimentary Geol*, **132**, 25-36.

Goodman, E. R. (1976) *Methods of Geological Engineering in Discontinuous Rocks*. West Publishing Company, 371p.

Goodman, E. R. (1989) *Introduction to Rock Mechanics*. John Wiley and Sons, 562p.

Goudie, A. S., Cooke, R. U. and Evans, I. S. (1970) Experimental investigation of rock weathering by salts. *Area*, **4**, 42-48.

Hachinohe, S., Hiraki, N. and Suzuki, T. (1999a) Weathering rates of Tertiary sandstone and mudstone in Japan. *Z. Geomorph. N. F.*, **119**, 57-69.

Hachinohe, S., Hiraki, N. and Suzuki, T. (1999b) Rates of weathering and temporal changes in strength of bedrock of marine terraces in Boso Peninsula, Japan. *Engng. Geol.*, **55**, 29-43.

Hall, K. and Hall, A. (1996) Weathering by wetting and drying: some experimental results. *Earth surf. processes landf.*, **21**, 365-376.

Halsay, D. P. (1996) *The weathering of sandstone, with particular reference to buildings in the west Midlands, UK.* Wolverhampton University. 261p.

Hatta, T., Matsukura, Y. and Yatsu, E. (1983) Mutual crystal orientation in weathering process from feldspar to secondary minerals. *Trans. Japan. Geomorph. Union*, **4**, 81-88 (in Japanese with English abstract).

Hiramatsu, Y., Oka, Y. and Kiyama, H. (1965) Rapid determination of the tensile strength of rocks with irregular test pieces. *Jour. Mining. Metallurgical Institute Japan.*, **81**, 1024-1030 (in Japanese with English abstract).

Hiroi, T. (1999) Quantitative analysis of rock-forming minerals by visible and near infrared remote sensing –silicate minerals as examples-. *Jour. Mineral.*

Soc. Japan., **28**, 109-116 (in Japanese with English abstract).

Hirono, T. and Nakashima, S. (2000) Image visualization and quantitative analysis of void structure in sedimentary rock using image processing. *Jour. Geol. Soc. Japan*, **106**, 165-168.

Huang, W. H. and Keller, W. D. (1973) Organic acid as agents of chemical weathering of silicate minerals. *Nature*, **239**, 149-151.

Ichinose, M. and Uchino, K. (1981) Experimental study on hygroscopisity of sandstones. *Rep. Fac. Tech., Kyushu Univ.*, **54**, 239-246 (in Japanese with English abstract).

Ichikuni, M. (1972) *Inorganic Geochemistry*, Baifuukan, Tokyo, 148p (in Japanese).

Ikehara, K. (1997) X-ray Computer Tomography: A nondestructive method for quantitative analysis of geological materials (part 1) - Instrument and imaging. *Chishitsu News (Geological Survey of Japan)*, **516**, 50-61 (in Japanese).

Isii, T., Itoh, M., Nakashima, H., Sugawara, H., Ohe, T. and Hirata, Y. (1998) The long-term degradation rate in natural bentonite formations according to the field data. *Jour. Clay Sci. Soc. Japan*, **38**, 10-22 (in Japanese with English abstract).

Ishijima, Y., Xue, Z. and Takahashi, M. (1991) Permeability of the Neogene sedimentary rocks and its interpretation by using the equivalent channel model. *Jour. Japan Soc. Eng. Geol.*, **32**, 209-220 (in Japanese with English abstract).

Ishijima, Y., Xue, Z. and Takahashi, M. (1991) Some basic problems on measurements of hydraulic properties of rock by the transient pulse method. *Jour. Mining and Materials processing Inst. Japan,* **109**, 511-516 (in Japanese with English abstract).

Jayawardena, U. S. and Izawa, E. (1994) Application of present indices of chemical weathering for Precambrian metamorphic rocks in Sri Lanka. *Bull. Int. Assoc. Engng. Geol.*, **49**, 55-61.

Kamei, G., Sato, H. and Shibata, M. (1995) A natural illustration of long-term diffusion of water in bentonite. *Jour. Atomic Power Soc. Japan.* **37**, 624-627 (in Japanese with English abstract).

Kasuya, K. (1978) Mutual relation on physical properties of rocks with an attempt on classification of rocks due to physical properties. *Jour. Japan Soc. Eng. Geol.*, **19**, 128-149 (in Japanese with English abstract).

Kikuchi, H., Kawamura, H., Furukawa, K., Okuzono, S. and Tanaka, S. (1998) Based on long-term measurements cut-slope weathering progress and collapse possibility. *Jour. Geotechnical Engineering (Japan. Soc. Civil Engineers)*, **588**, 151-164 (in Japanese with English abstract).

Kimiya, K. (1975a) Tensile strength as a physical scale of weathering in granitic rocks. *Jour. Geo. Soc. Japan*, **81**, 349-364 (in Japanese with English abstract).

Kimiya, K. (1975b) Rates of weathering of gravels of granitic rocks in Mikawa and Tomikusa areas. *Jour. Geo. Soc. Japan*, **81**, 683-696 (in Japanese with English abstract).

Kimura, K., Iwaya, T., Mimura, K., Sato, Y., Sato, T., Suzuki, Y. and Sakamaki, Y. (1990) *Geology of the Osuzuyama district, with geological sheet map at 1:50,000*, Geol. Surv. Japan. 137p (in Japanese with English abstract).

Kino, Y., Kageyama, K., Okumura, K., Endo, H., Fukuta, O., and Yokoyama, S. (1984) *Geology of the Miyazaki district, Quadrangle series, scale 1:50,000*, Geol. Surv. Japan. 100p (in Japanese with English abstract).

Koroneos, E. G., Tassojannopoulos, A. and Diamantopoulou, A. (1980) On the mechanical and physical properties of ten Hellenic marbles. *Engng. Geol.*, **16**, 263-290.

Kuchitsu, N., Kuroki, N., Inokuchi, S. and Mitsuishi, S. (1999) Basic reserch on the reflectance spectra of mineral pigments. *HOZON-KAGAKU (Tokyo National Research Institute of Cultural Properties)*, **38**, 108-123 (in Japanese with English abstract).

Krumbein, W. E. (1978) Environmental biogeochemistry and geomicrobiology (Vol. 2), The terrestrial environment. *Proc. of an International Symp. Ann Arbor Science,* Distributed by John Willey.

Lagasa, A. C. (1984) Chemical kinetics of water-rock interaction. *Jour. Geogr. Res.*, **89**, 4009-4025.

Lautridou, J. P. and Ozouf, J. C. (1982) Experimental frost shattering: 15 years of research at the 'Centre de Geomorphologie du CNRS': *Progress in Physical Geog.*, **6**, 215-232.

Lin, W., Takahashi, M., Nishida, K. and Zhang, M. (1999a) Equivalent channel models for permeability estimation and their application to sedimentary rocks. *Jour. Japan Soc. Eng. Geol.*, **39**, 533-539 (in Japanese with English abstract).

Lin, W. and Takahashi, M. (1999b) Permeability of Inada granite with high temperature history and its estimation by the equivalent channel models. *Jour. Japan Soc. Eng. Geol.*, **40**, 25-35 (in Japanese with English abstract).

Loughnan, F. C. (1969) *Chemical weathering of silicate minerals*, New York, Elsevier, 154p.

Machida, H. and Arai, F. (1992) *Atlas of tephra in and around Japan.* University of Tokyo Press, Tokyo, 276p (in Japanese).

Machida, H. and Arai, F. (1994) Implication of the time-marker Aso-3 tephra to the significant lowering of sea level in the marine isotope stage 5d. *Jour. Geogr.*, **103,** 749-759 (in Japanese with English abstract).

Makita, T., Fukutake, Y., Hoshino, N., Iguchi, K. and Niimi, K. (1991) Rock classification for deep underground caverns. *Jour. Japan Soc. Eng. Geol.*, **32**, 240-251 (in Japanese with English abstract).

Matsui, K. and Kato, Y. (1962) Notes on paleopedology of red soils in Japan. *Quat. Res. (Daiyonki Kenkyu)*, **2**, 161-179 (in Japanese with English abstract).

Matsukura, Y. (1994) A review of the studies on rock control in weathering processes. *Trans. Japan. Geomorph. Union*, **15**, 203-222 (in Japanese with

English abstract).

Matsukura, Y. (1997) Weathering Rates of bedrocks in artificial and natural slopes. *Jour. Japan Soc. Eng. Geol.*, **38**, 224-231 (in Japanese with English abstract).

Matsukura, Y. and Hirose, T. (1999) Five year measurements of rock tablet weathering on a forested hillslope in a humid temperature region. *Engng. Geol.*, **55**, 69-76.

Matsukura, Y., Maekado, A., Hatta, T. and Yatsu, E. (1983) Vertical changes in mineralogical, physical, chemical and mechanical properties due to deep weathering of Inada granitic rocks. *Trans. Japan. Geomorph. Union*, **4**, 65-80 (in Japanese with English abstract).

Matskura, Y. and Matsuoka, N. (1996) The effect of rock properties on rates of tafoni growth in coastal environment. *Z. Geomorph. N. F.*, **106**, 57-72.

Matsunaka, T. and Uwasawa, M. (1992) Near infrared diffuse reflectance sprctra of clay minerals. *Soil Sci. Plant Nutri.*, **64**, 329-331 (in Japanese with English abstract).

Matsumoto, A. and Ui, T. (1997) K-Ar age of Ata pyroclastic flow deposits, southern Kyushu, Japan. *Bull. Volc. Soc. Japan.*, **42**, 223-225 (in Japanese with English abstract).

Matsumoto, A., Uto, K., Ono, K. and Watanabe, K. (1991) K-Ar age determinations for Aso volcanic rocks. *Proc. Bull. Volc. Soc. Japan*, 73 (in Japanese).

McGreevy, J. (1981) Some perspectives on frost shattering. *Progress in Physical Geogr.*, **5**, 56-75.

Mitsushita, J., Ishizawa, K., Endo, T. and Takeuchi, T. (1998) Study for color measurement of rocks and its application to weathering classification and phyisical property evaluation. *Jour. Japan Soc. Eng. Geol.*, **38**, 370-385 (in Japanese with English abstract).

Nakano, T., Nakamura, K., Sometani, T. and Otsuka, H. (1997) Observation of 3-dimentional internal structure of rock using X-ray CT: (1) Density

calibration of CT value. *Geoinfomatics*, **8**, 239-255 (in Japanese with English abstract).

Nakano, T., Nakashima, Y., Nakamura, K. and Ikeda, S. (2000) Observation and analysis of internal structure of rocks using X-ray CT. *Jour. Geol. Soc. Japan,* **106**, 363-378 (in Japanese with English abstract)..

Nagano, T. and Nakashima, S. (1989) Study of colors and degrees of weathering of granitic rocks by visible diffuse reflectance spectroscopy. *Geochem. Jour.,* **23**, 75-83.

Nishizawa, O., Nakano, T., Noro, H. and Inazaki, T. (1995) Recent advances of X-ray CT technology for analyzing geologic materials. *Bull. Geol. Surv. Japan*, **46**, 565-571 (in Japanese with English abstract).

Nakamura, Y. (1998) weathering indices of rock materials. *Jour. Japan Soc. Eng. Geol.*, **39**, 221-229 (in Japanese with English abstract).

Nakashima, S., Ohki, S., and Ochiai, S. (1989) Infrared microspectroscopy analysis of the chemical state and distribution of hydrous species in minerals: *Geochem. Jour.,* **23**, 57-64.

Nakashima, S., Miyagi, I., Nakata, E., Sasaki, H., Nittono, S., Hirano, T., Sato, T., and Hayashi, H. (1992) Color measurement of some natural and synthetic minerals: *Rep. Res. Inst. Natural Resources, Mining College, Akita Univ.*, **57**, 57-76.

Nagaoka, S. (1984) Late Pleistocene tephrochronology in the region from the Osumi Peninsula to the Miyazaki Plain in the south Kyushu, Japan. *Jour. Geogr.,* **93**, 347-369 (in Japanese with English abstract).

Nagaoka, S. (1986) The landform evolution of the late Pleistocene in the Miyazaki Plain, south Kyushu, Japan. *Quat. Res.(Daiyonki Kenkyu)*, **25**, 139-163 (in Japanese with English abstract).

Nagaoka, S., Arai, F., Nagatomo, Y., Akagi, I., Inoue, Y. and Nishiyama, K. (1998) Stratigraphy of Pleistocene marine sediments in Miyazaki Plain. *Programme and Abstracts, Japan Assoc. Quat. Res.,* **28,** 168-169 (in Japanese).

Nagaoka, S. and Arai, F. (1999) Quaternary tephrochronology and tectonics of Miyazaki Plain. *Proc. Asoc. Japan. Geograph.*, **55**, 350-351 (in Japanese).

Nesbitt, H. W. and Young, G. M. (1982) Early proterozoic climates and plate motions inferred from major element chemistry of lutites. *Nature*, **299**, 715-717.

Nishida, K. (1986) *HUU-KA-ZANSEKIDO-NO-KOUGAKUTEKI-SEISITSU (Engineering Properties of weathered residual soils),* Kazima-Syuppann-Kai, Tokyo, 192p (in Japanese).

Nishiyama, T., Kusuda, H., and Saito, T. (1992) A few remarks on examination of cavities or microcracks produced in rocks using a fluorescent substance. *Jour. Japan Soc. Eng. Geol.*, **33**, 17-22 (in Japanese with English abstract).

Nishiyama, K., Yokota, S. and Iwamatsu, A. (1999) Distribution and rock properties of reddish weathered gravels within the Quaternary fan deposits. *Jour. Japan Soc. Eng. Geol.*, **40**, 2-13 (in Japanese with English abstract).

Okada, H. (1977) Preliminary study of sandstones of the Shimanto Supergroup in Kyushu, with special reference to petrographic zone. *Sci. Rep. Dep. Geol. Kyushu Univ.*, **12**, 203-214 (in Japanese with English abstract).

Ollier, C. (1984) *Weathering (second edition).* Longman London and New York., 270p.

Oguchi, C. and Matsukura, Y. (1994) A review of chemical weathering index. *Bull. Environm. Res. Center, Univ. Tsukuba*, **19**, 11-18.

Oguchi, C., Isobe, H., Komuro, K. and Matsukura, Y. (1995) Color measurements using a visible microspectrometer of weathering rinds on andesite blocks. *Ann. Rep. Inst. Geosci., Univ. Tsukuba*. **21**, 9-13.

Oguchi, C., Hatta, T. and Matsukura,Y. (1994) Changes in rock properties of porous rhyolite through 40,000 years in Kozu-shima Island, Japan. *Geogr. Rev. Japan*, **67A-11**, 775-793 (in Japanese with English abstract).

Oguchi, C. and Matsukura, Y. (1996) The change in microstructure of porous rhyolite due to weathering and its influence on the reduction of rock strength.

Trans. Japanese Geomor. Union. **17**, 1-15 (in Japanese with English abstract).

Oguchi, C., Hatta, T. and Matsukura, Y. (1999) Weathering rates over 40,000 years based on changing in rock properties of porous rhyolite. *Phys.Chem. Earth (A)*, **24**, 861-870.

Oguchi, C. and Matsukura, Y. (1999) Effect of porosity on the increase in weathering-rind thickness of andesite gravel. *Engng. Geol.*, **55**, 77-89.

Ota, T. and Kitani, H. (1997) Color changing of basic rock by artificial weathering. *Japan Soc. Eng. Geol. Proc.*, 117-120 (in Japanese).

Otani, J., Obara, Y., Sugawara, K. and Mukunoki, T. (2000a) Application of industrial X-ray computed tomography scanner to geotechnical engineering. *TSUCHI-TO-KISO (The Japanese Geotechnical Society)*, **48- 2**, 17-20 (in Japanese with English abstract).

Otani, J., Mukunoki, T. and Obara, Y. (2000b) Application of X-ray CT method for characterization of failure in soils. *Soils and Foundations*, **40**, 111-118.

Otsuka, Y. (1930a) Geological problem of Takanabe district, Miyazaki prefecture. *Geogr. Rev. Japan*, **6**, 1048-1073 (in Japanese with English abstract).

Otsuka, Y. (1930b) The crustal movement and the inclination of coastal terraces on the southeastern Kyushu. *Geogr. Rev. Japan.* **8**, 1-15 (in Japanese with English abstract).

Oyama, T., Chigira, M., Ohmura, N., Sasaki, K. and Nagaoka, T. (1998) Chemical weathering of sedimentary rocks in vadose zone –The weathering rates of mudstone on old unlined tunnel walls and the bacterial effects on it. *Jour. Japan Soc. Eng. Geol.*, **39**, 511-523 (in Japanese with English abstract).

Paichik, V. (1999) Influence of porosity and elastic modulus on uniaxial compressive strength in soft brittle porous sandstones. *Rock Mech. Rock Engng*, **32**, 303-309.

Paterson, M. S. (1983) The equivalent channel model for permeability and resistivity in fluid saturated rock – A re-appraisal. *Mech. Materials*, **2**, 345-352.

Pentecost, A. (1991) The weathering rates of same sandstone cliffs, central Weald, England. *Earth Surf. Processes Landf.*, **16**, 83-91.

Raynaud, S., Fabre, D., Mazerolle, F., Greaud, Y. and Latiere, H. (1989) Analysis of the internal structure of rocks and characterization of mechanical deformation by a non-destructive method: X-ray tomodensitometry. *Tectonophysics*, **159**, 149-159.

Reiche, P. (1943) Graphic representation of chemical weathering. *Jour. Sediment. Petrol.*, **13**, 58-68.

Ruxton, B. F. (1968) Measures of the degree of chemical weathering of rocks. *Jour. Geol.*, **76**, 518-527.

Saito, T., Abe, M. and Kunori, S. (1974a) Study on weathering of volcanic rocks (1). *Geophysical Exploration (Japan)*, **27**, 3-15 (in Japanese with English abstract).

Saito, T., Abe, M. and Kunori, S. (1974b) Study on weathering of volcanic rocks (2). *Geophysical Exploration (Japan)*, **27**, 16-26 (in Japanese with English abstract).

Suzuki, T., Hirano, M., Takahashi, K. and Yatsu, E. (1977) The interaction between the weathering processes of granites and the evolution of landforms in the Rokko mountains, Japan. *Bull. Sci. Tech. Chuo Univ.*, **20**, 343-389.

Sasaki, Y. and Otani, T. (1999) Development of a visible and near infrared multi-spectrograph, and its utilization for estimation of strength and type of rocks. *Japan Soc. Eng. Geol. Proc.*, 195-198 (in Japanese).

Scholle, P. (1979) *A color illustrated guide to constituents, textures, cements, and porosities of sandstone and associated rocks*. The American Association of Petroleum Geologists, Oklahoma, 201p.

Schwertman, U. and Murad, E. (1983) Effect of pH on the formation of goethite and hematite from ferrihydrite. *Clays and Clay Minerals*, **31**,

277-284.

Schwertman, U. and Murad, E. (1988) The nature of an iron oxide –organic iron association in a peaty environment. *Clay Minerals*, **23**, 291-299.

Sugawara, K., Kojima, R., Obara, Y., Sato, A. and Shimada, H. (1998) Crack opening analysis by means of the X-rays CT. *Jour. Mining and Materials Processing Inst. Japan*, **114**, 881-887 (in Japanese with English abstract).

Sugawara, K., Sato, A., Obara, Y. and Yanagisako, M. (1999) Measurement of permeability of rock by means of X-ray CT. *Jour. Mining and Materials Processing Inst. Japan*, **115**, 803-808 (in Japanese with English abstract).

Sunamura, T. (1996) A physical model for the rate of coastal tafoni development. *Jour. Geol.*, **104**, 741-748.

Suzuki, T. and Hachinohe, S. (1995) Weathering rates of bedrock forming marine terraces in Boso peninsula, Japan. *Trans. Japan. Geomorph. Union*, **16**, 93-113.

Suzuki, K. and Takahashi, M. (1994) A visualizing method of pores and cracks using filmy replica system. *Jour. Japan Soc. Eng. Geol.*, **35**, 77-78 (in Japanese with English abstract).

Suzuki, S. (1992) Paleoenvironment of the ultra-Tamba zone by means of modal and chemical compositions of sandstone. *Mem. Geol. Soc. Japan*, **38**, 71-83 (in Japanese with English abstract).

Taga, N., Tayama, S., Okuzono, S. and Yagisawa, T. (1992) Long-term measurements on weathering progress and stability of cut slope. *Soil and Foundation,* **39- 6**, 41-47 (in Japanese with English abstract).

Takahashi, M., Sugita, Y., Xue, Z., Oonishi, Y. and Ishijima, Y. (1993) Three principal stress effects on permeability of the Shirahama sandstone. *Jour. Mining and Materials Processing Inst. Japan,* **109**, 803-809 (in Japanese with English abstract).

Takahashi, M., Xue, Z., Oowada, A. and Ishijima, Y. (1992) On the study of interconnected pore network using a blue dyed epoxy impregnated thin section. *Jour. Japan Soc. Eng. Geol.*, **33**, 294-306 (in Japanese with English

abstract).

Takahashi, M., Lin, W., Nishida, K. and Zhang, M. (1999) Measurement of pore size distribution in rocks by mercury intrusion porosimeter. *TSUCHI-TO-KISO (The Japanese Geotechnical Society),* **47-4**, 30-32 (in Japanese with English abstract).

Tamura, H. and Suzuki, T. (1984) Pore size distribution and other physical properties of Tertiary sedimentary rocks. *Trans. Japan. Geomor. Union*, **5**, 311-328 (in Japanese with English abstract).

Tanaka, Y., Hachinohe, S. and Matsukura, Y. (1996) The influence of slaking susceptibility of rocks on the formation of Hoodoos in Drumheller badlands, Alberta, Canada. *Trans. Japan. Geomorph. Union*. **17**, 107-121.

Teraoka, Y. (1977) Comparison of the Cretaceous sandstones between the Shimanto Terrene and the median zone of Southwest Japan, with reference to the provenance of the Shimanto geosynclinical sediments. *Jour. Geol. Soc. Japan*, **83**, 795-810 (in Japanese with English abstract).

Teraoka, Y. (1979) Provenance of the Shimanto geosynclinical sediments inferred from sandstone compositions. *Jour. Geol. Soc. Japan*, **85**, 753-769 (in Japanese with English abstract).

Teraoka, Y., Suzuki, M., Hayashi, T. and Okumura K. (1995) Stratigraphical variation in chemical composition of sedimentary rocks in the Shimanto Supergroup of the Makinime - Mikado area, East Kyushu, Southwest Japan. *Bull. Fac. Educ. Hiroshima Univ., Part II*, **17**, 83-94 (in Japanese with English abstract).

Teraoka, Y., Okumura, K., Suzuki, M. and Kawakami, K (1999) Clastic sediments of the Shimanto Supergroup in Southwest Japan. *Bull. Geol. Surv. Japan*, **50**, 559-590 (in Japanese with English abstract).

The Japanese Geotechnical Society (1989) *GAN-NO-CYOUSA-TO-SHIKEN (Field survey and test of rocks)*, 371-377 (in Japanese).

The Japan Society of Civil Engineers (1977) *DAM-NO-CHISHITSU-CYOUSA (Engineering Geological Survey of Dam construction),* 162-170 (in

Japanese).

Torrent, J., Schwerman, U., Fechter, H. and Alfrez, F. (1983) Quantitative relationships between soil color and hematite content. *Soil Science*, **136**, 354-358.

Torrent, J., Guzman, R. and Parra, M. (1982) Influence of relative humidity on the crystallization of Fe (Ⅲ) oxides from ferrihydrite. *Clays and Clay Minerals*, **30**, 337-340.

Tungrul, A. and Zarif, I. (1998) The influence of mineralogical, textural and chemical characteristics on the durability of selected sandstones in Istanbul, Turkey. *Bull. Int. Asoc. Eng. Geol. Env.*, **57**, 185-190.

Uchida, T. and Tada, R. (1991) Pore properties of sandstone – Part 1. Experimental investigation-. *Jour. Japan Assoc. Petroleum Tech.*, **56**, 387-399 (in Japanese with English abstract).

Uchida, T. and Tada, R. (1992) Pore properties of sandstone – Part 2. Application of pore-size distribution to natural sandstone-. *Jour. Japan Assoc. Petroleum Tech.*, **57**, 213-222 (in Japanese with English abstract).

Uchida, T. (1992) Fundamental properties of fluid permeated rocks relevant to porosity and permeability. *Mining Geol.*, **42**, 175-190 (in Japanese with English abstract).

Uchino, K. and Ichinose, M. (1984) Investigation of pore structure of coal measure rocks. *Jour. Japan Soc. Eng. Geol.*, **25**, 195-205 (in Japanese with English abstract).

Ulusay, R., Tureli, K. and Ider, M. (1994) Prediction of engineering properties of a selected litharenite sandstone from its petrographic characteristics using correlation and multivariate statistical techniques. *Engng. Geol.*, **37**, 135-157.

Wakizaka, Y., Ohara, M., Takahashi, T., Furuichi, H., Harada, M. and Tanaka, M. (1998) Mineralogical and chemical properties of clays for discrimination of weak zone type: *8th Congr. Inter. Assoc. Engng. Geol. Environm.*, Vol. Ⅰ, 359-367.

Waragai, T. (1993) Weathering process of andesite lava in Mt. Hachimen, Yabakei, Oita Prefecture. *Bull. Fac. Sci. and Liter., Nihon Univ.*, **28**, 15-24.

Washburn, E. (1921) Note on a method of determining the distribution of pore sizes in a porous material. *Proc. National Academy of sciences*, **7**, 115-116.

Watanabe, T. (1990) Relative dating methods mainly applied to glacial and periglacial deposits. *Quat. Res. (Daiyonki Kenkyu)*, **29**, 49-77 (in Japanese with English abstract).

Webley, D. A. M., Henderson, M. E. K., and Taylor, I. F. (1963) The microbiology of rocks and weathered stones, *Jour. Soil Sci.*, **14**, 102-112.

White, K., Bryant, R. and Drake, N. (1998) Techniques for measuring rock weathering: application to a dated fan segment sequence in southern Tunisia. *Earth Surf. Processes Landf.*, **23**, 1031-1043.

Xue, Z., Ishijima, Y. and Takahashi, M. (1992) Permeability and microgeometry of sandstone under hydrostatic pressure. *Jour. Mining and Materials processing Inst. Japan,* **108**, 769-775 (in Japanese with English abstract).

Yamashita, S. and Suzuki, T. (1986) Changes in pore-size distribution of sedimentary rocks due to weathering and the resultant decrease in their strength. *Trans. Japan. Geomor. Union,* **7,** 257-273 (in Japanese with English abstract).

Yatsu, E. (1981) Weathering rates. *Trans. Japan. Geomor. Union*, **1**, 47-52 (in Japanese with English abstract).

Yatsu, E. (1988) *The nature of weathering - an introduction*, Sozosya, Tokyo, 624p.

Young, R. and Young, A. (1992) *Sandstone Landforms*. Springer-Verlag, 163p.

Yusa, Y., Arai, T., Kamei, G. and Takano, H. (1991) Natural analogue study on long-term leaching behavior of radioactive waste glass: weathering alteration of volcanic glasses from Fuji and Izu-Ohshima volcanoes, Japan. *Jour. Atomic Power Soc. Japan.* **33**, 890-905 (in Japanese with English abstract).

Tables

Table 1 Summary of previous studies of sandstone weathering

Reference	Locality	Geologic age	Analysis	Effective porosity (%)
Bell (1978)	England	?	mineral composition, particle size distribution, density, porosity, strength	13.4
Chigira and Sone (1991)	Japan	Miocene	density, porosity, pH, mineral composition, SEM, chemical composition	20.1～32.3
Ulusay et al. (1994)	Turkey	Carboniferous	mineral composition, particle size distribution, density, porosity, strength	3.13
Tugrul and Zarif (1998)	Turkey	Ordovician	chemical composition, slaking index, density, porosity, strength	2.92～17.39
Bell and Lindsay (1999)	South Africa	Silurian	mineral composition, particle size distribution, SEM, density, porosity, permeability, strength	6.25

Table 2 Correlation of terrace surfaces in Miyazaki Plain

Otsuka (1930a)	Endo et al. (1962)	Hoshino (1971)	Nagaoka (1986)	Endo and Suzuki (1986)	Nishiyama (2000)	marker tephra
						K-Ah, Kr-Kb
	Shinmachi S.	Mikazukibaru S.	Kunitomi II S.	Fukadoshi II S.	**Fukadoshi S.**	
	Dohjimaru S.		Kunitomi I S.	Fukadoshi I S.		
	Middle fluvial terrace S.	Hyuga Shirasu S.	Ito-PFD S.	Ito-PFD S.		AT
						Kr-Iw, Kr-AW
			Ohyodo S.	Ikatsuno S.	**Ikatsuno S.**	
						A-Iw
	Okadomi S.		Saitobaru II S.	Okadomi S.		
Post-Hibariyama S.	Hibariyama S.	Kawaminami Lower S.	Saitobaru I S.	Saitobaru S.	**Saitobaru S.**	
						Aso-4, A-Fk
			Nyutabaru III S.			
Takanabebaru S.	Nyutabaru S.	Kawaminami Upper S.	Nyutabaru II S.	Nyutabaru S.	**Nyutabaru S.**	
						K-Tz, Ata
Nyutabaru S.		Nyutabaru S.	Nyutabaru I S.	Baba S.	**Baba S.**	
Sanzaibaru S.	Sanzaibaru S.	Sanzaibaru S.	Sanzaibaru S.	Sanzaibaru S.	**Sanzaibaru S.**	Aso-3
Chausubaru S.	Chausubaru S.	Chausubaru S.	Chausubaru S.	Chausubaru S.	**Chausubaru S.**	Ata-Th
					Urushinobaru S.	
						Kkt
Pre-Chausubaru S.	Pre-Chausubaru S.	Pre-Chausubaru S.	Pre-Chausubaru S.	Higashibaru S.	**Higashibaru S.**	
					Kukino S.	Kb-Ks, Hwk
				Undivided higher terrace S.	**Siibaru S.**	

Table 3 Tephra layers distributed in Miyazaki Plain

	Name	Symbol	Age	Mode of occurrence
Younger tephra group	Kikai-Akahoya	K-Ah	6.3ka	Ash fall
	Kirishima-Kobayashi	Kr-Kb	16ka	Pumice fall
	Aira-Tn	AT	24ka	Ash fall
	Kirishima-Awaokoshi	Kr-Aw	(30～40ka?)	Pumice fall
	Kirishima-Iwaokoshi	Kr-Iw	(30～40ka?)	Pumice fall
	Aira-Iwato	A-Iw	(60～70ka?)	Ash fall
	Aso-4	Aso-4	89ka	Ash fall and Pyroclastic Flow
	Aira-Fukuyama	A-Fk	(90～100ka?)	Ash fall
	Kikai-Tozurahara	K-Tz	(90～100ka?)	Ash fall
	Ata	Ata	110ka	Ash fall and Pyroclastic Flow
	Aso-3	Aso-3	120ka	Ash fall
Older tephra group	Ata-Torihama	Ata-Th	250ka	Ash fall and Pyroclastic Flow
	Kakuto	Kkt	300ka	Ash fall and Pyroclastic Flow
	Kobayashi-Kasamori	Kb-Ks	500ka	Ash fall and Pyroclastic Flow
	Hiwaki	Hwk	600ka	Ash fall and Pyroclastic Flow

Table 4 Ages of the terraces based on tephrochronology

	Name	Symbol	Age (ka)
Younger tephra group	Fukadoshi surface	FD	20
	Ikatsuno surface	IK	40
	Saitobaru surface	ST	70 (?)
	Nyutabaru surface	NT	90
	Baba surface	BB	110
	Sanzaibaru surface	SZ	120
Older terrace group	Chausubaru surface	CH	250
	Urushinobaru surface	UB	300～250
	Higashibaru surface	HS	350
	Shiibaru surface	SB	500 (?)

Table 5 Results of X-ray diffraction analysis

Sample No.	Time (ka)	Qtz	Pl	Kln	Ill	Chl	Gt	Hem
P-18	0	◎	○	△	○	△	–	–
P-22	0	◎	○	△	○	△	–	–
P-27	0	◎	○	△	○	△	–	–
FT-3	20	◎	○	△	○	△	–	–
FT-13	20	◎	○	△	△	△	–	–
FT-16	20	◎	○	△	○	△	–	–
SA-6	70	◎	○	△	△	△	–	–
SA-14	70	◎	○	△	△	△	–	–
SA-16	70	◎	○	△	△	△	–	–
NT-2	90	◎	○	△	△	–	–	–
NT-8	90	◎	○	△	△	–	–	–
NT-19	90	◎	○	△	△	△	–	–
BB-11	110	◎	○	△	–	△	–	–
BB-12	110	◎	○	△	△	△	–	–
BB-17	110	◎	○	△	△	△	–	–
SZ-9	120	◎	○	△	△	–	–	–
SZ-11	120	◎	○	△	△	–	–	–
SZ-25	120	◎	○	△	△	–	–	–
CH-5	250	◎	△	△	△	–	–	–
CH-13	250	◎	△	△	△	–	–	–
CH-16	250	◎	–	△	△	–	△	–
PC-3	350	◎	–	△	△	–	△	△
PC-14	350	◎	–	–	△	–	△	△
PC-18	350	◎	–	–	△	–	△	△

Qtz:Quartz, Pl:plagioclase, Kln:kaolinite, Ill:illite, Chl:chlorite
Gt:Goethite, Hem:Hematite

Table 6 Results of colour measurement

Sample No.	Time (ka)	L^* max	a^* max	b^* max	L^* min	a^* min	b^* min	L^* av.	a^* av.	b^* av.
P-1	0	41.46	1.11	3.34	36.95	-0.76	-1.51	40.30	-0.46	-0.19
P-2	0	53.23	3.72	11.02	48.74	2.12	8.95	50.69	2.76	9.84
P-3	0	50.46	1.41	7.63	41.87	-0.87	2.03	44.73	0.10	3.67
P-4	0	49.94	-1.16	-0.02	45.98	-1.45	-1.32	48.46	-1.32	-0.82
P-5	0	53.66	-0.35	4.45	44.86	-1.20	0.81	49.87	-0.94	2.08
P-6	0	52.24	-0.57	2.84	45.81	-1.07	-2.45	49.57	-0.84	-1.05
P-7	0	49.31	0.23	-1.16	40.91	-0.21	-2.35	44.75	0.03	-1.55
P-8	0	38.89	-0.58	-1.28	36.17	-0.84	-3.04	37.79	-0.70	-2.35
P-9	0	42.65	-0.47	-3.45	40.79	-0.60	-3.99	42.01	-0.56	-3.84
P-10	0	45.78	-0.37	1.71	40.52	-0.76	-1.68	41.88	-0.52	-0.50
P-11	0	34.28	-0.40	-3.01	29.89	-0.54	-3.75	32.69	-0.48	-3.30
P-12	0	47.63	0.54	-0.80	36.87	-0.21	-1.90	40.01	0.30	-1.27
P-15	0	38.65	-0.28	-3.03	31.71	-0.83	-4.51	33.80	-0.56	-3.80
P-16	0	34.26	-0.47	-2.18	28.61	-0.68	-3.31	30.89	-0.57	-2.66
P-18	0	54.18	1.55	4.12	48.12	1.26	2.28	51.05	1.40	3.01
P-19	0	44.49	-0.62	0.94	38.65	-1.48	-2.50	40.75	-1.26	-1.31
P-20	0	44.53	-0.13	-1.06	36.11	-0.41	-3.03	39.50	-0.25	-2.23
P-21	0	50.24	-0.05	7.58	46.94	-0.51	5.78	48.94	-0.30	6.75
Average		45.88	0.17	1.54	39.97	-0.50	-0.86	42.65	-0.23	0.03

Sample No.	Time (ka)	L^* max	a^* max	b^* max	L^* min	a^* min	b^* min	L^* av.	a^* av.	b^* av.
FT-1	20	55.73	2.45	10.70	53.81	-0.70	7.69	54.92	0.18	8.65
FT-2	20	53.38	-0.55	8.10	41.49	-1.23	5.07	49.09	-0.95	5.87
FT-3	20	57.62	1.33	13.83	50.66	0.56	11.85	54.14	0.93	12.60
FT-4	20	62.09	-0.48	4.40	51.54	-1.05	3.14	54.73	-0.71	3.88
FT-5	20	61.81	0.73	9.90	53.46	-0.78	6.77	56.87	-0.19	7.81
FT-6	20	56.95	0.59	6.30	47.45	-0.05	1.96	50.63	0.33	3.77
FT-7	20	63.23	1.73	16.10	60.98	1.10	12.75	62.46	1.34	13.84
FT-8	20	53.92	3.63	10.72	48.71	0.92	6.62	51.57	2.26	8.84
FT-9	20	59.81	0.91	7.46	53.89	-0.31	4.21	56.69	0.18	5.91
FT-10	20	56.83	1.42	11.20	53.19	0.60	8.03	55.12	0.98	9.26
FT-11	20	58.96	-0.58	6.90	51.29	-1.06	4.71	53.71	-0.81	5.77
FT-12	20	59.73	1.78	16.44	58.27	0.89	14.23	58.94	1.34	15.65
FT-13	20	55.97	3.12	13.61	51.31	1.39	11.61	53.47	2.38	12.76
FT-14	20	54.84	0.39	13.24	52.72	0.08	11.79	53.33	0.31	12.47
FT-15	20	57.23	1.56	16.31	51.64	1.11	14.84	55.26	1.35	15.72
FT-16	20	50.36	-0.09	7.60	46.72	0.29	4.94	48.54	-0.20	6.20
FT-18	20	51.44	1.07	8.34	48.03	0.43	6.39	49.17	0.75	7.41
FT-19	20	58.99	3.05	12.92	50.75	0.13	9.46	55.51	0.71	11.01
FT-20	20	62.13	0.61	7.44	55.48	0.54	4.29	58.25	0.02	6.44
FT-21	20	62.10	0.76	8.95	57.57	-0.57	7.04	59.48	0.00	8.01
FT-22	20	51.77	2.50	9.30	44.90	-0.17	8.36	47.22	1.51	8.86
Average		57.38	1.23	10.46	51.61	0.10	7.89	54.24	0.56	9.08

Table 6 Results of colour measurement (continued)

Sample No.	Time (ka)	L^* max	a^* max	b^* max	L^* min	a^* min	b^* min	L^* av.	a^* av.	b^* av.
SA-1	70	58.08	6.76	20.57	50.66	-0.04	8.73	54.31	1.46	11.69
SA-2	70	62.37	5.22	17.44	47.65	1.76	8.9	57.45	2.98	12.27
SA-3	70	56.08	4.8	19.08	41.35	-0.68	5.69	53.3	0.3	8.19
SA-4	70	69.31	4.91	16.95	53.73	-0.61	5.09	64.36	1.43	10.08
SA-5	70	56.98	1.02	11.99	49.19	0.03	9.73	52.16	0.4	11.17
SA-6	70	60.09	0.21	10.23	54.57	-0.77	4.71	57.6	-0.43	6.75
SA-7	70	55.1	0.77	12.07	51.5	-0.72	6.17	52.79	-0.33	7.21
SA-9	70	59.67	4.72	13.79	52.53	1.23	9.63	55.85	2.8	11.94
SA-10	70	66.54	2.3	15.42	55.86	0.02	7.44	62.42	0.72	10.31
SA-11	70	63.27	2.81	13.27	50.19	-1.05	6.67	55.88	-0.25	8.08
SA-12	70	66.08	6.29	18.54	44.89	-0.62	5.29	60.87	2.02	11.55
SA-13	70	57.94	1.64	13.88	44.95	-0.17	8.28	50.18	0.73	10.13
SA-14	70	57.53	2.56	13.31	54.08	0.87	8.88	56.37	1.53	10.89
SA-15	70	67.77	1.99	19.33	59.01	0.01	8.94	61.05	1.02	16.38
SA-16	70	59.56	0.84	10.84	40.26	0.14	5.76	47.23	0.51	6.88
SA-17	70	54.67	3.05	11.22	44.16	0.83	7.37	47.1	1.62	8.99
SA-18	70	59.43	6.48	18.13	49.61	0.96	9.05	55.01	3.39	13.17
SA-19	70	61.01	2.84	21.79	45.07	0.08	6.3	51.69	1.29	10.07
SA-20	70	69.05	6.29	23.57	47.57	-0.4	9.49	59.28	2.74	14.39
Average		61.08	3.45	15.86	49.31	0.05	7.48	55.52	1.26	10.53

Sample No.	Time (ka)	L^* max	a^* max	b^* max	L^* min	a^* min	b^* min	L^* av.	a^* av.	b^* av.
NT-1	90	57.72	4.89	14.54	54.08	2.69	12.48	55.61	3.66	13.40
NT-2	90	58.84	2.60	18.65	57.00	0.12	9.14	58.08	1.07	13.13
NT-3	90	62.30	0.66	15.77	57.39	-0.21	12.55	59.33	0.18	14.43
NT-4	90	49.03	1.44	11.26	43.34	0.38	7.79	46.95	1.08	9.23
NT-5	90	68.97	3.98	23.53	61.79	-0.78	6.88	66.16	1.15	13.36
NT-6	90	57.55	8.53	25.95	48.80	6.25	19.63	54.76	7.45	23.26
NT-7	90	59.22	5.97	18.67	56.42	4.90	14.74	57.89	5.31	16.44
NT-8	90	61.13	1.74	12.65	56.49	1.42	9.42	58.76	1.59	11.04
NT-9	90	61.77	1.95	18.92	59.07	1.31	16.73	60.96	1.53	17.94
NT-10	90	51.24	1.81	10.25	47.98	1.38	7.79	49.71	1.59	8.93
NT-11	90	59.81	2.30	14.09	53.26	1.53	10.55	57.24	1.90	12.03
NT-12	90	66.80	2.34	11.22	63.22	1.71	5.82	64.30	1.97	7.53
NT-13	90	62.79	4.95	14.63	57.96	3.85	13.23	60.23	4.34	14.08
NT-14	90	59.35	7.70	25.13	52.16	5.47	19.02	55.84	6.32	21.03
NT-15	90	51.81	1.14	11.34	45.51	-0.30	1.94	47.98	0.47	6.70
NT-16	90	57.06	3.72	15.42	52.93	1.94	12.51	54.33	2.89	13.73
NT-17	90	55.75	1.30	10.37	51.16	0.67	8.33	53.10	0.93	9.20
NT-18	90	57.71	1.24	13.37	54.13	0.46	8.97	56.07	0.87	11.05
NT-19	90	58.17	0.74	11.89	52.96	0.14	8.52	54.66	0.49	10.20
NT-21	90	65.48	3.83	14.15	61.95	2.35	10.28	63.99	3.03	11.91
NT-22	90	45.52	1.52	10.10	43.74	0.43	9.59	44.63	0.98	9.85
NT-23	90	61.85	0.63	10.68	59.52	-0.14	6.80	60.73	0.14	8.58
NT-24	90	52.36	1.50	10.11	47.42	0.79	7.33	49.79	1.18	8.47
Average		58.36	2.89	14.90	53.84	1.58	10.44	56.13	2.18	12.41

Table 6 Results of colour measurement (continued)

Sample No.	Time (ka)	L^* max	a^* max	b^* max	L^* min	a^* min	b^* min	L^* av.	a^* av.	b^* av.
BB-1	110	62.91	1.45	19.95	60.45	0.86	17.98	61.64	1.18	19.02
BB-2	110	59.31	2.64	20.02	57.75	2.28	18.54	58.68	2.50	19.38
BB-3	110	64.32	2.25	20.92	61.82	1.65	19.21	63.35	1.86	19.97
BB-4	110	57.93	2.95	20.40	55.81	2.76	18.28	56.81	2.87	19.20
BB-5	110	60.55	4.21	22.66	59.53	3.16	21.11	60.14	3.76	21.99
BB-6	110	60.57	2.73	23.07	58.77	1.95	22.05	59.92	2.42	22.75
BB-7	110	56.43	3.86	22.58	54.51	3.01	19.64	55.46	3.58	21.04
BB-9	110	59.71	2.08	21.03	57.74	1.41	17.77	58.90	1.61	18.74
BB-10	110	50.86	1.43	13.49	47.71	0.13	9.79	49.33	0.62	11.38
BB-11	110	61.79	1.05	15.43	57.36	-0.34	12.28	59.14	0.54	13.71
BB-12	110	57.76	2.22	16.74	54.42	1.27	13.78	55.69	1.67	15.04
BB-13	110	56.86	3.80	19.20	52.58	1.06	14.37	55.07	2.01	15.70
BB-14	110	59.26	2.36	20.45	58.48	2.00	17.69	58.83	2.12	18.85
BB-15	110	63.07	3.89	16.44	61.44	1.34	14.38	62.34	1.95	15.20
BB-16	110	61.41	2.92	23.75	60.10	2.21	22.30	60.60	2.48	22.67
BB-17	110	60.05	3.04	23.16	58.68	2.39	22.13	59.48	2.74	22.53
Average		59.55	2.68	19.96	57.32	1.70	17.58	58.46	2.12	18.57

Sample No.	Time (ka)	L^* max	a^* max	b^* max	L^* min	a^* min	b^* min	L^* av.	a^* av.	b^* av.
SZ-1	120	62.85	6.39	30.00	56.59	2.34	24.07	61.14	3.57	26.80
SZ-2	120	63.72	4.97	29.11	60.75	1.54	23.44	62.32	2.79	26.51
SZ-3	120	68.37	6.01	24.00	60.00	1.74	20.01	64.37	3.97	22.07
SZ-5	120	61.09	2.02	19.49	45.19	0.65	16.98	55.25	1.18	18.01
SZ-6	120	60.07	1.18	17.91	53.92	-0.01	11.67	56.72	0.47	14.57
SZ-7	120	64.08	3.72	26.66	61.68	0.86	18.99	63.15	1.89	21.06
SZ-8	120	63.27	1.80	21.20	55.70	-0.53	13.05	60.60	0.80	17.45
SZ-9	120	64.03	3.93	27.50	56.48	1.41	20.14	60.30	2.81	22.48
SZ-10	120	66.31	0.80	21.30	64.31	-0.66	15.18	65.23	-0.11	17.70
SZ-11	120	69.61	6.62	28.79	59.48	-0.59	13.47	63.26	2.05	19.35
SZ-12	120	64.71	2.66	22.72	54.58	1.40	17.45	58.58	2.00	18.92
SZ-13	120	67.91	2.06	16.36	55.38	-1.14	10.28	61.25	-0.25	12.66
SZ-14	120	62.31	1.18	20.73	55.84	-0.27	13.46	59.81	0.57	18.22
SZ-15	120	63.06	2.70	21.06	56.22	1.09	19.93	59.07	2.00	20.41
SZ-16	120	67.97	0.62	19.35	56.83	0.10	11.03	63.71	0.37	16.30
SZ-18	120	60.12	2.64	22.78	49.46	0.67	6.64	56.38	1.79	12.63
SZ-19	120	68.97	0.44	20.37	65.21	-0.21	15.50	66.74	0.10	17.28
SZ-20	120	62.86	3.38	26.55	60.55	1.50	23.73	62.01	2.43	25.00
SZ-21	120	64.55	3.18	28.80	60.27	0.64	19.05	63.13	1.54	22.40
SZ-22	120	66.19	1.79	14.19	64.23	1.02	11.31	64.74	1.43	12.82
SZ-23	120	60.67	1.97	25.35	58.58	1.34	21.75	59.34	1.73	23.27
SZ-24	120	63.42	4.25	21.93	54.51	1.48	20.24	60.08	2.32	21.07
SZ-25	120	61.73	3.64	27.13	60.82	3.44	26.38	61.21	3.55	26.79
SZ-26	120	57.85	1.33	20.39	51.11	0.53	17.96	55.22	0.94	19.02
SZ-27	120	62.63	4.83	23.10	52.28	0.80	2.63	58.64	2.21	17.23
Average		63.93	2.96	23.07	57.20	0.77	16.57	60.89	1.69	19.60

Table 6 Results of colour measurement (continued)

Sample No.	Time (ka)	L^* max	a^* max	b^* max	L^* min	a^* min	b^* min	L^* av.	a^* av.	b^* av.
CH-2	250	57.27	4.35	23.56	54.38	0.32	12.22	56.00	2.28	18.60
CH-3	250	57.07	4.47	22.73	53.72	2.81	19.28	55.20	3.67	20.77
CH-5	250	61.05	8.48	29.20	52.21	4.19	24.80	58.86	5.26	26.04
CH-6	250	55.89	4.61	18.41	48.44	2.88	14.73	53.21	3.52	16.52
CH-7	250	59.61	7.35	29.99	56.73	3.27	24.57	58.66	4.65	26.55
CH-8	250	65.46	4.16	17.09	60.44	3.39	12.63	63.38	3.77	15.42
CH-9	250	60.57	6.12	27.30	59.09	4.41	25.38	59.80	5.27	26.46
CH-10	250	63.82	10.39	29.97	57.77	7.61	18.66	60.90	8.87	23.47
CH-11	250	61.51	13.11	31.53	53.96	6.33	26.85	57.69	9.85	29.20
CH-12	250	52.11	15.88	18.96	43.53	11.09	15.35	46.76	13.81	17.18
CH-13	250	59.01	5.33	23.01	55.01	3.76	19.15	57.23	4.69	20.71
CH-14	250	69.05	13.22	36.73	53.79	5.44	23.72	59.02	7.90	28.53
CH-16	250	60.32	7.31	23.53	58.55	6.55	21.23	59.55	6.93	22.46
CH-18	250	67.43	5.32	28.64	57.78	3.98	20.57	62.30	4.51	26.97
CH-19	250	63.71	7.55	31.51	60.03	5.38	25.82	61.18	6.22	29.45
CH-21	250	58.04	7.59	28.47	55.44	5.49	26.50	57.31	6.30	27.19
CH-22	250	58.63	7.57	28.23	47.49	5.23	24.52	55.43	6.26	26.46
CH-23	250	66.63	6.36	23.97	57.53	2.29	18.42	63.08	4.52	20.26
CH-24	250	54.38	8.00	28.22	47.47	6.68	25.30	49.64	7.24	27.05
CH-25	250	58.39	4.45	24.73	49.18	3.16	20.27	55.44	3.76	22.67
Average		60.50	7.58	26.29	54.13	4.71	21.00	57.53	5.96	23.60

Sample No.	Time (ka)	L^* max	a^* max	b^* max	L^* min	a^* min	b^* min	L^* av.	a^* av.	b^* av.
PC-1	350	60.47	18.89	24.82	48.99	10.87	18.54	57.25	12.46	20.31
PC-2	350	56.36	18.64	25.76	49.23	9.73	19.97	52.63	14.59	22.30
PC-3	350	58.34	17.37	24.45	54.84	14.93	23.07	56.63	16.44	23.76
PC-4	350	55.59	19.52	28.23	51.79	17.12	25.76	54.05	18.43	27.20
PC-5	350	56.74	17.82	24.34	48.63	12.43	19.62	53.62	15.80	21.90
PC-6	350	59.86	12.50	21.61	51.47	6.86	16.28	50.31	8.84	17.11
PC-7	350	58.15	15.78	22.12	54.36	11.31	17.52	56.19	12.82	20.02
PC-8	350	60.60	15.39	20.76	53.78	12.80	18.27	57.64	14.37	19.22
PC-10	350	50.05	20.96	30.56	45.65	18.78	27.17	48.12	20.08	28.51
PC-11	350	54.36	14.13	24.20	51.26	11.31	19.08	52.52	12.98	20.36
PC-12	350	54.11	18.07	23.77	51.34	15.97	22.58	52.53	16.82	23.09
PC-13	350	52.94	17.73	25.22	49.80	16.65	22.73	51.99	17.29	23.97
PC-14	350	56.98	13.32	22.76	52.92	10.41	18.24	54.60	11.68	20.76
PC-15	350	53.10	16.26	27.77	48.12	9.68	19.15	50.21	14.18	23.05
PC-16	350	55.45	19.12	22.04	53.33	14.63	19.93	54.36	16.09	20.86
PC-18	350	53.05	11.13	23.98	48.79	9.23	21.84	51.34	10.41	23.10
PC-21	350	51.06	20.22	29.84	49.81	18.17	27.05	50.25	19.07	27.95
Average		55.72	16.87	24.84	50.83	12.99	20.99	53.19	14.84	22.56

Table 7 Physical properties

Sample No.	Effective porosity n_e (%)	Apparent specific gravity G_n	Apparent dry specific gravity G_d	Apparent wet specific gravity G_t	Moisture content W_r (%)	Degree of saturation S_r (%)	Absorption rate of water a_b (%)
P-1	1.00	2.64	2.63	2.64	0.00	45.00	0.38
P-2	4.09	2.54	2.53	2.57	0.00	22.22	1.62
P-3	1.05	2.65	2.64	2.65	0.00	46.67	0.40
P-4	1.10	2.63	2.63	2.64	0.00	26.67	0.42
P-5	1.91	2.62	2.61	2.63	0.00	25.71	0.73
P-6	1.13	2.64	2.64	2.65	0.00	33.33	0.43
P-7	1.25	2.77	2.76	2.78	0.00	25.00	0.45
P-8	1.84	2.66	2.65	2.67	0.00	50.00	0.69
P-9	1.70	2.74	2.74	2.75	0.00	14.29	0.62
P-10	2.66	2.64	2.63	2.65	0.00	38.46	1.01
P-11	0.75	2.74	2.74	2.75	0.00	8.33	0.27
P-12	1.87	2.75	2.74	2.76	0.00	22.22	0.68
P-13	1.88	2.73	2.72	2.74	0.00	20.00	0.69
P-14	4.17	2.64	2.63	2.67	0.01	37.50	1.59
P-15	1.09	2.71	2.71	2.72	0.00	20.00	0.40
P-16	1.76	2.74	2.73	2.75	0.00	10.00	0.64
P-17	3.33	2.67	2.65	2.69	0.01	40.00	1.26
P-18	3.76	2.59	2.58	2.62	0.00	25.00	1.46
P-19	1.68	2.65	2.65	2.66	0.00	9.09	0.63
P-20	0.99	2.75	2.75	2.76	0.00	16.67	0.36
P-21	3.28	2.60	2.59	2.63	0.00	29.41	1.26
P-22	1.91	2.72	2.72	2.74	0.00	25.00	0.70
P-23	2.76	2.64	2.63	2.66	0.00	33.33	1.05
P-24	2.37	2.68	2.67	2.70	0.00	25.00	0.88
Average	2.06	2.67	2.67	2.69	0.00	27.04	0.78

Table 7 Physical properties (continued)

Sample No.	Effective porosity n_e (%)	Apparent specific gravity G_n	Apparent dry specific gravity G_d	Apparent wet specific gravity G_t	Moisture content W_r (%)	Degree of saturation S_r (%)	Absorption rate of water a_b (%)
FT-1	4.07	2.58	2.56	2.60	0.01	36.84	1.59
FT-2	5.42	2.56	2.55	2.60	0.01	27.27	2.13
FT-3	10.34	2.41	2.40	2.50	0.01	16.67	4.32
FT-4	3.77	2.56	2.56	2.59	0.00	25.00	1.48
FT-5	4.48	2.55	2.54	2.59	0.00	24.14	1.76
FT-6	5.13	2.52	2.50	2.56	0.00	23.81	2.05
FT-7	6.48	2.48	2.47	2.53	0.01	24.07	2.63
FT-8	5.36	2.51	2.49	2.55	0.01	30.00	2.15
FT-9	4.64	2.49	2.48	2.53	0.00	21.57	1.87
FT-10	7.81	2.51	2.49	2.56	0.01	25.81	3.14
FT-11	3.63	2.58	2.56	2.60	0.00	31.82	1.42
FT-12	7.07	2.49	2.47	2.54	0.01	23.81	2.86
FT-13	5.87	2.52	2.51	2.57	0.00	20.00	2.34
FT-14	6.50	2.51	2.50	2.56	0.00	17.86	2.60
FT-15	7.66	2.48	2.47	2.55	0.00	10.53	3.10
FT-16	3.98	2.57	2.56	2.60	0.00	20.00	1.55
FT-17	9.20	2.44	2.42	2.51	0.01	20.97	3.80
FT-18	6.79	2.43	2.42	2.49	0.00	17.76	2.81
FT-19	4.11	2.56	2.55	2.59	0.00	23.29	1.61
FT-20	5.27	2.51	2.50	2.55	0.00	20.93	2.11
FT-21	4.92	2.58	2.57	2.62	0.00	16.67	1.91
FT-22	4.14	2.54	2.53	2.57	0.00	18.75	1.64
Average	5.76	2.52	2.50	2.56	0.01	22.62	2.31

Table 7 Physical properties (continued)

Sample No.	Effective porosity n_e (%)	Apparent specific gravity G_n	Apparent dry specific gravity G_d	Apparent wet specific gravity G_t	Moisture content W_r (%)	Degree of saturation S_r (%)	Absorption rate of water a_b (%)
SA-1	5.34	2.52	2.51	2.56	0.00	18.22	2.13
SA-2	7.29	2.47	2.47	2.54	0.00	11.71	2.96
SA-3	4.74	2.53	2.52	2.57	0.00	22.49	1.88
SA-4	8.27	2.42	2.41	2.49	0.00	12.61	3.43
SA-5	4.48	2.55	2.54	2.59	0.00	13.33	1.76
SA-6	6.21	2.51	2.49	2.55	0.01	24.24	2.49
SA-7	3.67	2.56	2.55	2.59	0.00	14.81	1.44
SA-8	7.06	2.47	2.45	2.52	0.01	18.52	2.88
SA-9	4.80	2.53	2.52	2.57	0.00	20.34	1.91
SA-10	8.96	2.43	2.42	2.51	0.01	13.75	3.71
SA-11	7.21	2.48	2.46	2.54	0.01	17.78	2.93
SA-12	5.91	2.49	2.48	2.54	0.00	16.67	2.38
SA-13	7.39	2.47	2.46	2.53	0.01	20.59	3.01
SA-14	8.79	2.42	2.41	2.49	0.01	15.09	3.65
SA-15	13.98	2.29	2.28	2.42	0.01	11.59	6.14
SA-16	6.75	2.48	2.47	2.54	0.01	18.99	2.73
SA-17	7.32	2.47	2.46	2.53	0.01	19.40	2.98
SA-18	7.65	2.46	2.45	2.53	0.00	15.53	3.12
SA-19	8.83	2.41	2.40	2.49	0.01	14.06	3.68
SA-20	9.97	2.39	2.38	2.48	0.01	12.40	4.19
SA-21	5.94	2.51	2.50	2.56	0.01	23.08	2.38
Average	7.17	2.47	2.46	2.53	0.00	16.91	2.94

Table 7 Physical properties (continued)

Sample No.	Effective porosity n_e (%)	Apparent specific gravity G_n	Apparent dry specific gravity G_d	Apparent wet specific gravity G_t	Moisture content W_r (%)	Degree of saturation S_r (%)	Absorption rate of water a_b (%)
NT-1	8.16	2.47	2.46	2.54	0.00	14.58	3.32
NT-2	10.71	2.41	2.39	2.50	0.01	16.05	4.48
NT-3	13.04	2.34	2.33	2.46	0.01	11.11	5.61
NT-4	9.98	2.40	2.38	2.48	0.01	18.27	4.19
NT-5	18.61	2.20	2.18	2.37	0.01	9.15	8.53
NT-6	21.50	2.13	2.11	2.33	0.01	8.96	10.17
NT-7	19.30	2.18	2.16	2.35	0.01	7.27	8.93
NT-8	11.82	2.38	2.37	2.49	0.01	12.50	4.99
NT-9	15.35	2.28	2.27	2.42	0.01	10.10	6.77
NT-10	9.44	2.45	2.44	2.53	0.01	18.18	3.87
NT-11	9.35	2.44	2.43	2.52	0.01	14.00	3.85
NT-12	12.19	2.36	2.35	2.48	0.00	7.41	5.18
NT-13	15.76	2.28	2.27	2.43	0.01	7.69	6.93
NT-14	26.60	1.98	1.97	2.23	0.01	6.98	13.53
NT-15	10.40	2.44	2.42	2.52	0.01	19.15	4.30
NT-16	12.33	2.37	2.36	2.48	0.01	14.29	5.23
NT-17	9.52	2.43	2.42	2.51	0.00	10.53	3.94
NT-18	8.75	2.43	2.41	2.50	0.01	15.38	3.63
NT-19	11.38	2.40	2.39	2.50	0.01	13.16	4.76
NT-20	9.56	2.50	2.49	2.59	0.00	12.50	3.84
NT-21	13.24	2.35	2.34	2.47	0.00	8.16	5.66
NT-22	12.85	2.40	2.37	2.50	0.01	21.74	5.42
NT-23	10.09	2.43	2.41	2.52	0.01	14.29	4.18
NT-24	11.08	2.38	2.37	2.48	0.01	13.95	4.68
Average	12.96	2.35	2.34	2.47	0.01	12.73	5.67

Table 7 Physical properties (continued)

Sample No.	Effective porosity n_e (%)	Apparent specific gravity G_n	Apparent dry specific gravity G_d	Apparent wet specific gravity G_t	Moisture content W_r (%)	Degree of saturation S_r (%)	Absorption rate of water a_b (%)
BB-1	12.88	2.35	2.33	2.46	0.01	12.50	5.52
BB-2	12.29	2.36	2.34	2.46	0.01	15.69	5.25
BB-3	15.68	2.28	2.26	2.41	0.01	16.33	6.95
BB-4	17.00	2.22	2.21	2.38	0.01	9.21	7.71
BB-5	16.17	2.27	2.25	2.41	0.01	9.88	7.18
BB-6	14.07	2.32	2.30	2.44	0.01	12.50	6.11
BB-7	16.84	2.26	2.23	2.40	0.01	14.29	7.55
BB-8	19.79	2.22	2.19	2.39	0.01	15.79	9.05
BB-9	13.63	2.32	2.31	2.44	0.01	10.77	5.90
BB-10	9.57	2.47	2.44	2.54	0.01	25.53	3.92
BB-11	15.97	2.29	2.26	2.42	0.01	13.16	7.05
BB-12	12.84	2.35	2.33	2.46	0.01	13.95	5.50
BB-13	14.86	2.32	2.29	2.44	0.01	16.36	6.49
BB-14	12.48	2.37	2.35	2.47	0.01	14.43	5.32
BB-15	10.39	2.40	2.39	2.49	0.01	16.28	4.35
BB-16	19.62	2.17	2.16	2.35	0.01	9.76	9.10
BB-17	18.33	2.22	2.19	2.37	0.02	18.18	8.37
Average	14.85	2.30	2.28	2.43	0.01	14.39	6.55

Table 7 Physical properties (continued)

Sample No.	Effective porosity n_e (%)	Apparent specific gravity G_n	Apparent dry specific gravity G_d	Apparent wet specific gravity G_t	Moisture content W_r (%)	Degree of saturation S_r (%)	Absorption rate of water a_b (%)
SZ-1	19.37	2.12	2.11	2.30	0.01	8.16	9.19
SZ-2	24.39	1.96	1.94	2.19	0.01	6.01	12.55
SZ-3	14.38	2.23	2.22	2.37	0.00	5.22	6.47
SZ-5	16.59	2.19	2.18	2.34	0.01	9.73	7.62
SZ-6	10.43	2.40	2.38	2.49	0.01	20.00	4.38
SZ-7	17.15	2.18	2.17	2.34	0.01	9.55	7.92
SZ-8	13.58	2.29	2.28	2.41	0.01	11.45	5.96
SZ-9	14.93	2.25	2.23	2.38	0.01	12.36	6.68
SZ-10	19.72	2.10	2.08	2.28	0.01	9.17	9.48
SZ-11	16.31	2.21	2.20	2.36	0.01	9.88	7.42
SZ-12	12.51	2.32	2.31	2.44	0.00	7.75	5.41
SZ-13	11.89	2.32	2.31	2.43	0.00	6.67	5.14
SZ-14	21.78	2.06	2.04	2.26	0.01	5.45	10.66
SZ-15	13.59	2.27	2.26	2.40	0.01	8.74	6.01
SZ-16	19.21	2.12	2.11	2.30	0.00	5.48	9.11
SZ-17	21.28	2.07	2.06	2.28	0.00	4.44	10.31
SZ-18	10.41	2.36	2.36	2.46	0.00	4.95	4.42
SZ-19	15.17	2.27	2.25	2.41	0.01	8.31	6.73
SZ-20	25.34	2.03	2.01	2.26	0.01	8.85	12.63
SZ-21	19.46	2.17	2.15	2.34	0.01	10.26	9.06
SZ-22	12.77	2.34	2.33	2.46	0.00	5.95	5.48
SZ-23	17.96	2.23	2.20	2.38	0.01	11.76	8.15
SZ-24	18.06	2.22	2.20	2.38	0.01	11.54	8.21
SZ-25	16.21	2.27	2.25	2.41	0.01	12.36	7.21
SZ-26	20.22	2.15	2.13	2.33	0.01	11.11	9.51
SZ-27	14.28	2.30	2.28	2.43	0.01	14.80	6.25
SZ-28	19.57	2.19	2.16	2.36	0.01	12.35	9.04
Average	16.91	2.21	2.19	2.36	0.01	9.34	7.81

Table 7 Physical properties (continued)

Sample No.	Effective porosity n_e (%)	Apparent specific gravity G_n	Apparent dry specific gravity G_d	Apparent wet specific gravity G_t	Moisture content W_r (%)	Degree of saturation S_r (%)	Absorption rate of water a_b (%)
CH-2	13.71	2.20	2.19	2.33	0.01	10.48	6.26
CH-3	14.90	2.17	2.16	2.31	0.01	9.54	6.91
CH-5	19.49	2.09	2.07	2.27	0.01	7.75	9.40
CH-6	13.44	2.24	2.22	2.35	0.01	13.70	6.05
CH-7	19.05	2.04	2.03	2.22	0.01	7.09	9.40
CH-8	16.70	2.14	2.13	2.30	0.00	6.30	7.83
CH-9	21.69	2.01	1.99	2.21	0.01	6.06	10.88
CH-10	15.68	2.21	2.19	2.34	0.01	15.53	7.17
CH-11	29.57	1.78	1.75	2.05	0.02	10.71	16.89
CH-12	19.04	2.10	2.08	2.27	0.01	10.67	9.15
CH-13	25.68	1.88	1.87	2.12	0.01	6.48	13.75
CH-14	21.09	1.99	1.98	2.19	0.01	7.37	10.66
CH-15	24.83	1.98	1.96	2.20	0.01	9.23	12.70
CH-16	22.47	1.97	1.96	2.18	0.01	8.27	11.49
CH-17	25.60	1.91	1.89	2.14	0.02	11.27	13.57
CH-18	24.74	1.93	1.90	2.15	0.01	11.43	13.02
CH-19	26.28	1.82	1.80	2.06	0.01	9.27	14.62
CH-21	22.62	1.98	1.95	2.18	0.01	11.05	11.58
CH-22	22.12	1.96	1.94	2.16	0.01	9.00	11.40
CH-23	25.48	1.92	1.89	2.15	0.01	9.75	13.46
CH-24	24.26	1.99	1.97	2.21	0.01	7.74	12.30
CH-25	18.60	2.08	2.06	2.25	0.01	11.74	9.02
Average	21.23	2.02	2.00	2.21	0.01	9.57	10.79

Table 7 Physical properties (continued)

Sample No.	Effective porosity n_e (%)	Apparent specific gravity G_n	Apparent dry specific gravity G_d	Apparent wet specific gravity G_t	Moisture content W_r (%)	Degree of saturation S_r (%)	Absorption rate of water a_b (%)
PC-1	18.20	2.05	2.03	2.21	0.01	10.26	8.97
PC-2	30.19	1.88	1.80	2.11	0.04	26.25	16.74
PC-3	22.22	1.87	1.85	2.07	0.01	10.00	12.01
PC-4	29.21	1.72	1.69	1.99	0.02	10.17	17.25
PC-5	22.68	1.95	1.93	2.16	0.01	9.72	11.74
PC-6	21.17	2.00	1.94	2.15	0.03	27.18	10.92
PC-7	21.41	1.93	1.91	2.12	0.01	9.82	11.23
PC-8	27.57	1.77	1.73	2.00	0.02	13.43	15.95
PC-9	24.82	1.90	1.85	2.09	0.03	20.29	13.45
PC-10	27.00	1.79	1.74	2.01	0.03	19.35	15.53
PC-11	20.74	1.98	1.93	2.14	0.02	21.43	10.74
PC-12	27.13	1.93	1.84	2.12	0.04	30.00	14.71
PC-13	27.42	1.78	1.74	2.02	0.02	14.71	15.74
PC-14	17.17	2.05	2.03	2.20	0.01	13.73	8.46
PC-15	21.19	2.04	1.98	2.19	0.03	25.60	10.68
PC-16	23.94	1.86	1.82	2.06	0.02	15.19	13.12
PC-17	22.12	1.93	1.87	2.09	0.03	23.94	11.81
PC-18	26.04	1.86	1.81	2.07	0.03	20.00	14.41
PC-19	30.88	1.73	1.68	1.99	0.03	16.22	18.33
PC-20	29.06	1.79	1.73	2.02	0.03	20.59	16.83
PC-21	28.98	1.75	1.70	1.99	0.03	17.43	17.09
Average	24.72	1.88	1.84	2.09	0.02	17.87	13.61

Table 8 Results of pore size distribution analysis

	P-1 (0 ka)	P-2 (0 ka)	P-3 (0 ka)
pore size (μ m)	pore volume (mm^3/g)	pore volume (mm^3/g)	pore volume (mm^3/g)
0.0041 - 0.0051	0.28	0.21	0.52
0.0051 - 0.0064	0.50	0.26	0.67
0.0064 - 0.0080	0.44	0.43	0.47
0.0080 - 0.0100	0.47	0.21	0.45
0.0100 - 0.0130	0.49	0.26	0.58
0.0130 - 0.0160	0.36	0.26	0.47
0.0160 - 0.0200	0.25	0.22	0.39
0.0200 - 0.0260	0.35	0.48	0.54
0.0260 - 0.0330	0.19	0.34	0.24
0.0330 - 0.0410	0.18	0.69	0.26
0.0410 - 0.0510	0.11	0.62	0.14
0.0510 - 0.0640	0.09	0.85	0.12
0.0640 - 0.0800	0.08	1.31	0.08
0.0800 - 0.1000	0.08	2.90	0.06
0.1000 - 0.1300	0.06	3.59	0.08
0.1300 - 0.1600	0.06	0.97	0.05
0.1600 - 0.2000	0.05	0.34	0.03
0.2000 - 0.2600	0.07	0.31	0.07
0.2600 - 0.3300	0.04	0.14	0.04
0.3300 - 0.4100	0.08	0.15	0.07
0.4100 - 0.5100	0.04	0.11	0.04
0.5100 - 0.6400	0.08	0.10	0.04
0.6400 - 0.8000	0.05	0.08	0.06
0.8000 - 1.0000	0.08	0.08	0.04
1.0000 - 1.3000	0.07	0.08	0.04
1.3000 - 1.6000	0.07	0.04	0.04
1.6000 - 2.0000	0.04	0.04	0.04
2.0000 - 2.6000	0.06	0.08	0.04
2.6000 - 3.3000	0.07	0.06	0.04
3.3000 - 4.1000	0.11	0.06	0.06
4.1000 - 5.1000	0.08	0.06	0.04
5.1000 - 6.4000	0.00	0.03	0.00
6.4000 - 8.0000	0.00	0.06	0.06
8.0000 - 10.0000	0.31	0.24	0.06
10.0000 - 13.0000	0.12	0.24	0.26
13.0000 - 16.0000	0.75	0.00	0.00
16.0000 - 19.0000	0.00	0.00	0.00
19.0000 -	0.00	0.54	0.32
V_a 3.3000 - 33.0000	3.33	2.67	4.33
V_b 0.3300 - 3.3000	0.82	11.72	0.93
V_c 0.0330 - 0.3300	0.64	0.82	0.45
V_d 0.0030 - 0.0330	1.37	1.23	0.80
total	6.16	16.44	6.51

Table 8 Results of pore size distribution analysis (continued)

	FT-1 (20ka)	FT-3 (20 ka)	FT-4 (20 ka)
pore size (μ m)	pore volume (mm^3/g)	pore volume (mm^3/g)	pore volume (mm^3/g)
0.0041 - 0.0051	0.02	0.60	0.31
0.0051 - 0.0064	0.18	0.69	0.37
0.0064 - 0.0080	0.09	0.46	0.26
0.0080 - 0.0100	0.12	0.46	0.14
0.0100 - 0.0130	0.16	0.46	0.14
0.0130 - 0.0160	0.14	0.37	0.18
0.0160 - 0.0200	0.22	0.42	0.26
0.0200 - 0.0260	0.61	0.44	0.70
0.0260 - 0.0330	0.51	0.50	0.76
0.0330 - 0.0410	0.89	0.76	1.51
0.0410 - 0.0510	0.90	0.67	1.11
0.0510 - 0.0640	0.98	0.82	1.03
0.0640 - 0.0800	0.98	0.86	0.72
0.0800 - 0.1000	1.00	1.05	0.59
0.1000 - 0.1300	0.95	1.76	0.51
0.1300 - 0.1600	0.61	1.65	0.33
0.1600 - 0.2000	0.36	1.85	0.16
0.2000 - 0.2600	0.47	4.24	0.20
0.2600 - 0.3300	0.22	3.76	0.08
0.3300 - 0.4100	0.17	3.45	0.08
0.4100 - 0.5100	0.05	1.19	0.07
0.5100 - 0.6400	0.05	0.76	0.06
0.6400 - 0.8000	0.02	0.42	0.04
0.8000 - 1.0000	0.03	0.38	0.06
1.0000 - 1.3000	0.00	0.28	0.06
1.3000 - 1.6000	0.00	0.20	0.04
1.6000 - 2.0000	0.00	0.13	0.06
2.0000 - 2.6000	0.00	0.23	0.04
2.6000 - 3.3000	0.00	0.15	0.04
3.3000 - 4.1000	0.00	0.20	0.04
4.1000 - 5.1000	0.00	0.18	0.06
5.1000 - 6.4000	0.00	0.09	0.08
6.4000 - 8.0000	0.00	0.26	0.17
8.0000 - 10.0000	0.09	0.18	0.08
10.0000 - 13.0000	0.19	0.81	0.34
13.0000 - 16.0000	0.00	0.00	0.00
16.0000 - 19.0000	0.00	0.00	0.00
19.0000 -	0.52	1.16	0.69
V_a 3.3000 - 33.0000	2.05	4.40	3.12
V_b 0.3300 - 3.3000	7.36	17.42	6.24
V_c 0.0330 - 0.3300	0.32	7.19	0.55
V_d 0.0030 - 0.0330	0.80	2.88	1.46
total	10.53	31.89	11.37

Table 8 Results of pore size distribution analysis (continued)

	SA-5 (70ka)	SA-11 (70ka)	SA-13 (70ka)
pore size (μ m)	pore volume (mm^3/g)	pore volume (mm^3/g)	pore volume (mm^3/g)
0.0041 - 0.0051	0.27	0.55	0.51
0.0051 - 0.0064	0.36	0.58	0.56
0.0064 - 0.0080	0.15	0.38	0.27
0.0080 - 0.0100	0.11	0.33	0.24
0.0100 - 0.0130	0.12	0.32	0.28
0.0130 - 0.0160	0.14	0.20	0.22
0.0160 - 0.0200	0.12	0.21	0.19
0.0200 - 0.0260	0.25	0.31	0.31
0.0260 - 0.0330	0.25	0.21	0.26
0.0330 - 0.0410	0.50	0.41	0.41
0.0410 - 0.0510	0.56	0.44	0.42
0.0510 - 0.0640	0.90	0.58	0.58
0.0640 - 0.0800	1.14	0.71	0.81
0.0800 - 0.1000	1.84	1.06	0.99
0.1000 - 0.1300	1.87	1.73	1.37
0.1300 - 0.1600	1.09	1.75	1.29
0.1600 - 0.2000	0.73	1.75	1.26
0.2000 - 0.2600	1.19	2.98	2.27
0.2600 - 0.3300	0.57	2.37	1.33
0.3300 - 0.4100	0.66	2.96	2.17
0.4100 - 0.5100	0.31	1.28	1.08
0.5100 - 0.6400	0.12	0.72	0.92
0.6400 - 0.8000	0.06	0.41	0.48
0.8000 - 1.0000	0.04	0.22	0.41
1.0000 - 1.3000	0.04	0.18	0.30
1.3000 - 1.6000	0.02	0.12	0.21
1.6000 - 2.0000	0.02	0.06	0.12
2.0000 - 2.6000	0.02	0.12	0.23
2.6000 - 3.3000	0.02	0.09	0.21
3.3000 - 4.1000	0.04	0.12	0.27
4.1000 - 5.1000	0.04	0.09	0.15
5.1000 - 6.4000	0.01	0.08	0.07
6.4000 - 8.0000	0.09	0.24	0.10
8.0000 - 10.0000	0.36	0.44	0.31
10.0000 - 13.0000	0.17	0.44	0.52
13.0000 - 16.0000	0.00	0.00	0.00
16.0000 - 19.0000	0.00	0.00	0.00
19.0000 -	0.34	1.34	0.85
V_a 3.3000 - 33.0000	1.77	3.09	2.84
V_b 0.3300 - 3.3000	10.39	13.78	10.73
V_c 0.0330 - 0.3300	1.31	6.16	6.13
V_d 0.0030 - 0.0330	1.05	2.75	2.27
total	14.52	25.78	21.97

Table 8 Results of pore size distribution analysis (continued)

	NT-10 (90ka)	NT-17 (90ka)	NT-24 (90ka)
pore size (μ m)	pore volume(mm^3/g)	pore volume(mm^3/g)	pore volume(mm^3/g)
0.0041 - 0.0051	0.73	0.99	1.08
0.0051 - 0.0064	0.77	0.89	0.84
0.0064 - 0.0080	0.38	0.60	0.39
0.0080 - 0.0100	0.30	0.37	0.37
0.0100 - 0.0130	0.26	0.34	0.44
0.0130 - 0.0160	0.29	0.27	0.34
0.0160 - 0.0200	0.25	0.23	0.32
0.0200 - 0.0260	0.52	0.42	1.10
0.0260 - 0.0330	0.35	0.25	1.35
0.0330 - 0.0410	0.71	0.50	3.16
0.0410 - 0.0510	0.99	0.42	2.76
0.0510 - 0.0640	1.81	0.57	2.45
0.0640 - 0.0800	1.85	0.62	1.58
0.0800 - 0.1000	1.86	0.71	1.22
0.1000 - 0.1300	2.16	1.38	1.28
0.1300 - 0.1600	1.72	1.81	0.99
0.1600 - 0.2000	1.29	2.14	1.08
0.2000 - 0.2600	2.33	4.34	1.81
0.2600 - 0.3300	1.64	3.58	1.24
0.3300 - 0.4100	3.48	5.83	1.74
0.4100 - 0.5100	1.58	3.74	1.31
0.5100 - 0.6400	0.85	2.89	0.87
0.6400 - 0.8000	0.32	1.42	0.55
0.8000 - 1.0000	0.29	1.01	0.36
1.0000 - 1.3000	0.20	0.60	0.25
1.3000 - 1.6000	0.15	0.32	0.10
1.6000 - 2.0000	0.10	0.14	0.10
2.0000 - 2.6000	0.15	0.27	0.15
2.6000 - 3.3000	0.10	0.10	0.10
3.3000 - 4.1000	0.15	0.20	0.10
4.1000 - 5.1000	0.19	0.20	0.02
5.1000 - 6.4000	0.16	0.11	0.00
6.4000 - 8.0000	0.33	0.32	0.32
8.0000 - 10.0000	0.33	0.48	0.16
10.0000 - 13.0000	0.49	0.32	0.66
13.0000 - 16.0000	0.00	0.00	0.00
16.0000 - 19.0000	0.00	0.00	0.00
19.0000 -	1.34	1.47	0.96
V_a 3.3000 - 33.000(	3.85	4.36	6.23
V_b 0.3300 - 3.3000	16.36	16.07	17.57
V_c 0.0330 - 0.3300	7.22	16.32	5.53
V_d 0.0030 - 0.0330	2.99	3.10	2.22
total	30.42	39.85	31.55

Table 8 Results of pore size distribution analysis (continued)

	BB-3 (110ka)	BB-7 (110ka)	BB-9 (110ka)
pore size (μ m)	pore volume (mm^3/g)	pore volume (mm^3/g)	pore volume (mm^3/g)
0.0041 - 0.0051	0.94	0.90	0.93
0.0051 - 0.0064	1.00	0.73	1.07
0.0064 - 0.0080	0.60	0.56	0.63
0.0080 - 0.0100	0.48	0.55	0.63
0.0100 - 0.0130	0.52	0.61	0.60
0.0130 - 0.0160	0.38	0.45	0.50
0.0160 - 0.0200	0.32	0.53	0.40
0.0200 - 0.0260	0.65	0.65	0.68
0.0260 - 0.0330	0.51	0.48	0.52
0.0330 - 0.0410	0.81	0.76	0.85
0.0410 - 0.0510	0.71	0.60	0.71
0.0510 - 0.0640	0.94	0.73	0.87
0.0640 - 0.0800	1.00	0.68	0.93
0.0800 - 0.1000	1.17	0.73	0.93
0.1000 - 0.1300	2.00	1.01	1.35
0.1300 - 0.1600	2.30	0.83	1.33
0.1600 - 0.2000	2.13	0.83	1.13
0.2000 - 0.2600	5.06	1.64	2.48
0.2600 - 0.3300	3.13	1.31	2.30
0.3300 - 0.4100	3.14	3.13	5.06
0.4100 - 0.5100	1.76	3.80	6.39
0.5100 - 0.6400	1.24	4.94	6.02
0.6400 - 0.8000	0.59	5.24	4.46
0.8000 - 1.0000	0.38	5.89	2.20
1.0000 - 1.3000	0.33	6.60	1.15
1.3000 - 1.6000	0.16	2.97	0.65
1.6000 - 2.0000	0.11	1.16	0.46
2.0000 - 2.6000	0.21	1.21	0.50
2.6000 - 3.3000	0.11	0.60	0.40
3.3000 - 4.1000	0.16	0.66	0.45
4.1000 - 5.1000	0.11	0.60	0.40
5.1000 - 6.4000	0.08	0.13	0.23
6.4000 - 8.0000	0.19	0.71	0.35
8.0000 - 10.0000	0.38	1.08	0.73
10.0000 - 13.0000	0.78	0.88	1.05
13.0000 - 16.0000	0.00	0.00	0.00
16.0000 - 19.0000	0.00	0.00	0.00
19.0000 -	0.95	2.14	2.31
V_a 3.3000 - 33.000(	5.40	5.46	5.96
V_b 0.3300 - 3.3000	19.25	9.12	12.88
V_c 0.0330 - 0.3300	8.03	35.54	27.29
V_d 0.0030 - 0.0330	2.65	6.20	5.52
total	35.33	56.32	51.65

Table 8 Results of pore size distribution analysis (continued)

	SZ-3 (120ka)	SZ-12 (120ka)	SZ-16 (120ka)
pore size (μ m)	pore volume(mm^3/g)	pore volume(mm^3/g)	pore volume(mm^3/g)
0.0041 - 0.0051	0.60	1.07	1.09
0.0051 - 0.0064	0.83	1.18	1.14
0.0064 - 0.0080	0.49	0.54	0.59
0.0080 - 0.0100	0.52	0.52	0.56
0.0100 - 0.0130	0.60	0.54	0.58
0.0130 - 0.0160	0.46	0.52	0.68
0.0160 - 0.0200	0.32	0.32	0.50
0.0200 - 0.0260	0.97	0.69	0.70
0.0260 - 0.0330	0.43	0.43	0.59
0.0330 - 0.0410	0.64	0.80	0.91
0.0410 - 0.0510	0.92	0.64	0.70
0.0510 - 0.0640	0.77	0.83	0.76
0.0640 - 0.0800	0.78	0.77	1.06
0.0800 - 0.1000	1.06	0.90	0.56
0.1000 - 0.1300	1.23	1.20	1.41
0.1300 - 0.1600	1.12	1.12	1.14
0.1600 - 0.2000	0.95	1.18	0.85
0.2000 - 0.2600	1.84	2.21	1.74
0.2600 - 0.3300	1.44	1.96	1.76
0.3300 - 0.4100	2.84	4.37	2.28
0.4100 - 0.5100	2.96	4.22	2.79
0.5100 - 0.6400	4.13	5.86	3.70
0.6400 - 0.8000	4.45	4.77	5.04
0.8000 - 1.0000	5.69	2.93	5.28
1.0000 - 1.3000	9.13	1.73	7.22
1.3000 - 1.6000	8.68	0.86	6.28
1.6000 - 2.0000	4.33	0.46	5.75
2.0000 - 2.6000	4.22	0.63	13.55
2.6000 - 3.3000	1.27	0.23	2.46
3.3000 - 4.1000	1.06	0.40	2.00
4.1000 - 5.1000	0.23	0.23	0.88
5.1000 - 6.4000	0.00	0.15	0.38
6.4000 - 8.0000	0.00	0.40	0.85
8.0000 - 10.0000	0.00	0.40	0.82
10.0000 - 13.0000	0.00	0.60	1.03
13.0000 - 16.0000	0.00	0.00	0.00
16.0000 - 19.0000	0.00	0.00	0.00
19.0000 -	0.00	2.84	2.49
V_a 3.3000 - 33.000(	5.22	5.81	6.43
V_b 0.3300 - 3.3000	10.75	11.61	10.89
V_c 0.0330 - 0.3300	47.70	26.06	54.35
V_d 0.0030 - 0.0330	1.29	5.02	8.45
total	64.96	48.50	80.12

Table 8 Results of pore size distribution analysis (continued)

	CH-2(250ka)	CH-19 (250ka)	CH-22 (250ka)
pore size (μ m)	pore volume (mm^3/g)	pore volume (mm^3/g)	pore volume (mm^3/g)
0.0041 - 0.0051	1.82	0.00	1.74
0.0051 - 0.0064	1.90	0.00	1.96
0.0064 - 0.0080	1.17	0.00	1.43
0.0080 - 0.0100	1.40	0.00	0.93
0.0100 - 0.0130	1.29	0.00	1.12
0.0130 - 0.0160	0.96	0.00	0.89
0.0160 - 0.0200	0.68	0.00	0.76
0.0200 - 0.0260	1.39	0.03	1.29
0.0260 - 0.0330	0.79	0.33	0.63
0.0330 - 0.0410	1.46	0.72	1.29
0.0410 - 0.0510	1.22	0.82	1.11
0.0510 - 0.0640	1.29	1.15	1.12
0.0640 - 0.0800	1.32	1.50	1.20
0.0800 - 0.1000	1.68	1.25	1.12
0.1000 - 0.1300	1.71	1.90	1.51
0.1300 - 0.1600	1.76	1.28	1.30
0.1600 - 0.2000	1.75	1.61	1.20
0.2000 - 0.2600	2.46	2.59	2.19
0.2600 - 0.3300	2.50	2.29	1.78
0.3300 - 0.4100	3.58	3.94	3.21
0.4100 - 0.5100	3.18	3.57	2.99
0.5100 - 0.6400	3.93	4.59	3.39
0.6400 - 0.8000	4.29	4.59	3.75
0.8000 - 1.0000	4.93	5.25	4.19
1.0000 - 1.3000	7.01	6.23	5.00
1.3000 - 1.6000	5.86	5.90	4.37
1.6000 - 2.0000	6.15	3.93	4.28
2.0000 - 2.6000	10.29	8.20	7.76
2.6000 - 3.3000	8.65	6.62	6.16
3.3000 - 4.1000	19.37	12.79	10.34
4.1000 - 5.1000	8.15	15.93	13.83
5.1000 - 6.4000	1.96	19.25	7.09
6.4000 - 8.0000	2.00	7.41	7.58
8.0000 - 10.0000	2.29	2.33	4.10
10.0000 - 13.0000	1.50	2.07	2.81
13.0000 - 16.0000	0.00	0.00	0.00
16.0000 - 19.0000	0.00	0.00	0.00
19.0000 -	2.54	2.79	3.79
V_a 3.3000 - 33.0000	11.40	0.36	10.75
V_b 0.3300 - 3.3000	17.15	15.11	13.82
V_c 0.0330 - 0.3300	57.87	52.82	45.10
V_d 0.0030 - 0.0330	37.81	62.57	49.54
total	124.23	130.86	119.21

Table 8 Results of pore size distribution analysis (continued)

	PC-8 (350ka)	PC-10 (350ka)	PC-13 (350ka)
pore size (μ m)	pore volume (mm^3/g)	pore volume (mm^3/g)	pore volume (mm^3/g)
0.0041 - 0.0051	0.00	2.28	2.42
0.0051 - 0.0064	0.00	2.55	1.32
0.0064 - 0.0080	0.00	1.57	1.75
0.0080 - 0.0100	0.04	1.25	1.60
0.0100 - 0.0130	0.72	1.30	1.90
0.0130 - 0.0160	0.85	1.08	1.39
0.0160 - 0.0200	0.72	0.93	1.34
0.0200 - 0.0260	1.66	1.68	2.68
0.0260 - 0.0330	0.98	1.68	2.12
0.0330 - 0.0410	2.17	2.17	3.65
0.0410 - 0.0510	2.25	2.44	3.82
0.0510 - 0.0640	2.38	2.44	5.40
0.0640 - 0.0800	3.27	2.55	5.52
0.0800 - 0.1000	3.27	2.88	6.03
0.1000 - 0.1300	4.59	3.04	7.62
0.1300 - 0.1600	3.78	2.55	6.13
0.1600 - 0.2000	2.93	2.01	15.46
0.2000 - 0.2600	5.48	3.52	9.95
0.2600 - 0.3300	2.97	2.50	8.03
0.3300 - 0.4100	5.52	3.91	22.78
0.4100 - 0.5100	4.63	3.63	23.03
0.5100 - 0.6400	5.53	4.02	16.38
0.6400 - 0.8000	5.94	4.34	6.28
0.8000 - 1.0000	5.95	4.66	3.20
1.0000 - 1.3000	8.92	6.84	2.16
1.3000 - 1.6000	8.16	4.99	1.24
1.6000 - 2.0000	8.32	4.78	0.72
2.0000 - 2.6000	15.13	10.31	0.82
2.6000 - 3.3000	11.21	8.68	0.31
3.3000 - 4.1000	20.05	21.59	0.42
4.1000 - 5.1000	7.06	10.53	0.36
5.1000 - 6.4000	4.97	1.46	0.00
6.4000 - 8.0000	2.42	4.61	0.00
8.0000 - 10.0000	1.19	3.09	0.36
10.0000 - 13.0000	1.78	3.04	0.72
13.0000 - 16.0000	0.00	0.00	0.00
16.0000 - 19.0000	0.00	0.00	0.00
19.0000 -	2.72	4.61	1.08
V_a 3.3000 - 33.0000	4.97	14.32	16.52
V_b 0.3300 - 3.3000	33.09	26.10	71.61
V_c 0.0330 - 0.3300	79.31	56.16	76.92
V_d 0.0030 - 0.0330	40.19	48.93	2.94
total	157.56	145.51	167.99

Table 9 Pore size distribution and permeability

Sample No.	V_a (mm^3/g)	V_b (mm^3/g)	V_c (mm^3/g)	V_d (mm^3/g)	V_{sum} (mm^3/g)	Specific surface area S (m^2/g)	Mean pore radius r (μm)	Bulk density ρ (g/cm^3)	Permeability k (cm/s)
P-1 (0 ka)	1.37	0.64	0.82	3.33	6.16	0.80	13.665	2.62	4.45E-12
P-2 (0 ka)	1.23	0.82	11.72	2.67	16.44	0.81	0.097	2.53	7.03E-11
P-3 (0 ka)	0.85	0.45	0.93	4.33	6.56	1.10	0.005	2.63	3.16E-12
FT-1 (20 ka)	0.80	0.32	7.36	2.05	10.53	0.51	0.076	2.56	5.19E-11
FT-3 (20 ka)	2.88	7.19	17.42	4.40	31.89	1.46	0.258	2.40	1.81E-10
FT-4 (20 ka)	1.46	0.55	6.24	3.12	11.37	0.87	0.036	2.15	2.28E-11
SA-5 (70 ka)	1.05	1.31	10.39	1.77	14.52	0.72	0.096	2.53	8.17E-11
SA-11 (70 ka)	2.75	6.16	13.78	3.09	25.78	1.18	0.258	2.45	1.71E-10
SA-13 (70 ka)	2.27	6.13	10.73	2.84	21.97	1.03	0.202	2.45	1.34E-10
NT-10 (90 ka)	2.99	7.22	16.36	3.85	30.42	1.54	0.326	2.06	1.40E-10
NT-17 (90 ka)	3.10	16.32	16.07	4.36	39.85	1.67	0.336	2.05	2.52E-10
NT-24 (90 ka)	2.22	5.53	17.57	6.23	31.55	2.08	0.045	2.36	9.18E-11
BB-3 (110 ka)	2.65	8.03	19.25	5.40	35.33	1.91	0.259	1.92	1.32E-10
BB-7 (110 ka)	6.20	35.54	9.12	5.46	56.32	1.84	1.157	1.91	6.12E-10
BB-9 (110 ka)	5.52	27.29	12.88	5.96	51.65	1.93	0.430	1.97	3.70E-10
SZ-3 (120 ka)	1.29	47.70	10.75	5.22	64.96	1.60	1.411	2.22	1.21E-09
SZ-12 (120 ka)	5.02	26.06	11.61	5.81	48.50	2.02	0.551	2.31	3.63E-10
SZ-16 (120 ka)	8.45	54.35	10.89	6.43	80.12	2.20	2.334	2.10	1.34E-09
CH-2 (250 ka)	37.81	57.87	17.15	11.40	124.23	3.65	3.901	2.18	1.72E-09
CH-19 (250 ka)	62.57	52.82	15.11	0.36	130.86	0.46	4.994	1.58	-
CH-22 (250 ka)	49.54	45.10	13.82	10.75	119.21	3.56	3.901	1.94	1.51E-09
PC-8 (350 ka)	40.19	79.31	33.09	14.32	166.91	1.45	3.114	1.73	1.41E-08
PC-10 (350 ka)	48.93	56.16	26.10	14.32	145.51	4.66	3.988	1.74	1.36E-09
PC-13 (350 ka)	2.94	76.92	71.61	16.52	167.99	6.01	0.416	1.74	1.26E-09

Table 10 Results of X-ray CT analysis

Time (ka)	Original data												Average
0	1377	1349	1516	1348	1335	1235	1331	1594	1230	-	-	-	1368
20	1363	1379	1353	1311	1311	1321	1271	-	-	-	-	-	1330
40	1309	1271	1194	1213	1324	1133	-	-	-	-	-	-	1241
70	1273	1248	1314	1108	1285	1112	1193	1331	1293	1256	1159	1283	1241
90	1292	1344	1272	1297	1292	1257	1331	1308	1377	-	-	-	1308
110	1093	1171	1151	1192	1268	1129	-	-	-	-	-	-	1167
120	938	966	1093	1123	997	1154	926	984	-	-	-	-	1023
250	926	955	934	809	1074	952	823	918	779	-	-	-	908
350	855	917	881	822	909	831	807	884	-	-	-	-	863

Table 11 Chemical composition (weight %) from XRF data

Sample No.	SiO_2	TiO_2	Al_2O_3	MnO	MgO	CaO	Na_2O	K_2O	P_2O_5	$FeO^*Fe_2O_3$	*CIA*	*PI*
P-1(0 ka)	70.00	0.32	9.72	0.01	0.98	0.18	2.16	0.91	0.07	4.87	74.96	82.75
FT-2 (20 ka)	68.14	0.49	13.22	0.01	1.09	0.09	2.36	2.61	0.08	3.38	72.31	80.42
FT-4 (20 ka)	72.75	0.38	10.11	0.01	0.84	0.05	2.21	2.47	0.06	2.27	68.12	85.46
FT-5 (20 ka)	69.44	0.40	11.34	0.01	0.76	0.04	2.33	2.46	0.06	2.61	70.14	83.28
SA-11 (70 ka)	66.11	0.42	12.80	0.02	0.87	0.06	2.58	2.03	0.06	3.09	73.24	80.62
SA-12 (70 ka)	69.65	0.37	11.22	0.01	0.39	0.03	2.25	2.46	0.05	1.96	70.29	84.09
SA-17 (70 ka)	67.66	0.42	12.56	0.05	0.81	0.07	2.18	2.19	0.06	3.19	73.93	81.12
SZ-12 (120 ka)	67.28	0.42	12.90	0.00	0.72	0.04	2.22	1.60	0.07	2.96	76.96	80.93
SZ-15 (120 ka)	67.20	0.46	13.24	0.01	0.91	0.04	1.60	2.20	0.05	3.30	77.48	80.25
SZ-16 (120 ka)	67.92	0.45	14.84	0.00	0.80	0.05	1.52	2.75	0.02	1.82	77.46	80.30
CH-11 (250 ka)	64.50	0.35	16.02	0.03	0.55	0.04	0.38	2.41	0.05	2.45	85.01	77.74
CH-13 (250 ka)	66.80	0.34	13.39	0.11	1.03	0.04	1.02	2.26	0.06	3.10	80.15	80.20
CH-22 (250 ka)	65.39	0.34	12.84	0.01	0.74	0.03	0.59	2.74	0.04	2.68	79.22	80.82
PC-12 (350 ka)	66.10	0.51	10.17	0.03	0.37	0.02	0.06	1.29	0.10	6.82	88.13	79.55
PC-15 (350 ka)	62.61	0.50	9.32	0.01	0.32	0.00	0.02	1.11	0.14	8.09	89.17	78.24
PC-21 (350 ka)	62.87	0.49	15.24	0.01	0.51	0.03	0.04	1.96	0.05	2.93	88.20	77.58

Table 12 Results of the point load strength test

Sample No.	Time (ka)	point load strength, σ_t (kgf)	strength index, τ
P-1	0	90.31	1.96
2	0	575.15	2.76
3	0	363.27	2.56
4	0	343.75	2.54
5	0	688.78	2.84
6	0	367.47	2.57
7	0	558.68	2.75
8	0	1065.09	3.03
9	0	473.34	2.68
10	0	1940.63	3.29
11	0	1800.00	3.26
12	0	540.00	2.73
13	0	551.02	2.74
14	0	408.67	2.61
15	0	1134.00	3.05
16	0	555.43	2.74
17	0	282.81	2.45
18	0	526.30	2.72
19	0	1350.00	3.13
20	0	639.84	2.81
21	0	1012.24	3.01
22	0	295.54	2.47
23	0	393.39	2.59
25	0	207.56	2.32
26	0	314.19	2.50
27	0	471.88	2.67
28	0	349.92	2.54
29	0	493.71	2.69
Average	0	635.46	2.71
FT-1	20	580.17	2.76
2	20	3000.00	3.48
3	20	197.22	2.29
4	20	324.85	2.51
5	20	388.89	2.59
6	20	45.00	1.65
7	20	96.69	1.99
8	20	316.41	2.50
9	20	86.77	1.94
10	20	450.00	2.65
11	20	131.00	2.12
12	20	102.73	2.01
13	20	311.54	2.49
14	20	1750.00	3.24
15	20	130.80	2.12
17	20	140.14	2.15
18	20	275.00	2.44
19	20	288.89	2.46
20	20	192.86	2.29
22	20	74.79	1.87
23	20	280.00	2.45
24	20	118.75	2.07
26	20	74.25	1.87
Average	20	406.81	2.35

Table 12 Results of the point load strength test (continued)

Sample No.	Time (ka)	point load strength, σ_t (kgf)	strength index, τ
SA-1	70	498.27	2.70
2	70	1597.63	3.20
3	70	135.54	2.13
4	70	582.16	2.77
6	70	159.56	2.20
7	70	336.33	2.53
8	70	174.52	2.24
9	70	413.22	2.62
10	70	241.83	2.38
11	70	119.53	2.08
13	70	2644.90	3.42
15	70	660.11	2.82
16	70	1193.88	3.08
17	70	2208.00	3.34
18	70	119.01	2.08
19	70	5400.00	3.73
20	70	319.83	2.50
21	70	1687.50	3.23
22	70	244.32	2.39
23	70	111.83	2.05
24	70	120.71	2.08
25	70	16.00	1.20
Average	70	862.94	2.58
NT-1	90	122.50	2.09
2	90	456.00	2.66
3	90	119.44	2.08
5	90	369.00	2.57
6	90	276.48	2.44
7	90	154.82	2.19
8	90	77.78	1.89
11	90	772.19	2.89
12	90	135.74	2.13
13	90	121.88	2.09
14	90	290.63	2.46
15	90	261.00	2.42
16	90	42.47	1.63
17	90	154.82	2.19
18	90	314.20	2.50
19	90	564.80	2.75
20	90	407.81	2.61
21	90	263.67	2.42
22	90	177.93	2.25
24	90	155.00	2.19
Average	90	261.91	2.32

Table 12 Results of the point load strength test (continued)

Sample No.	Time (ka)	point load strength, σ_t (kgf)	strength index, τ
SZ-4	120	38.44	1.58
6	120	63.00	1.80
8	120	16.00	1.20
9	120	56.06	1.75
10	120	5.92	0.77
11	120	0.62	-0.21
12	120	64.82	1.81
15	120	32.14	1.51
16	120	10.34	1.01
17	120	3.40	0.53
19	120	47.26	1.67
21	120	21.77	1.34
23	120	110.51	2.04
27	120	47.09	1.67
28	120	1.65	0.22
29	120	2.30	0.36
30	120	66.46	1.82
31	120	2.47	0.39
32	120	0.97	-0.01
34	120	0.41	-0.39
35	120	25.93	1.41
36	120	20.71	1.32
37	120	17.07	1.23
38	120	28.13	1.45
39	120	24.25	1.38
41	120	358.02	2.55
44	120	16.89	1.23
Average	120	50.45	1.21
CH-1	250	55.56	1.74
2	250	56.16	1.75
3	250	236.11	2.37
5	250	0.80	-0.10
6	250	34.81	1.54
7	250	259.13	2.41
8	250	169.08	2.23
11	250	29.20	1.47
12	250	42.37	1.63
13	250	209.39	2.32
16	250	71.05	1.85
17	250	54.18	1.73
18	250	65.32	1.82
20	250	17.56	1.24
21	250	26.03	1.42
23	250	394.34	2.60
24	250	30.39	1.48
Average	250	103.03	1.74

Figures

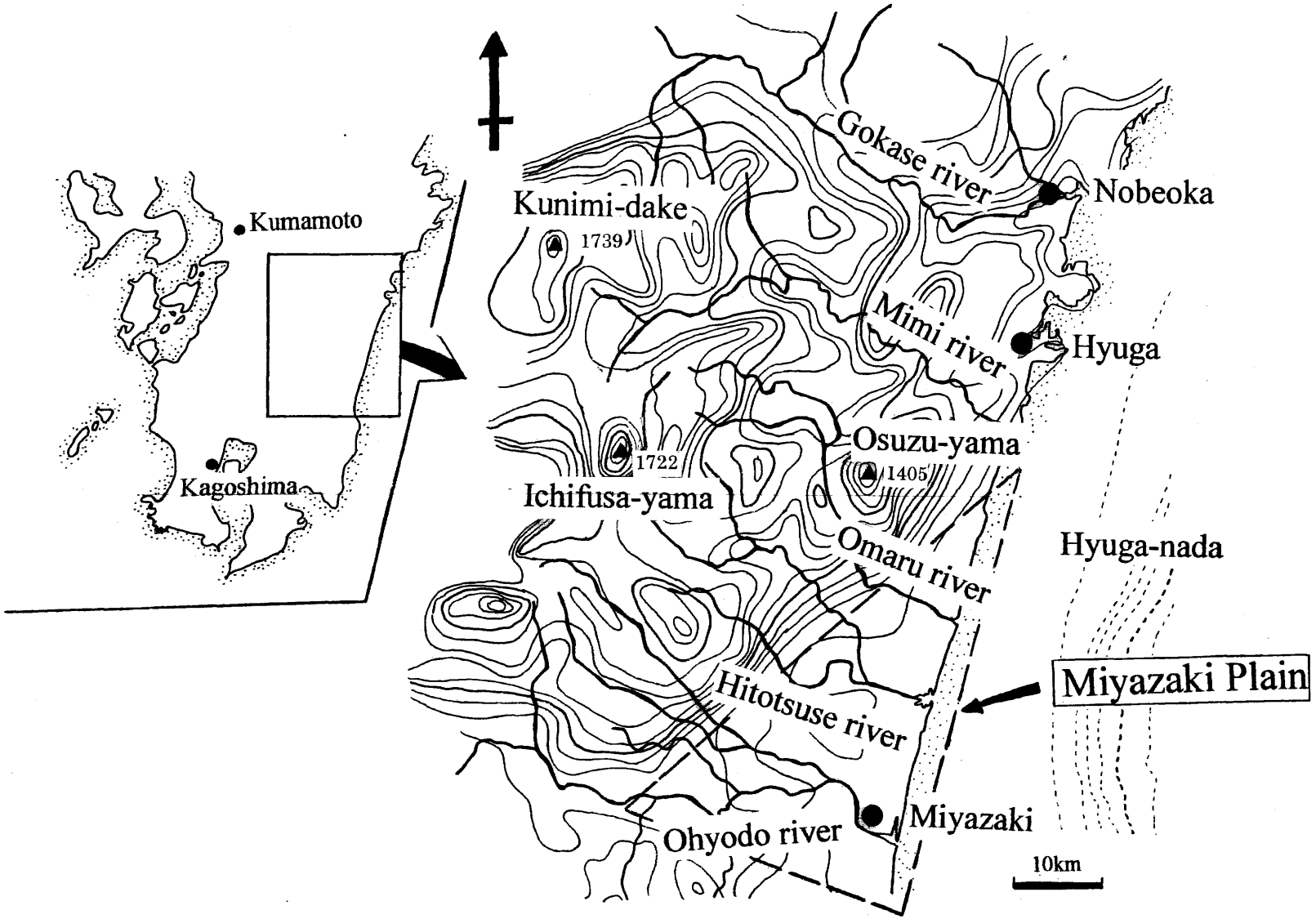

Fig. 1 Summit level map around the Miyazaki Plain (after Endo and Suzuki, 1986). Contour interval is 100m.

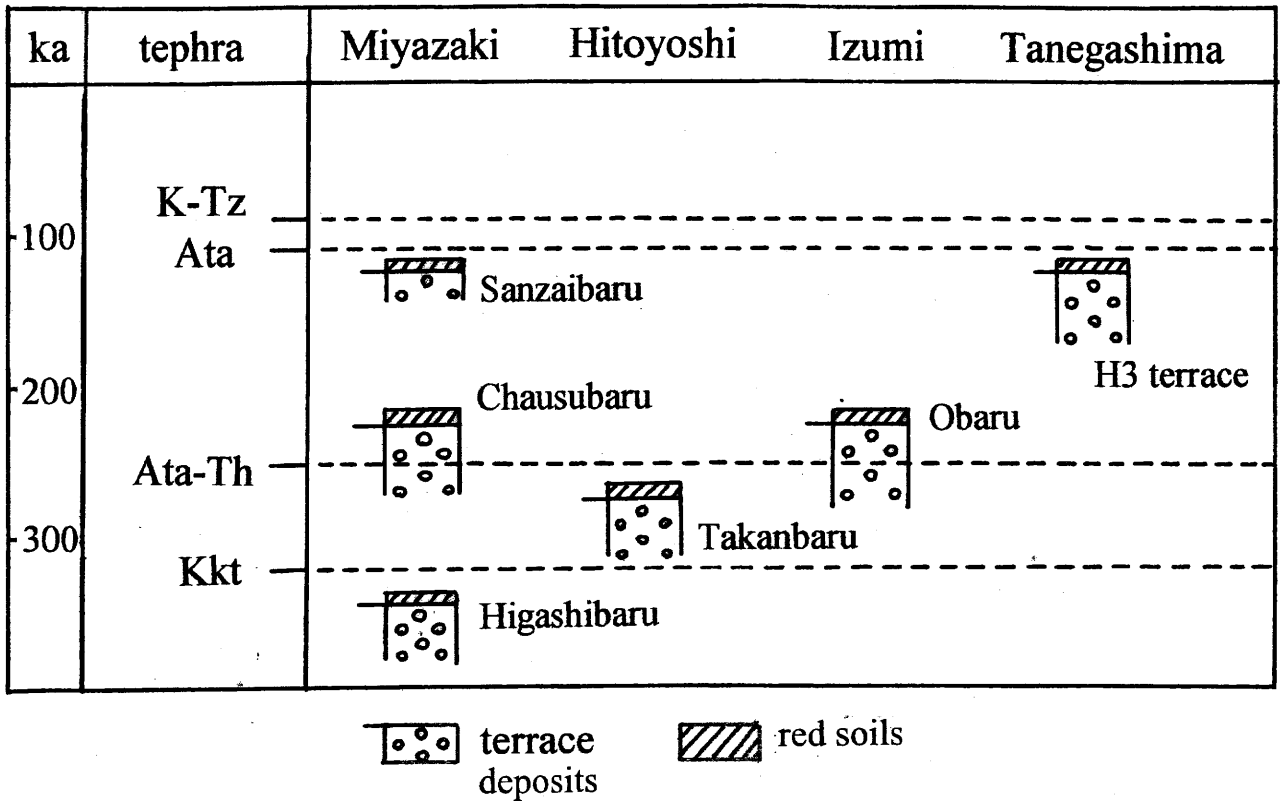

Fig. 2 Chronology of the middle to late Pleistocene terrace deposits and the paleo red soils in south Kyushu based on Tephrochronology.

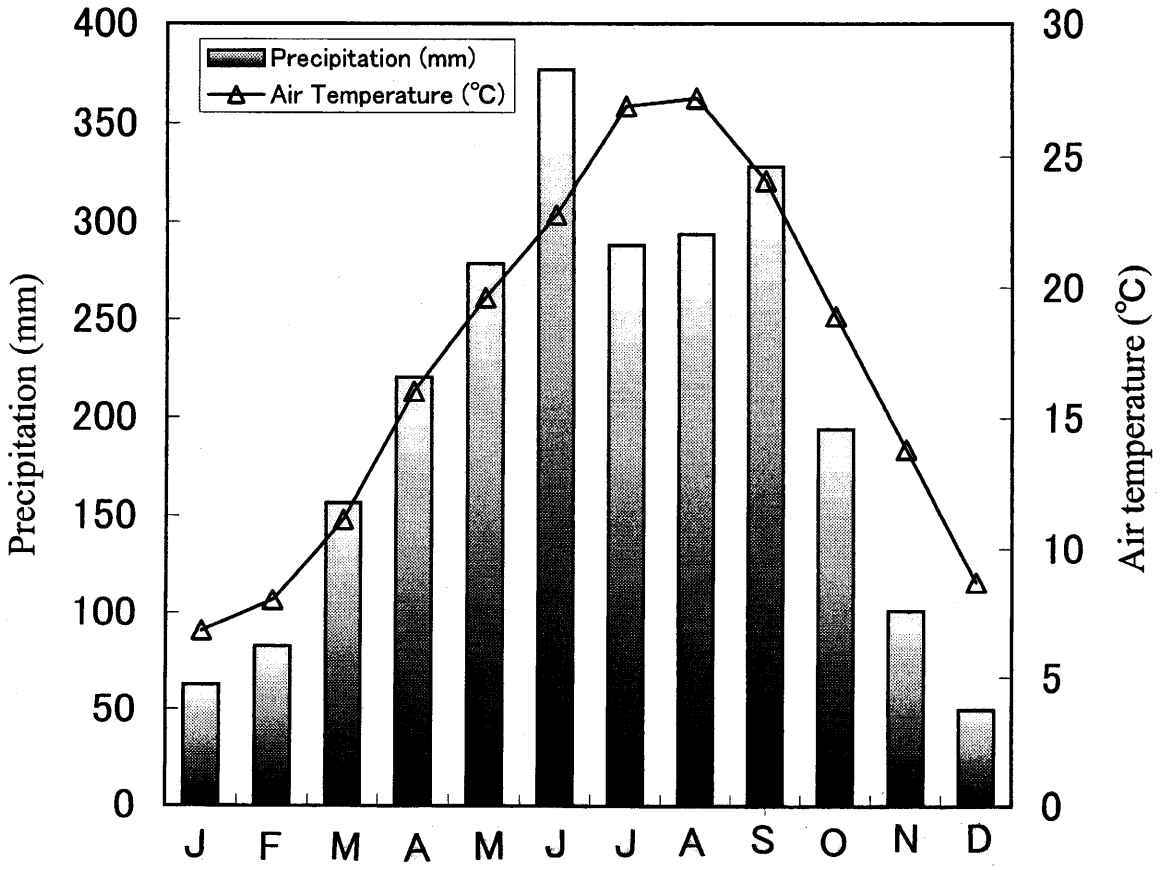

Fig. 3 Meteorological data for the three decades 1961-1990 at the Miyazaki Meteorological Station.

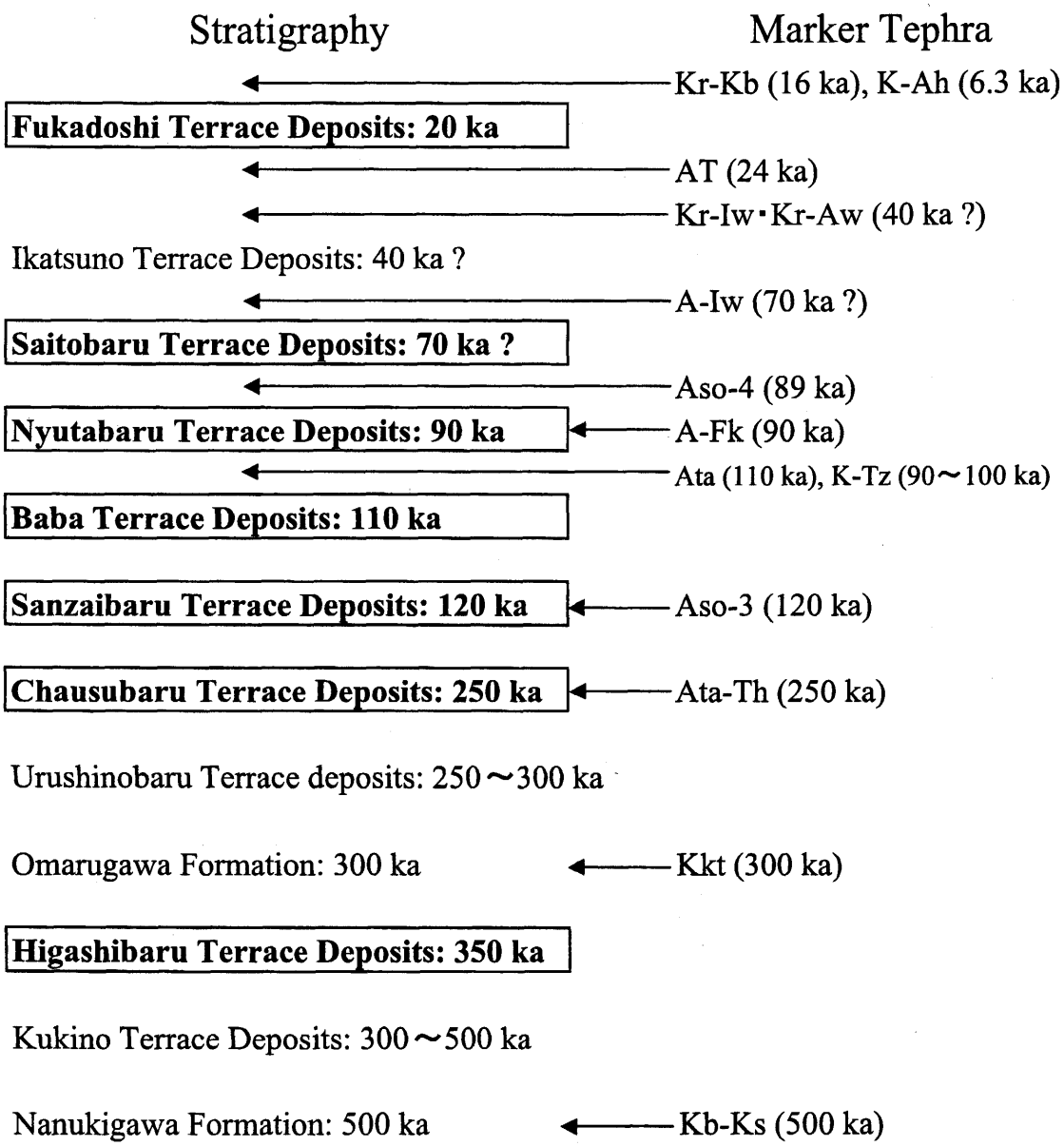

Fig. 4 Stratigraphy of the middle to late Pleistocene sediments in the Miyazaki Plain.

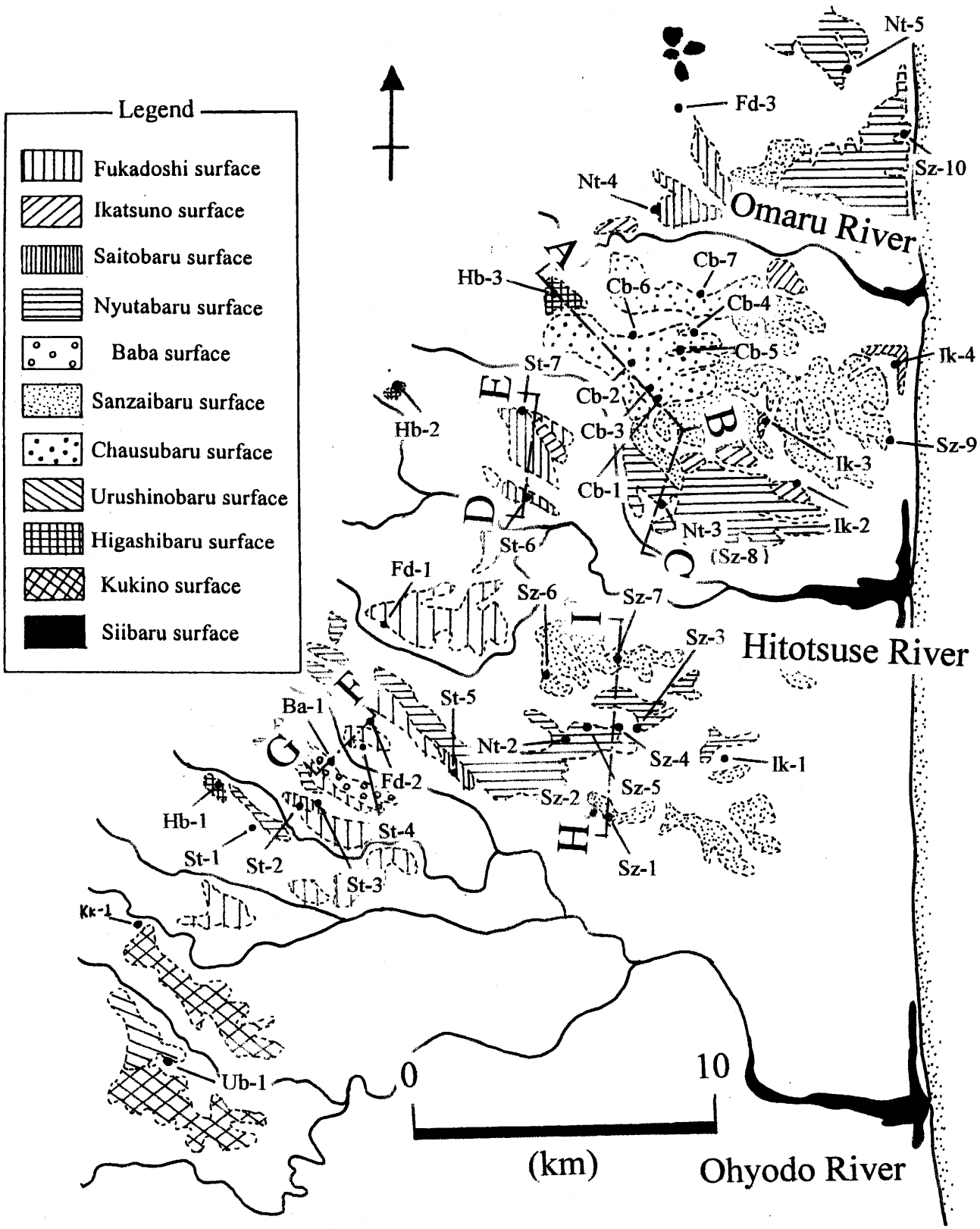

Fig. 5 Geomorphological map showing distribution of the terrace surfaces in the Miyazaki Plain.

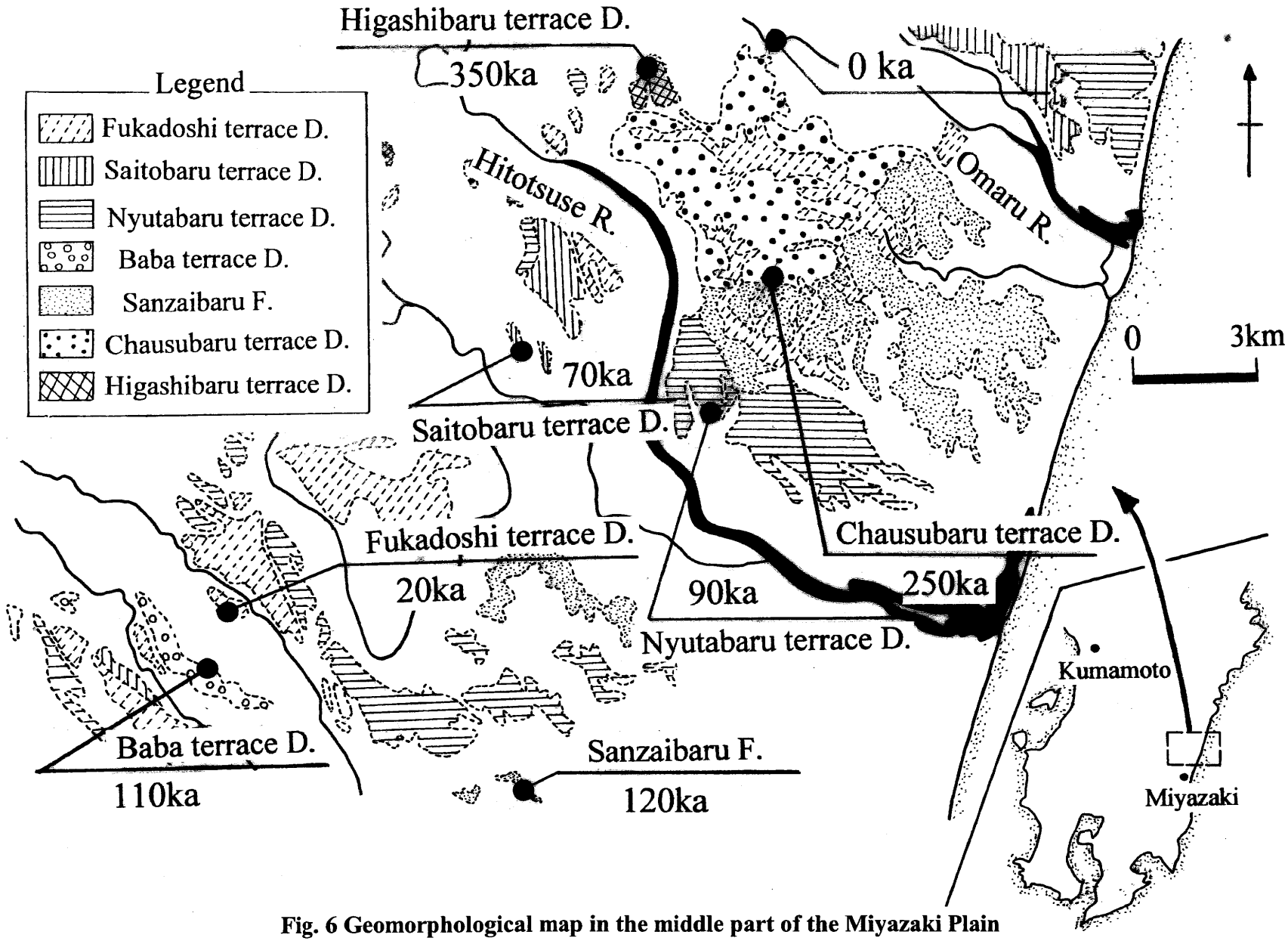

Fig. 6 Geomorphological map in the middle part of the Miyazaki Plain and sampling points.

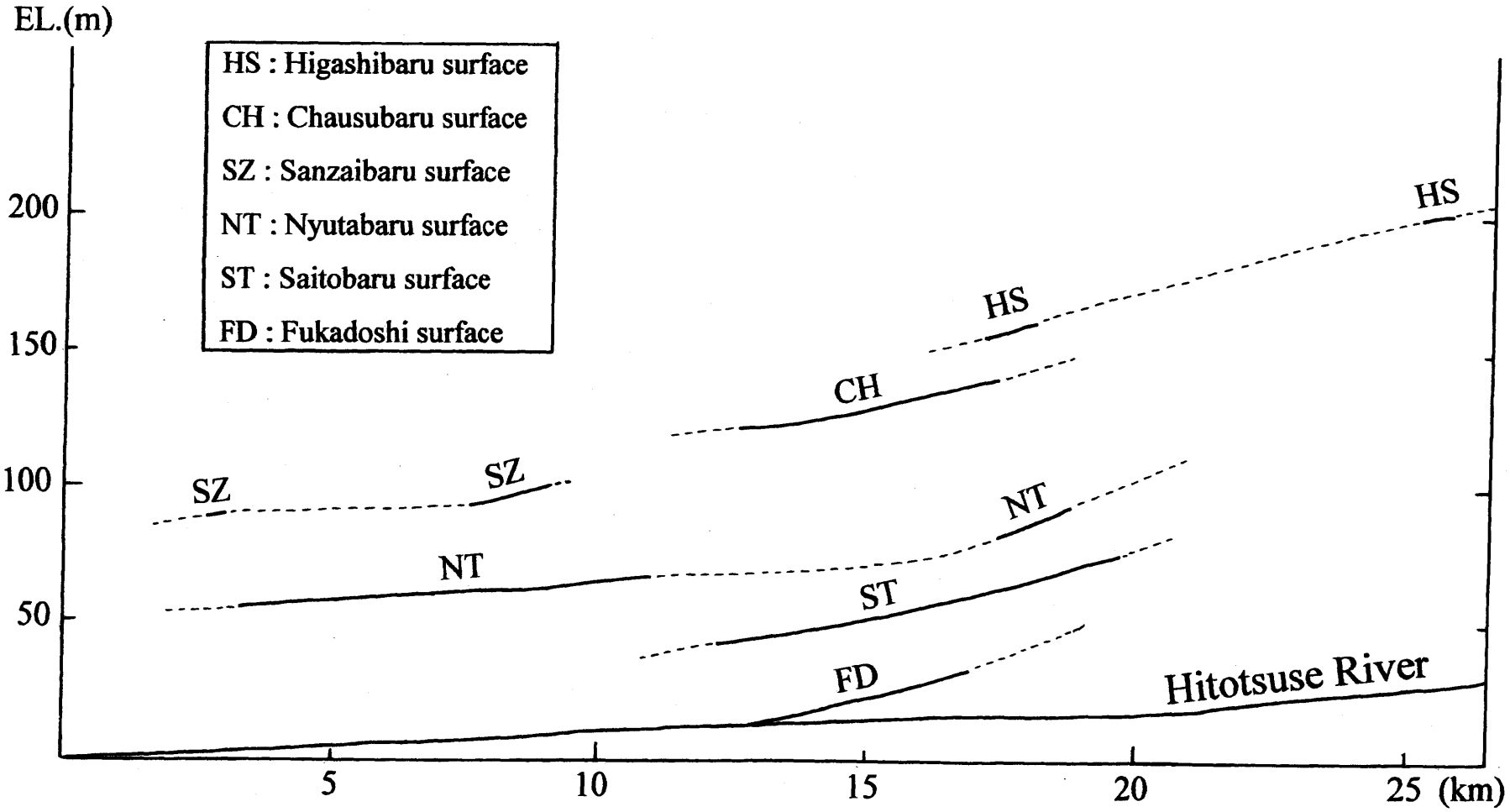

Fig. 7 Longitudinal profiles of the terrace surfaces along the Hitotsuse River.

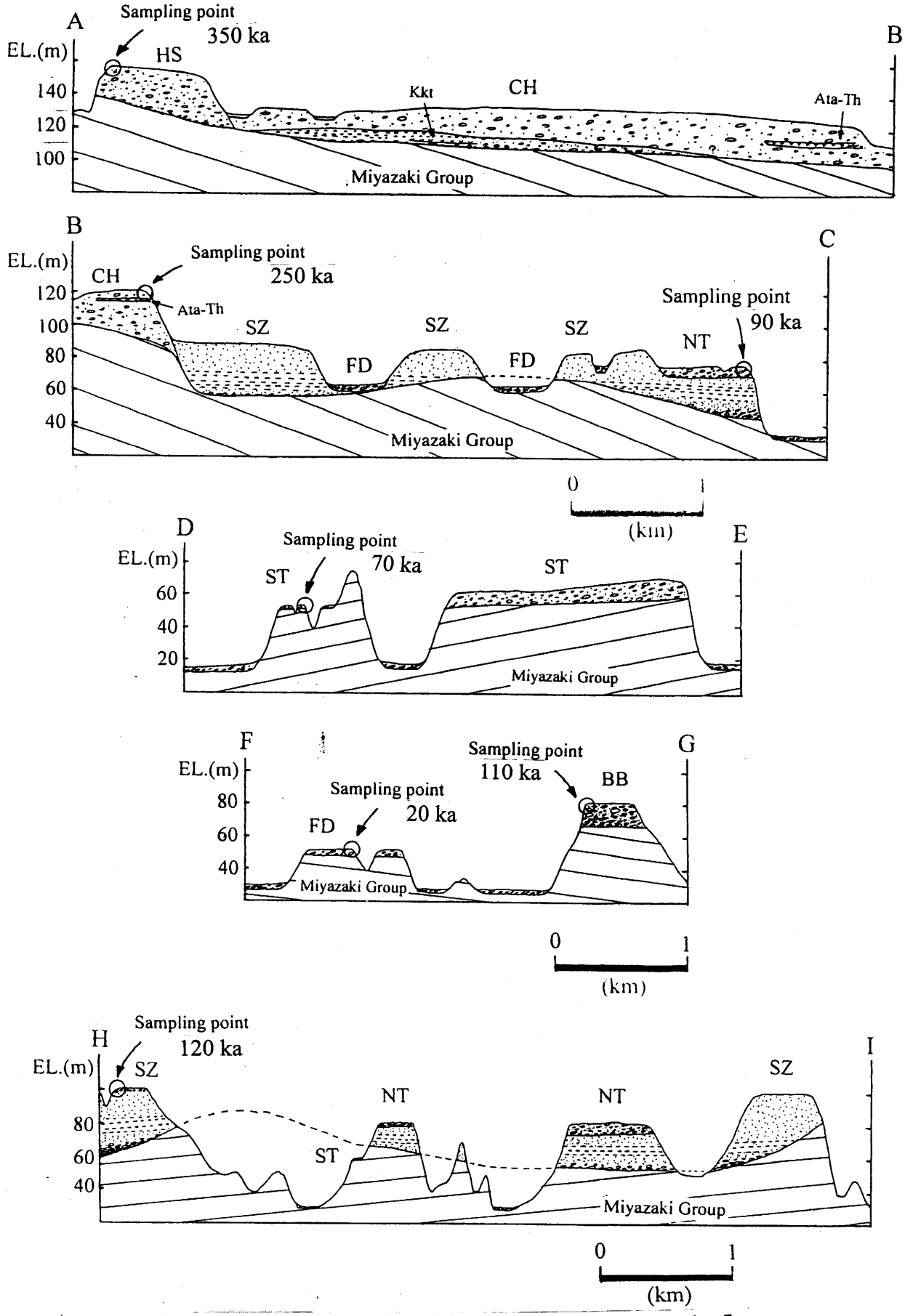

Fig. 8 Geological sections. Profile lines are shown in Fig. 5.

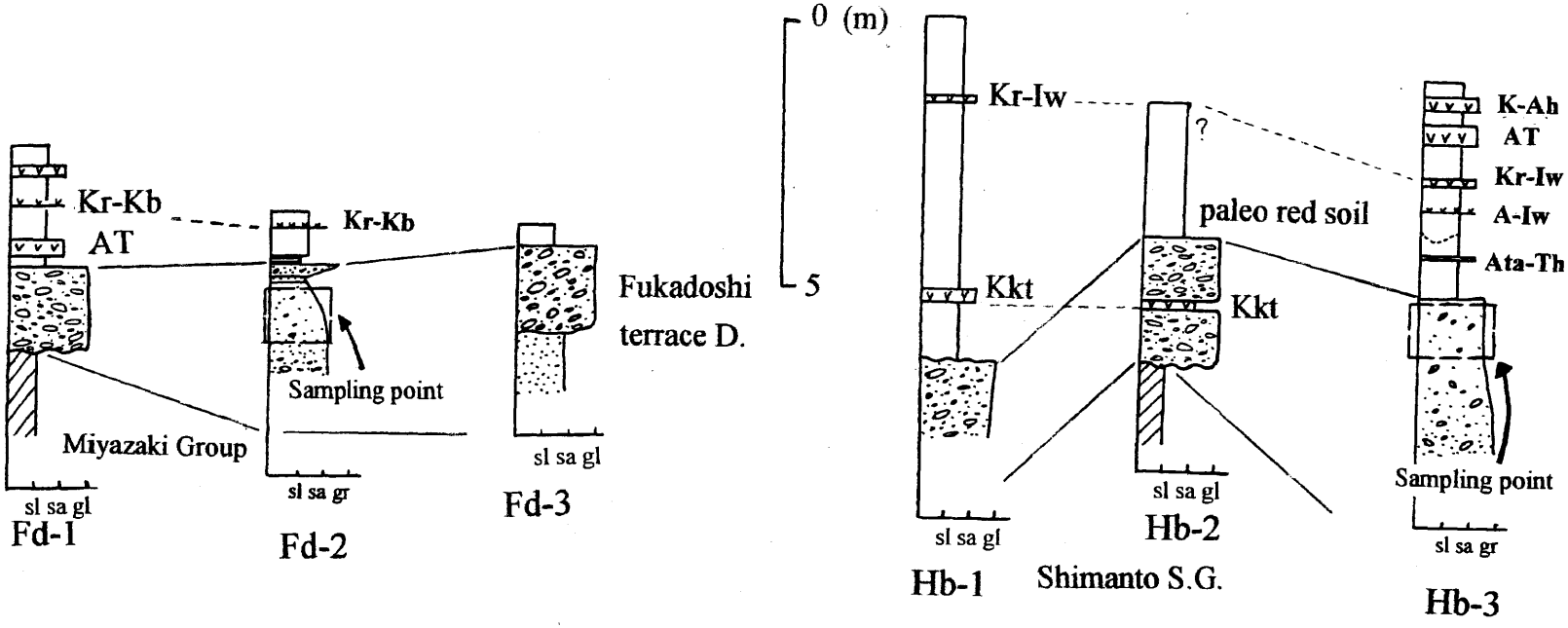

Fig. 9 Columnar sections of the Fukadoshi and the Higashibaru terrace deposits. Locations are shown in Fig. 5.

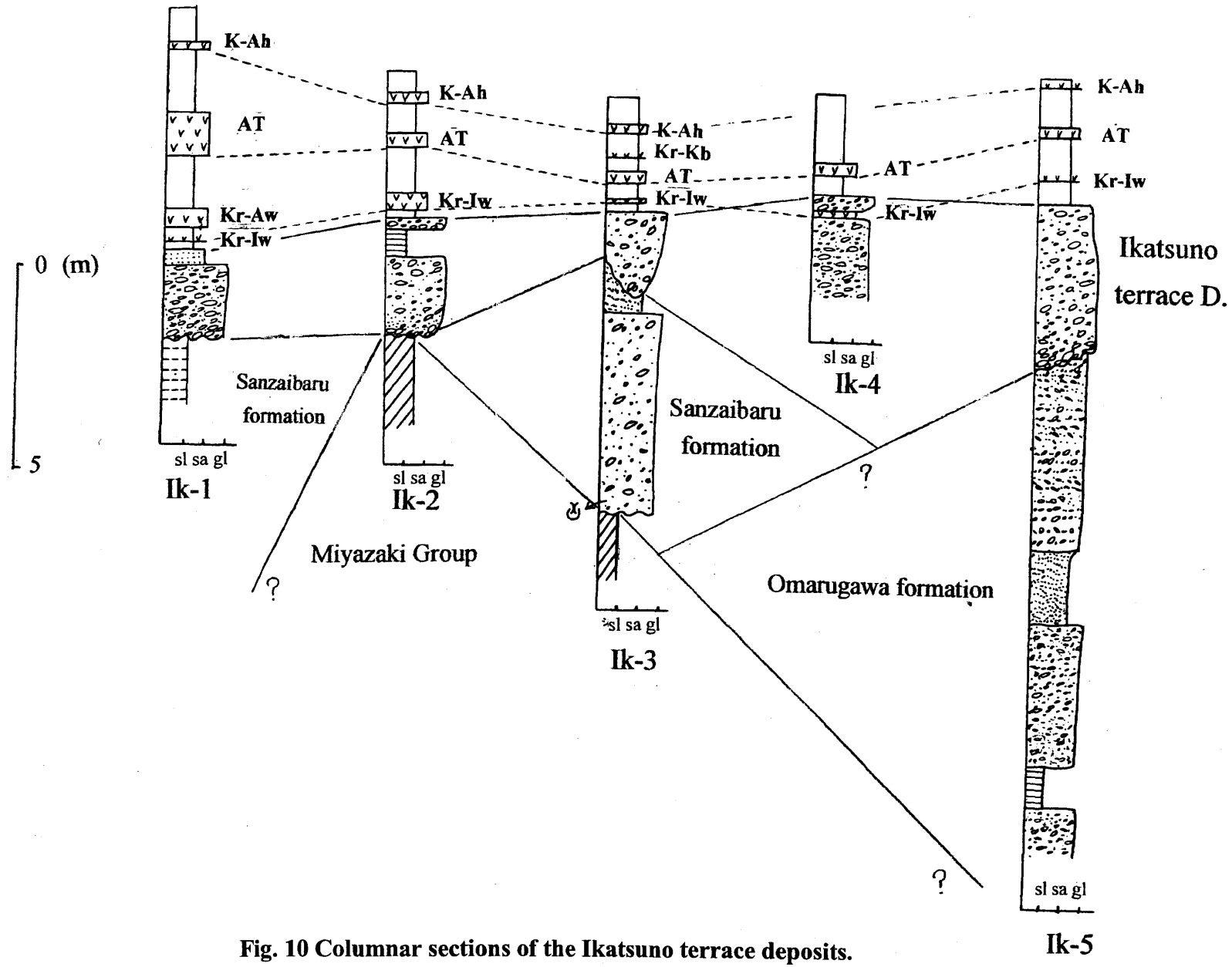

Fig. 10 Columnar sections of the Ikatsuno terrace deposits. Locations are shown in Fig. 5.

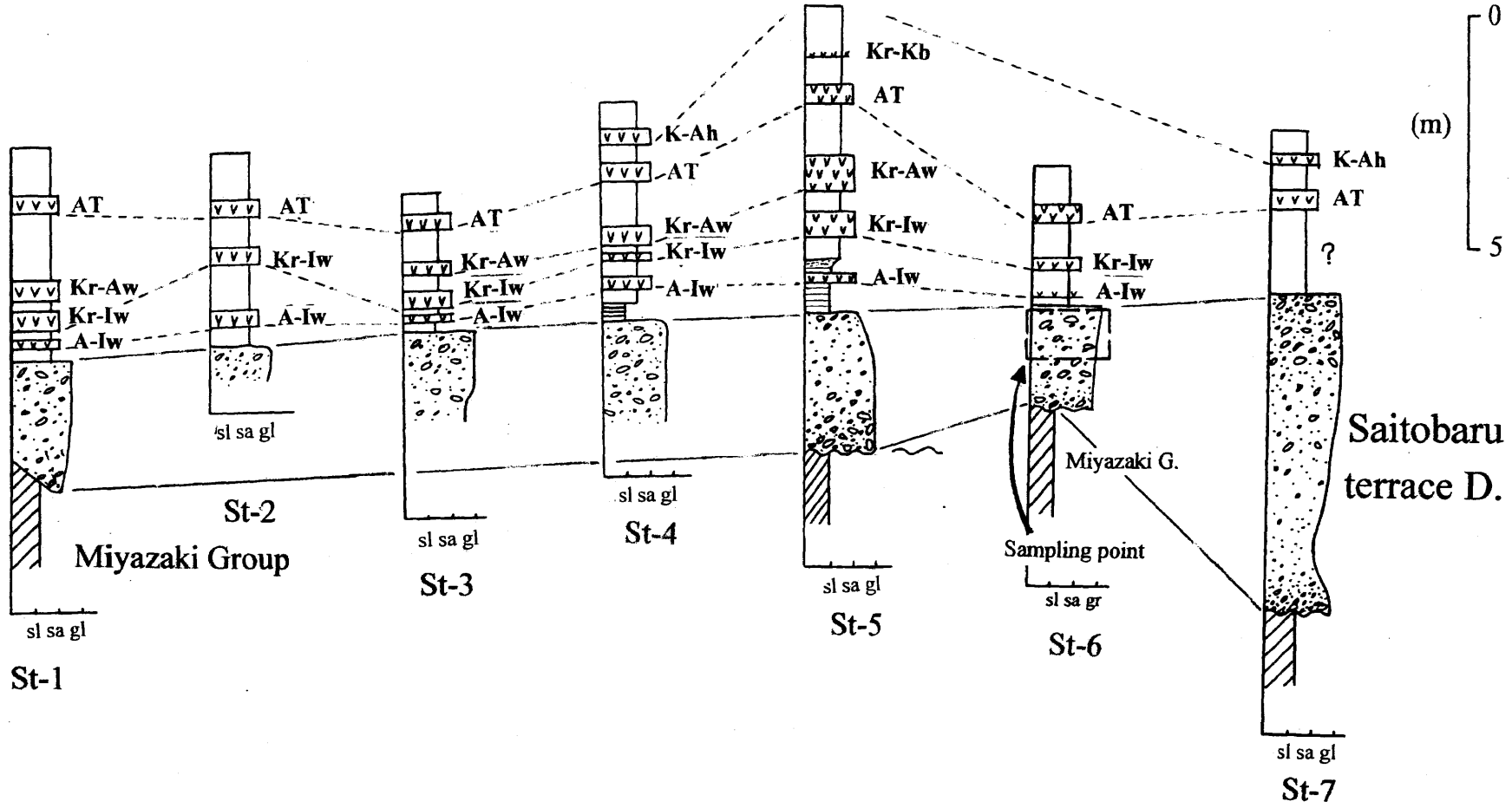

Fig. 11 Columnar sections of the Saitobaru terrace deposits.
Locations are shown in Fig. 5.

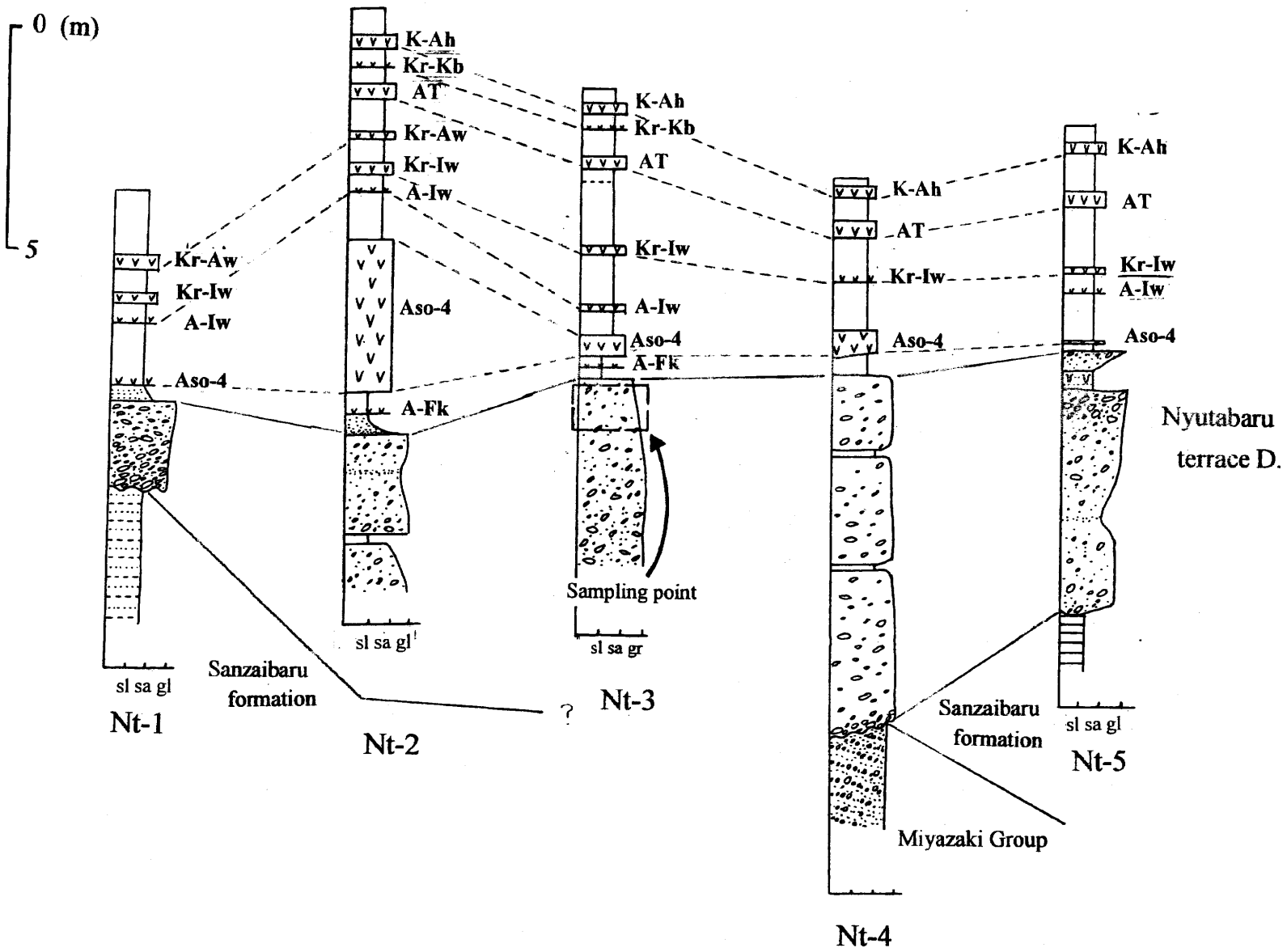

Fig. 12 Columnar sections of the Nyutabaru terrace deposits.
Locations are shown in Fig. 5.

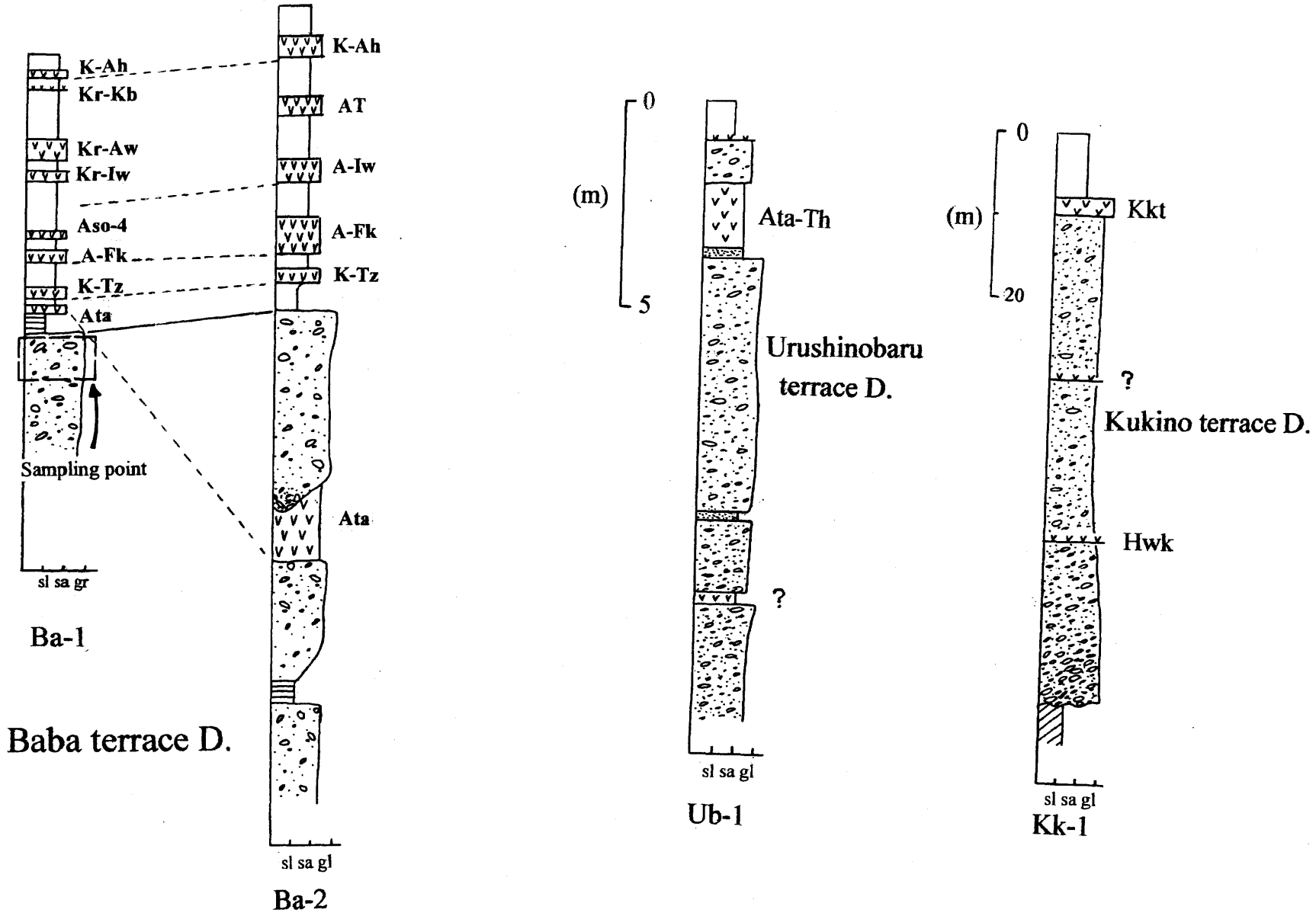

Fig. 13 Columnar sections of the Baba, Urushinobaru, and the Kukino terrace deposits. Locations are shown in Fig. 5.

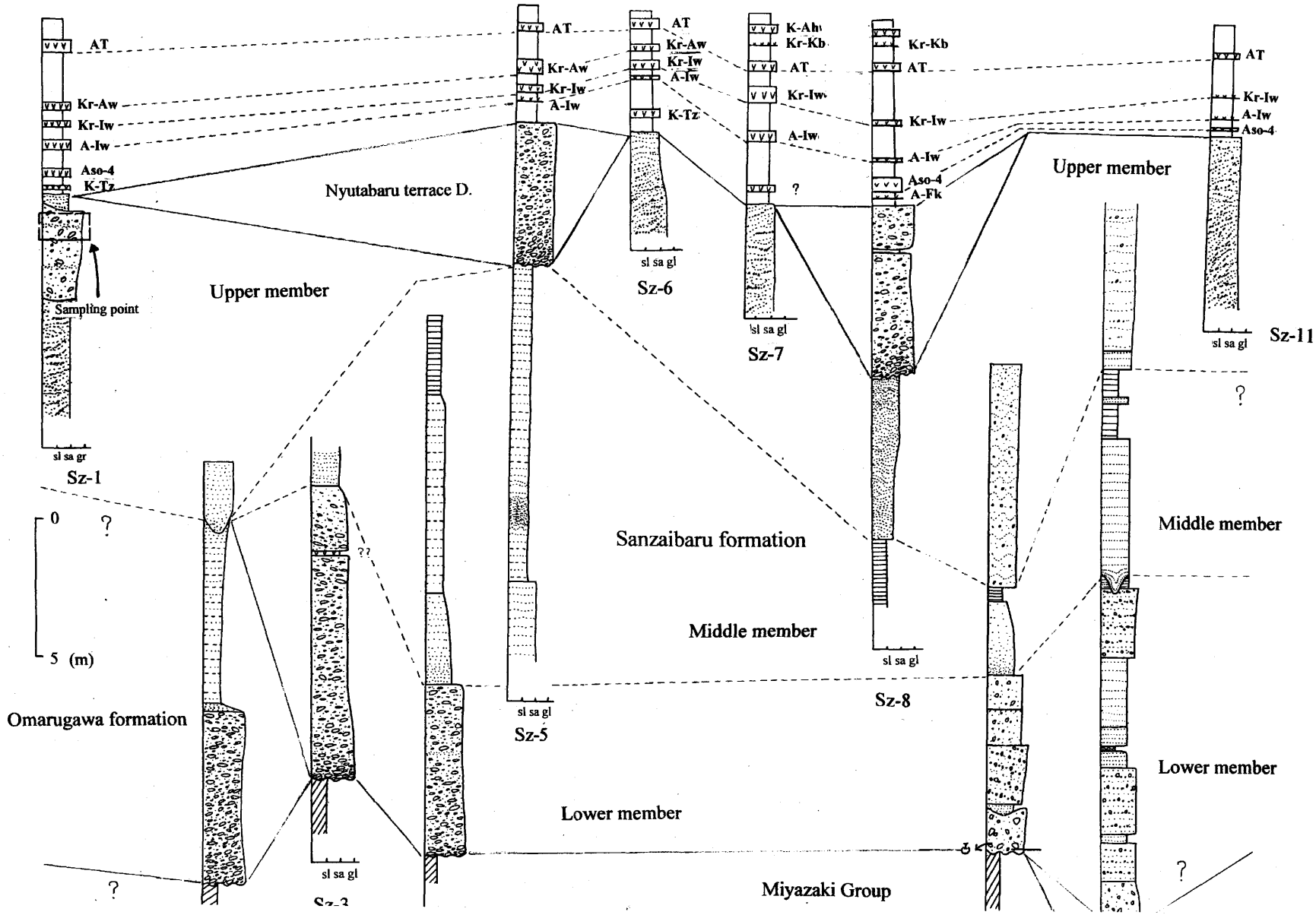

Fig. 14 Columnar sections of the Sanzaibaru formation.
Locations are shown in Fig.5.

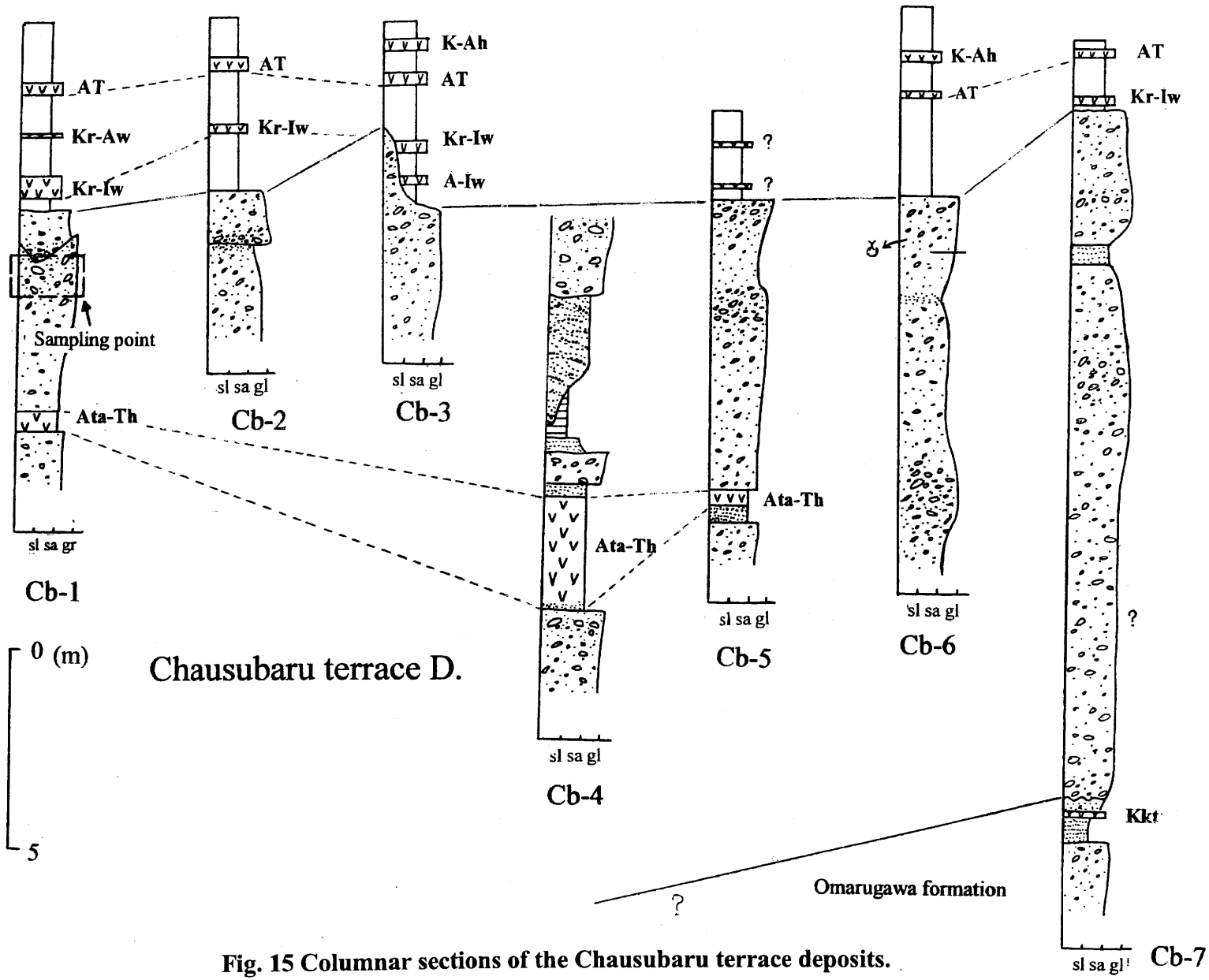

Fig. 15 Columnar sections of the Chausubaru terrace deposits. Locations are shown in Fig. 5.

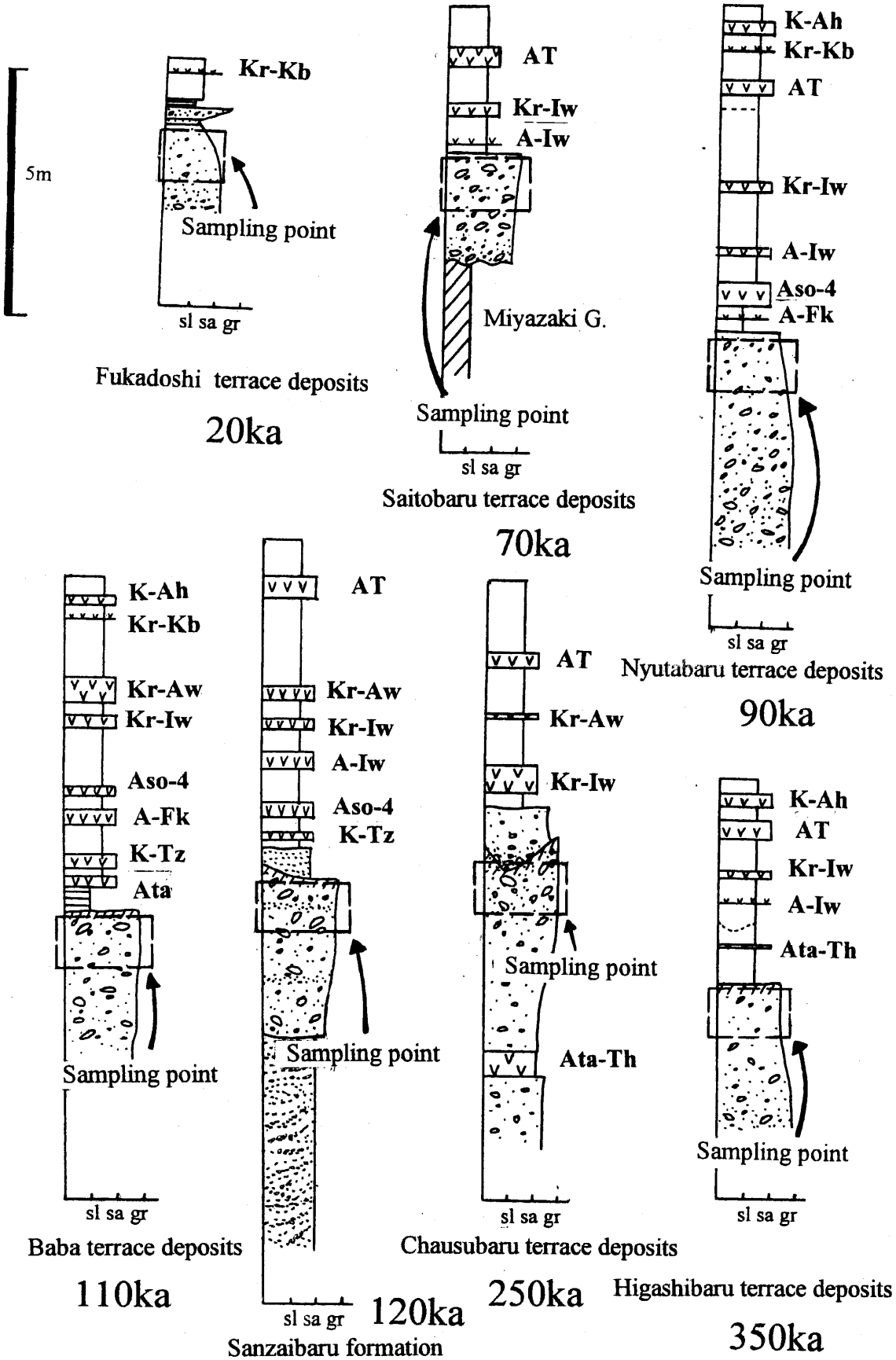

Fig. 16 Columnar sections of sampling points.

Fig. 17 Floodplain of the Omaru river (0 ka).

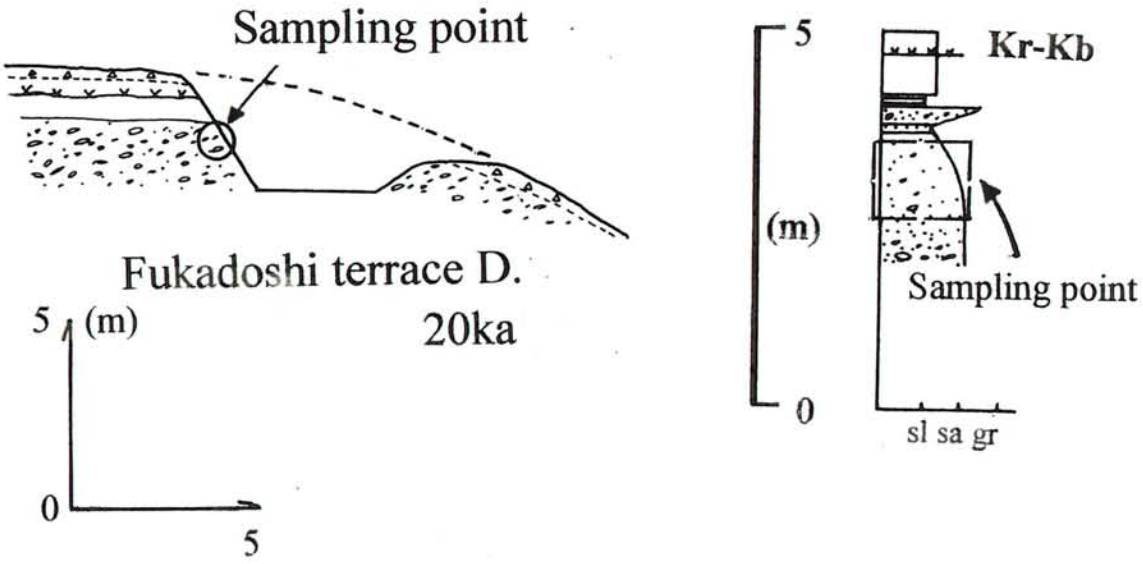

Fig. 18 Outcrop at the Fukadoshi terrace deposits (20 ka).

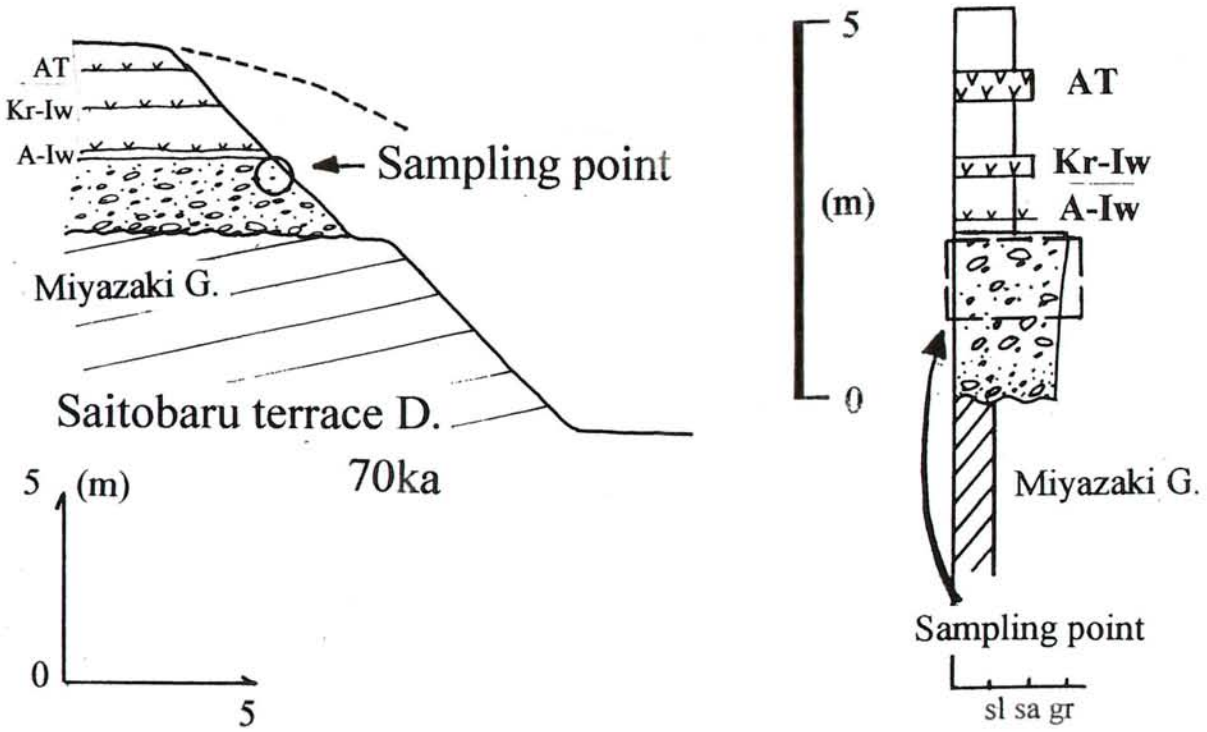

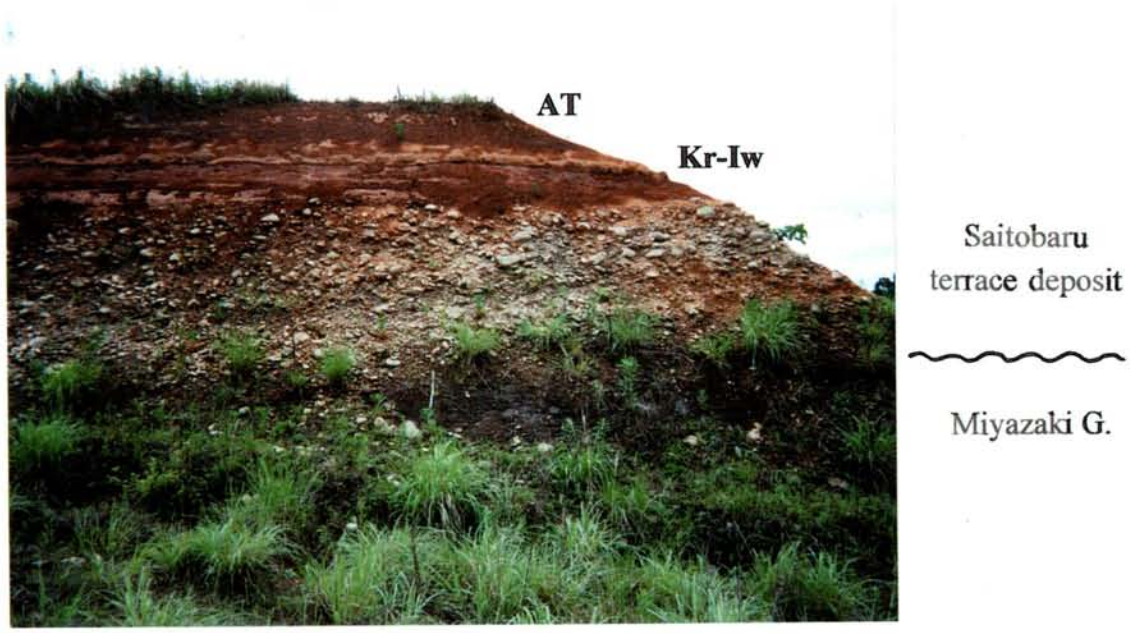

Fig. 19 Outcrop at the Saitobaru terrace deposits (70 ka).

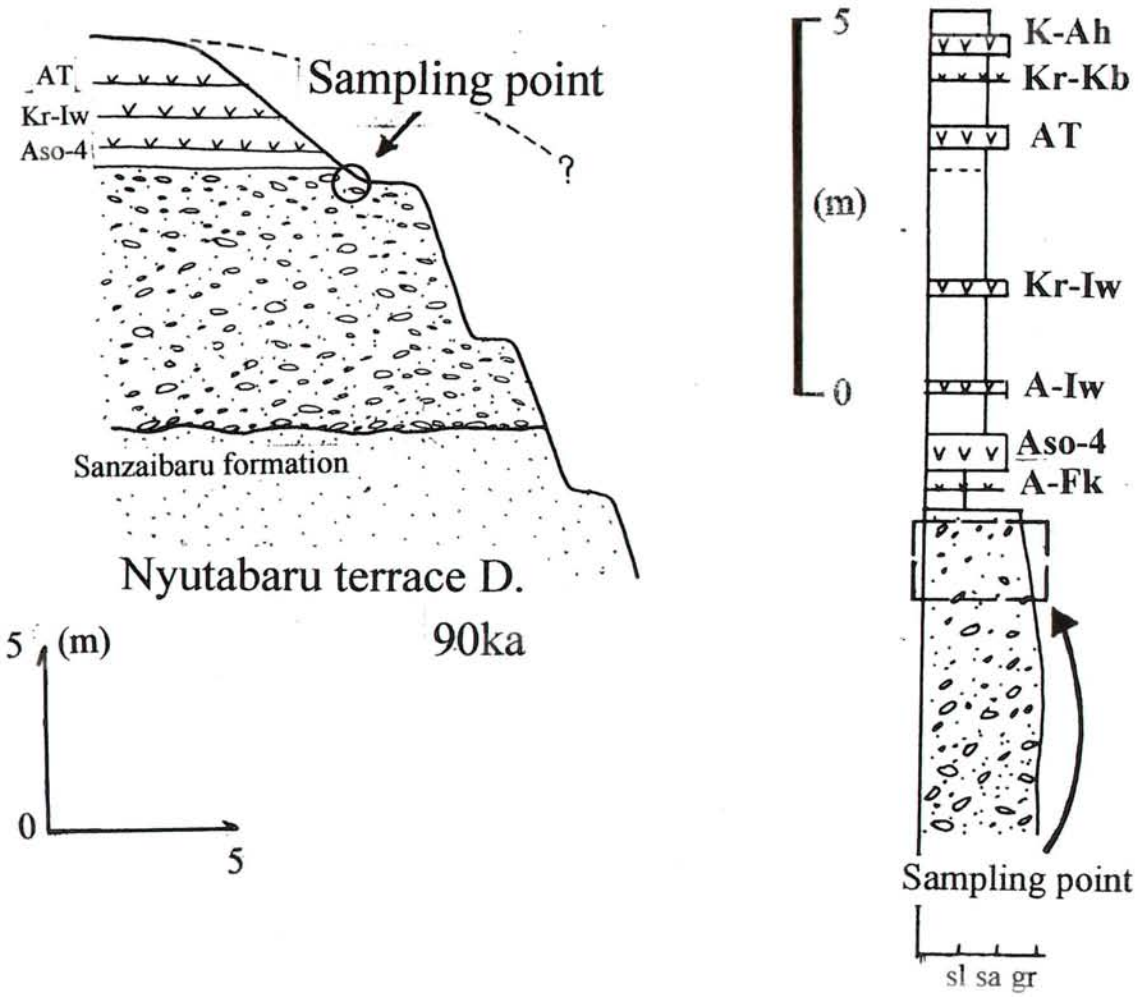

Fig. 20 Outcrop at the Nyutabaru terrace deposits (90 ka).

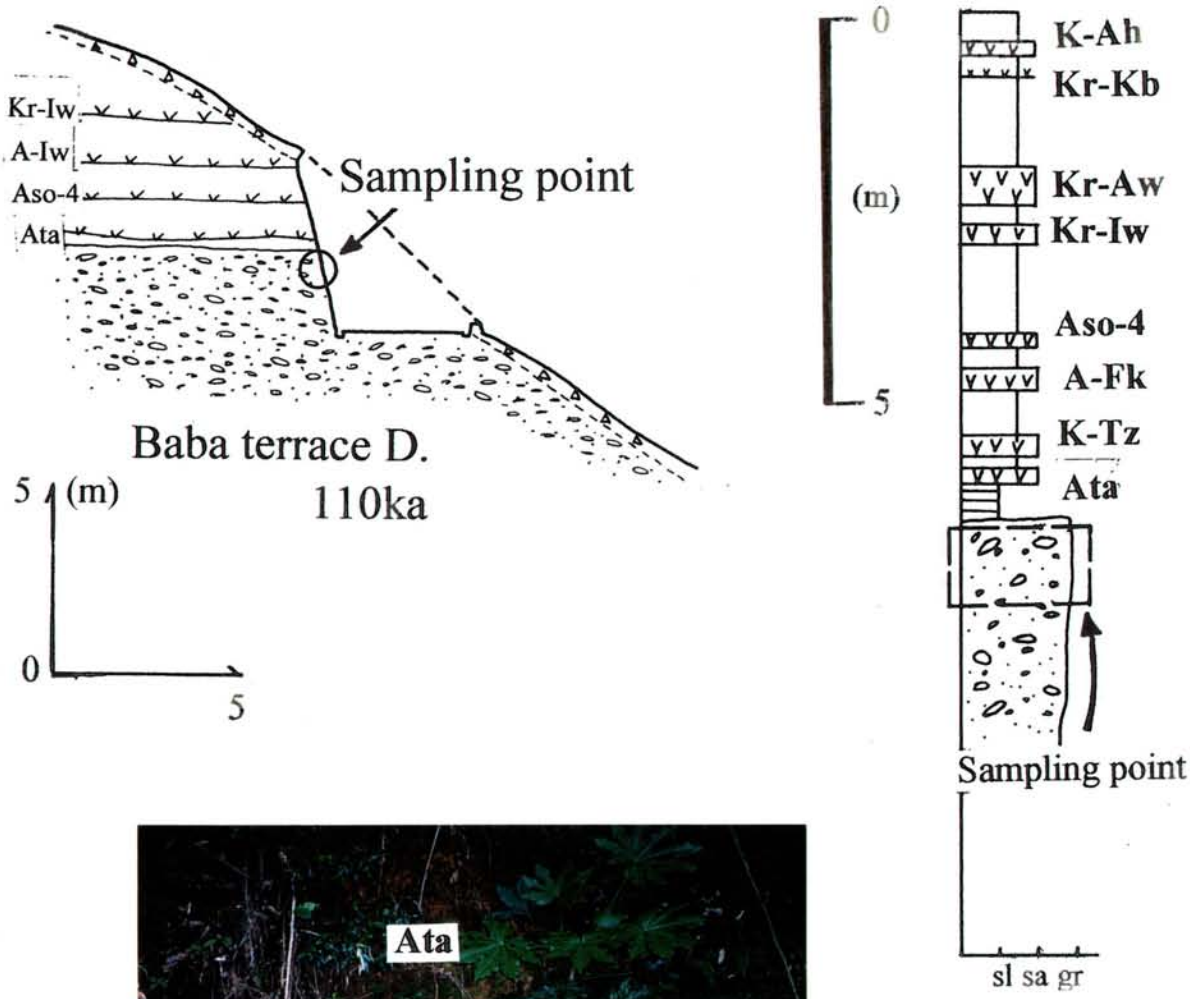

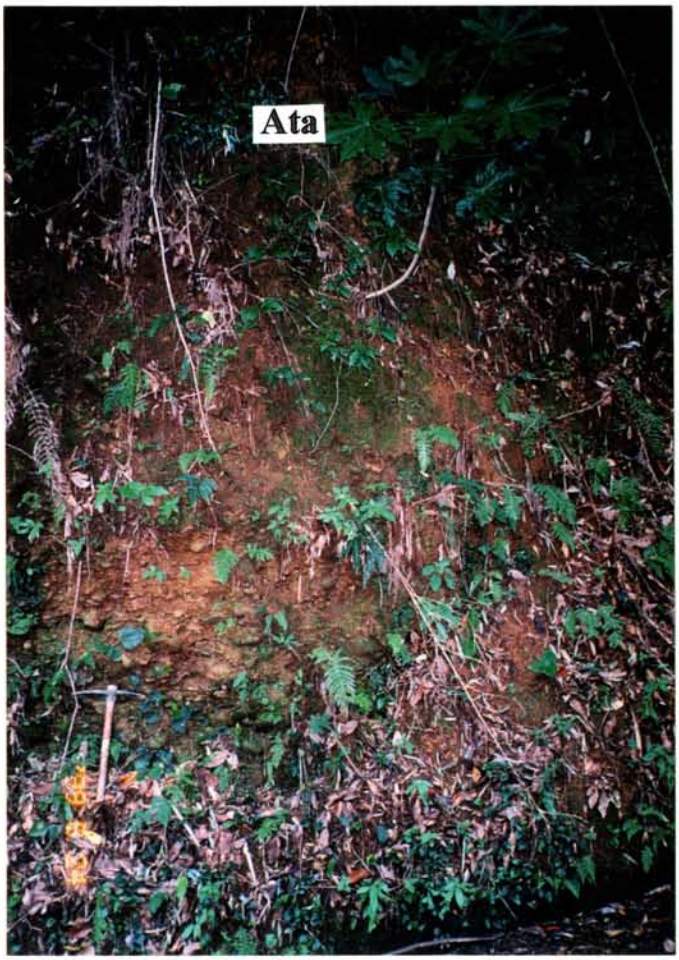

Fig. 21 Outcrop at the Baba terrace deposits (110 ka).

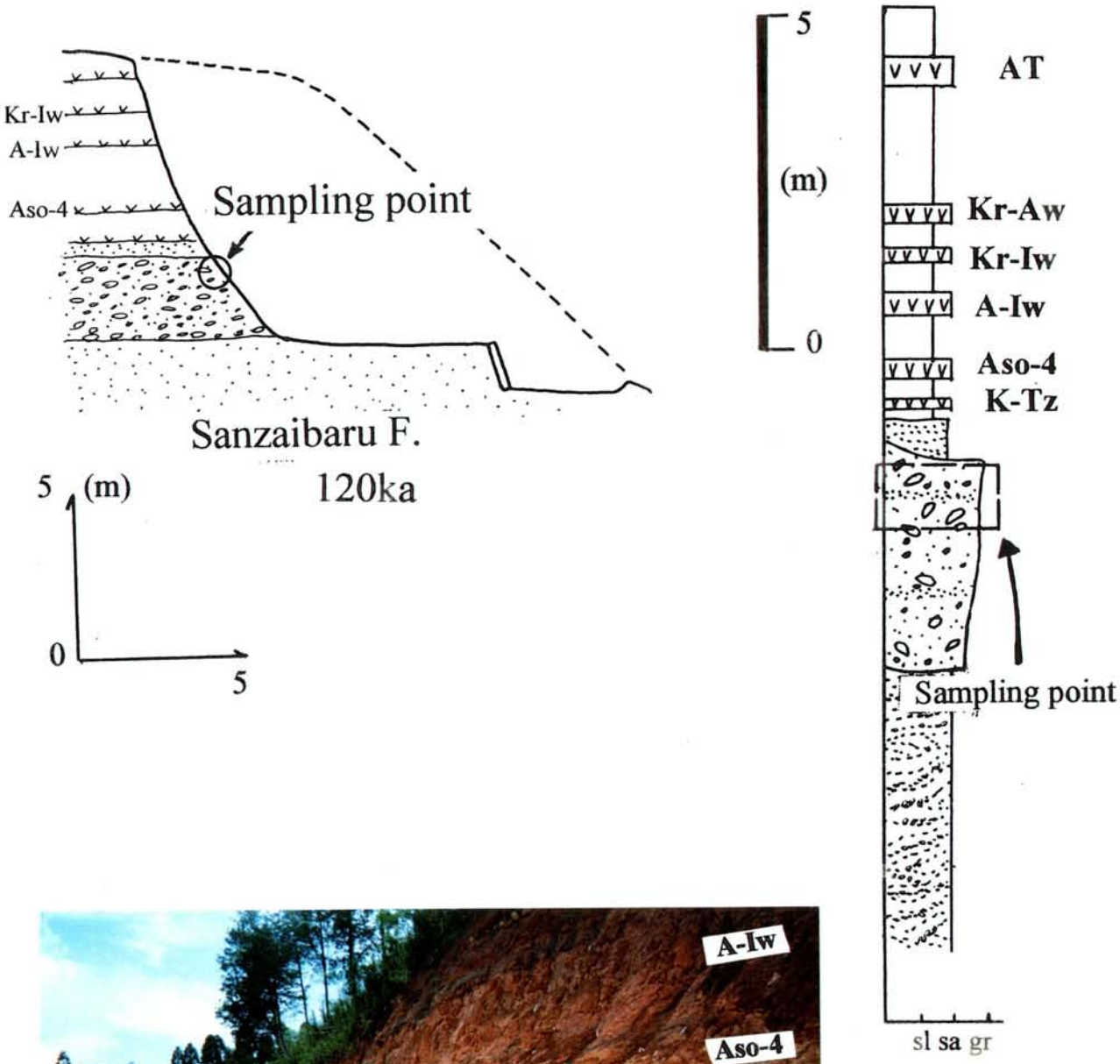

Fig. 22 Outcrop at the Sanzaibaru terrace deposits (120 ka).

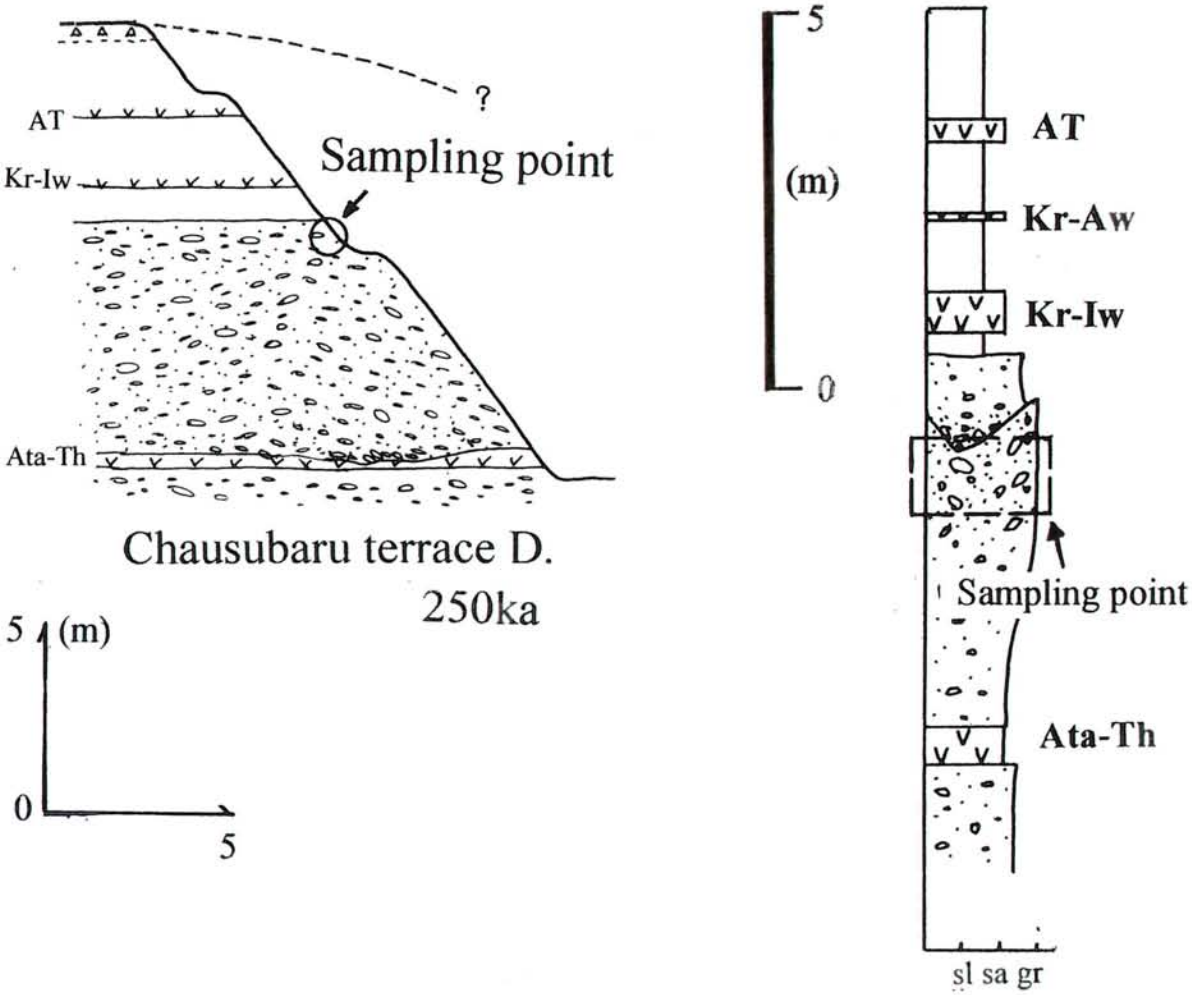

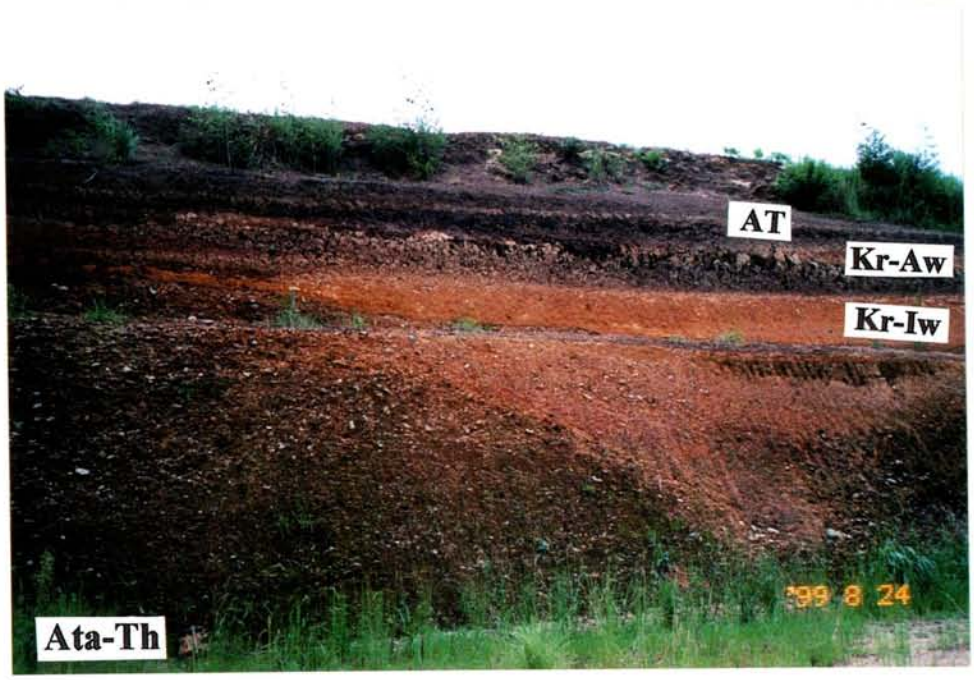

Fig. 23 Outcrop at the Chausubaru terrace deposits (250 ka).

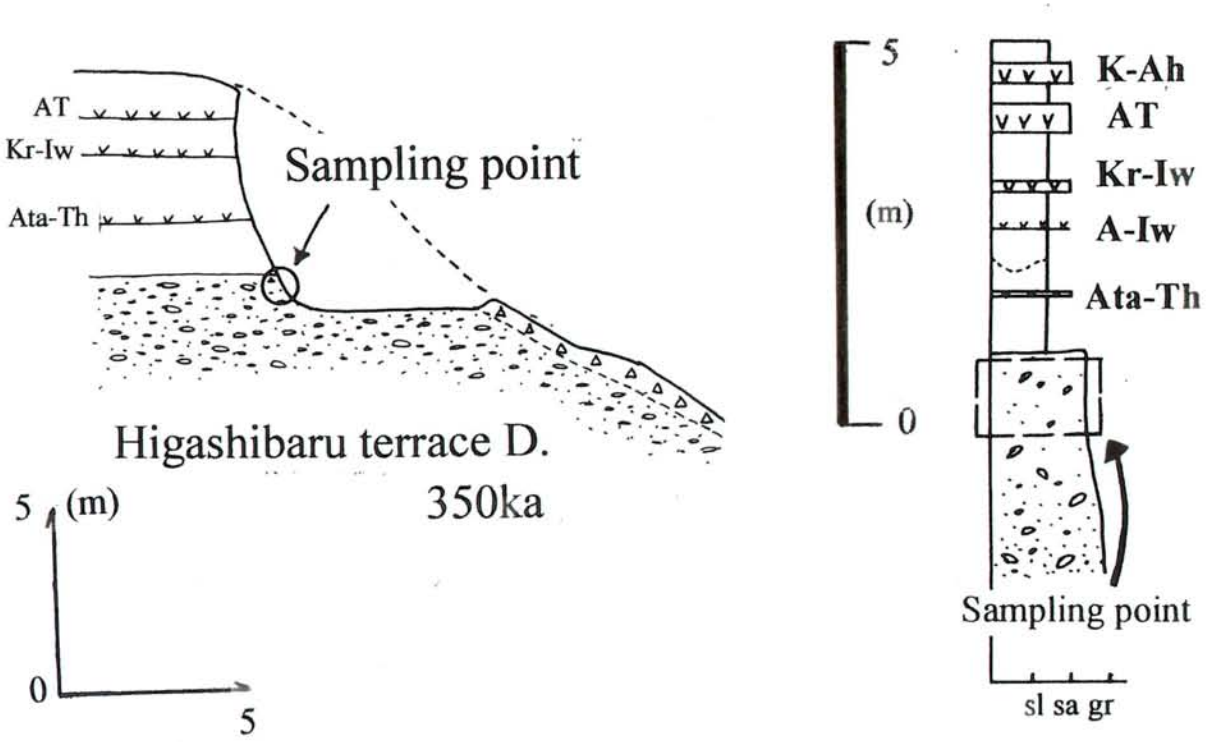

Fig. 24 Outcrop at the Higashibaru terrace deposits (350 ka).

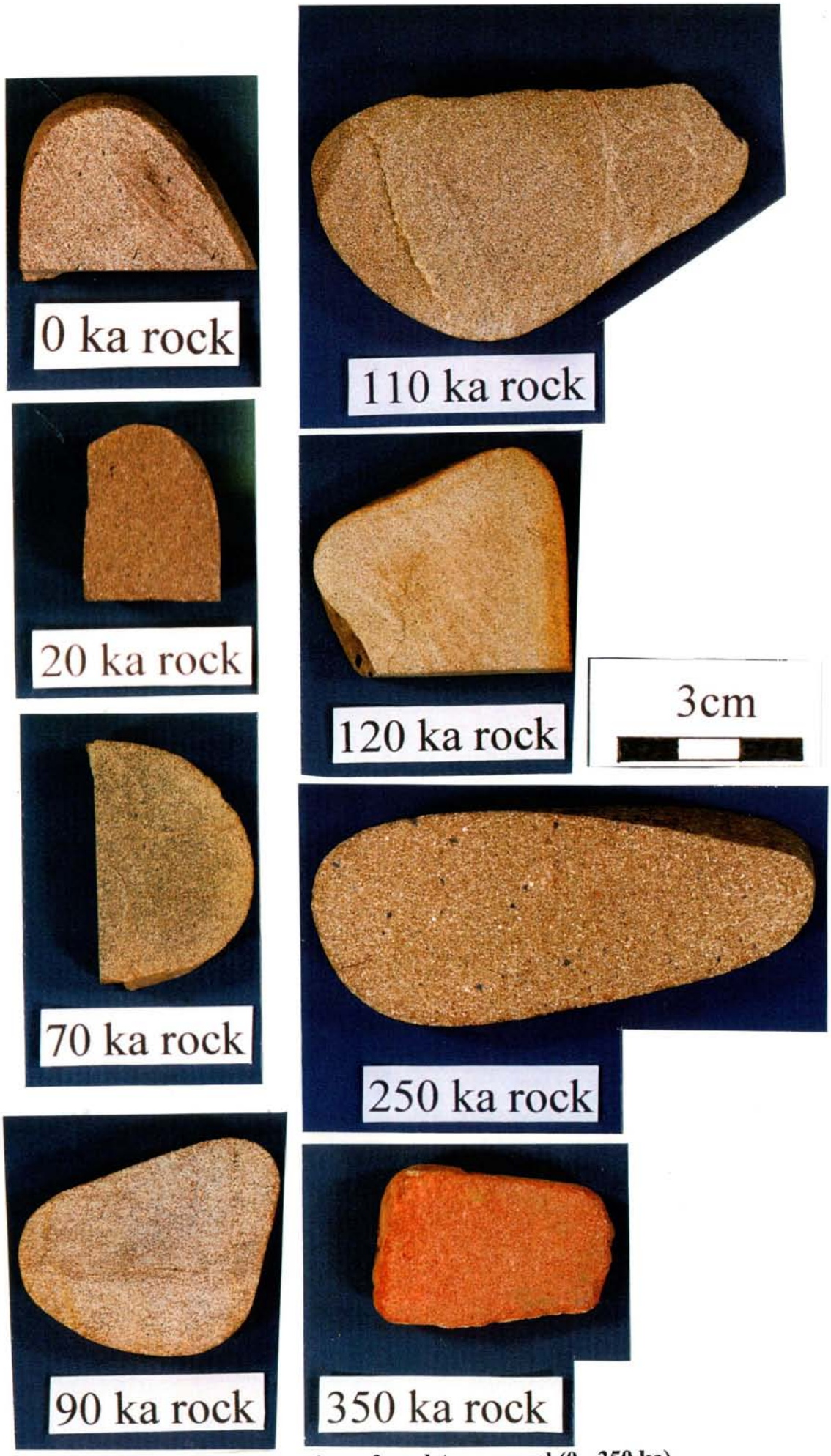

Fig. 25 Cutting surface of sandstone gravel (0 - 350 ka).

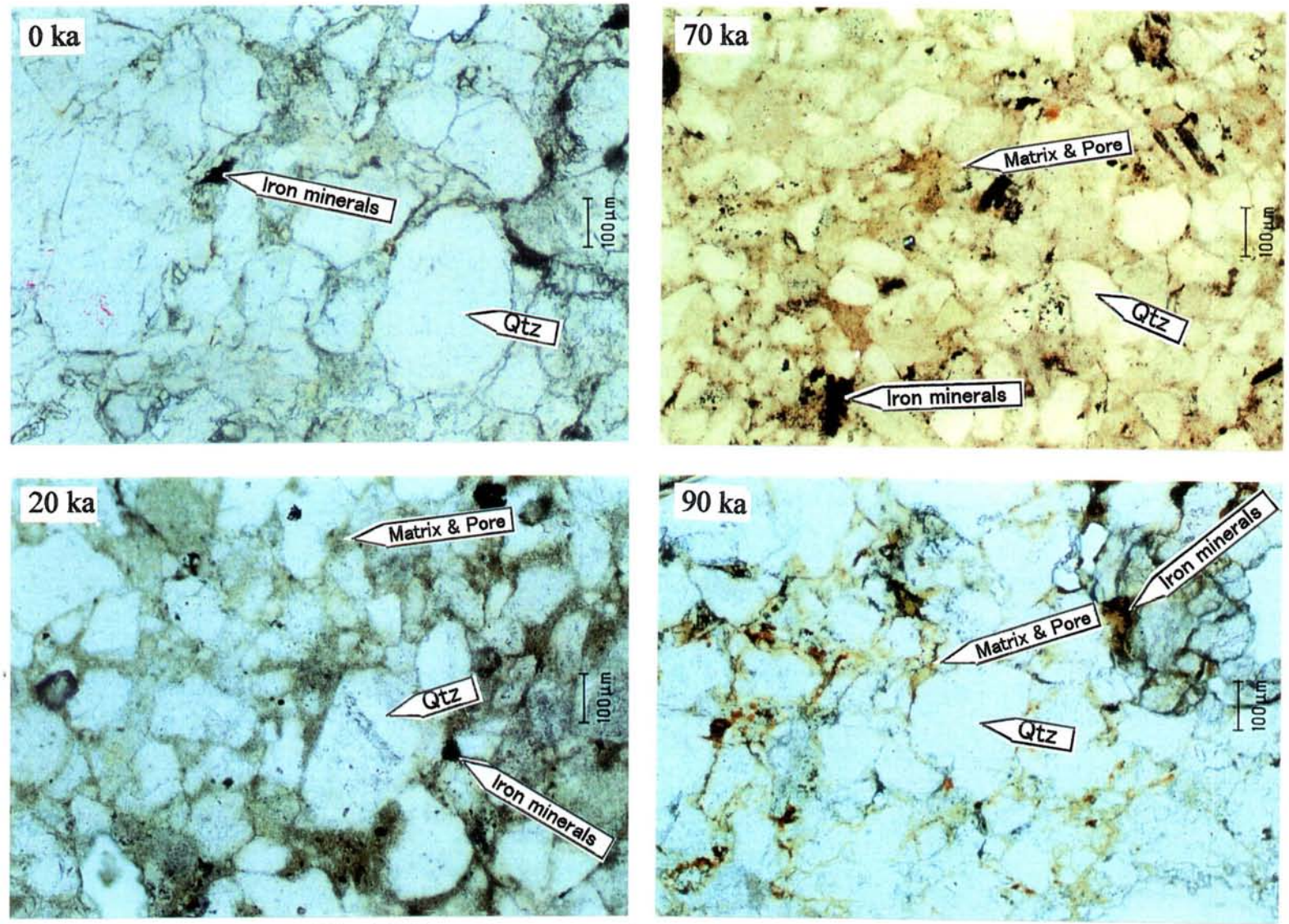

Fig. 26 Photomicrographs of sandstone in thin section (open nicols, 0 - 90 ka).

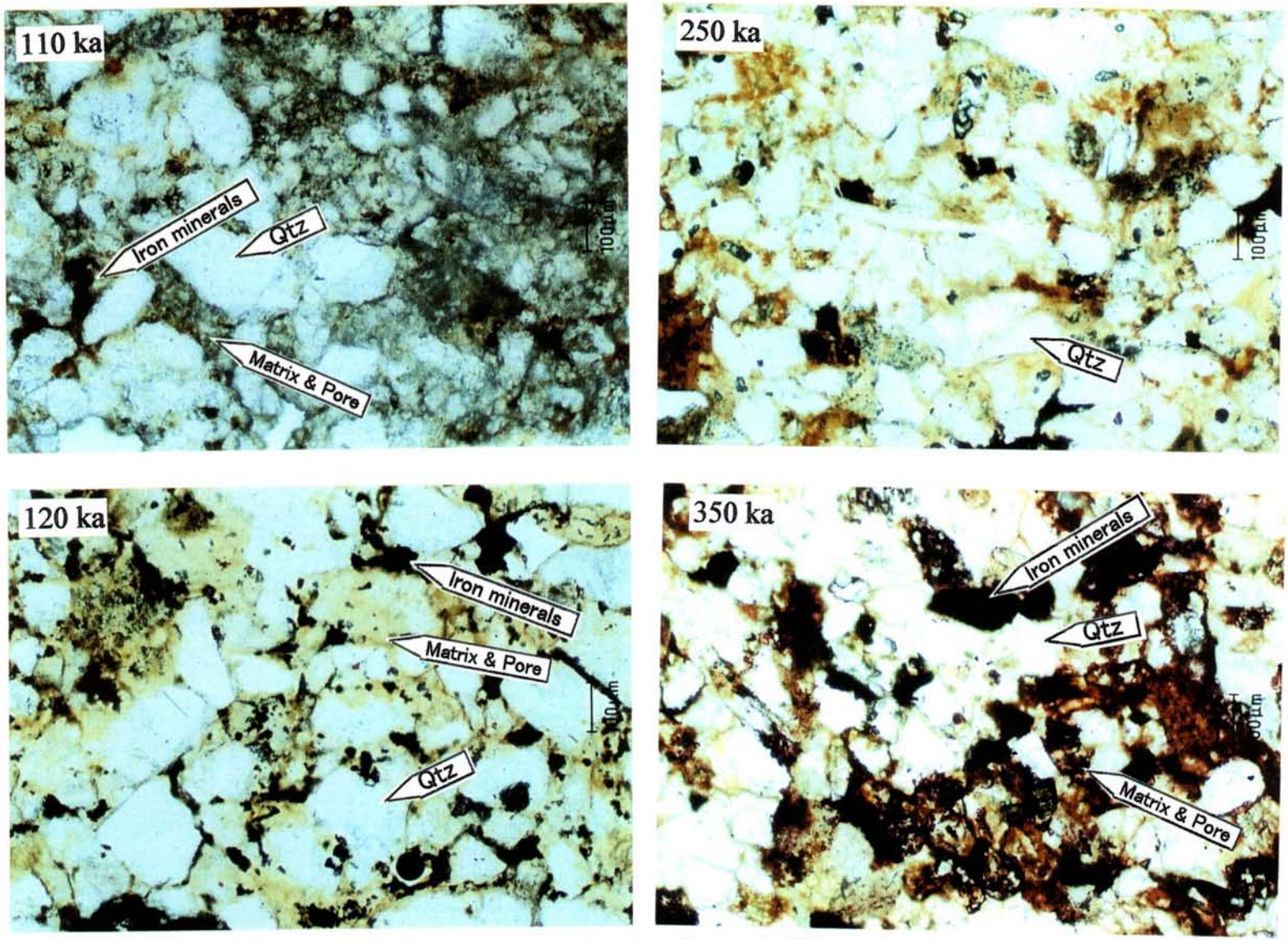

Fig. 27 Photomicrographs of sandstone in thin section (open nicols, 110 - 350 ka).

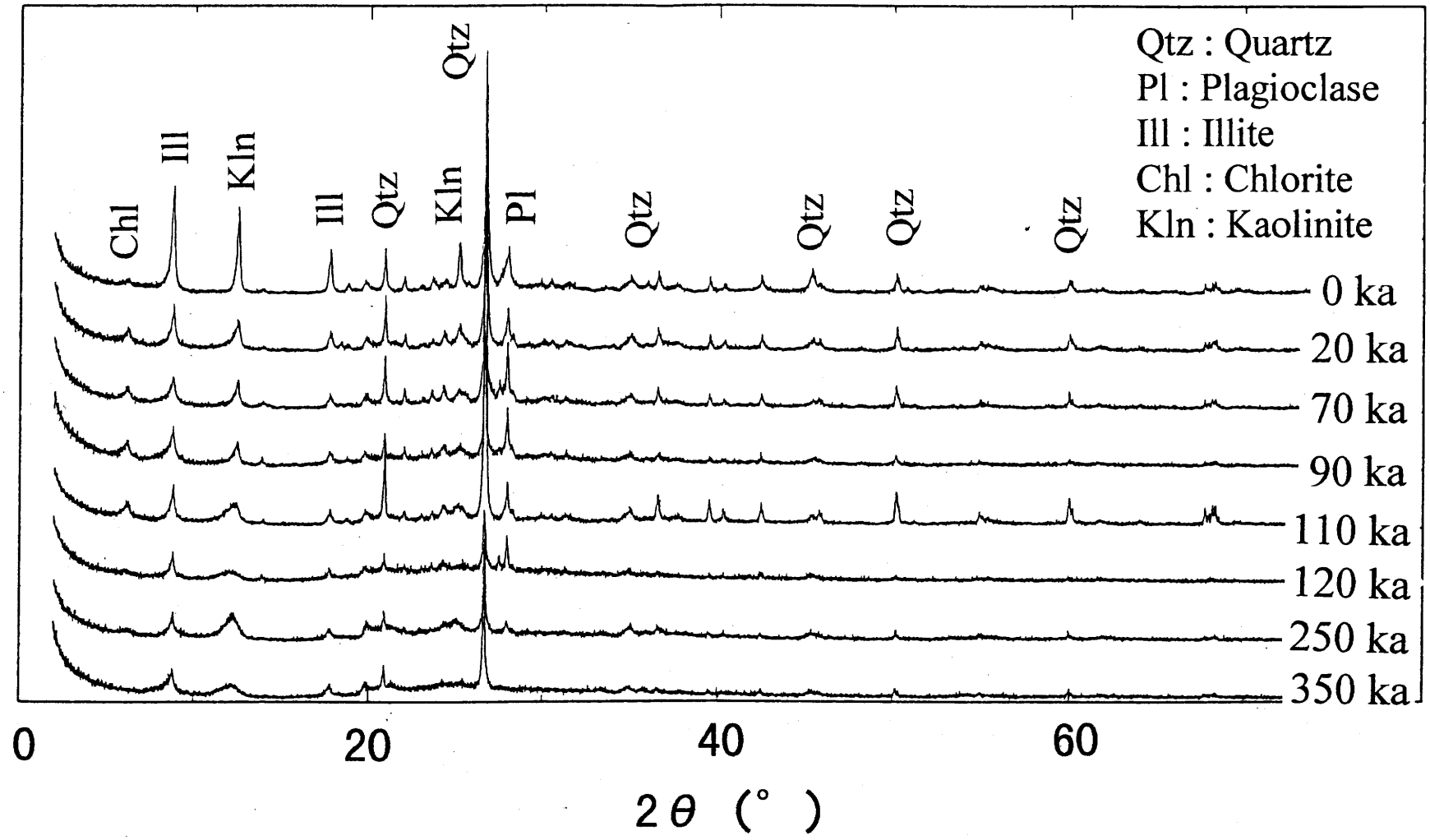

Fig. 28 X-ray diffraction patterns of matrix minerals in sandstone.

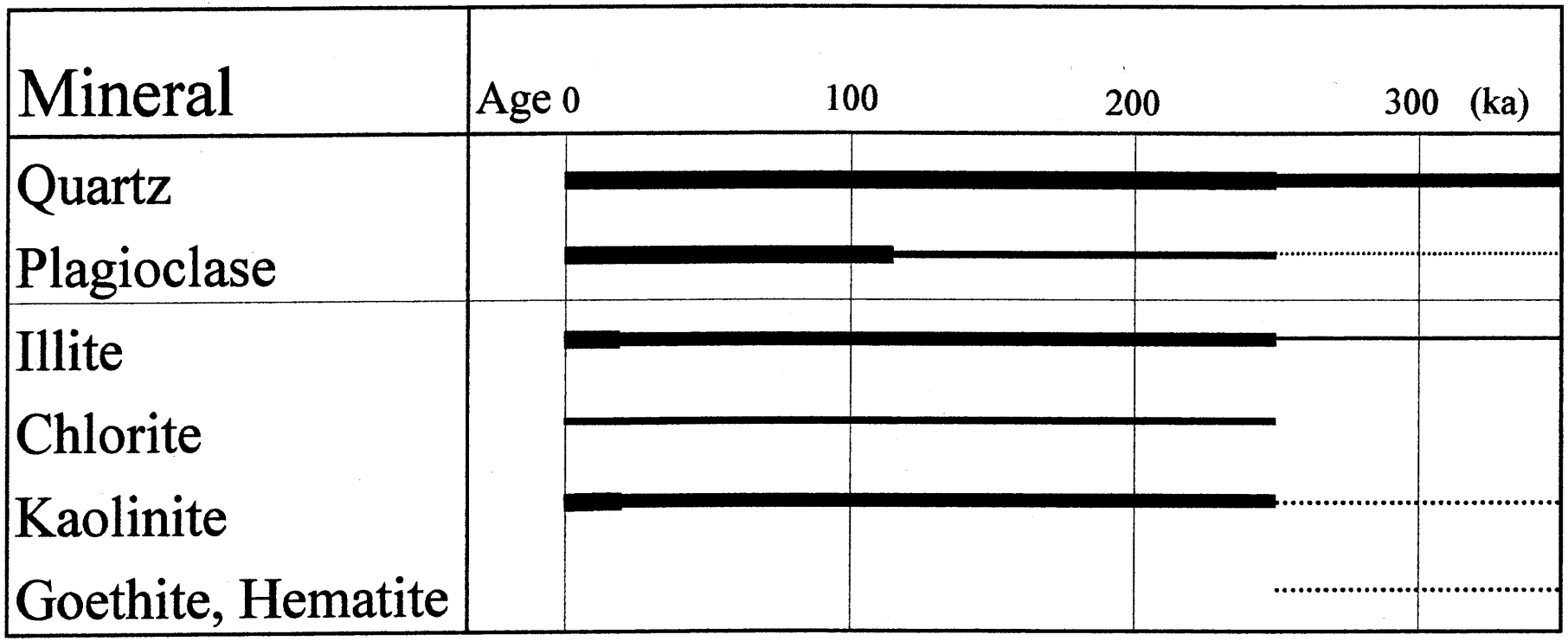

Fig. 29 Changes in matrix minerals during 350 ka using XRD data.

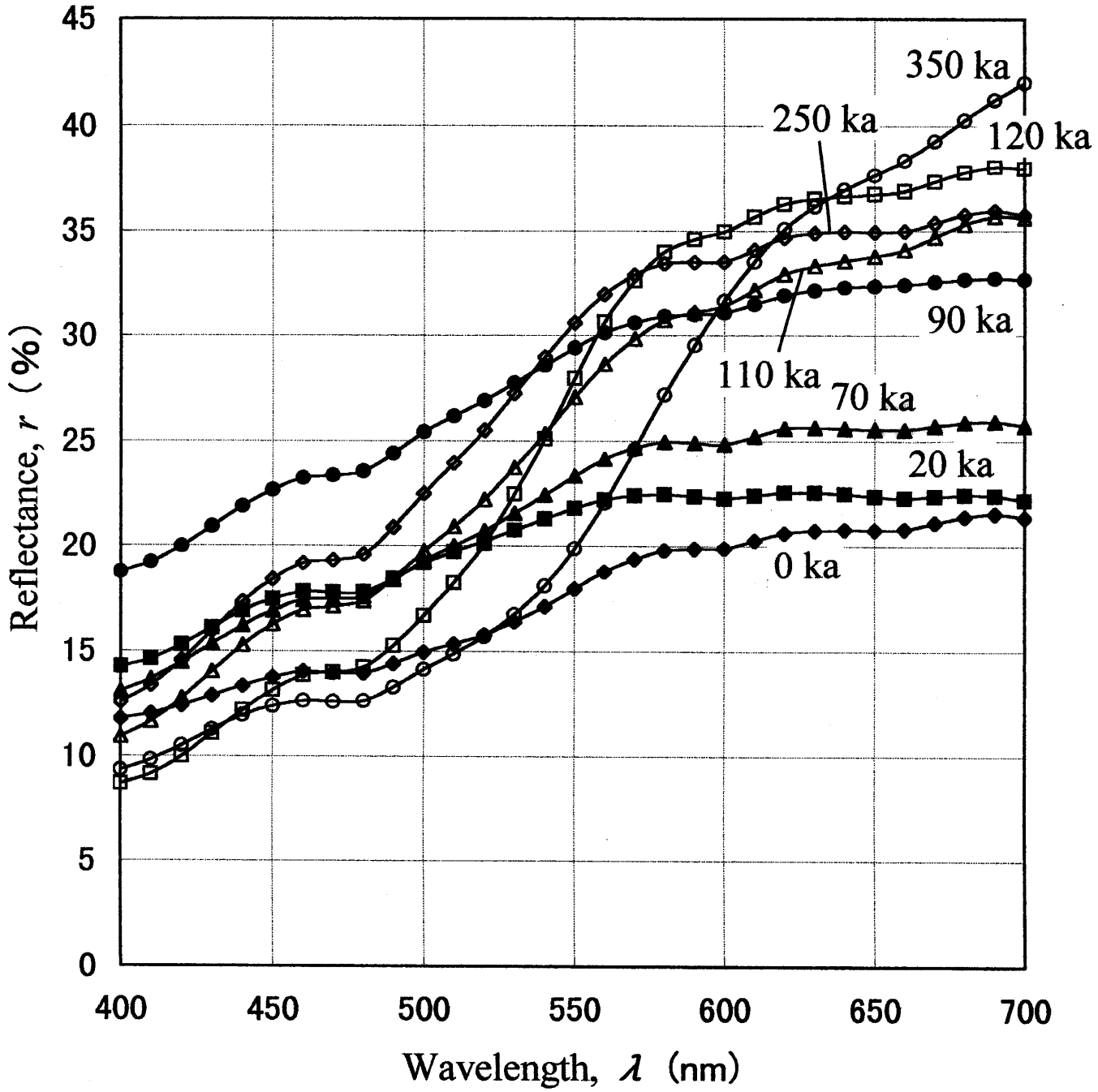

Fig. 30 Temporal changes in visible diffuse reflectance spectra.

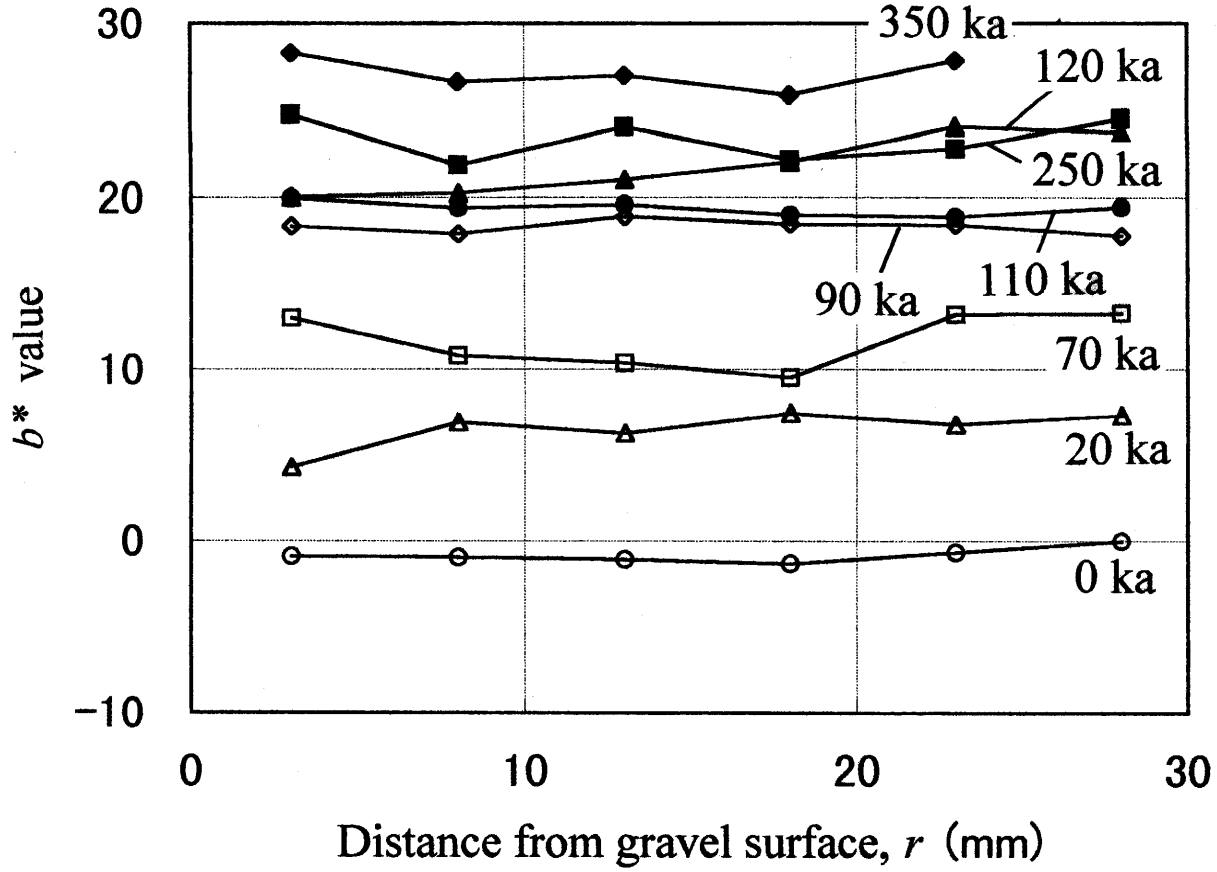

Fig. 31 Distribution of b^*-value measured on cutting surface of gravel.

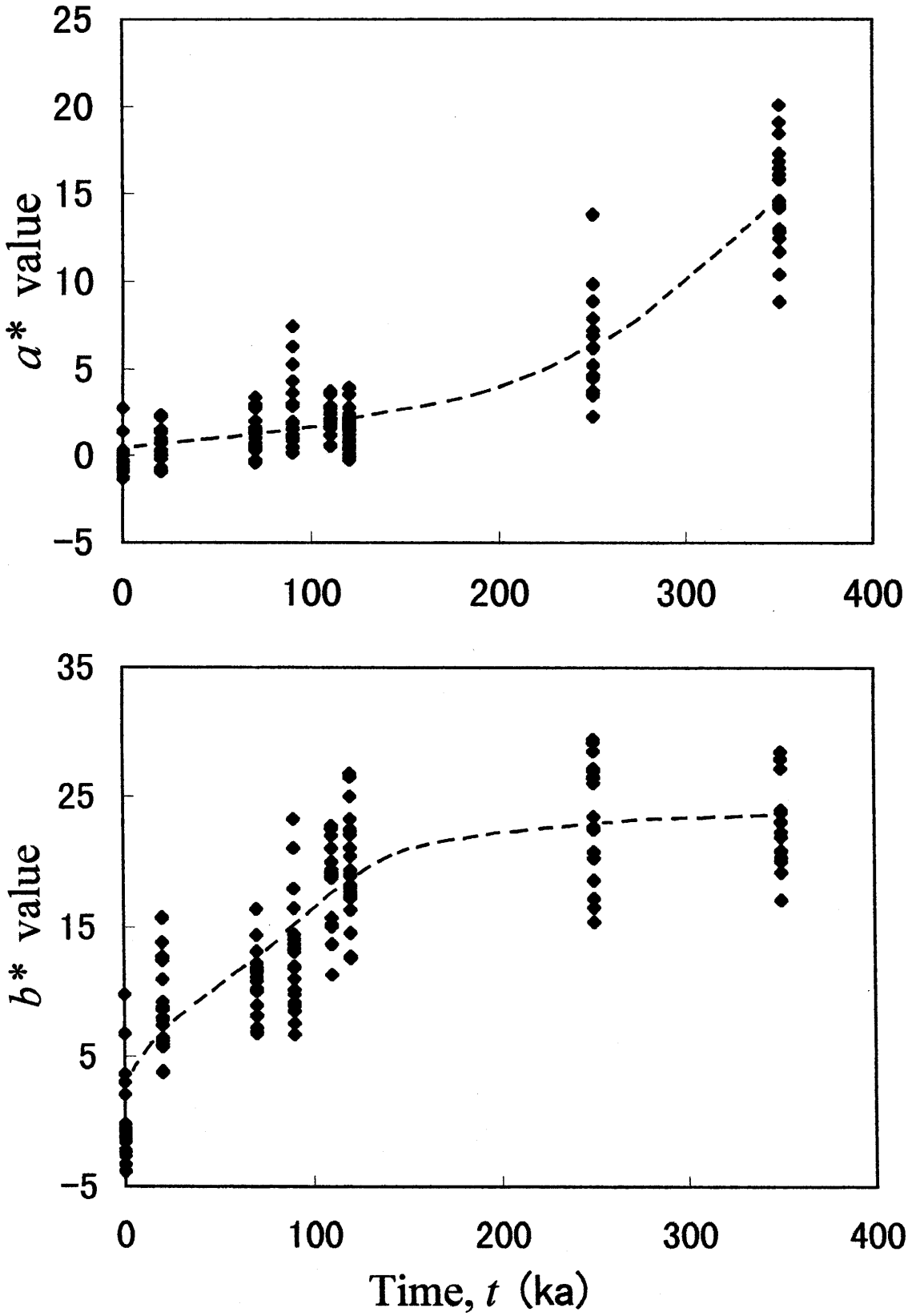

Fig. 32 Temporal changes in colour indices (*a- and *b**- values).**

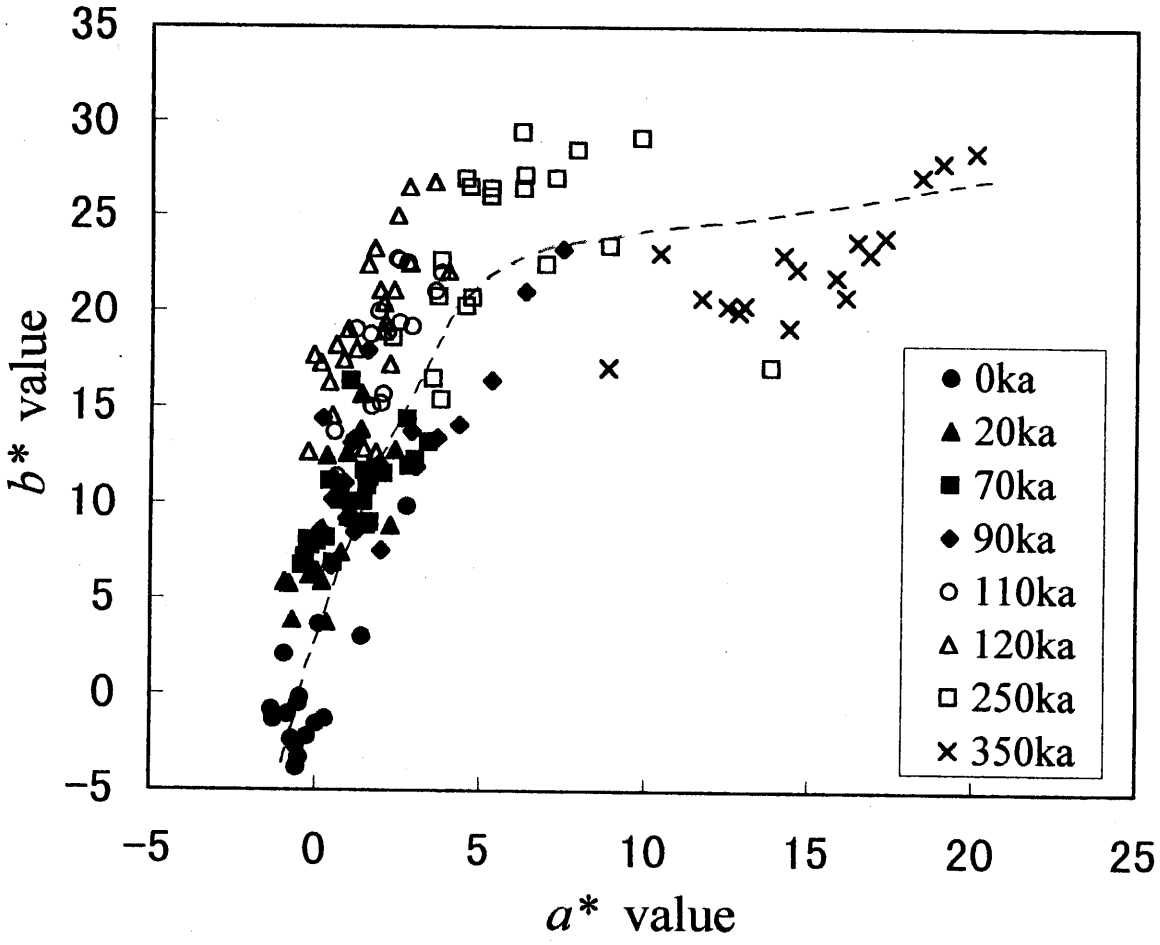

Fig. 33 Data plot on *a- *b** diagram.**

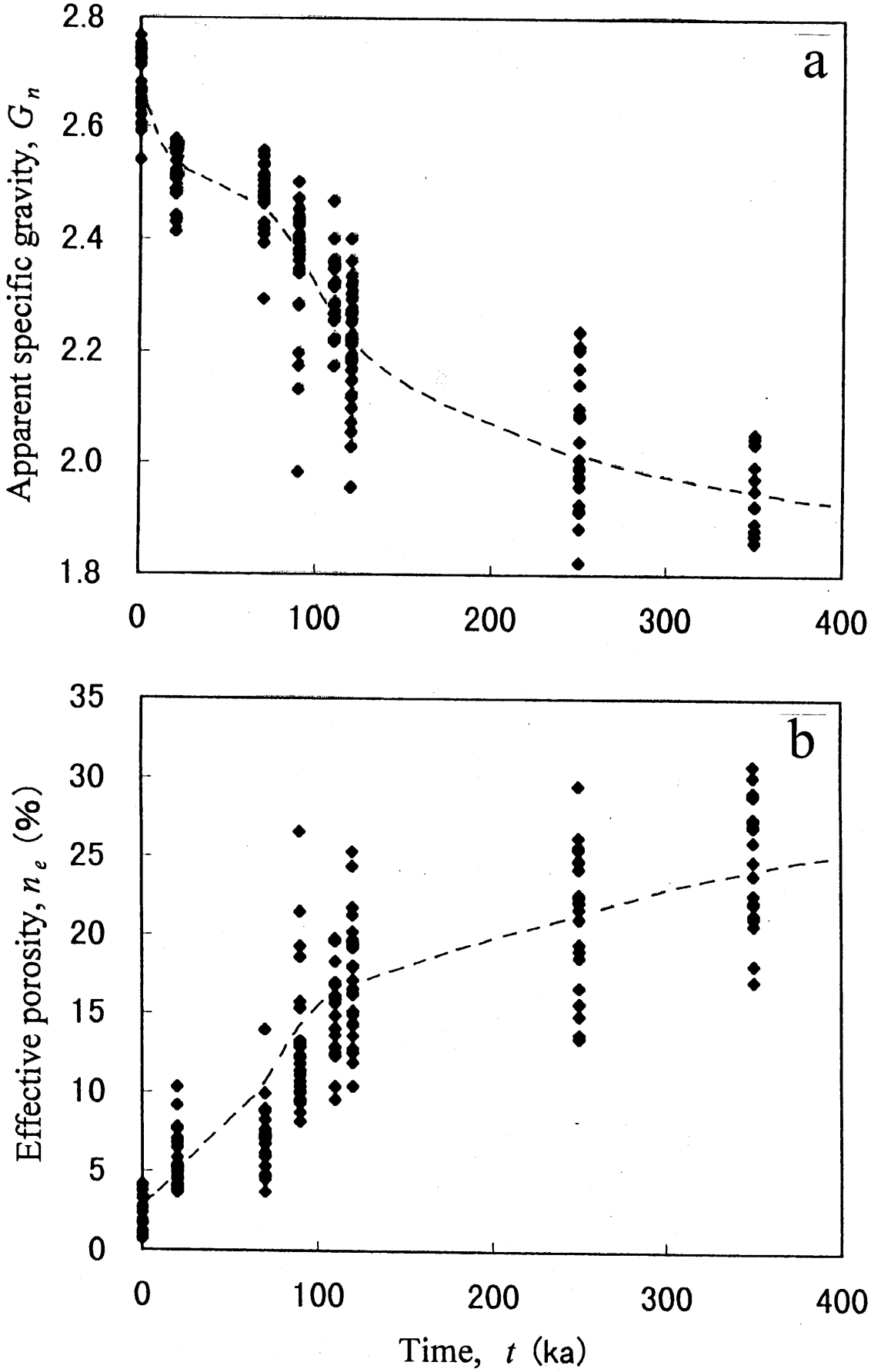

Fig. 34 Temporal changes in specific gravity, G_n (a), and effective porosity, n_e (b).

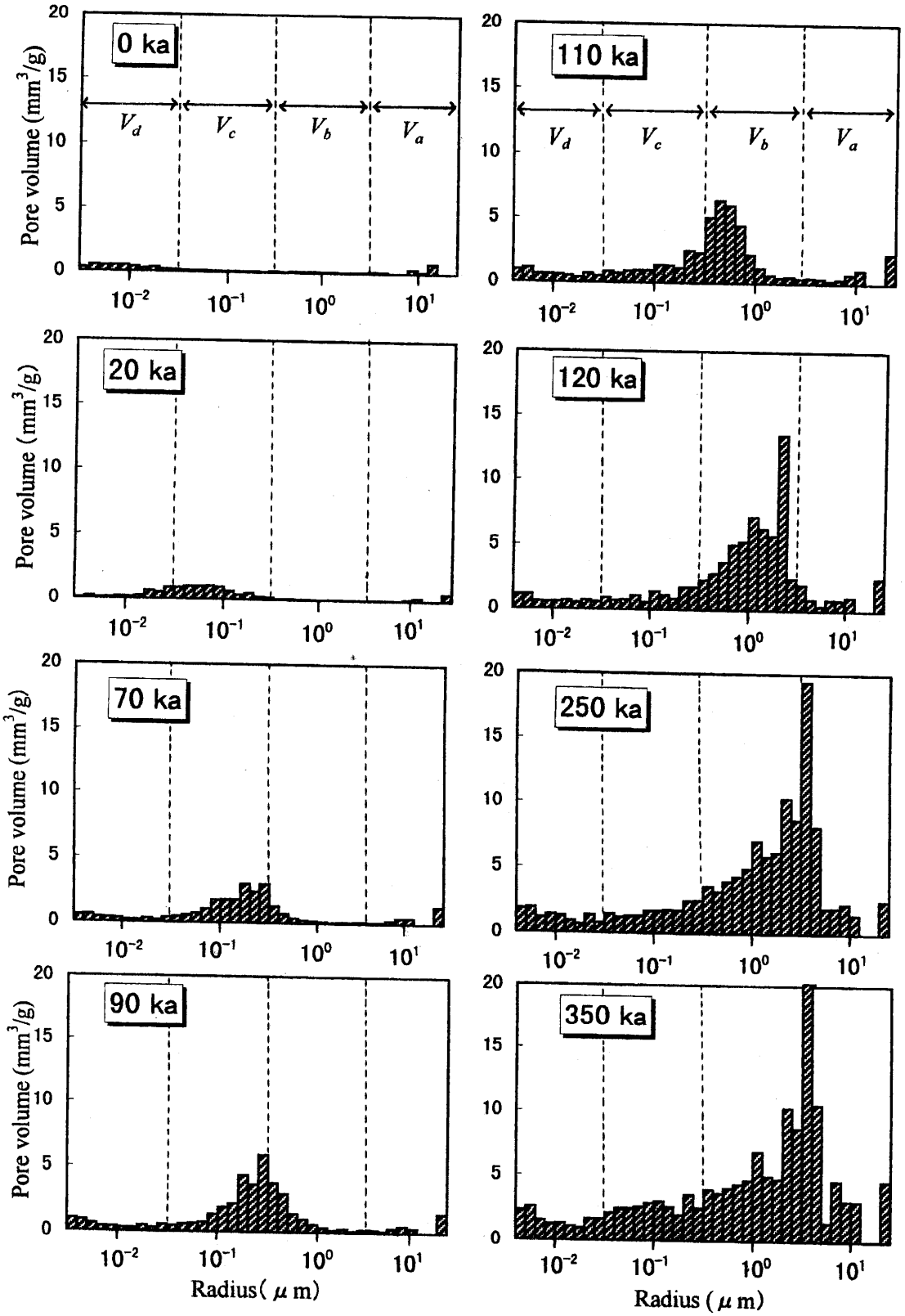

Fig. 35 Histograms of pore size distribution measured by the mercury intrusion porosimeter.

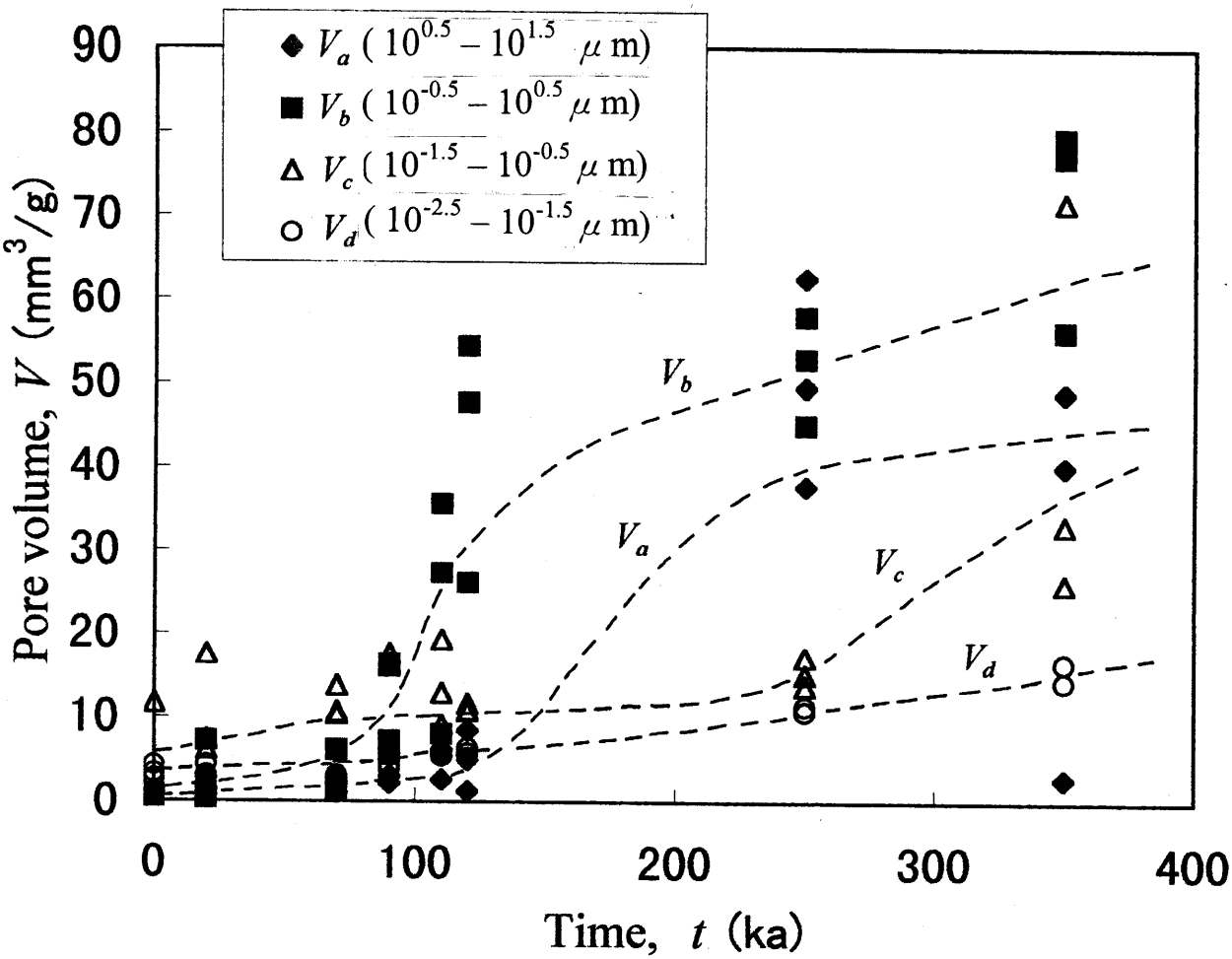

Fig. 36 Temporal changes in pore volume for four sub-ranges of pore size.

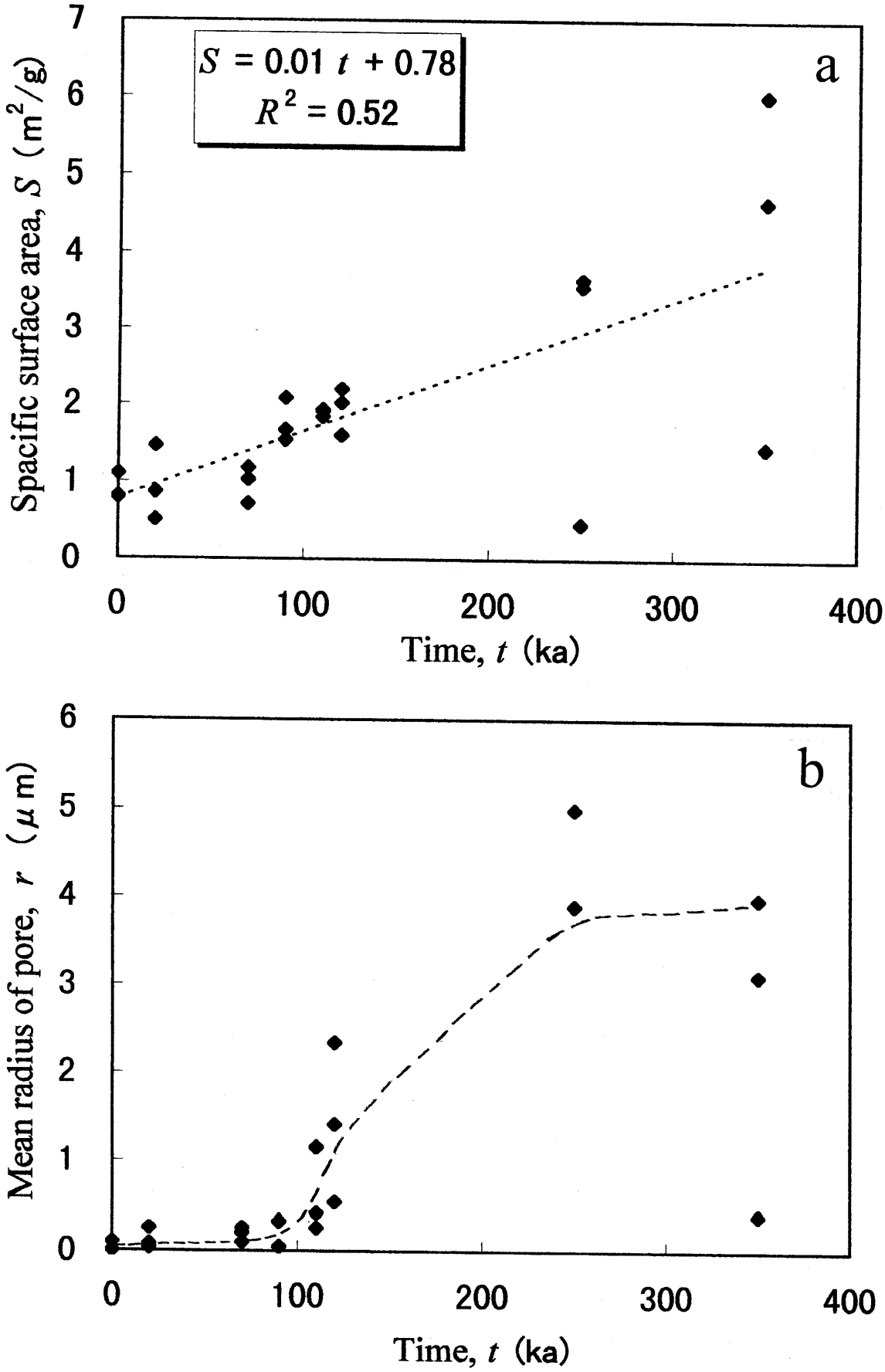

Fig. 37 Temporal changes in specific surface area, *S* (a), and mean pore radius, *r* (b).

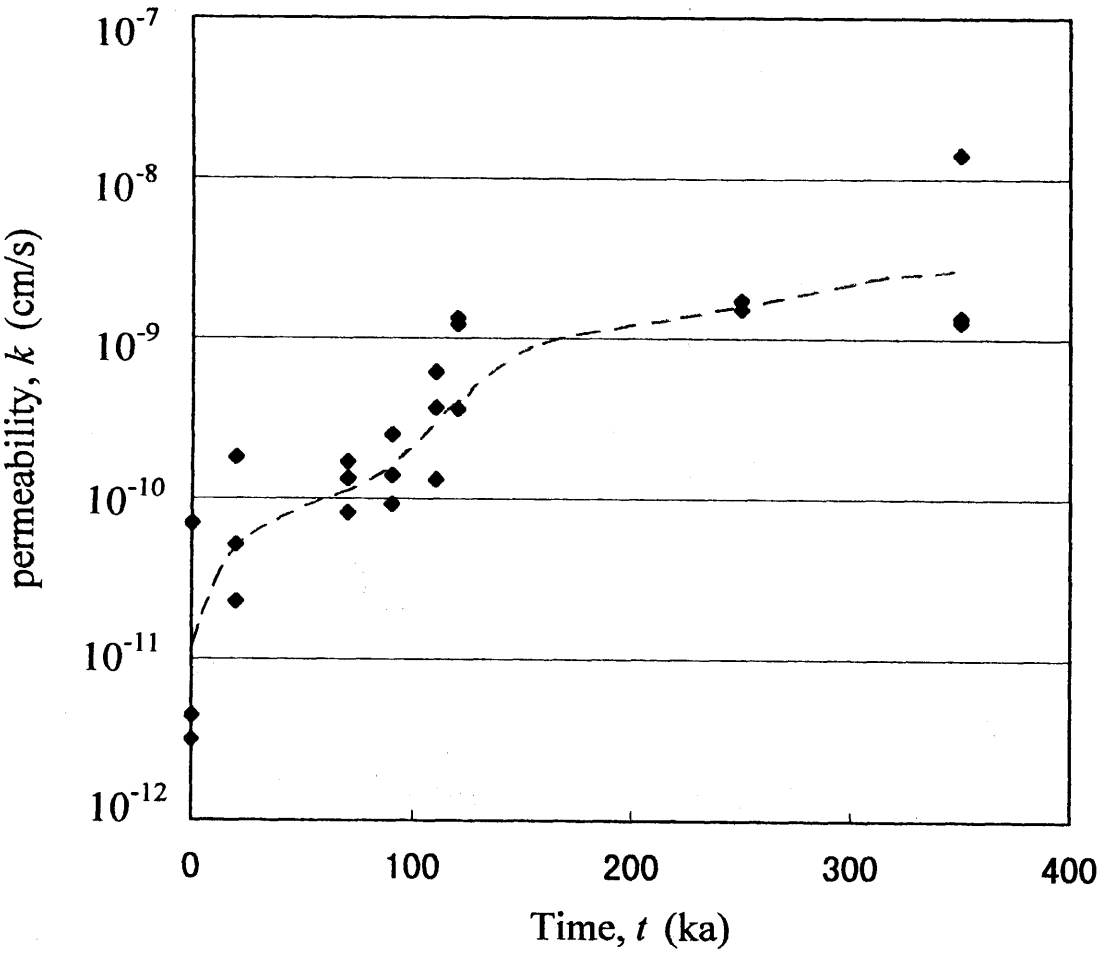

Fig. 38 Temporal changes in permeability using PSD data.

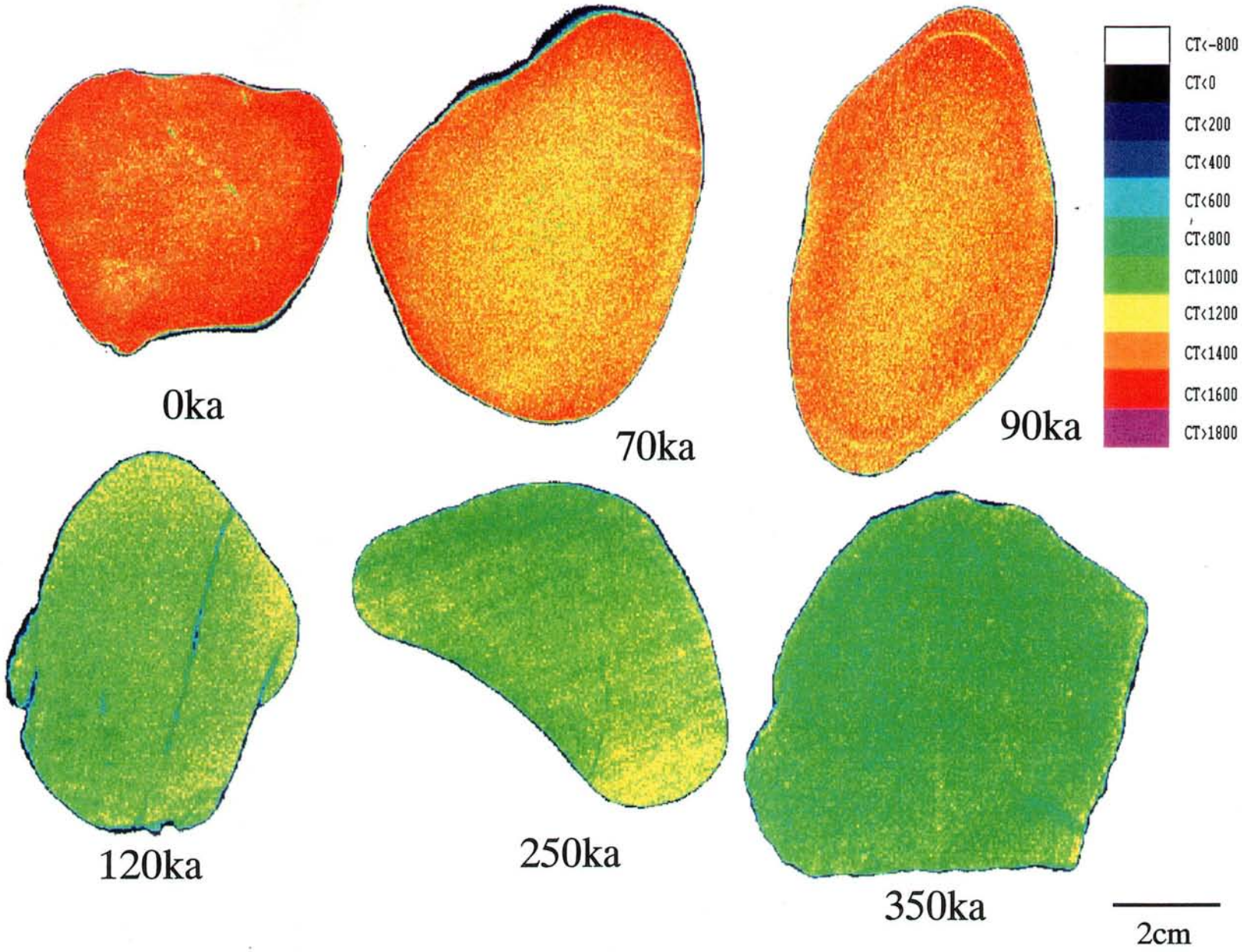

Fig.39 Typical examples of X-ray CT images of sandstone gravel.

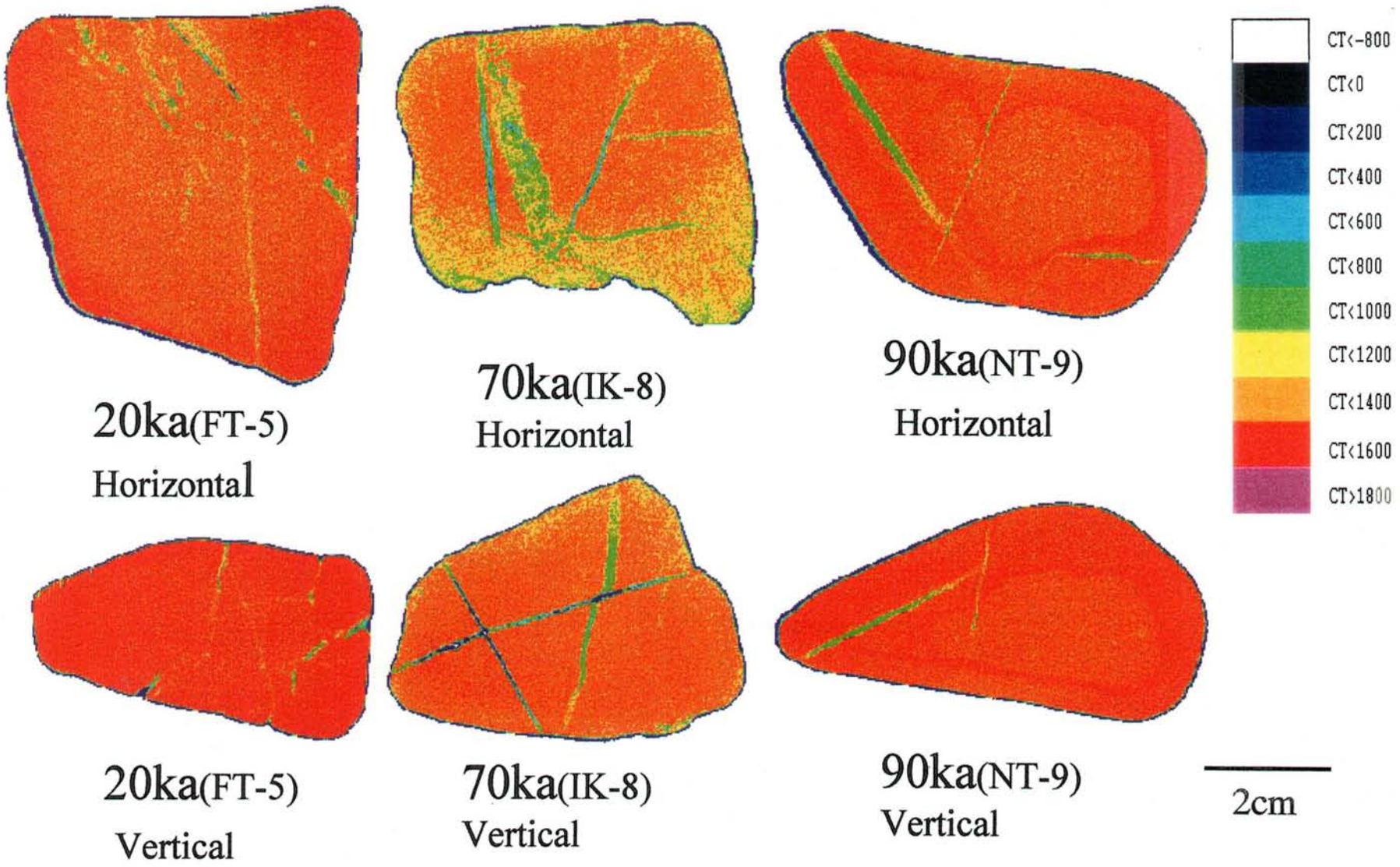

Fig. 40 X-ray CT images of sandstone gravels included cracks.

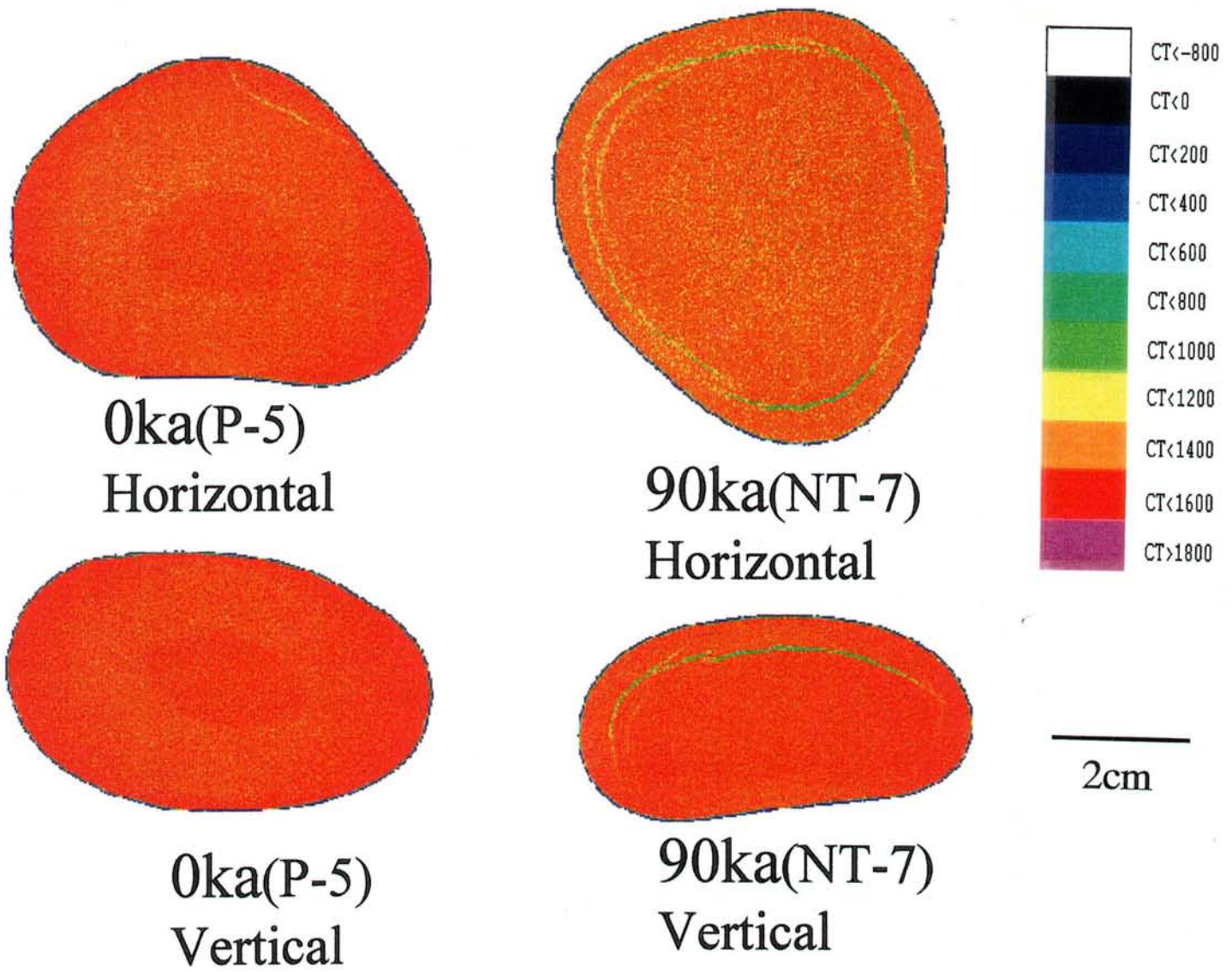

Fig. 41 X-ray CT images of sandstone gravels with weathering rinds.

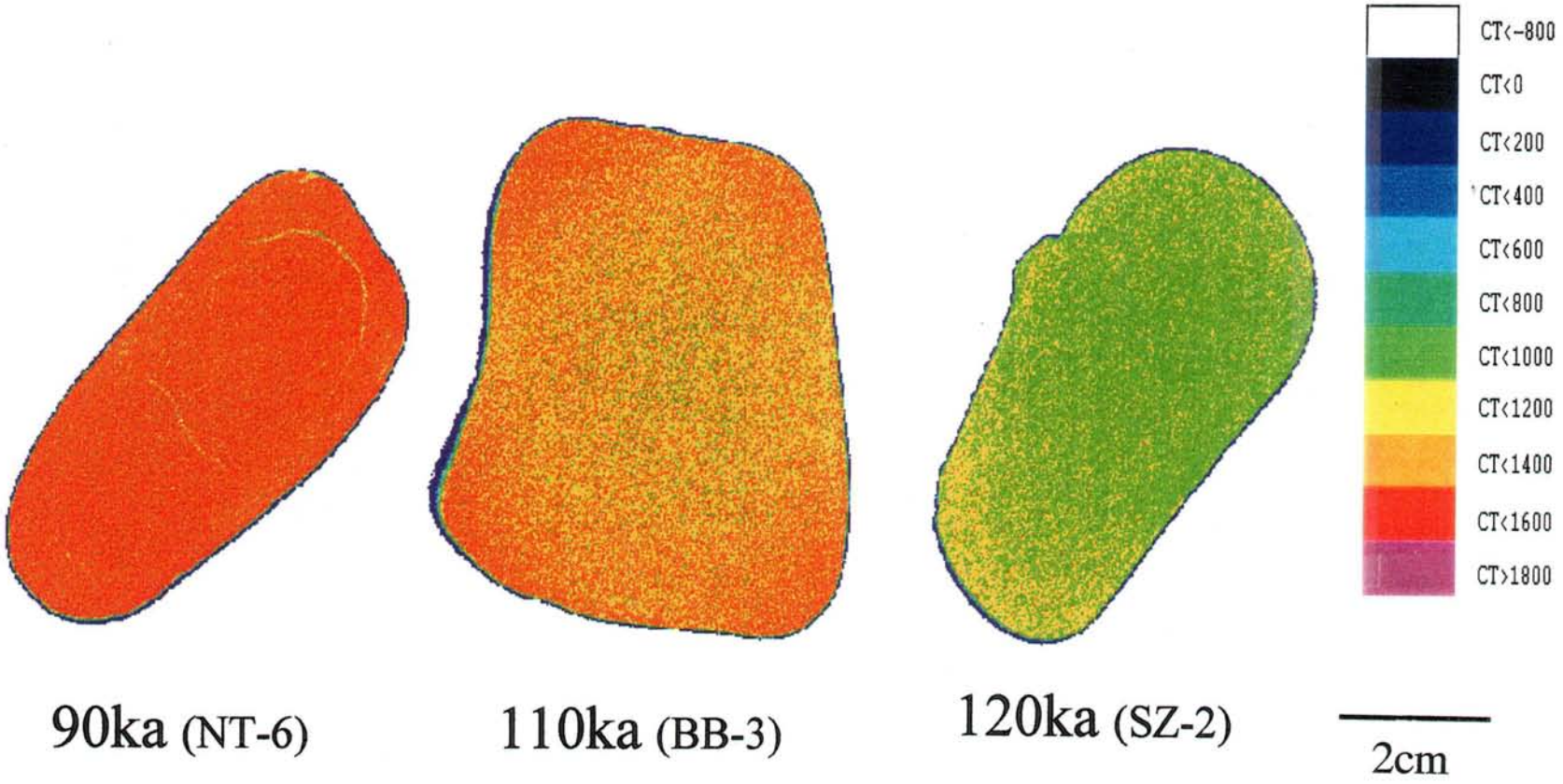

Fig. 42 Changes in X-ray CT images during 90 to 120 ka.

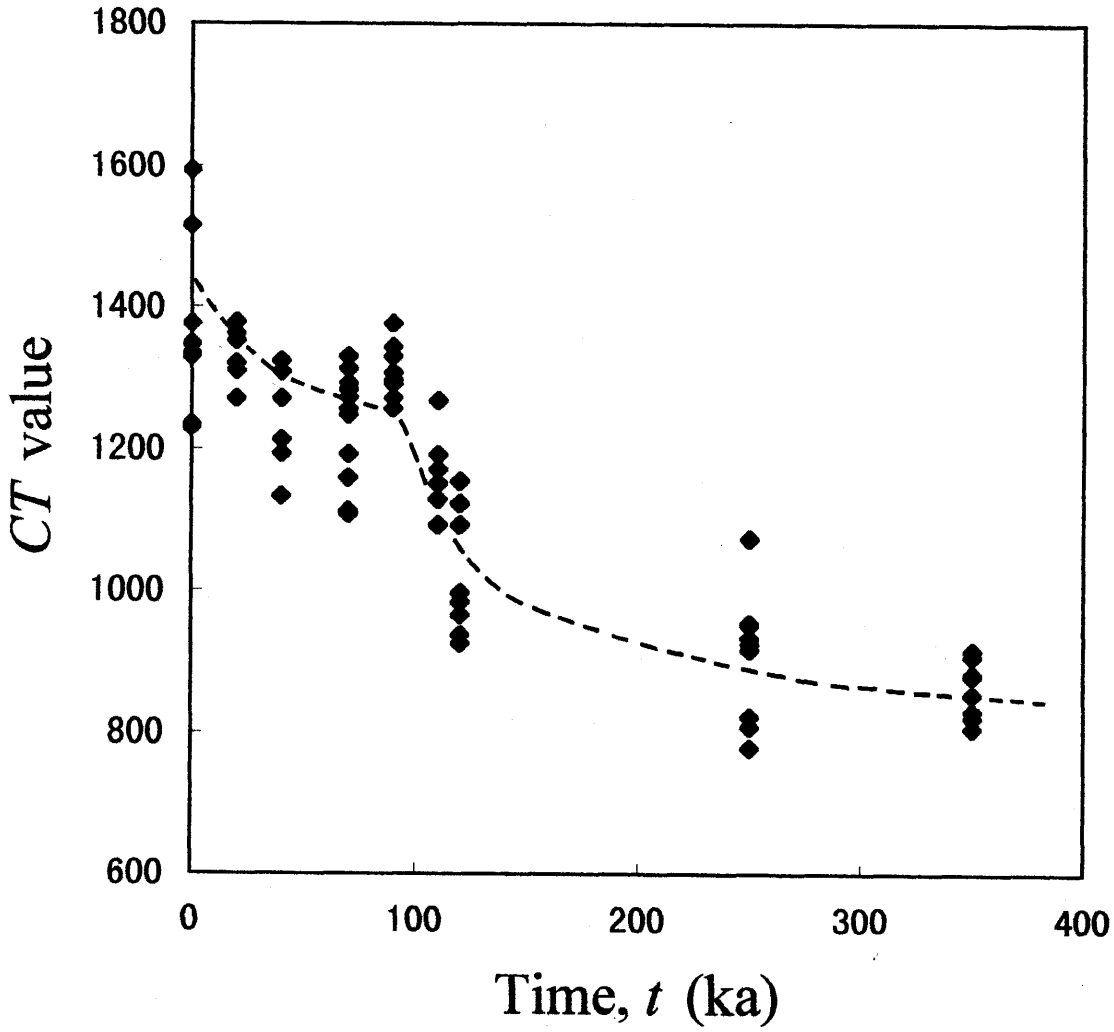

Fig. 43 Temporal changes in mean CT value, CT_m.

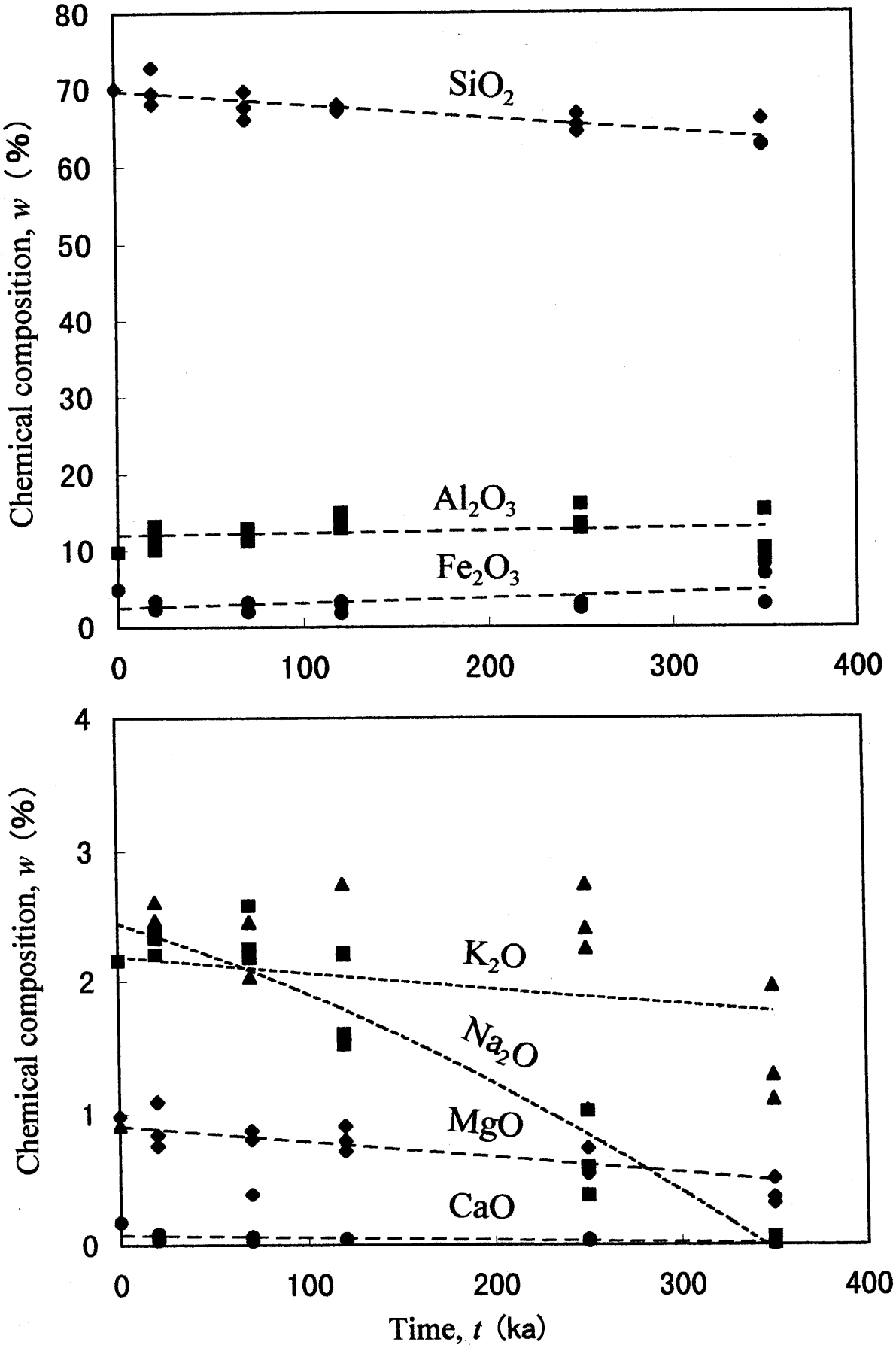

Fig. 44 Temporal changes in chemical composition.

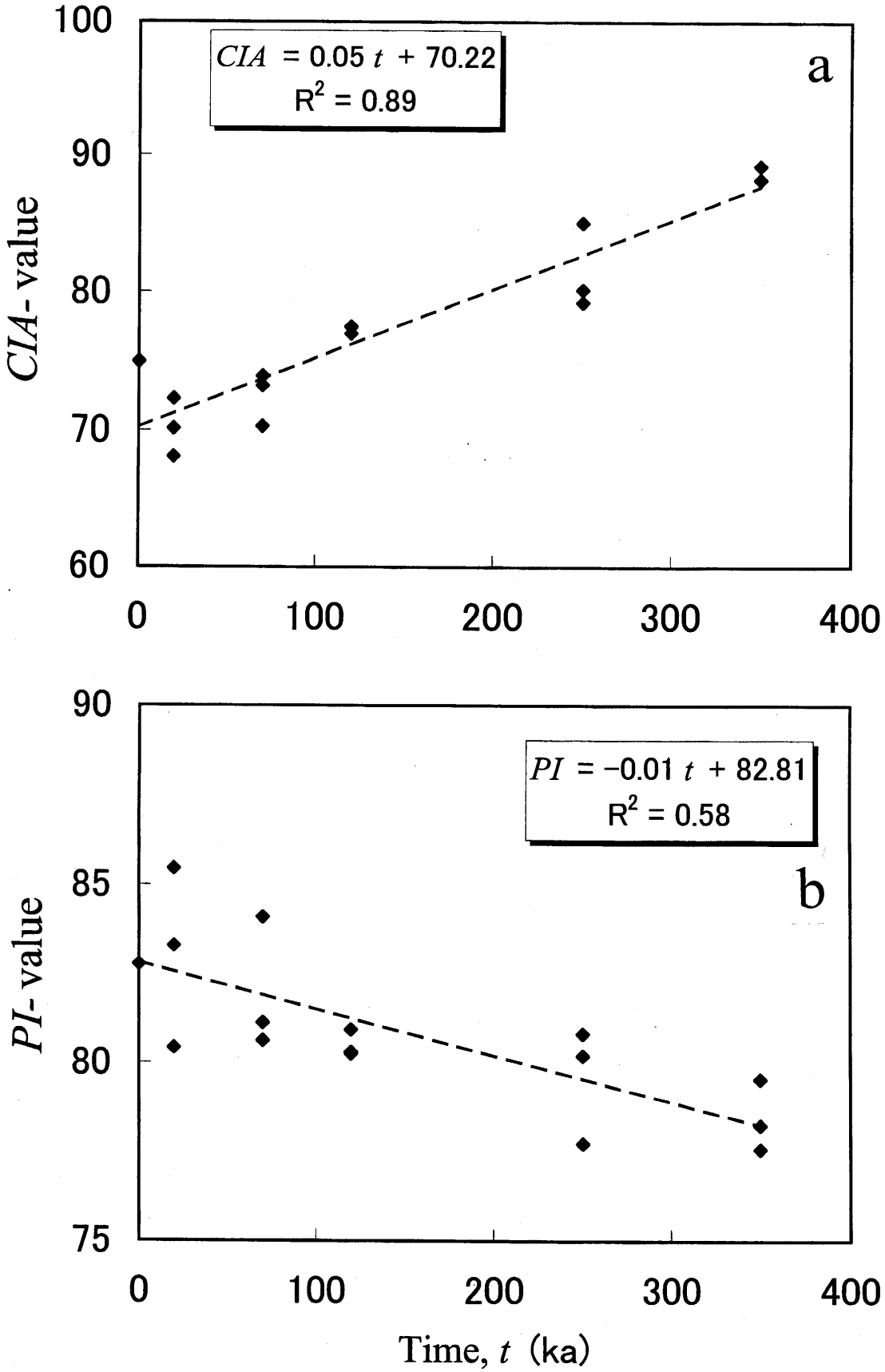

Fig. 45 Temporal changes in chemical weathering indices (*CIA* and *PI* values).

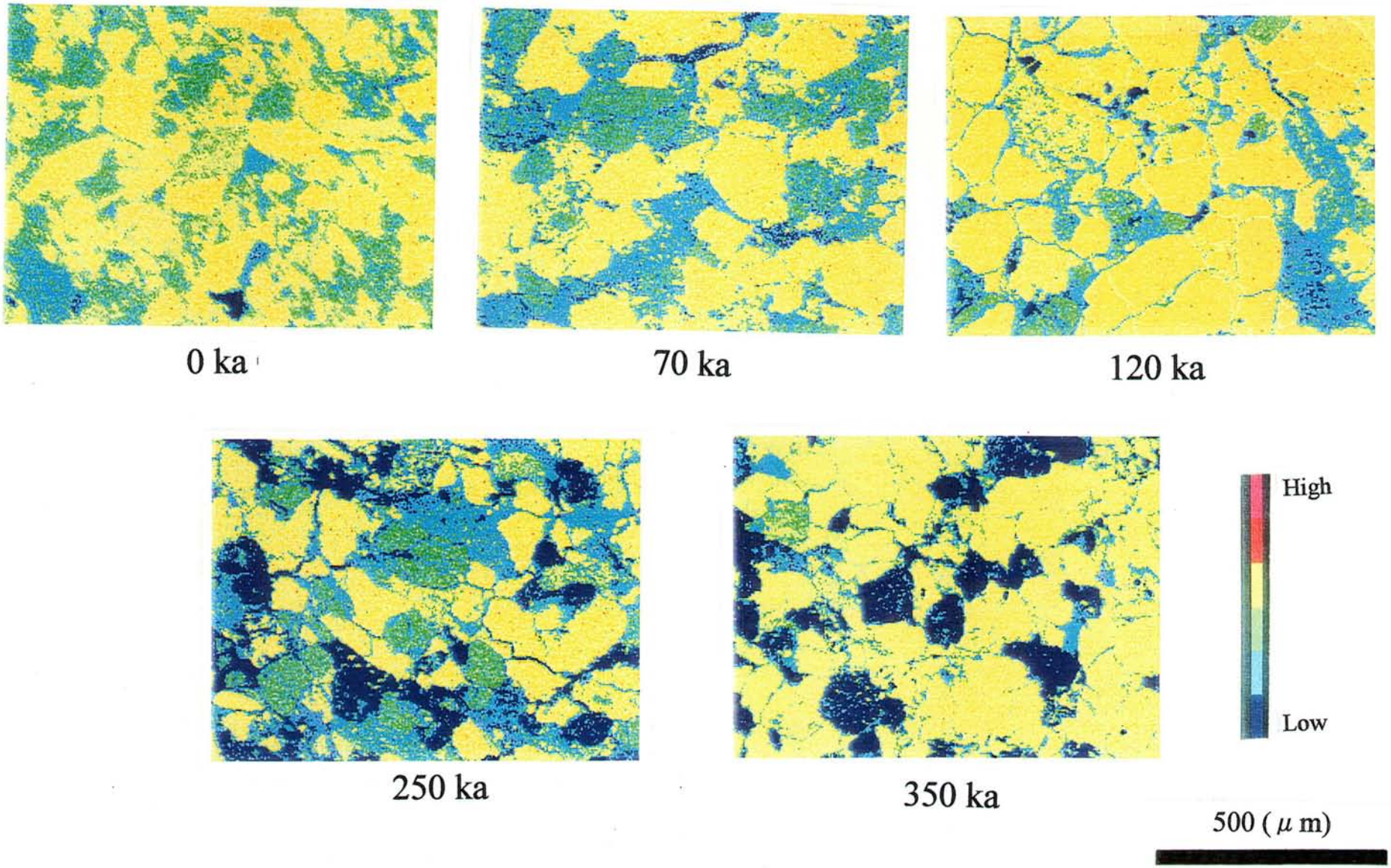

Fig. 46 Changes in Si concentration constructed by EDS.

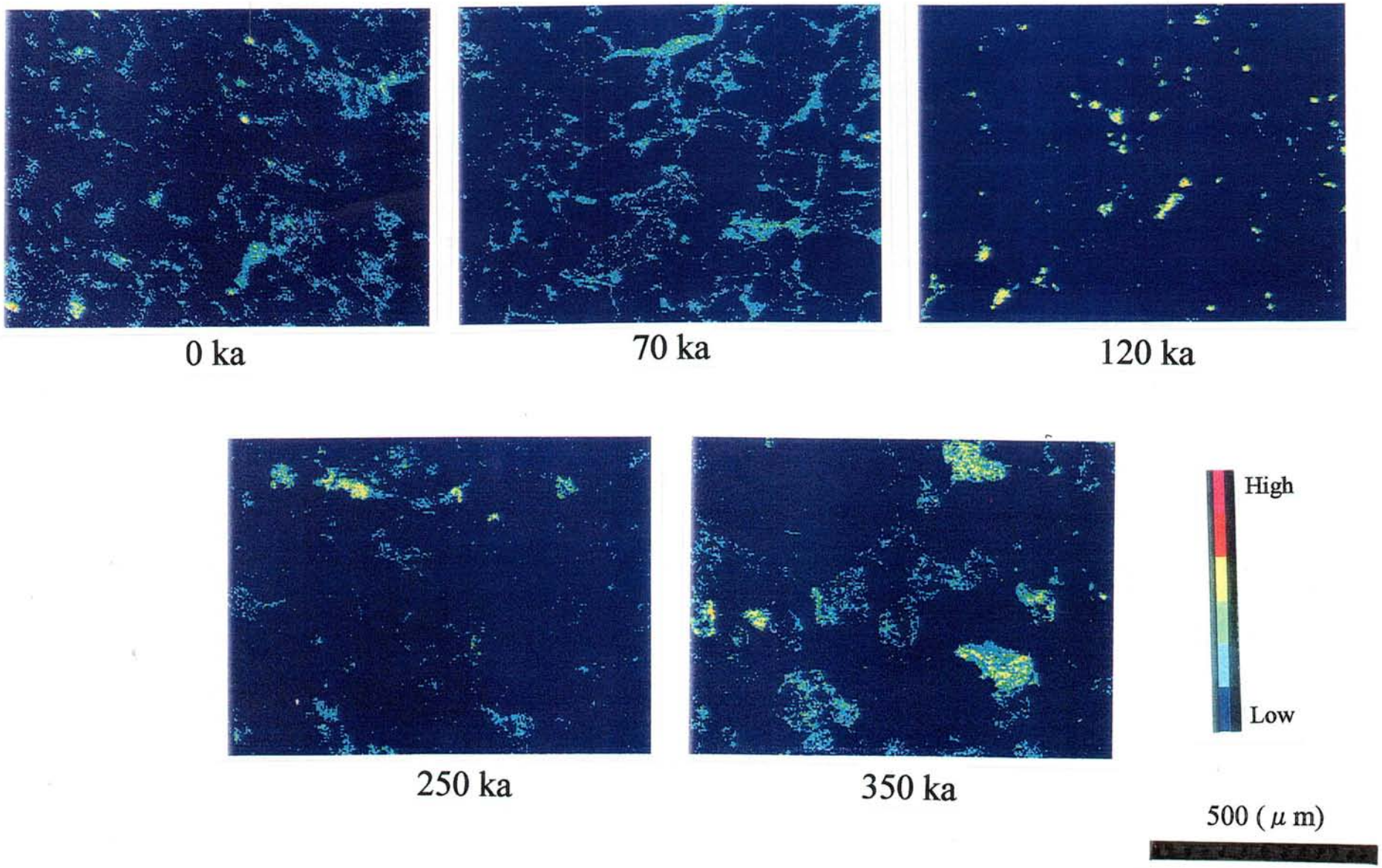

Fig. 47 Changes in Fe concentration constructed by EDS.

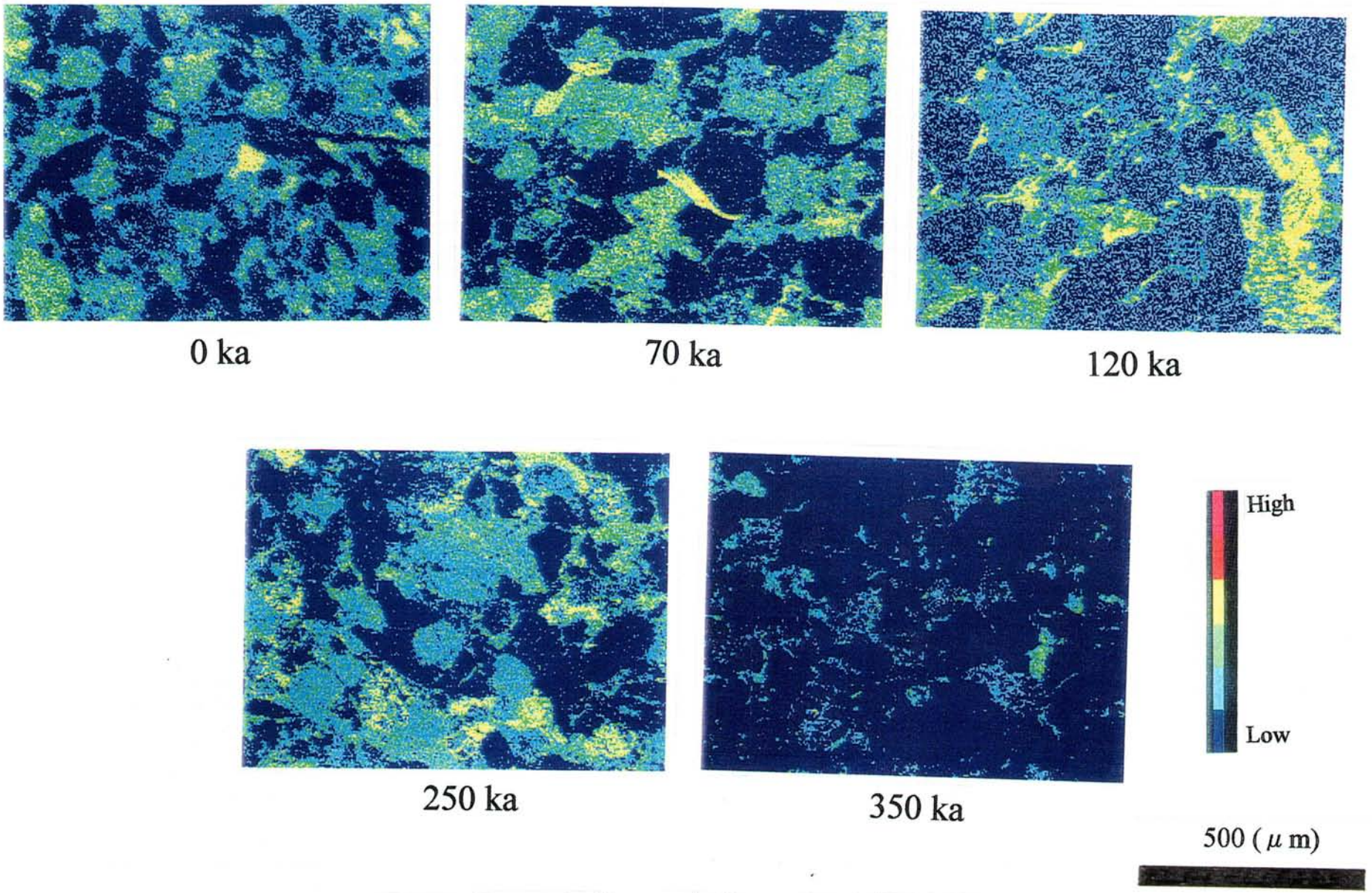

Fig. 48 Changes in Al concentration constructed by EDS.

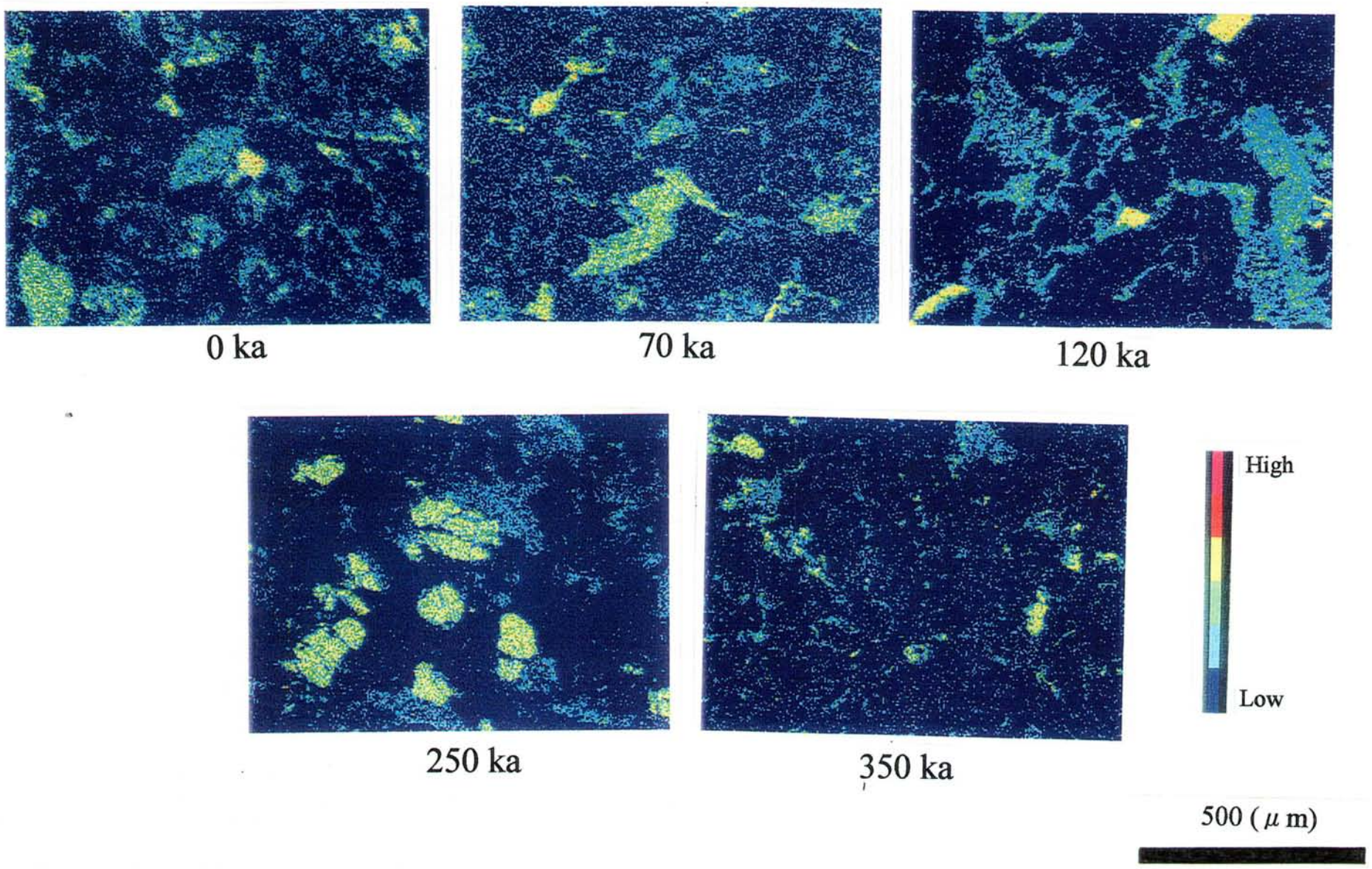

Fig. 49 Changes in K concentration constructed by EDS.

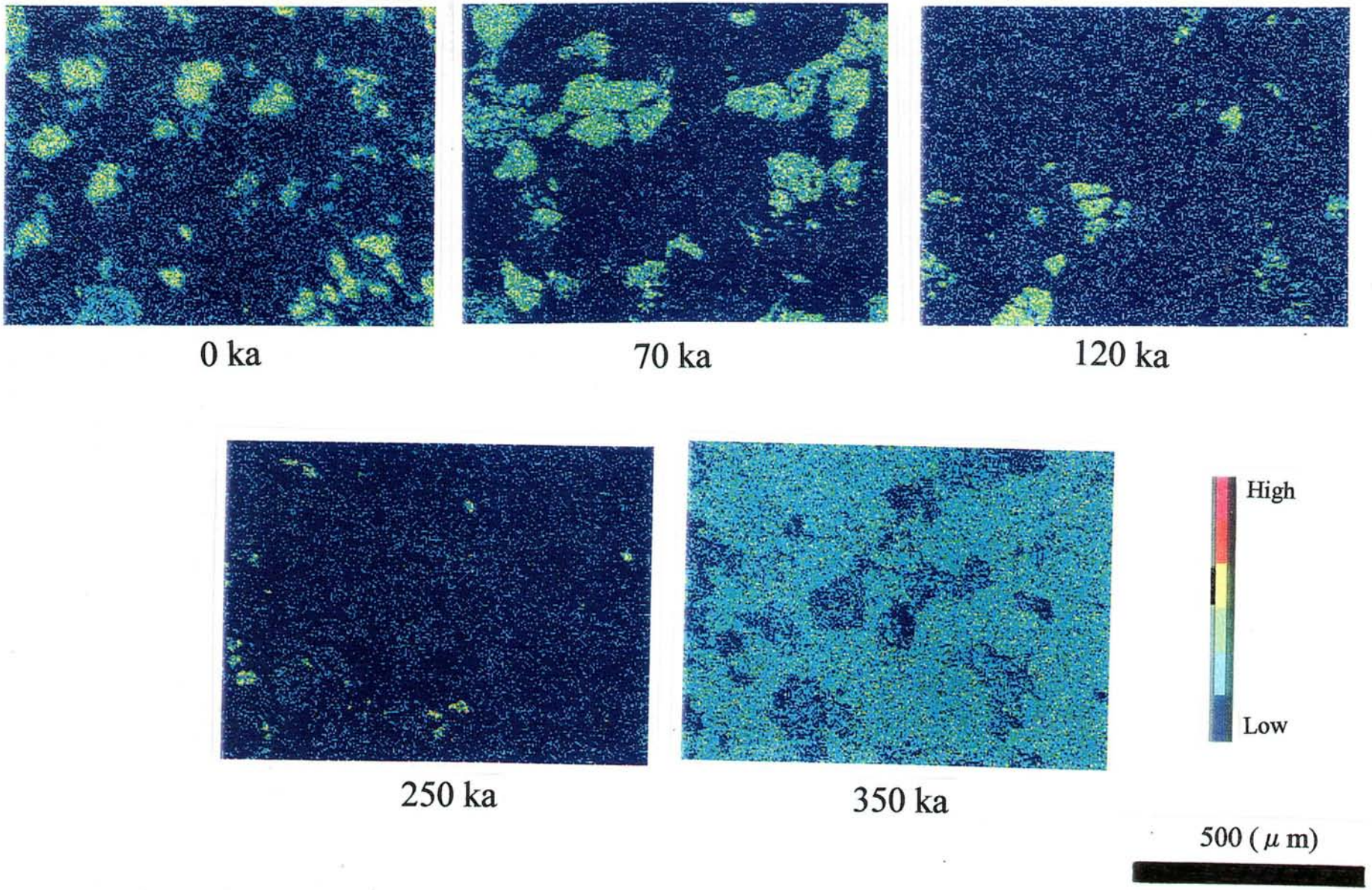

Fig. 50 Changes in Na concentration constructed by EDS.

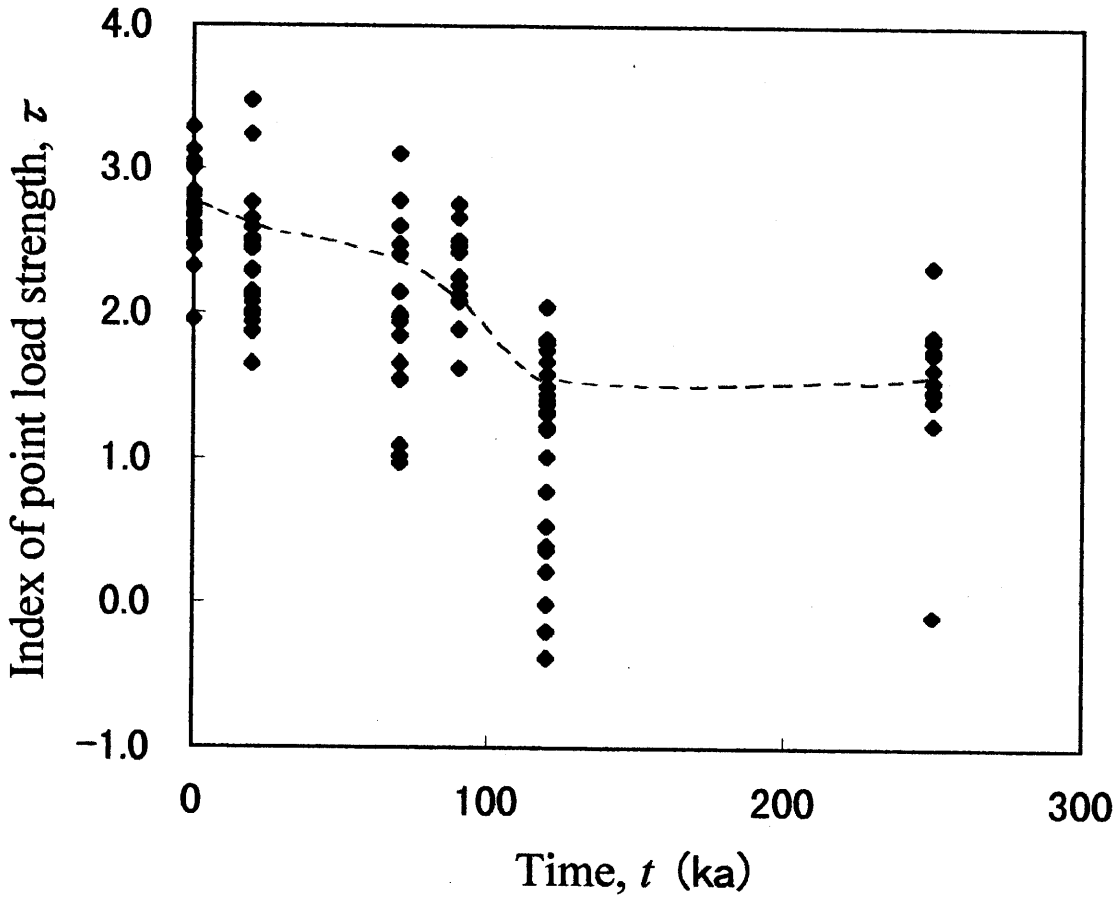

Fig. 51 Temporal changes in index of point load strength,τ.

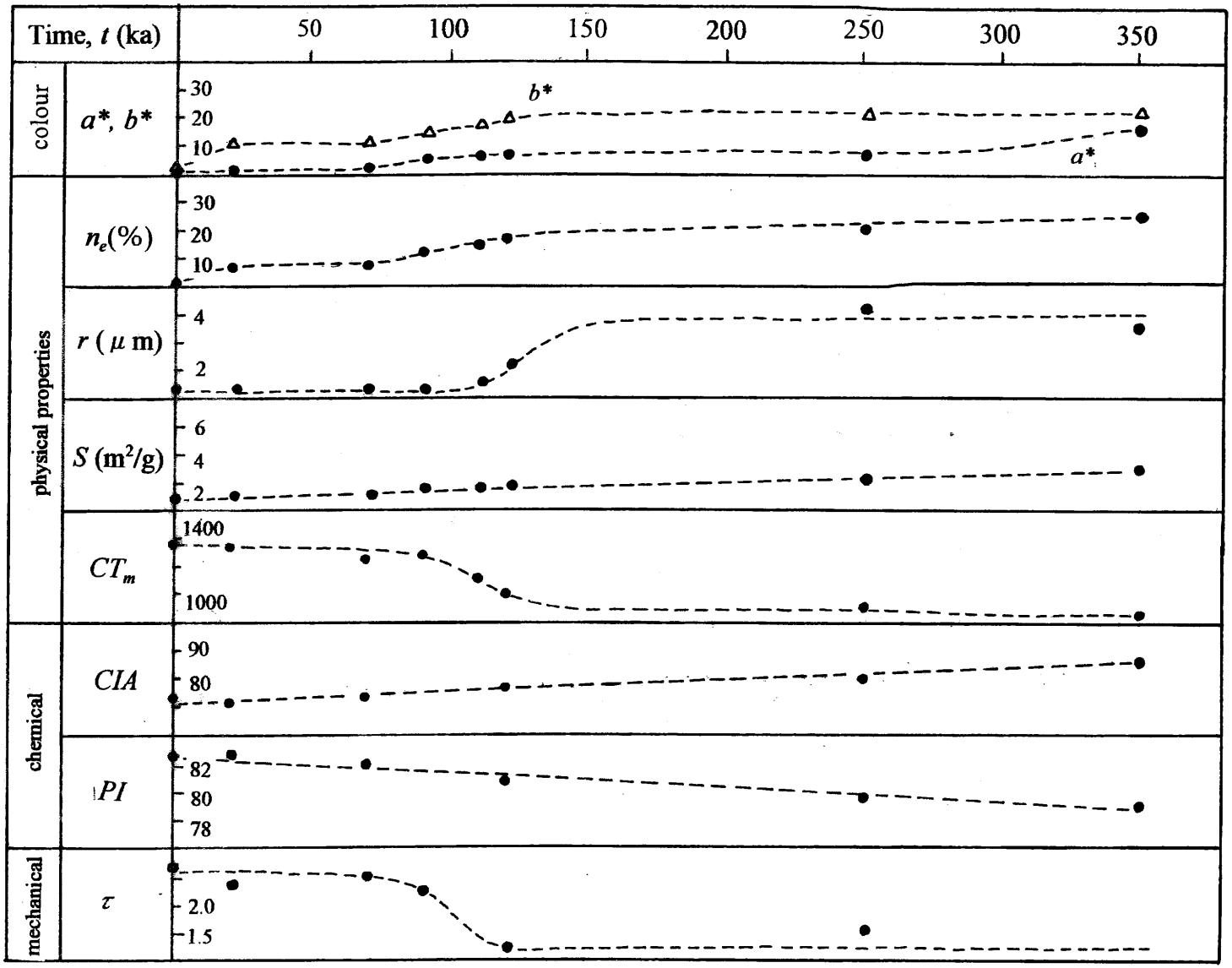

Fig. 52 An idealized diagram representry temporal changes in rock properties.

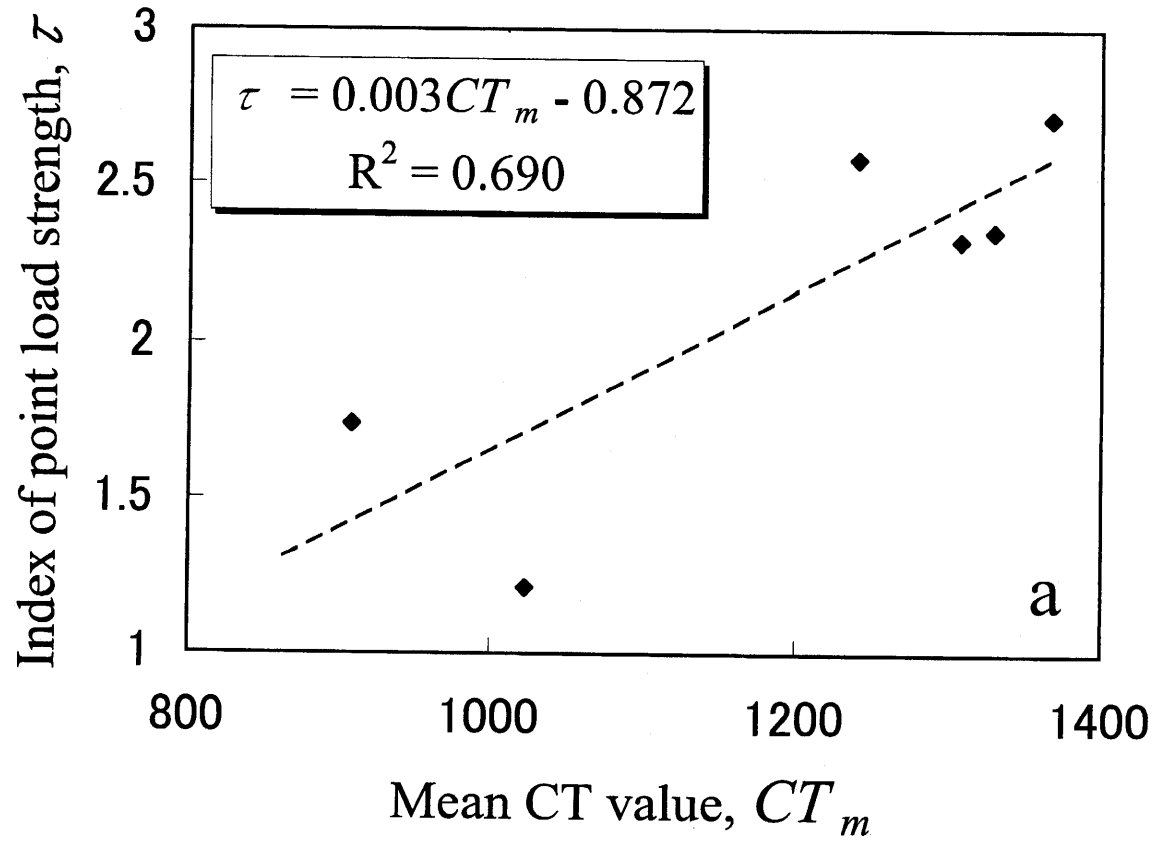

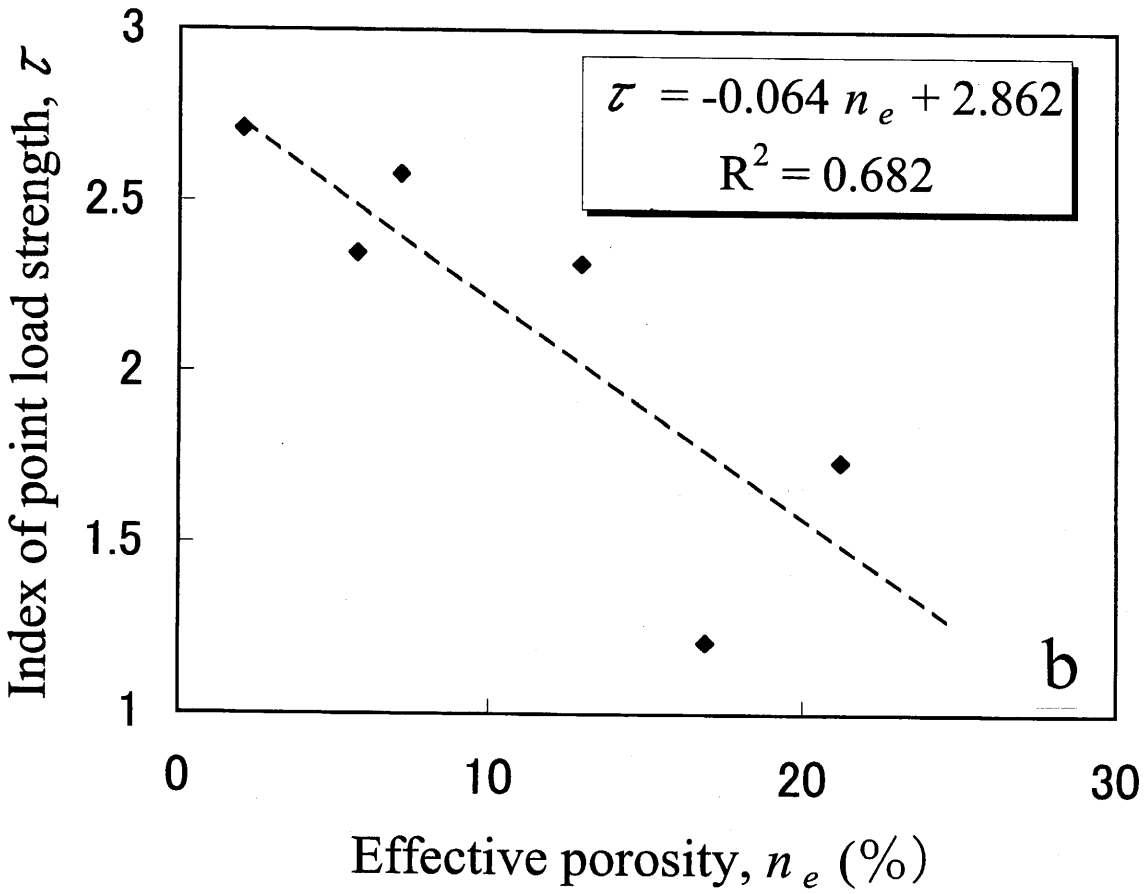

Fig. 53 Point load strength index, τ, as a function of CT_m (a), and effective porosity, n_e (b).

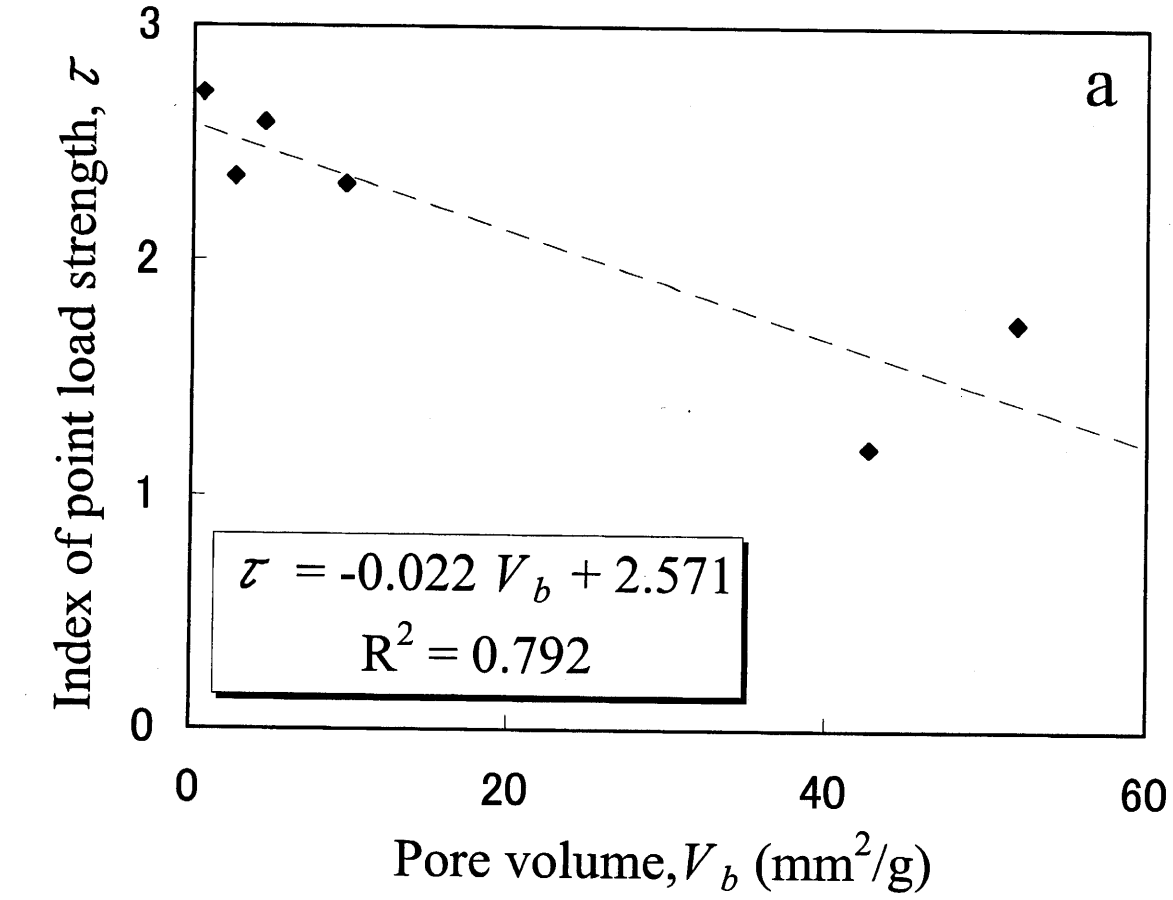

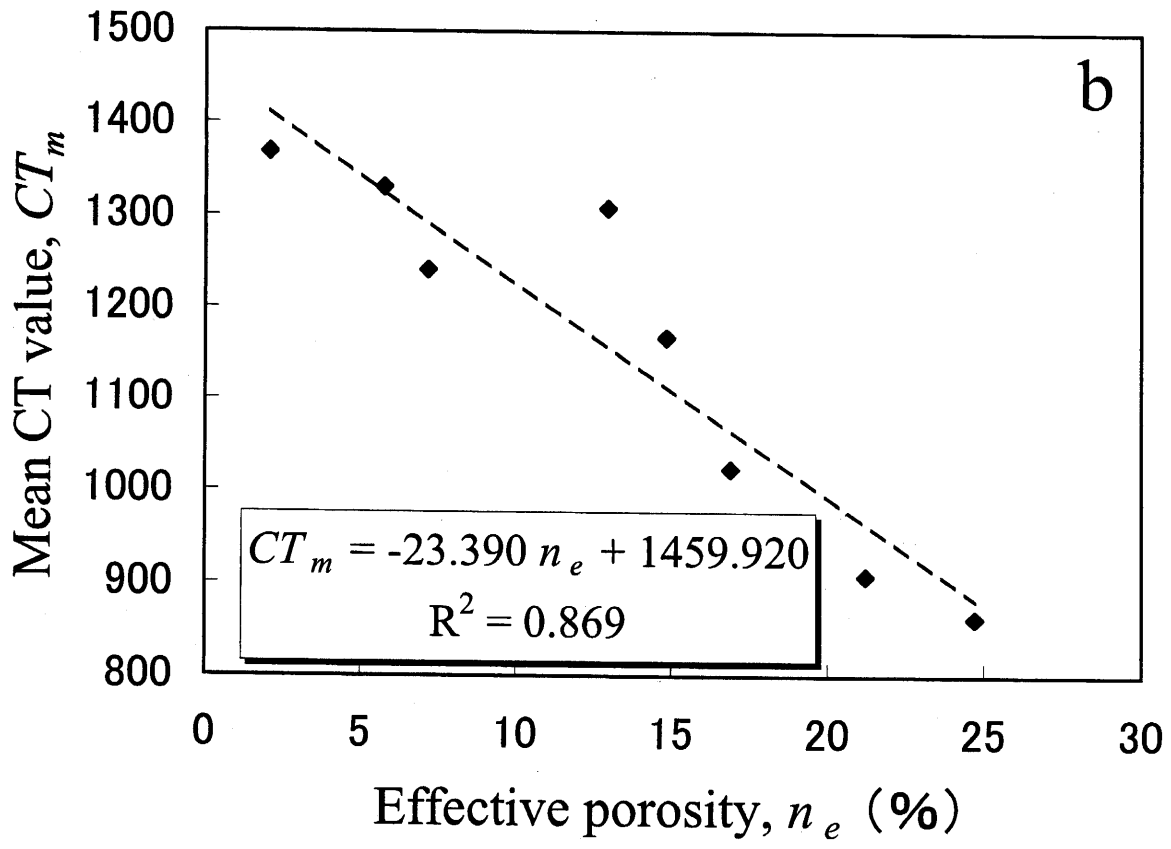

Fig. 54 Relationships between pore volume, V_b, and point load strength, τ, (a) and CT_m and n_e (b).

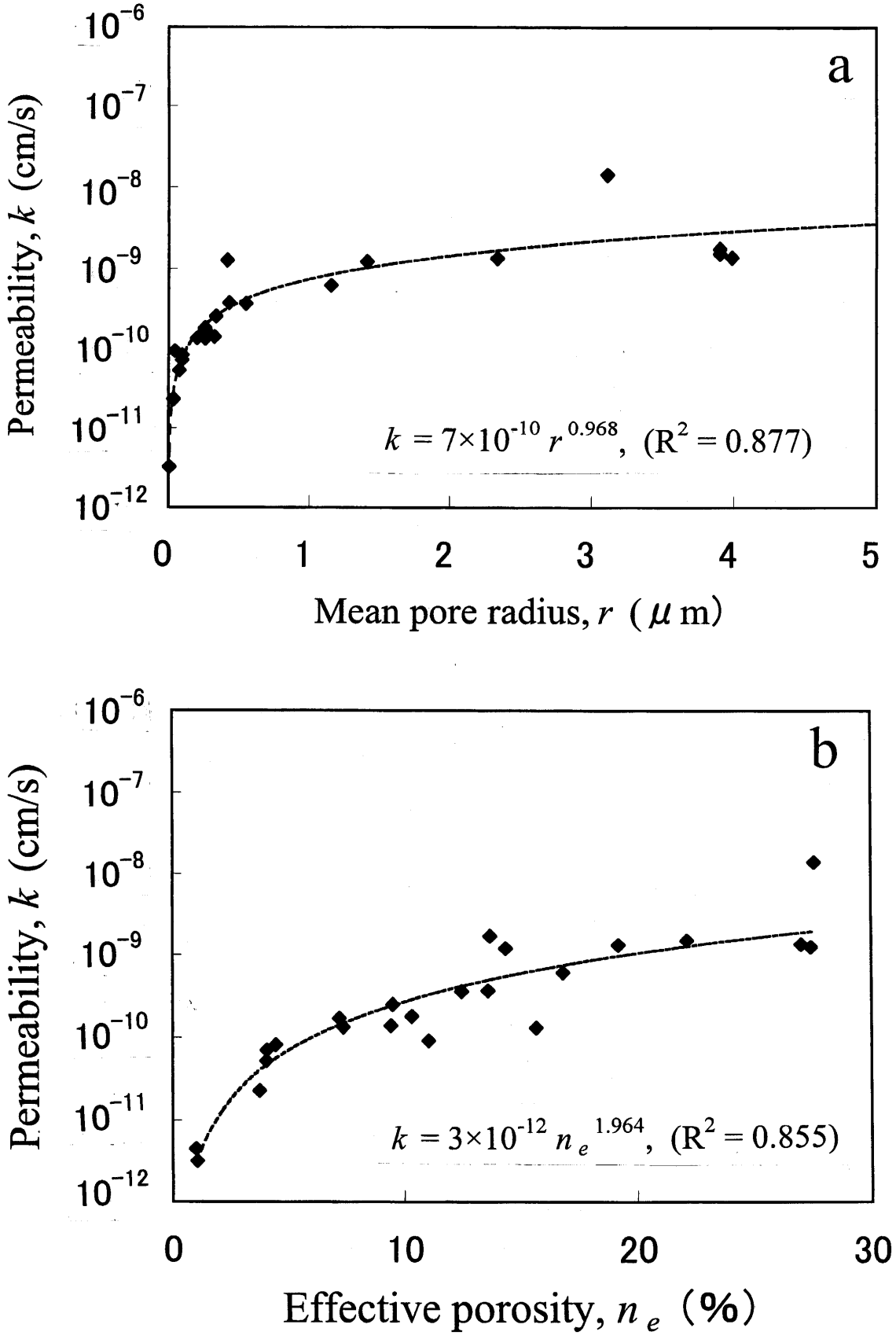

Fig. 55 Permeability, k, as a function of mean pore radius, r (a), and effective porosity, n_e (b).

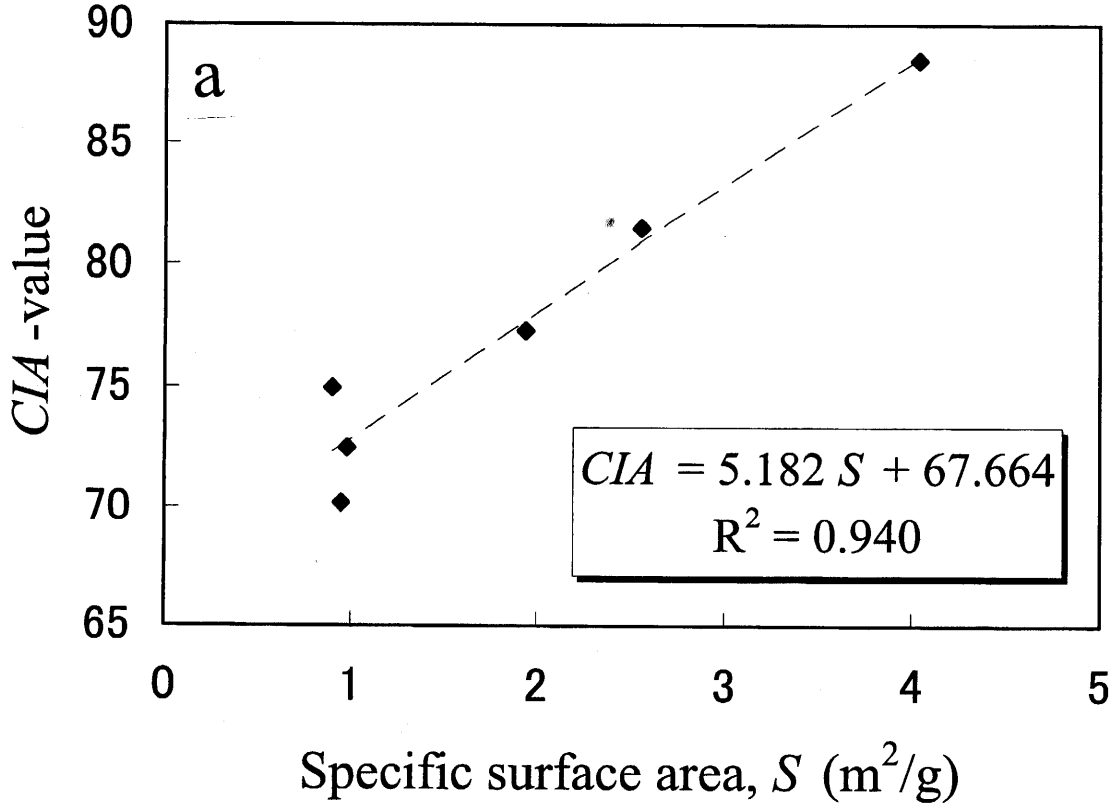

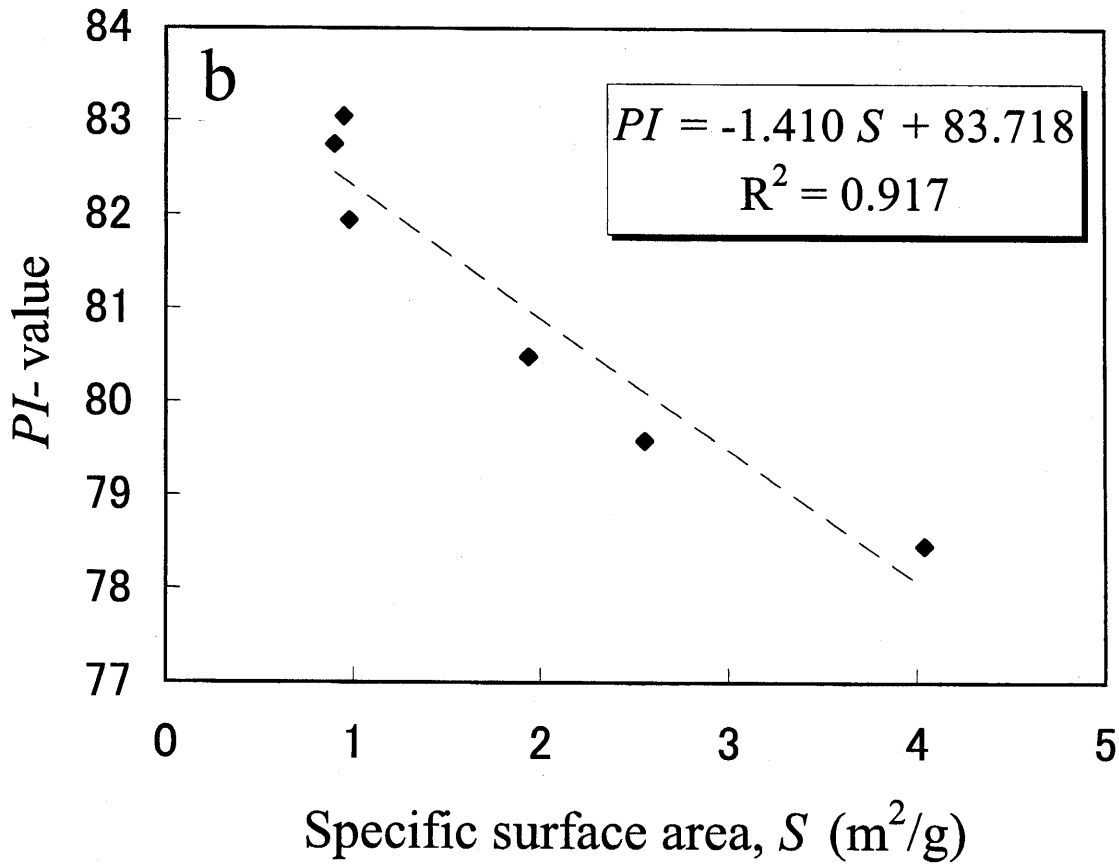

Fig. 56 Specific surface area, *S*, as a function of *CIA*-value (a), and *PI*-value (b).

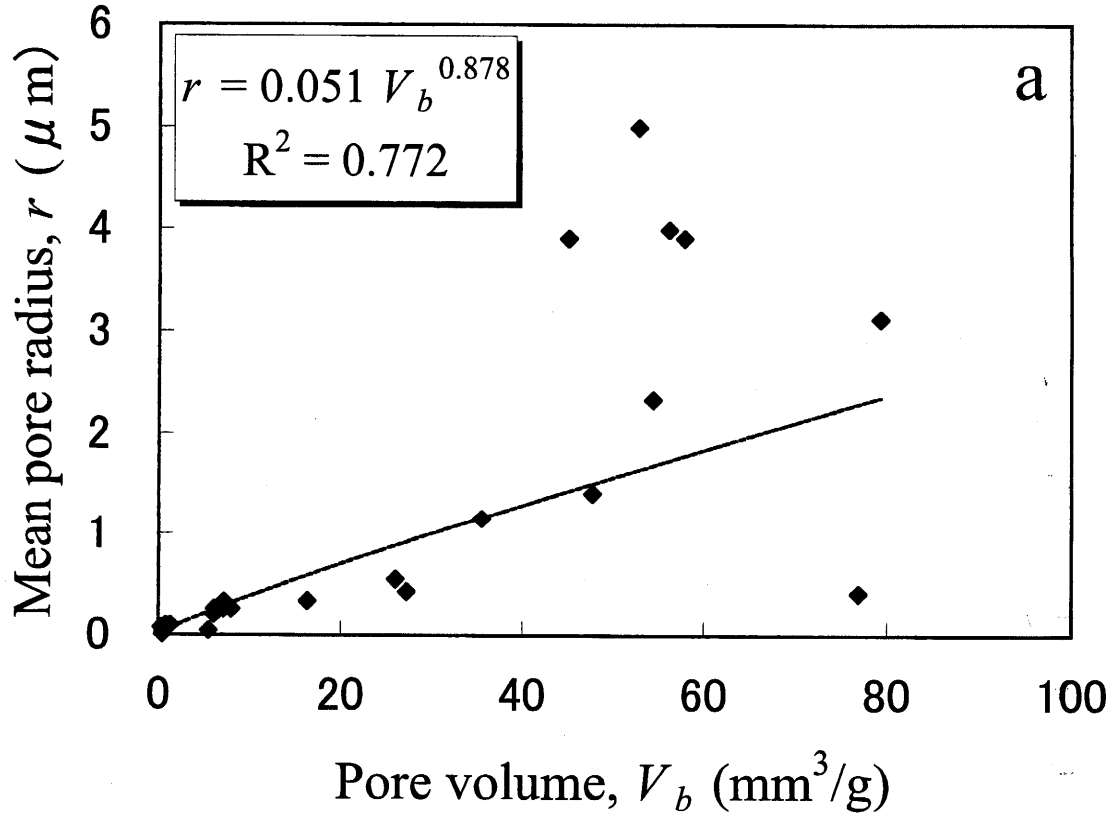

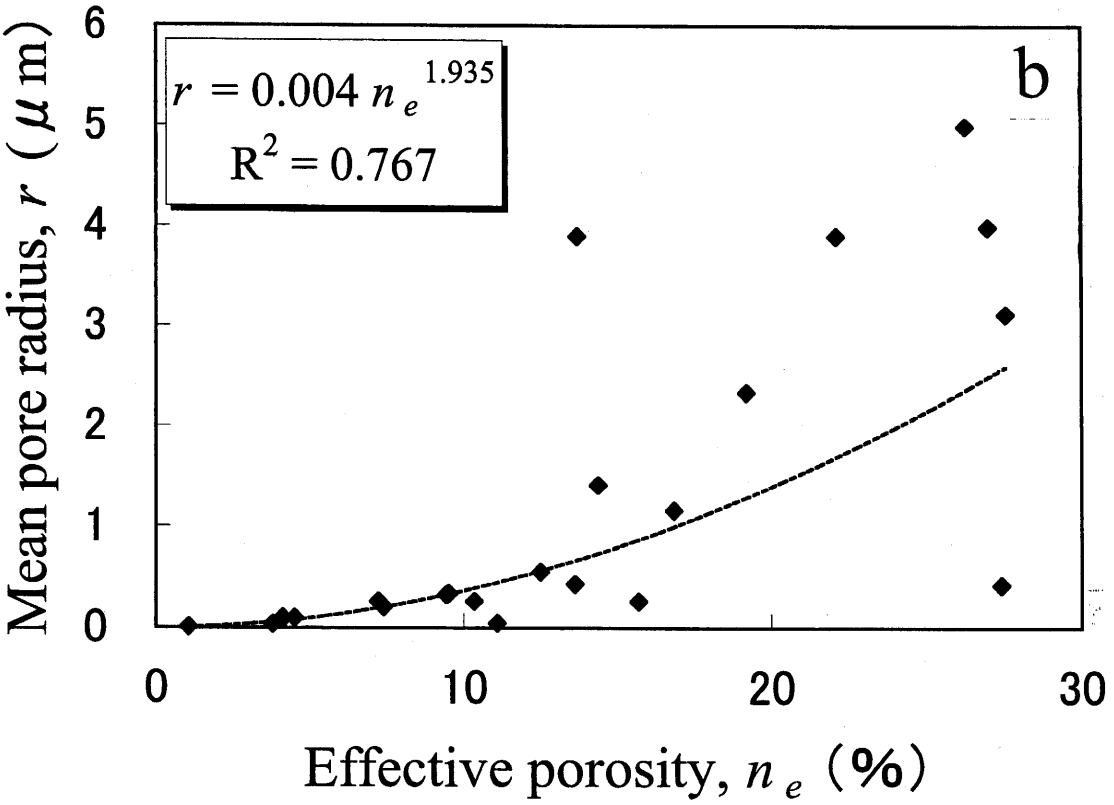

Fig. 57 Mean pore radius, r, as a function of pore volume, V_b (a) and effective porosity, n_e (b).

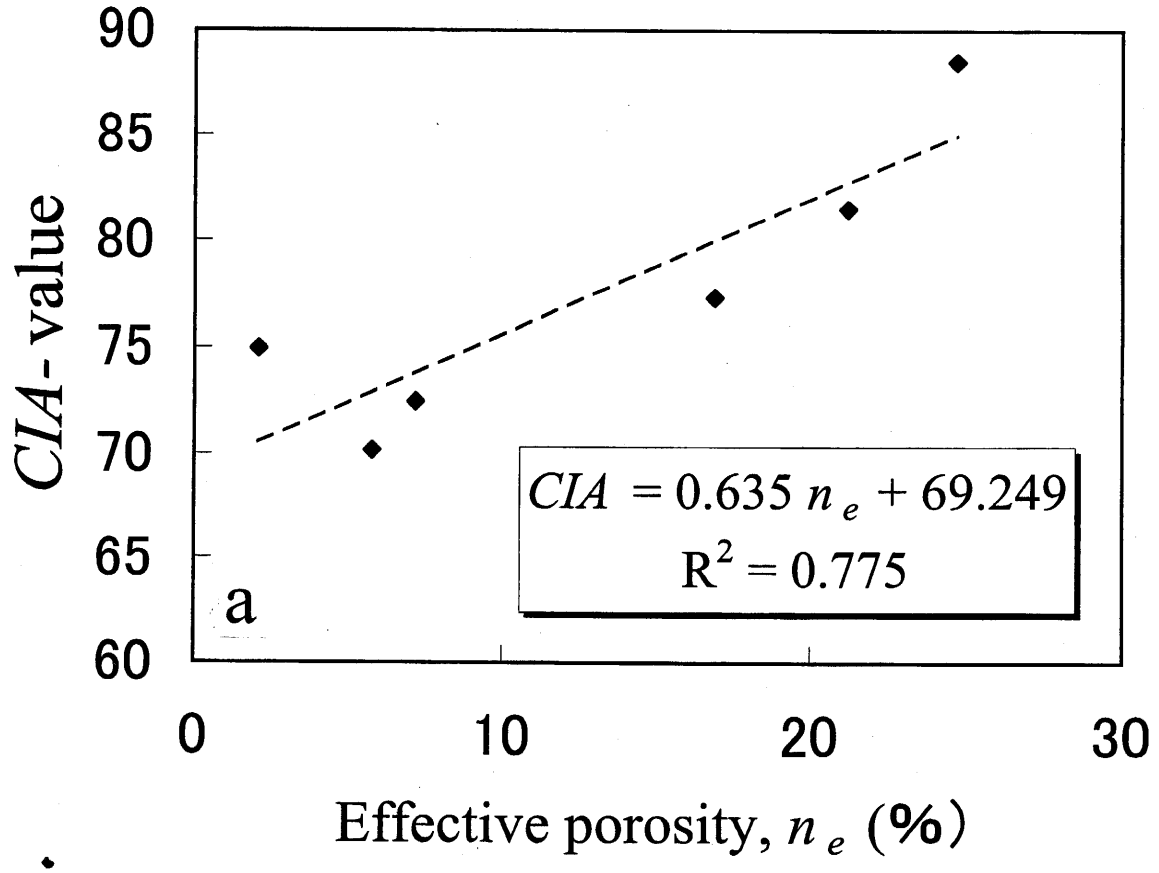

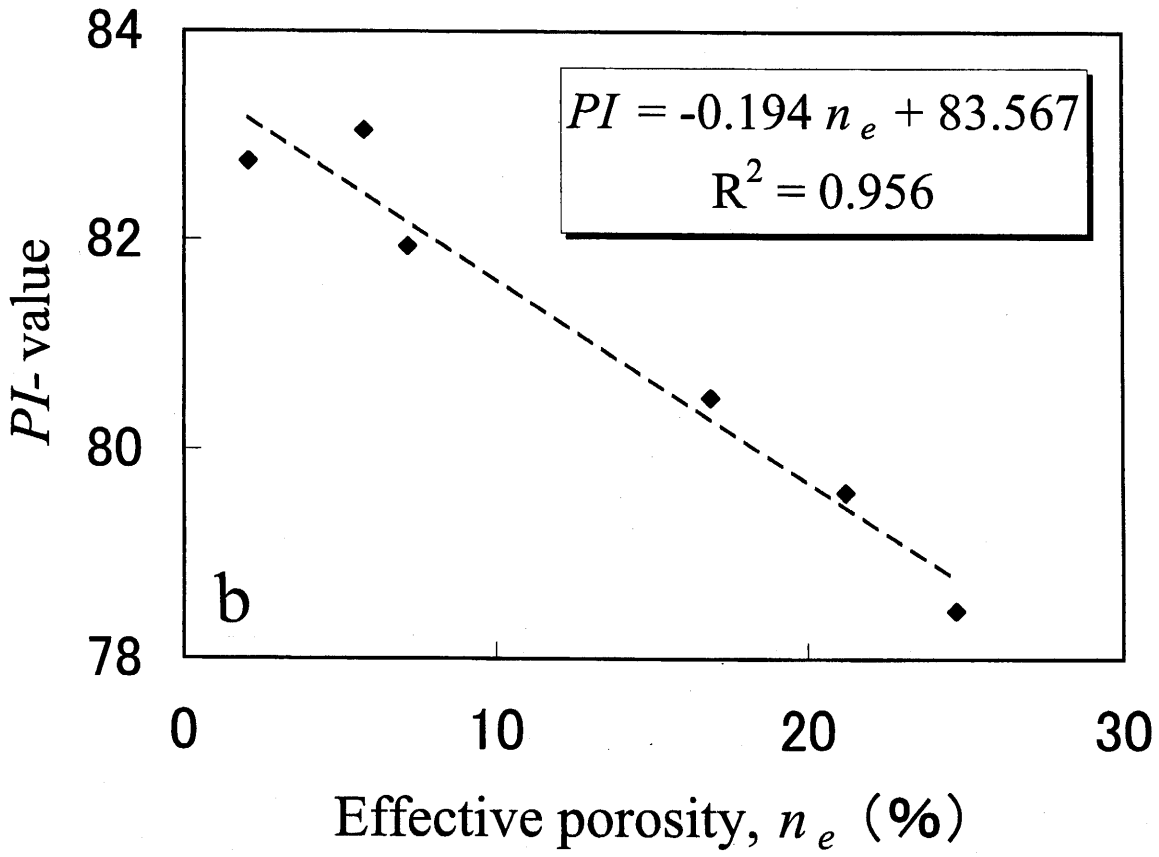

Fig. 58 Effective porosity, n_e, as a function of *CIA*-value (a), and *PI*-value (b).

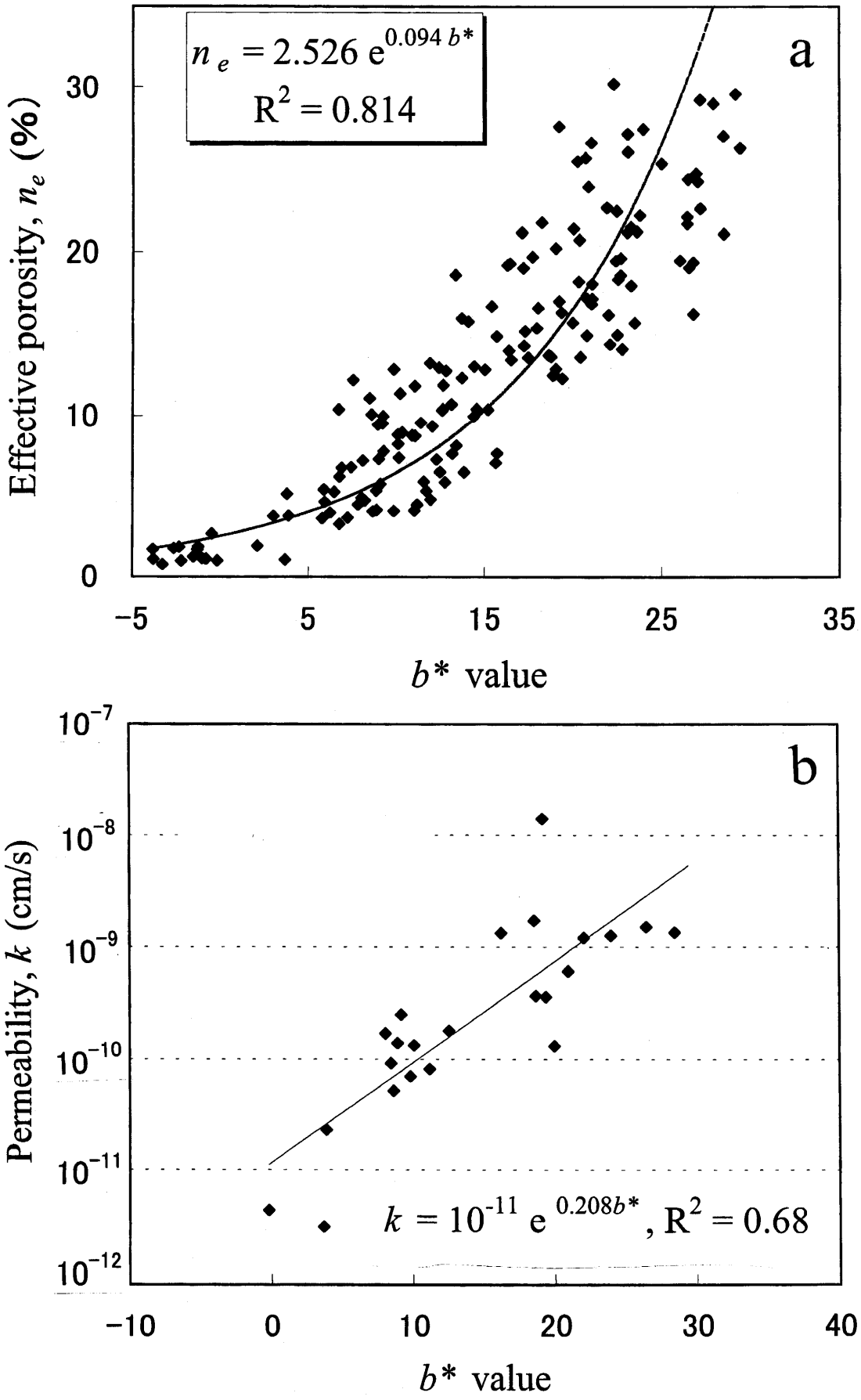

Fig. 59 Relationships between effective porosity, n_e and b^*-value (a), and permeability, k, and b^*-value (b).

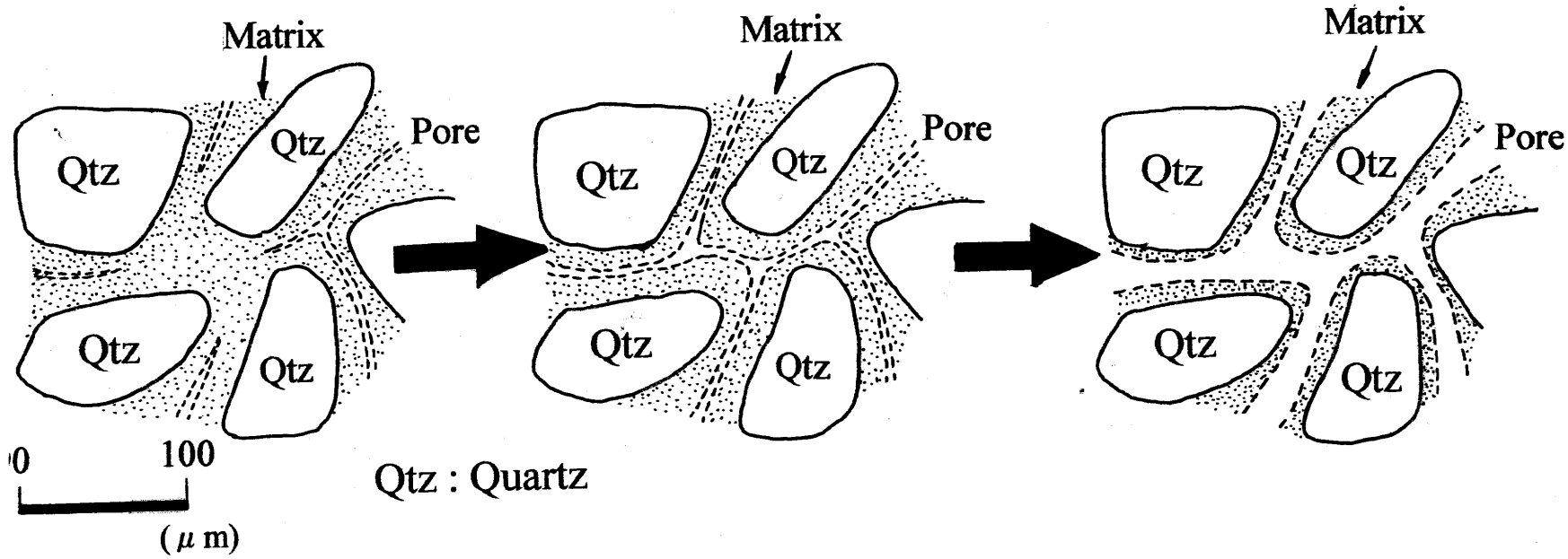

Fig. 60 Changes in pore structure of sandstone gravel.

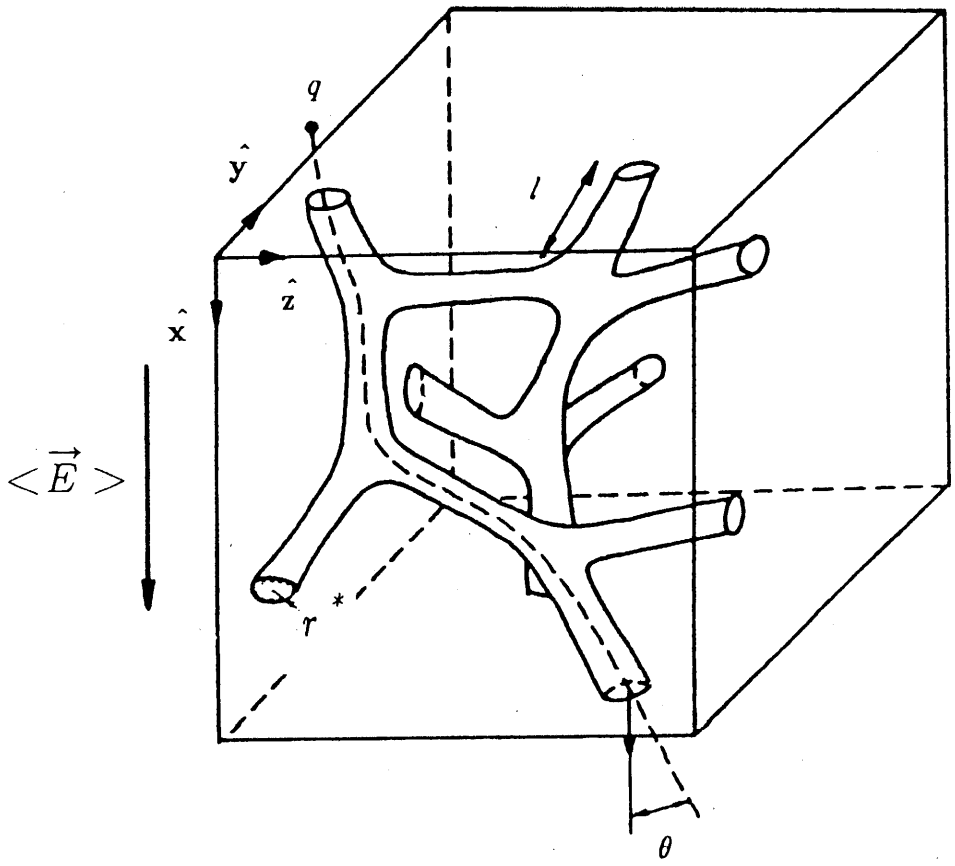

Fig. 61 Model of pore structure in sandstone (after Doyen, 1988).

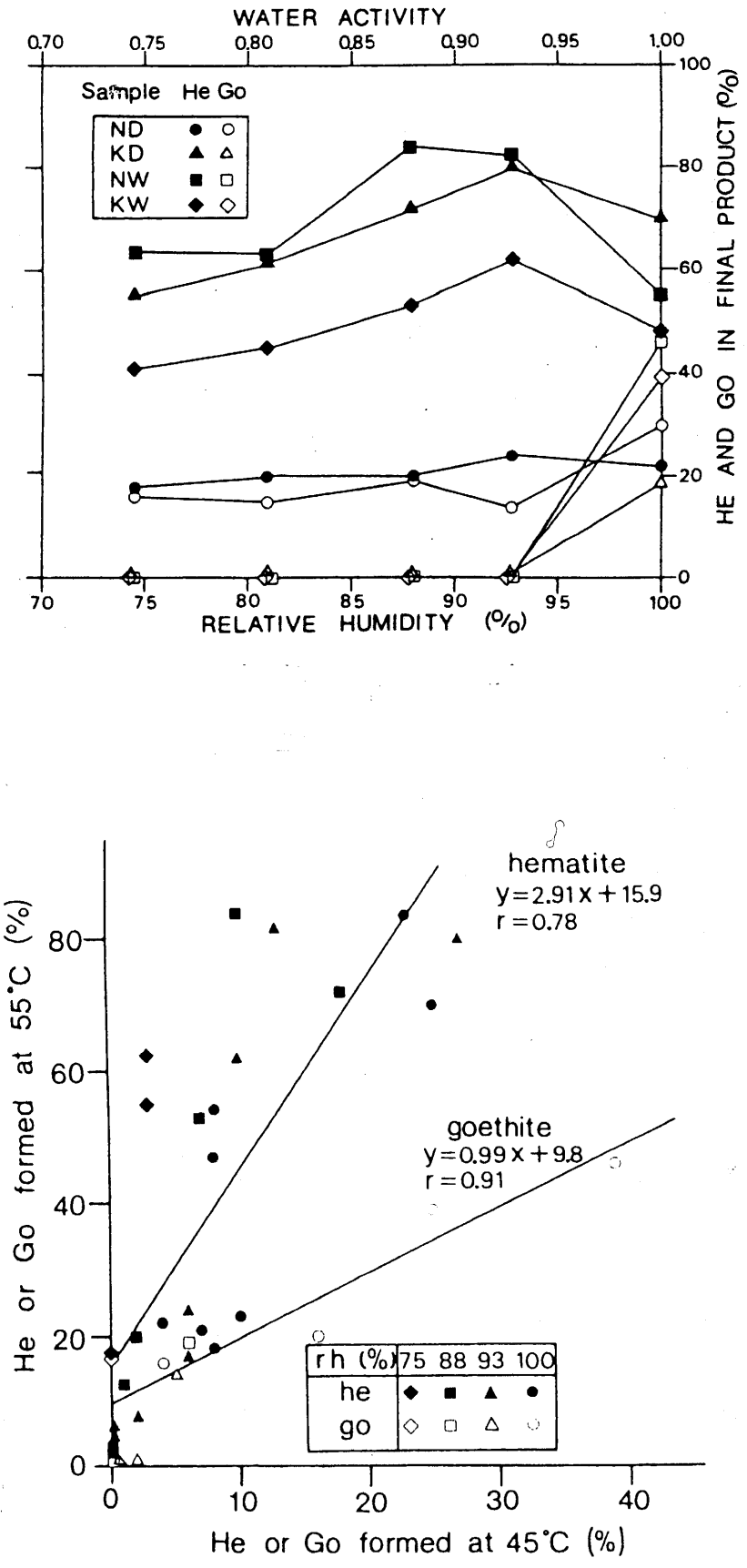

Fig. 62 Changes in Fe minerals (after Torrent et al., 1982).

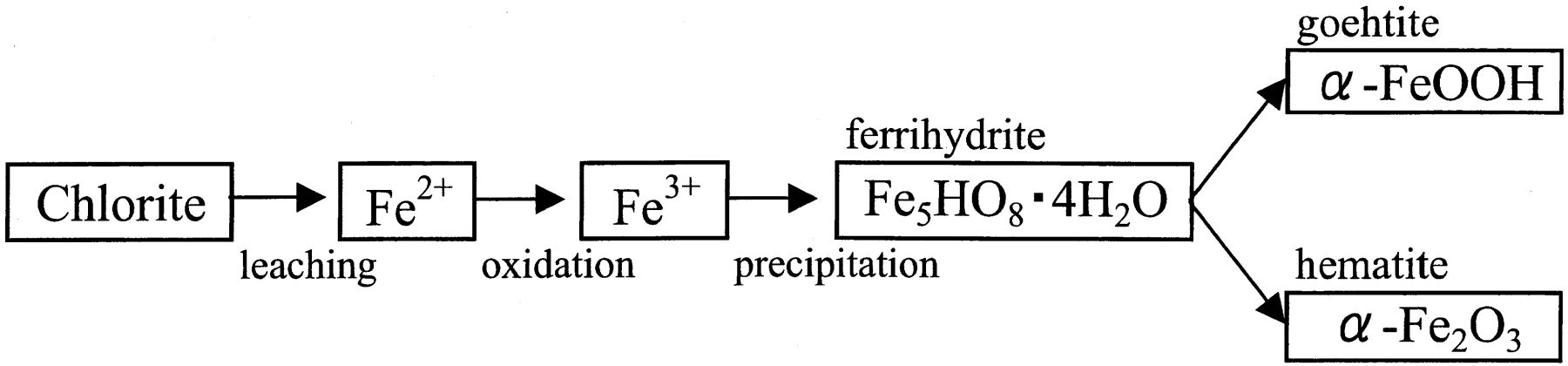

Fig. 63 Changes in Fe minerals in sandstone gravel.

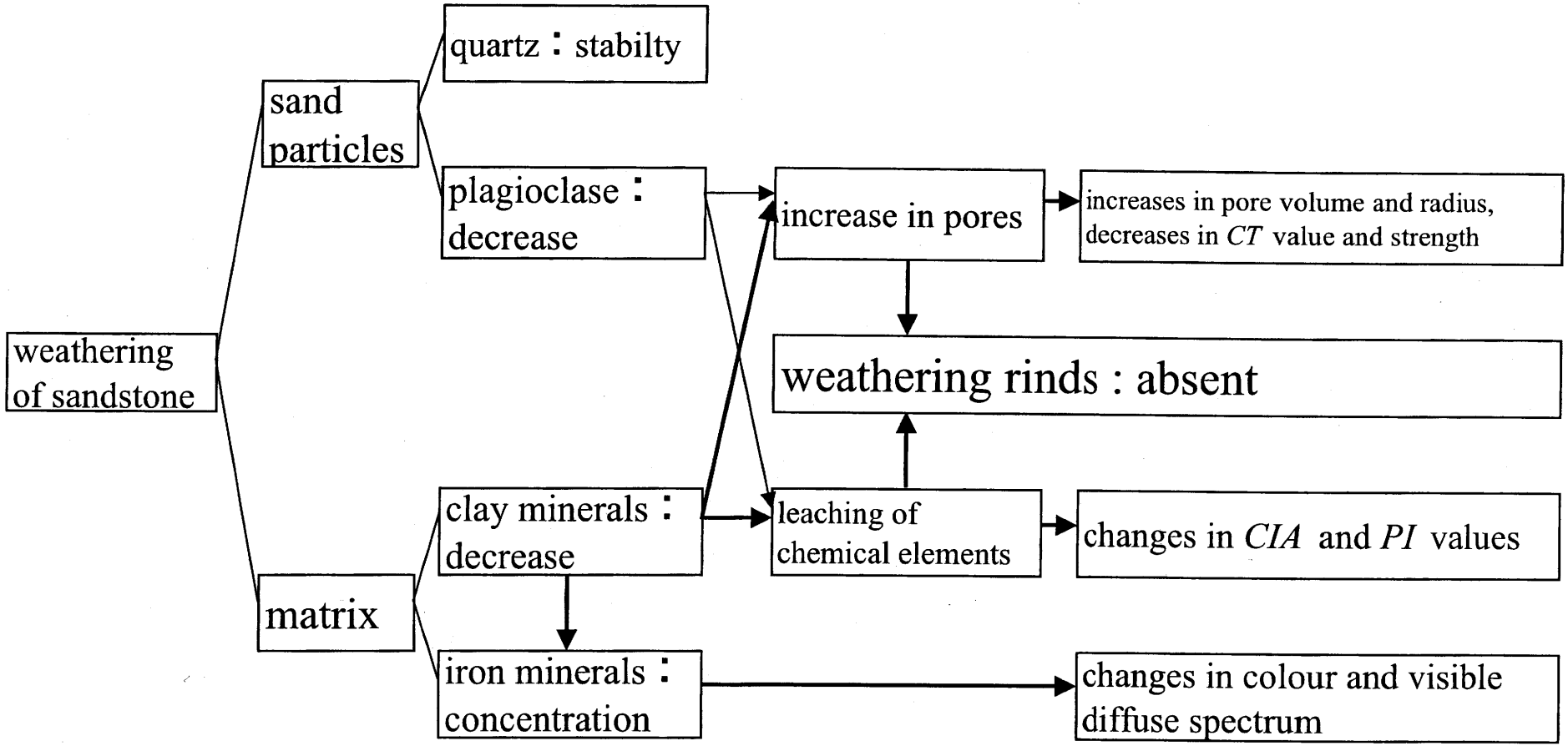

Fig. 64 General diagram of weathering mechanism of sandstone.

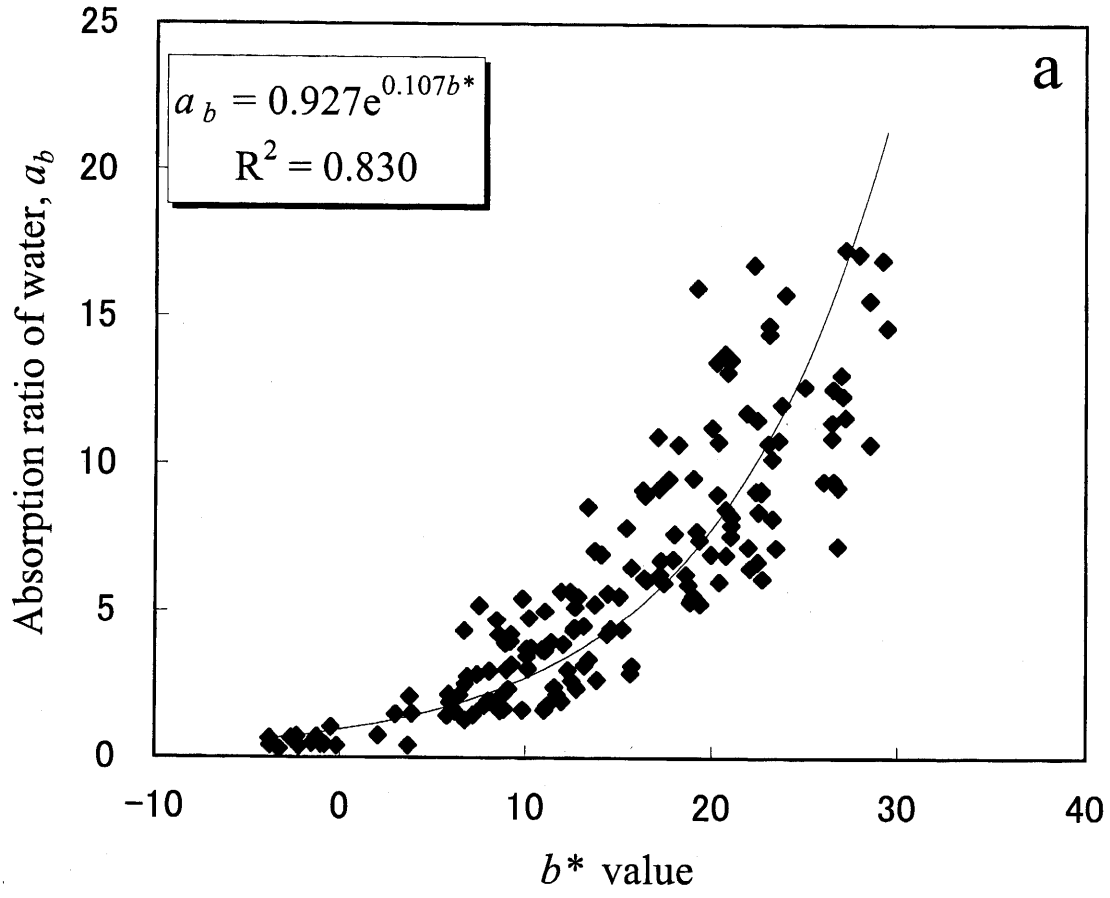

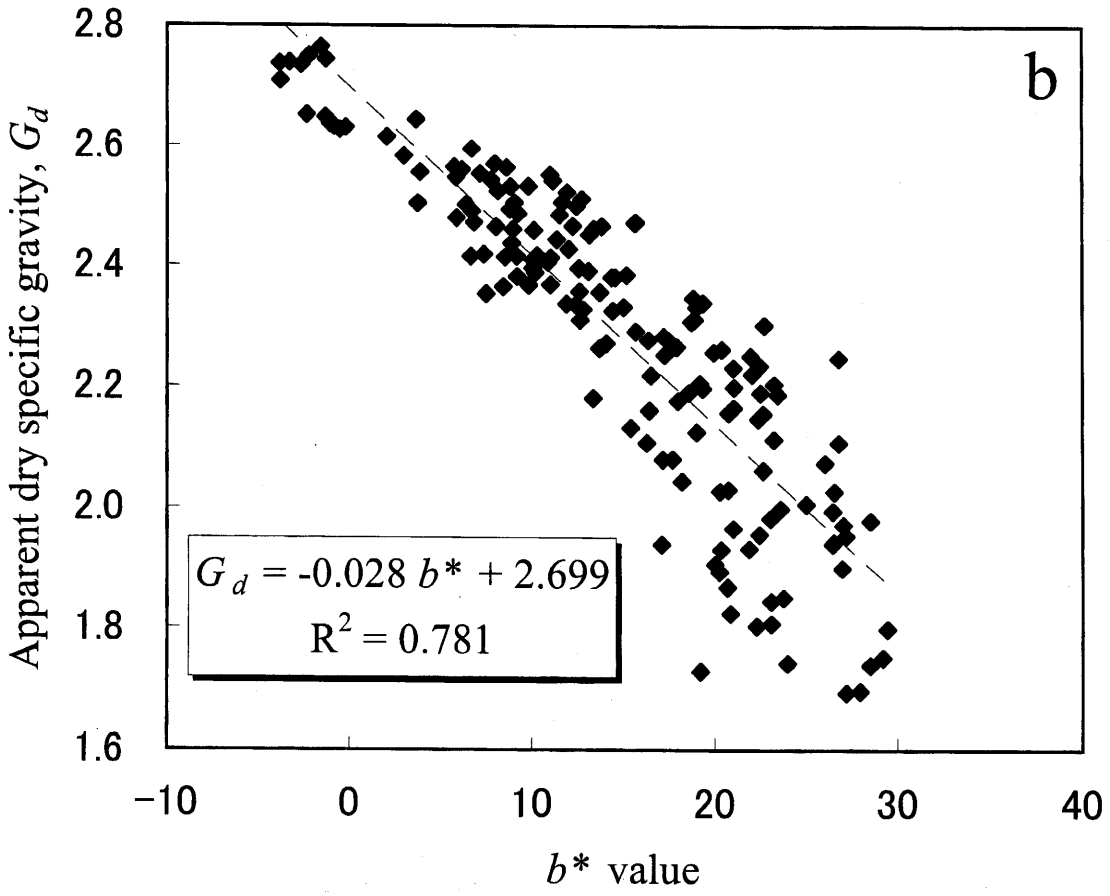

Fig. 65 The $b*$-value, as a functions of absorption ratio of water, a_b (a), and apparent specific gravity, G_d (b).